THE UNIVERSITY of EDINBURGH

Title	Probing dark matter with intrinsic and extrinsic galaxy alignments
Author	Brown, Michael
Qualification	PhD
Year	2003

Probing Dark Matter with Intrinsic and Extrinsic Galaxy Alignments

MICHAEL BROWN

Institute for Astronomy
School of Physics

University of Edinburgh
Doctor of Philosophy

May 2003

Abstract

I present the results of an investigation into the distribution of Dark Matter via observations and analysis of both the intrinsic alignment of galaxy shapes and the weak gravitational lensing signal due to the large-scale structure of the Universe.

The distribution of Dark Matter in the non-local Universe ($z \sim 0.5$) is investigated with a statistical weak lensing or 'cosmic shear' analysis of the COMBO-17 survey — a unique dataset with deep R-band imaging and accurate photometric redshift information for galaxies to $m_{\rm R} \leq 24.0$. A full maximum likelihood reconstruction of the weak lensing convergence power spectrum, $C_\ell^{\kappa\kappa}$ is applied to the data and a strong measurement of the convergence power is found over the five fields of the survey. This analysis represents the most direct measurement of the clustering properties of the Dark Matter ever obtained. The measurements are compared to the currently popular ΛCDM cosmological model and show good agreement. The results have also been used to measure cosmological parameters. The normalisation of the matter power spectrum is constrained to be $\sigma_8 = (0.72 \pm 0.09)(\Omega_m/0.3)^{-0.50}$ where the errors quoted are 1-σ due to the intrinsic dispersion in galaxy ellipticities, cosmic and sampling variance. Finally, the weak lensing measurements have been combined with results from the 2dF Galaxy Redshift Survey and with those from recent Cosmic Microwave Background experiments. With these additional constraints, the normalisation of the matter power spectrum is found to be $\sigma_8 = 0.73^{+0.06}_{-0.03}$ and the matter density to be $\Omega_m = 0.27 \pm 0.02$.

The alignment of galaxy shapes in the local Universe ($z \sim 0.1$) is detected and measured with the digitized SuperCOSMOS Sky Survey. In this analysis, the shapes of 2×10^6 galaxies from approximately 10 000 deg^2 of sky are analysed and are found to be correlated with one another at a small but significant level. A new minimum variance estimator is applied to this sample of galaxies yielding ellipticity variance measurements in the range $2 \times 10^{-4} \geq \sigma_\varepsilon^2(\theta) \geq 1 \times 10^{-5}$ over a range of scales between 1 and 100 arcmin. This correlation is detected in two colours, $b_{\rm J}$ and R and, most significantly, in the cross-correlation between the two bands, which is less likely to be contaminated by systematics. These measurements are compared with recent analytical and numerical predictions made for the intrinsic shape alignment and rough agreement is found, although the predictions for the alignment are inconclusive at present. The implications of these measurements for weak lensing studies are examined. The measurements imply that the intrinsic shape alignment effect will dominate over the weak lensing signal for shallow surveys (*e.g.* the Sloan Digital Sky Survey) while it will contribute $\lesssim$10% of the signal seen in deeper weak lensing studies with $z \sim 1$.

Declaration

I hereby declare that this thesis entitled *Probing Dark Matter with Intrinsic and Extrinsic Galaxy Alignments* is not substantially the same as any that I have submitted for a degree or diploma or other qualification at any other University. I further state that no part of my thesis has already been or is being concurrently submitted for any such degree, diploma or other qualification.

Parts of the work contained in this thesis have been published in refereed scientific journals.

> Chapter 3 is based on work presented in the paper *"The shear power spectrum from the COMBO-17 survey"*, Brown M.L, Taylor A.N., Bacon D.J., Gray M.E., Dye S., Meisenheimer K., Wolf C., 2003, MNRAS, 341, 100.
>
> Chapter 4 is based on work presented in the paper *''Measurement of intrinsic alignments in galaxy ellipticities"*, Brown M.L., Taylor A.N., Hambly N.C., Dye S., 2002, MNRAS, 333, 501.

This thesis is the outcome of my own work except where specifically indicated in the text.

Michael Brown
Edinburgh,
May 2003.

Acknowledgements

First of all, I'd like to thank Andy for doing a great job in helping and guiding me up to this point. Also, thanks must go to collaborators I've worked with: David & Meg (definitely two of the top three weak lensers in Edinburgh!), Alan, Catherine, Nigel and also the Combo-17 collaboration for access to their excellent data.

Of course, not all (in fact, not that much!) of the last four years have been about science. For ensuring that this was the case, much appreciation must go to my flatmate, Rachel and my office mates over the last few years: Louisa, Ali, James, Olivia, Tara and Ian.

I am in my heart, of course, a family man and so, sincere thanks also go to James, Margaret & my mate, Gemma, Patrick, Loretta & little Mikey and not forgetting, of course, Vina.

Finally, and most important of all, I'd like to thank my Mum (a remarkable and inspirational woman!) and my Dad for turning me out the way I am today.

Go raibh mile maith agaibh,
Michael.

Contents

List of Figures

List of Tables

CHAPTER 1

Introduction

This thesis is primarily concerned with the subject of cosmology – the study of the content, nature and origin of the Universe as a whole. Throughout the last century, our understanding of this subject has made great leaps forward with major advances in both theory and observations. Consequently, we now have a vast array of methods and analysis techniques which can be used to probe the Universe on cosmological scales.

In this introductory chapter, we review the theoretical framework and major analysis techniques of observational cosmology. We concentrate on those statistical aspects of cosmology that will be useful for later chapters. We first consider the Friedmann-Lemaître-Robertson-Walker standard cosmological model, which we use as a basis for all that follows. We then go on to list the various observational probes of cosmology that are available to us, and we describe how we can qualify and quantify what we observe.

Since this thesis is primarily concerned with investigating matter (particularly, *dark matter*) in the Universe, in this chapter, we also describe how to measure the total matter distribution, and we outline the motivation for believing in the existence of dark matter. Finally, we briefly list and discuss the various dark matter candidates.

1.1 Standard Models of Cosmology

The nature of space-time can be described by (*e.g.* Peacock 1999) the *metric*, $g_{\mu\nu}$, which can be used to construct the "separation", ds of two events in the 4-dimensional space-time:

$$ds^2 = g_{\mu\nu} dx^\mu dx^\nu. \tag{1.1}$$

Invoking the cosmological principle (which states that the Universe is both homogeneous and isotropic) requires the metric to take the following form:

$$ds^2 = c^2 dt^2 - a^2(t) \left[dw^2 + f_k^2(w) \left(d\theta^2 + \sin^2\theta d\phi^2 \right) \right], \tag{1.2}$$

where w, θ and ϕ are the usual spherical polar coordinates, t is the time and $a(t)$ is the scale factor of the Universe. Equation (1.2) is known as the **Robertson-Walker (RW) metric** after the two scientists who first derived it independently in 1936. The function, $f_k(w)$ is either a trigonometric, linear or hyperbolic function of the radial coordinate, w, depending on whether the curvature, k is positive, zero or negative:

$$f_k(w) = \begin{cases} k^{-1/2} \sin(k^{1/2} w) & \text{if } k > 0 \\ w & \text{if } k = 0 \\ -k^{-1/2} \sinh(-k^{1/2} w) & \text{if } k < 0 \end{cases}. \tag{1.3}$$

Alternatively, the metric can be written in terms of $r = f_k(w)$ as

$$ds^2 = c^2 dt^2 - a^2(t) \left[\frac{dr^2}{1 - kr^2} + r^2 \left(d\theta^2 + \sin^2\theta d\phi^2 \right) \right]. \tag{1.4}$$

The metric evolves according to Einstein's gravitational field equations:

$$R^{\mu\nu} - \frac{1}{2} g^{\mu\nu} R = -\frac{8\pi G}{c^4} T^{\mu\nu}, \tag{1.5}$$

where $g^{\mu\nu}$ is the matrix inverse to $g_{\mu\nu}$, $R^{\mu\nu}$ is the Ricci tensor, R is the Ricci scalar and $T^{\mu\nu}$ is the **energy-momentum tensor** (or *stress-energy tensor*). For example, the energy-momentum tensor of a perfect fluid can be written as (*e.g.* Peacock 1999)

$$T^{\mu\nu} = (\rho + p/c^2) U^\mu U^\nu - p g^{\mu\nu}, \tag{1.6}$$

where we have introduced the density, ρ, pressure, p and 4-velocity, U^μ of the fluid. The reasoning behind the energy-momentum tensor's name becomes apparent when we use it to express conservation of 4-momentum (composed of normal vector momentum and energy):

$$T^{\mu\nu}_{;\nu} = 0. \tag{1.7}$$

What results from combining equations (1.4) and (1.5) is two independent Einstein equations:

$$\left(\frac{\dot{a}}{a}\right)^2 + \frac{kc^2}{a^2} = \frac{8\pi G}{3}\rho, \tag{1.8}$$

$$2\left(\frac{\ddot{a}}{a}\right) + \left(\frac{\dot{a}}{a}\right)^2 + \frac{kc^2}{a^2} = -8\pi G\frac{p}{c^2}. \tag{1.9}$$

Equation (1.8) is the Friedmann equation, which relates the total density, ρ (including contributions from matter, radiation and vacuum) of the Universe to its global geometry. We see immediately from equation (1.8) that for a given rate of expansion, there exists a **critical density**, ρ_c for which $k = 0$:

$$\rho_c = \frac{3H(t)^2}{8\pi G}. \tag{1.10}$$

Here, we have introduced the Hubble parameter, $H(t) = \dot{a}(t)/a(t)$. Subtracting (1.8) from (1.9) gives:

$$\frac{\ddot{a}}{a} = -4\pi G\left(\frac{\rho}{3} + \frac{p}{c^2}\right). \tag{1.11}$$

This is the acceleration equation. We can also use equations (1.8) and (1.9) to construct the density continuity equation (or fluid equation):

$$\dot{\rho} + 3\frac{\dot{a}}{a}\left(\rho + \frac{p}{c^2}\right) = 0. \tag{1.12}$$

The Friedmann and fluid equations can be used to give us various cosmological models. Some models for "flat" universes (ones in which $k = 0$) and the effect of a non-zero cosmological constant are described below.

1.1.1 Dust Dominated Universe

The term, "dust" is used to refer to all pressureless matter. For a dust dominated universe, the pressure, p is zero and this gives:

$$\rho \propto \frac{1}{a^3} \quad \text{or} \quad \rho = \frac{\rho_0}{a^3}, \tag{1.13}$$

where the scale-factor of the Universe at the current epoch, a_0 has been set to 1. Thus, from equation (1.8),

$$a(t) = \left(\frac{t}{t_0}\right)^{2/3} \quad ; \quad \rho(t) = \frac{\rho_0 t_0^2}{t^2}. \tag{1.14}$$

Then, Hubble's parameter is given by:

$$H(t) = \frac{\dot{a}}{a} = \frac{2}{3t}. \tag{1.15}$$

1.1.2 Radiation Dominated Universe

A radiation dominated universe is one which is dominated by relativistic particles, *i.e.* photons and neutrinos. The equation of state for a radiation dominated universe is:

$$p = \frac{\rho c^2}{3}, \tag{1.16}$$

which, combined with Friedmann's equation gives:

$$a(t) = \left(\frac{t}{t_0}\right)^{1/2} \quad ; \quad \rho(t) = \frac{\rho_0}{a^4} = \frac{\rho_0 t_0^2}{t^2}, \tag{1.17}$$

where again, ρ_0 and t_0 are the values of the density and age of the Universe at the present epoch.

1.1.3 Mixtures

We can also investigate how a universe with mixtures of radiation and dust would behave by writing:

$$\rho_{\rm m} \propto \frac{1}{a^3} \quad ; \quad \rho_{\rm r} \propto \frac{1}{a^4}\,,$$

where $\rho = \rho_{\rm m} + \rho_{\rm r}$. For a radiation dominated mixture,

$$a(t) \propto t^{1/2} \; ; \; \rho_{\rm r} \propto \frac{1}{t^2} \; ; \; \rho_{\rm m} \propto \frac{1}{t^{3/2}}\,, \tag{1.18}$$

and for a dust dominated mixture,

$$a(t) \propto t^{2/3} \; ; \; \rho_{\rm m} \propto \frac{1}{t^2} \; ; \; \rho_{\rm r} \propto \frac{1}{t^{8/3}}\,. \tag{1.19}$$

In equation (1.18), $\rho_{\rm r}$ falls off more rapidly than $\rho_{\rm m}$ and so a mixture universe dominated by radiation is an unstable situation. Eventually the dust will come to dominate. Conversely, we see in equation (1.19) that $\rho_{\rm m}$ falls off less rapidly than $\rho_{\rm r}$ and so a dust dominated mixture is stable.

The models described above are only valid for flat universes ($k = 0$ and the Universe expands forever!). However, k can take values other than 0. Consider again the Friedmann equation:

$$\left(\frac{\dot{a}}{a}\right)^2 + \frac{kc^2}{a^2} = \frac{8\pi G}{3}\rho\,.$$

If $k < 0$, it is clear that $\left(\frac{\dot{a}}{a}\right)^2 > 0$ for all ρ and a. So, the rate of expansion of the Universe, $\dot{a}$ never reaches 0 and again, the Universe expands forever. The $k < 0$ universe is referred to as an "open" universe. If $k > 0$, the expansion of the Universe stops when;

$$\frac{8\pi G}{3}\rho = \frac{kc^2}{a^2}\,.$$

When this happens, gravitational attraction takes over and the Universe collapses (towards presumably a "big crunch"). A universe with $k > 0$ is referred to as a "closed" universe.

1.1.4 Cosmological Constant

General relativity allows for the introduction of a "constant of integration" in the solution to the field equations. A non-zero value of this **cosmological constant**, Λ can be thought of as representing the energy density of empty space. Since Λ represents an energy density, it can also contribute to the density of the Universe. For a universe comprised of dust, radiation and a cosmological constant then, the total density is

$$\rho = \rho_{\rm m} + \rho_{\rm r} + \rho_\Lambda, \tag{1.20}$$

where ρ_Λ is the energy density content of Λ. We have already seen that the matter density scales as $\rho_{\rm m} \propto a^{-3}$ and the radiation density as $\rho_{\rm r} \propto a^{-4}$. The energy density in Λ, on the other hand is a constant: $\rho_\Lambda = \frac{\Lambda}{8\pi G} = \text{const}$. If we define a **density parameter** as the ratio of density to critical density, equation (1.10):

$$\Omega = \frac{\rho}{\rho_c} = \frac{8\pi G\rho}{3H^2}, \tag{1.21}$$

then (denoting density parameters at the current epoch with a subscript, 0) we can write the total density of the Universe as

$$\frac{8\pi G\rho}{3} = H_0^2(\Omega_{\Lambda,0} + \Omega_{\rm m,0}a^{-3} + \Omega_{\rm r,0}a^{-4}). \tag{1.22}$$

We now have the total density of the Universe expressed in terms of the observables, $\Omega_{\rm m,0}, \Omega_{\rm r,0}$ and $\Omega_{\Lambda,0}$. Note that, although the energy density of Λ, ρ_Λ, is a constant, the corresponding density parameter, Ω_Λ is a function of the scale factor, a (since the critical density is a function of a!). For a flat ($k = 0$) universe, we need $\sum_i \Omega_i = 1$ at all times and so the inclusion of a cosmological constant can alter our above conclusions regarding open and closed universes drastically. The effect of a non-zero cosmological constant is demonstrated in Fig. 1.1. The line, $k = 0$ represents the boundary between open and closed universes and points on this line ($\Omega_\Lambda + \Omega_{\rm m} = 1$) correspond to flat models. The introduction of a non-zero cosmological constant allows new types of universes to be envisaged. For example, a closed universe with a low matter density is possible as long as Ω_Λ is large enough. Also, if Ω_Λ is very large, universes can be conceived without the need for a "big bang" (upper left hand corner of Fig. 1.1). Note that with the inclusion of the cosmological constant, the Friedmann equation is normally written as

$$\left(\frac{\dot{a}}{a}\right)^2 + \frac{kc^2}{a^2} = \frac{8\pi G}{3}\rho + \frac{\Lambda}{3}, \tag{1.23}$$

and the density parameter for Λ is

$$\Omega_\Lambda = \frac{\Lambda}{3H^2}. \tag{1.24}$$

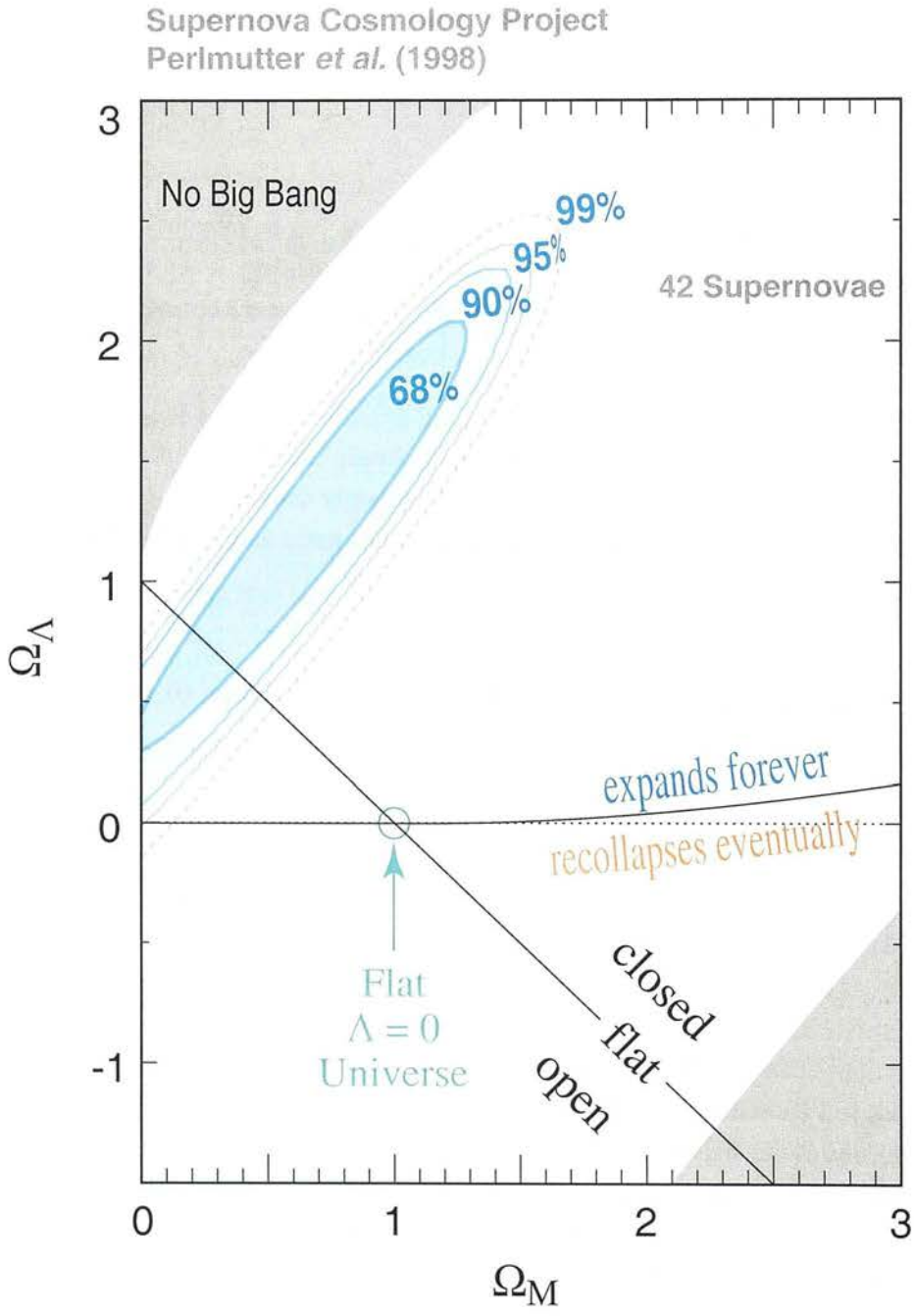

Figure 1.1: The $\Omega_\Lambda - \Omega_m$ parameter space. The diagonal line represents the boundary between open and closed models. The contours plotted are the constraints obtained from the recent Supernovae Ia measurements. (taken from the Supernova Cosmology Project's webpage at `http://www-supernova.lbl.gov`)

The cosmological constant is, in fact, a particular case of a negative pressure component of the Universe. More generally, we can consider the "dark energy" component of the Universe with a density parameter, $\Omega_{\rm de}$. The dark energy - whatever that may be - will, in general, have an equation of state,

$$w_{\rm de}c^2 = \frac{p_{\rm de}}{\rho_{\rm de}}, \tag{1.25}$$

where $p_{\rm de}$ is the pressure and $\rho_{\rm de}$ is the dark energy density. We see from the acceleration equation, equation (1.11), that if the condition, $\rho c^2 + 3p < 0$ is satisfied, then $\ddot{a} > 0$ and the rate of the Universe's expansion *increases*. This happens for $w_{\rm de}c^2 < -1/3$. There are many models which can satisfy this constraint on the equation of state of which the currently popular ΛCDM model ($w_{\rm de}c^2 = -1$) is just one. For example, the so-called "quintessence" models (*e.g.* Wang et al. 2000) have an evolving $w_{\rm de}$ which effectively increases with redshift. These "dark energy" models have become popular in recent years because of tentative observational evidence from Supernova type Ia measurements that the expansion of the Universe is actually speeding up (*e.g.* Garnavich et al. 1998; Riess et al. 1998; Perlmutter et al. 1999). The constraints in the $\Omega_\Lambda - \Omega_{\rm m}$ plane, as obtained from the Perlmutter et al. observations are also shown in Fig. 1.1.

1.1.5 Observational Parameters

Density Parameter:

We have already defined the density parameter Ω, as the ratio of the actual density of the Universe to the critical density:

$$\Omega(t) = \frac{\rho(t)}{\rho_c(t)}.$$

Note that since both ρ and ρ_c are, in general, functions of time, the density parameter is also a function of time. What is measurable from observations is Ω_0 - the value of the density parameter at the current epoch. To keep formulae as simple as possible, from now on, we will drop the subscript, 0 when referring to current epoch density parameters. Density parameters at earlier times will be denoted as $\Omega(z)$ or $\Omega(a)$. We saw earlier that the density of the Universe can be split up into parts, *i.e.* $\rho_{\rm r}$, $\rho_{\rm m}$ and ρ_Λ for the contributions due to radiation, matter and vacuum energy respectively. Ω can therefore be split up into $\Omega_{\rm r}$, $\Omega_{\rm m}$ and Ω_Λ.

Hubble Constant:

As we have already seen, the quantity, $(\dot{a}/a)$ in the Friedmann equation is known as the Hubble parameter, $H(t)$:

$$H(t) = \frac{\dot{a}(t)}{a(t)}.$$

The value of $H(t)$ at the current epoch is known as the Hubble constant, H_0 - a constant in space, not time. Accurately determining the value of the Hubble constant has been one of the major goals of

observational cosmology in the last 30 years. Note that H_0 is often written as:

$$H_0 = 100h \text{ kms}^{-1}\text{Mpc}^{-1}, \tag{1.26}$$

where h is a parameter satisfying $0 < h < 1$. One of the so called "key projects" of the Hubble Space Telescope (HST) was to accurately determine the value of H_0 using a variety of methods. The final result from the HST Key Project gives a measurement of $H_0 = 72 \pm 8\,\text{kms}^{-1}\text{Mpc}^{-1}$ (Freedmann et al. 2001). In order to derive the time evolution of the Hubble parameter, we firstly rewrite equation (1.23) as

$$H(t)^2 = H_0^2 \left[\Omega_\text{m} a(t)^{-3} + \Omega_\text{r} a(t)^{-4} - \frac{kc^2}{a(t)^2 H_0^2} + \Omega_\Lambda\right], \tag{1.27}$$

where again, we have dropped the subscript, 0 from the density parameters for simplicity. We can replace the third term in brackets simply by inserting the current values of the scale factor ($a|_{=0} = a_0 = 1$) and Hubble parameter ($H|_{t=0} = H_0$). This gives

$$\frac{kc^2}{a(t)^2 H_0^2} = (\Omega - 1)a(t)^{-2}, \tag{1.28}$$

which, upon substitution back into equation (1.27), yields the time evolution of the Hubble parameter:

$$H(t)^2 = H_0^2 \left[\Omega_\text{m} a(t)^{-3} + \Omega_\text{r} a(t)^{-4} + \Omega_\Lambda - (\Omega - 1)a(t)^{-2}\right], \tag{1.29}$$

where we have set $\Omega = \Omega_\text{m} + \Omega_\text{r} + \Omega_\Lambda$. Note that, since Ω_r is so small (see Section 1.1.8), for the majority of situations, the second term in brackets in equation (1.29) can be dropped except for very early times in the Universe's history when radiation dominates over matter.

Using equation (1.29), we can also determine the dependence of the matter and vacuum density parameters, Ω_m & Ω_Λ on the scale factor, a. For a matter dominated universe, we find:

$$\begin{aligned}
\Omega_\text{m}(a) &= \frac{8\pi G}{3H^2(a)}\rho_{\text{m},0}\, a^{-3} = \frac{\Omega_\text{m}}{a + \Omega_\text{m}(1-a) + \Omega_\Lambda(a^3 - a)}, \\
\Omega_\Lambda(a) &= \frac{\Lambda}{3H^2(a)} = \frac{\Omega_\Lambda a^3}{a + \Omega_\text{m}(1-a) + \Omega_\Lambda(a^3 - a)}.
\end{aligned} \tag{1.30}$$

We note from these expressions that as we look back further into the Universe's history (*i.e.* as $a \to 0$), then $\Omega_\text{m} \to 1$ and $\Omega_\Lambda \to 0$. Therefore, at early stages ($a \ll 1$) in the evolution of the Universe, all matter dominated Friedmann-Lemaître cosmological models will behave as an *Einstein-de Sitter* universe - a flat ($k = 0$) universe with $\Omega_\text{m} = 1$ and $\Omega_\Lambda = 0$.

Deceleration Parameter:

Another useful observational parameter is the deceleration parameter, q_0:

$$q_0 = -\frac{\ddot{a}(t_0)}{a(t_0)}\frac{1}{H_0^2} = -\frac{a(t_0)\ddot{a}(t_0)}{\dot{a}^2(t_0)}, \tag{1.31}$$

which quantifies the deceleration rate of the expanding Universe. Measuring q_0 essentially measures the quantity, $\Omega_{\rm m}/2 - \Omega_\Lambda$ and thus with a separate determination of $\Omega_{\rm m}$ (from *e.g.* gravitational lensing methods) restrictions can be put on the value of Λ. The detection of the accelerated expansion of the Universe with Supernovae type Ia measurements, mentioned in Section 1.1.4 and demonstrated in Fig. 1.1 is essentially a measurement of q_0. Measurements of $\Omega_{\rm m}$ and q_0 are essentially independent tests of general relativistic theories and can be used to put strong constraints on cosmological models of the Universe.

1.1.6 Cosmological Redshift

The fact that the Universe is expanding means that light photons are *redshifted* as they propagate from source to observer. Consider a light signal emitted by a comoving source (one at rest with respect to the cosmological expansion) at a time, t_e which is then observed at a time, t_o at the coordinate origin, $w = 0$. Since this is a radial photon of light, $ds = 0$ and we have $|c\,dt| = a\,dw$, from the metric, equation (1.2). The comoving distance between source and observer is constant by definition and so,

$$w_{eo} = \int_o^e dw = \int_{t_e}^{t_o} \frac{cdt}{a(t)} = \text{const.} \tag{1.32}$$

Differentiating with respect to t_e, we have:

$$\frac{dw_{eo}}{dt_e} = \frac{d}{dt_e}\int_{t_e}^{t_o} \frac{cdt}{a(t)} = 0, \tag{1.33}$$

and hence,

$$\frac{dt_o}{dt_e} = \frac{a(t_o)}{a(t_e)}. \tag{1.34}$$

Now, the inverse time intervals, $1/dt_e$ & $1/dt_o$ are just the emitted and observed light frequencies (ν_e & ν_o) and so,

$$\frac{dt_o}{dt_e} = \frac{\nu_e}{\nu_o} = \frac{\lambda_o}{\lambda_e}. \tag{1.35}$$

The redshift of a light signal is defined as the relative change in wavelength between emission and observation, *i.e.* $z = \frac{\lambda_o - \lambda_e}{\lambda_e}$, which together with equations (1.34) & (1.35) yields the relation between the scale factor of the Universe at the time of emission and observation and the observed redshift of the light:

$$1 + z = \frac{a(t_o)}{a(t_e)}. \tag{1.36}$$

Thus, the light is redshifted by the amount the Universe has expanded between emission and observation.

1.1.7 Distances in Cosmology

In a curved space-time, the meaning of "distance" is no longer unique. That is, the distance one measures between two events depends on the particular definition of "distance" employed. Here we describe four commonly used distance measures - proper distance, comoving distance, angular diameter distance and luminosity distance.

Proper Distance

The proper distance between two events at redshifts, z_2 and $z_1 < z_2$ is defined as the light-travel time between the two events. It is given by $dD_{\rm prop} = -cdt$ and hence, $dD_{\rm prop} = -c\frac{da}{\dot{a}} = -c\frac{da}{aH}$. Substituting for $H(t)$ using equation (1.29) and integrating yields the proper distance formula:

$$D_{\rm prop}(z_1, z_2) = \frac{c}{H_0}\int_{a(z_2)}^{a(z_1)} da\, \left[\Omega_{\rm m}a^{-1} + (1-\Omega) + \Omega_\Lambda a^2\right]^{-1/2}, \tag{1.37}$$

where we have ignored the contribution from Ω_r.

Comoving Distance

This is the distance on the spatial hypersurface, $t = t_0$ between the worldlines of a source and an observer comoving with the cosmic flow. It is, therefore, simply the coordinate distance between a source at z_2 and observer at z_1, *i.e.* $dD_{\rm com} = dw$. Thus, from equation (1.2) with $ds = 0$ we have $dD_{\rm com} = -a^{-1}c\,dt = -c\,da(a\dot{a})^{-1} = -c\,da\,(a^2H)^{-1}$. Again, substituting for $H(t)$ yields the comoving distance:

$$D_{\rm com}(z_1, z_2) = \frac{c}{H_0}\int_{a(z_2)}^{a(z_1)} da\, \left[\Omega_{\rm m}a + (1-\Omega)a^2 + \Omega_\Lambda a^4\right]^{-1/2}. \tag{1.38}$$

Angular Diameter Distance

The angular diameter distance is defined in analogy with the relation in Euclidean space between the physical cross-sectional area, dA of an object and the solid angle, $d\Omega$ that the object subtends as measured by an observer, *i.e.* $dA = D_{\rm ang}^2 d\Omega$. For an object at redshift, z_2 the surface area of a sphere of radius, $r = a(z_2)f_k[w(z_1, z_2)]$ centered on the object will be $A = 4\pi r^2 = 4\pi a^2(z_2)f_k^2[w(z_1, z_2)]$ and the angle subtended will be 4π. Hence,

$$\frac{dA}{4\pi a^2(z_2)f_k^2[w(z_1, z_2)]} = \frac{d\Omega}{4\pi}, \tag{1.39}$$

where $a(z_2)$ is the scale factor corresponding to a redshift of z_2. The angular diameter distance is then,

$$\begin{aligned} D_{\rm ang} &= \left(\frac{dA}{d\Omega}\right)^{1/2} = a(z_2) f_k[w(z_1, z_2)] \\ &= a(z_2) f_k[D_{\rm com}(z_1, z_2)]. \end{aligned} \tag{1.40}$$

where the final equality results from the definition of the comoving distance.

Luminosity Distance

The luminosity distance is defined in analogy with the Euclidean inverse-square law between the luminosity, L of a source at z_2 and the resulting flux, S received by an observer at z_1. In terms of $D_{\rm ang}$ and $D_{\rm com}$, the luminosity distance is given by

$$D_{\rm lum} = \left(\frac{a(z_1)}{a(z_2)}\right)^2 D_{\rm ang}(z_1, z_2) = \frac{a(z_1)^2}{a(z_2)} f_k[D_{\rm com}(z_1, z_2)]. \tag{1.41}$$

This relation can be understood in terms of the effects of the expansion of the Universe and time dilation on the light photons. Firstly, the photons are redshifted by a factor, $a(z_1)a(z_2)^{-1}$ due to the cosmological expansion. Second, the effect of time dilation means that the arrival frequency of photons at the observer is reduced by another factor, $a(z_1)a(z_2)^{-1}$. The third effect is also due to the Universe's expansion – the surface of the sphere, centered on the observer, on which the photons arrive, grows in area between emission at z_2 and arrival at z_1 by a factor, $[a(z_1)a(z_2)^{-1}]^2$. Putting these three effects together yields a total factor of $[a(z_1)a(z_2)^{-1}]^4$ in the flux and thus leads to the factor of $[a(z_1)a(z_2)^{-1}]^2$ in the first equality in equation (1.41).

All these distance measures are larger for a lower matter density, $\Omega_{\rm m}$ and a higher cosmological constant, Ω_Λ. The various distance measures differ greatly at large redshifts, although locally they all follow the Hubble law,

$$\text{distance} = \frac{cz}{H_0} + O(z^2). \tag{1.42}$$

The behaviour of the various distance measures with redshift for two demonstrative cosmological models is shown in Fig. 1.2.

1.1.8 Cosmic Microwave Background Radiation

The Cosmic Microwave Background (CMB) is a background radiation covering the whole sky that is extremely isotropic (the same in all directions). It corresponds to a perfect black body spectrum with a temperature of $2.728K$ and is isotropic to one part in 10^5. The total energy density in the CMB can be calculated from the observed temperature:

$$\epsilon_{\rm rad} = \alpha T^4 = \rho_{\rm rad} c^2, \tag{1.43}$$

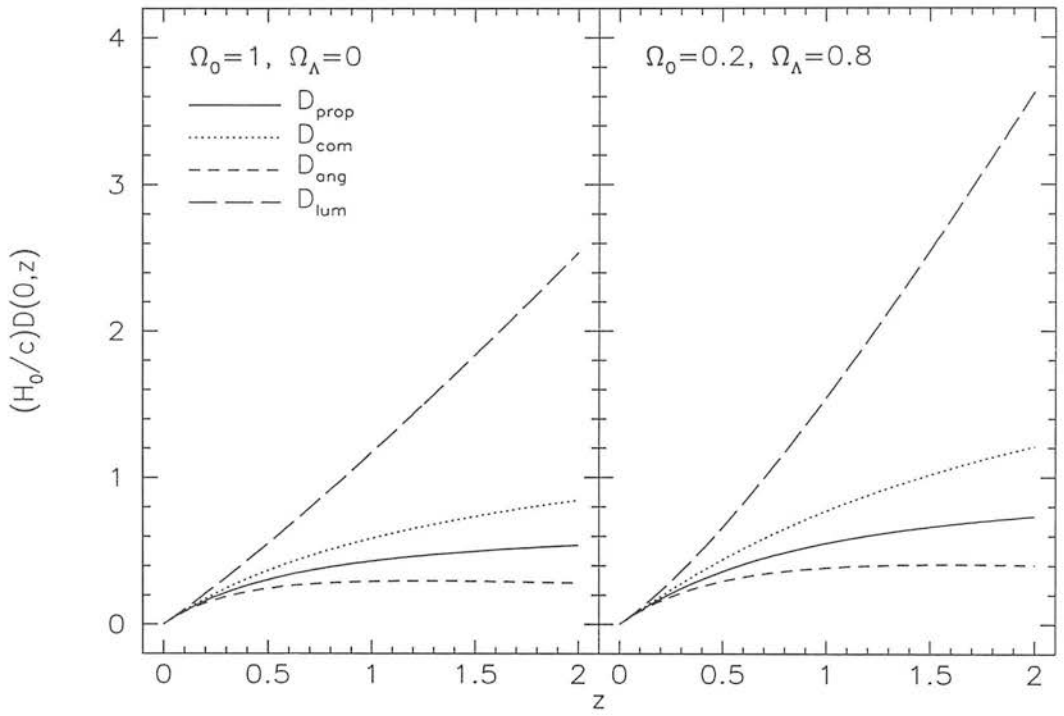

Figure 1.2: The dependence on redshift of the various distance measures described in the text. The curves are for the proper distance (solid curve), comoving distance (dotted curve), angular diameter distance (short dashed curve) and the luminosity distance (long dashed curve). These are plotted for an Einstein-de Sitter Universe (left-hand side) and for a flat $\Omega_{\rm m} = 0.2, \Omega_\Lambda = 0.8$ ΛCDM Universe (right-hand side). From Bartelmann & Schneider 2001.

where α is the Stefan-Boltzmann constant. Since the CMB dominates the energy density in radiation of all wavelengths, it can be used to estimate the radiation contribution to Ω:

$$\Omega_{\rm rad} = 2.47 \times 10^{-5} h^{-2}. \tag{1.44}$$

We've already seen that $\rho_{\rm rad}$ scales as $1/a^4$. Combining this with equation (1.43) gives the temperature evolution of the Universe:

$$T \propto \frac{1}{a}. \tag{1.45}$$

Thus the Universe cools as it expands and the discovery of the microwave background was a major vindication of the hot big bang theory.

The origin of the microwave background is well understood in terms of the hot big bang theory. The ionization potential of the hydrogen atom is 13.6 eV. This is the amount of energy it takes to excite an electron from the ground state of the H atom to the vacuum level. If we imagine traveling back in time, we will eventually get to a stage where the Universe has become so hot that all the photons will have an energy, $E_{ph} > 13.6\,{\rm eV}$. Any hydrogen atoms that form will be immediately

ionized through collisions with photons. The Universe at this time basically consists therefore of a sea of electrons, photons, nuclei (mostly protons) and dark matter (see later), *i.e.* a hot ionized plasma. Photons strongly interact with free electrons via Thompson scattering and so the mean free path of photons at this stage in the Universe is very short. The Universe at this time is said to be "opaque to radiation" because photons cannot travel very far without interacting with a free electron and thus radiation cannot propagate. As the Universe expanded, the temperature decreased according to equation (1.45) and the energy of the photons correspondingly decreased. At some point, the photons no longer had enough energy to ionize the hydrogen atoms that formed. Very quickly, all the electrons and nuclei came together to form atoms and there was no longer any free electrons for the photons to interact with. The photons could then escape and travel unimpeded for the entire remainder of the Universe's evolution. This process is known as "decoupling" and the Universe is said to have become "transparent to radiation". The temperature of the Universe at this time was $\sim 2500K$.

In the early Universe, the photons, electrons, etc. were in a highly interacting thermal state and the radiation therefore constituted a black body curve. Since the expansion of the Universe cools the radiation while maintaining the blackbody spectrum, the CMB we see today also fits a black body curve extremely well. Due to the finite speed of light, the photons which comprise the CMB which we observe today have been traveling towards us for a large fraction of the history of the Universe. These photons originated on a large celestial sphere centered on the observer called "the surface of last scattering".

1.1.9 The Early Universe

Radiation or Matter dominated?

The relativistic and non-relativistic contributions to Ω can be approximated by:

$$\Omega_{\rm rel} \sim 4.17 \times 10^{-5} h^{-2} \quad ; \quad \Omega_{\rm non-rel} \sim \Omega_0 \, ,$$

and the corresponding densities evolve according to:

$$\rho_{\rm rel} \propto \frac{1}{a^4} \quad ; \quad \rho_{\rm non-rel} \propto \frac{1}{a^3} \, .$$

We can thus find an expression for the relative amounts of relativistic and non-relativistic material in the Universe for any given value of the scale factor, a:

$$\frac{\Omega_{\rm rel}}{\Omega_{\rm non-rel}} = \frac{4.17 \times 10^{-5}}{\Omega_0 h^2} \frac{1}{a}. \tag{1.46}$$

For example, the temperature of the Universe at the time of decoupling was $\sim 2500K$. Comparing this to the current temperature of $2.728K$, we find using equation (1.45) that the scale factor at the

decoupling era is given by (setting $a(t_0) = 1$):

$$a_{\rm dec} = \frac{1}{1000}.$$

Combining this with equation (1.46), we find:

$$\frac{\Omega_{\rm rel}}{\Omega_{\rm non-rel}} = \frac{0.04}{\Omega_0 h^2}. \tag{1.47}$$

It is very likely that $\Omega_0 h^2 > 0.04$ and so, the non-relativistic contribution to Ω is greater than the relativistic contribution at this time. The Universe at this time is said to be "matter dominated". The epoch of matter-radiation equality is obtained when $\Omega_{\rm rel} = \Omega_{\rm non-rel}$. At this time,

$$\begin{aligned} \Omega_0 h^2 &= \frac{4.17 \times 10^{-5}}{a}, \\ a = a_{\rm eq} &= \frac{1}{24000 \Omega_0 h^2}. \end{aligned} \tag{1.48}$$

At earlier times, since a decreases, if we go back far enough, the Universe becomes "radiation dominated". The entire temperature evolution of the Universe can then be deduced from the above analysis.

Nucleosynthesis

The theory of nucleosynthesis describes how the primeval nuclei formed in the early Universe. It relies on three pieces of empirical evidence. Firstly, the mass of the proton ($m_p = 938.3\,{\rm MeV}$) is less than the mass of the neutron ($m_n = 939.6\,{\rm MeV}$). Secondly, the decay of a neutron to a proton with a half-life of $t_{1/2} = 940\,{\rm secs}$. The third piece of evidence we require to formulate nucleosynthesis is the fact that neutrons bound in nuclei decay on much longer timescales than 940 secs. On these short timescales, neutrons bound in nuclei are essentially stable against decay. Nucleosynthesis occurred a few minutes after the big bang and its understanding is analogous to that of decoupling. Before ~ 400 seconds, photons had enough energy ($\sim$ MeV) to split nuclei apart. That is, at this time, the binding energy of a light nucleus (^{2}H, ^{3}He, ^{4}He and ^{7}Li) would be less than the typical energy of a photon. Thus nuclei could not be formed at this time. Eventually, as the Universe cools, the typical energy of a photon becomes less than the binding energies of these light nuclei and so, they are stable. Thus, nucleosynthesis may take place. Before nucleosynthesis occurred but late enough that the protons and neutrons were non-relativistic ($k_B T \ll m_p c^2$), the nuclei were in thermal equilibrium and their relative populations are described by a Maxwell-Boltzmann distribution:

$$\frac{N_n}{N_p} = \left(\frac{m_n}{m_p}\right)^{3/2} \exp\left(\frac{-(m_n - m_p)c^2}{k_B T}\right). \tag{1.49}$$

Now, since $m_n \approx m_p$, while $k_B T \gg (m_n - m_p)c^2$, the number of neutrons and protons is very nearly equal. The decay of a neutron to a proton occurs via:

$$n \rightleftharpoons p + e^- + \nu_e + 0.8\mathrm{MeV}. \tag{1.50}$$

Once the thermal energy drops below 0.8 MeV, the forward reaction is favoured and thermal equilibrium ceases. By this time,

$$\frac{N_n}{N_p} \approx \exp\left(\frac{-1.3\mathrm{MeV}}{0.8\mathrm{MeV}}\right) \approx \frac{1}{5}. \tag{1.51}$$

By the time nucleosynthesis has finished, the number of neutrons that have decayed via equation (1.50) is small but non-negligible. After this time, all the neutrons are tied up in nuclei and are stable against decay on short timescales. The final ratio of neutrons to protons in the Universe is $\sim 1/7$. The elements formed in the early Universe are mostly ^{1}H and ^{4}He (and traces of ^{3}He, ^{7}Li and ^{2}H). The most stable nucleus is ^{4}He and this is why a lot of ^{4}He forms. However, there is not enough neutrons to form ^{4}He with all the protons and the left-over protons form ^{1}H. We can use this information to work out the fraction of baryonic matter that is in the form of ^{4}He nuclei. This number is given the symbol, Y_4. A ^{4}He nucleus consists of two protons and two neutrons. Assuming the vast majority of the neutrons are used up in ^{4}He nuclei, the number of ^{4}He nuclei is:

$$N_{^4\mathrm{He}} = \frac{N_n}{2}\,.$$

We also know that the mass of a ^{4}He nucleus is ~ 4 times the mass of a ^{1}H nucleus and so the fraction of mass in ^{4}He is:

$$Y_4 = \frac{4N_n}{N_n + N_p}\frac{1}{2} = \frac{2N_n}{N_n + N_p} = \frac{2}{1 + \frac{N_p}{N_n}} \approx 0.25\,. \tag{1.52}$$

So, 25% of baryonic matter is ^{4}He directly after nucleosynthesis and this matches the observed relative abundances very well (*e.g.* Kirkmann et al. 2001). Observations of the abundance of elements in the Universe can be used in conjunction with nucleosynthesis theory to constrain the value of the baryonic mass density of the Universe. It turns out that the primordial abundance of the light elements is dependent on the reciprocal of the entropy per baryon, η which, in turn, is related to the baryonic density parameter, Ω_B via (*e.g.* Peacock 1999)

$$\eta = n_\mathrm{B}/n_\gamma = 2.74 \times 10^{-8}(T_\mathrm{CMB}/2.73K)^{-3}\Omega_\mathrm{B}h^2, \tag{1.53}$$

where n_B & n_γ are the number density of baryons and photons respectively, and T_CMB is the temperature of the CMB radiation. Thus, if we can account for the baryon-to-photon ratio (see next section), then observations of elemental abundances can be used to put reasonably tight constraints on Ω_B. Particularly useful in this respect is the observed deuterium abundance seen in quasar absorption lines as the light passes through primordial gas clouds (*e.g.* Webb et al. 1991; O' Meara et al. 2001). This

constrains the value of Ω_B as:

$$0.016 \leq \Omega_B h^2 \leq 0.024. \tag{1.54}$$

Baryogenesis

A theory of baryogenesis is required to explain the fact that as far as we know, there exists virtually no antimatter in the Universe. It is also needed to account for the baryon-to-photon ratio, $\eta \sim 10^{-8}$ mentioned in the previous section. The lack of antimatter constitutes a matter-antimatter asymmetry in the Universe. The basic idea for any baryogenesis theory is to create this asymmetry very early in the Universe when $k_B T \gg m_p c^2$. At this time, there exists a thermal equilibrium between photons and proton-antiproton pairs according to:

$$\gamma + \gamma \rightleftharpoons p + \overline{p}. \tag{1.55}$$

Since we have a thermal equilibrium, the forward and backward rates of the above reaction are equal and one would expect as many protons and antiprotons as photons of light. A matter-antimatter asymmetry is then created by creating an extra proton for every billion or so that exist. An exact theory of how this is achieved is still to be discovered but such a mechanism would have to satisfy the three general **Sakharov conditions** of baryosynthesis:

- $\Delta B \neq 0$ reactions;
- CP violation;
- non-equilibrium conditions.

The first condition expresses baryon-number violation while the second condition requires CP (charge-parity) violation. Note that particle physics requires that CPT (charge-parity-time) symmetry is always conserved and so the second condition above requires a time asymmetry between particles and antiparticles. In fact, CP violation has been observed in the laboratory via the differing decay rates of the neutral kaons, K_0 and $\overline{K}_0$. Assuming that a mechanism for baryogenesis is found, the lack of antimatter is then a natural consequence of the theory. As the Universe cools the energy available to the photons is reduced and the forward reaction in equation (1.55) will not occur. Now, the protons and antiprotons annihilate each other according to the reverse reaction and the only matter left over (apart from all the photons) is the extra protons that were created when the matter-antimatter asymmetry was created. This process will give the required baryon density (found from observations) since only one proton is required for every billion photons of light.

1.1.10 The Need for Inflation

The theory of inflation was introduced to augment a big bang theory that, on its own cannot completely explain the Universe we live in. There are three main problems with the big bang theory and these are outlined below.

The Flatness problem

The Friedmann equation can be written as:

$$\begin{aligned} H^2 &= \frac{8\pi G}{3}\rho_c\,\Omega - \frac{kc^2}{a^2} \\ &= H^2\Omega - \frac{kc^2}{a^2}, \end{aligned} \tag{1.56}$$

$$\text{or } |\Omega - 1| = \frac{|k|c^2}{a^2H^2}. \tag{1.57}$$

It is clear from equation (1.57) that if $\Omega = 1$, it remains so for all time. We know that the current value of Ω is somewhere in the range, $0.1 < \Omega < 10$ and so our Universe is very nearly flat. Using our solutions for radiation and dust dominated Universes, we find:

$$\begin{aligned} |\Omega - 1| &\propto t \text{ for radiation.} \\ |\Omega - 1| &\propto t^{2/3} \text{ for dust.} \end{aligned} \tag{1.58}$$

Since $|\Omega - 1|$ increases with time in both models, we know that if $\Omega > 1$ initially, it must increase with time. If $\Omega < 1$ initially, it will decrease with time. Either way Ω will be driven away from 1 unless $\Omega = 1$ is exactly true. So, the Universe should become more and more curved with time and a flat geometry is unstable (unless its perfectly flat!). The problem is that the Ω we see today is still very close to 1 and it must have been even closer to 1 in the early Universe. In fact, using equations (1.57) & (1.58) we can estimate the value of $|\Omega - 1|$ at certain times during the evolution of the Universe given what we know today (Ω_0 and t_0). At the decoupling era, we need $|\Omega - 1| \leq 10^{-3}$. Earlier on, at the time of matter-radiation equality, we need $|\Omega - 1| \leq 10^{-6}$. At nucleosynthesis, we need $|\Omega - 1| \leq 10^{-16}$ and at the time of electro-weak symmetry breaking we need $|\Omega - 1| \leq 10^{-28}$. It is clear that Ω started off very close to 1 indeed in the very early Universe. It would obviously be much more desirable that Ω was exactly 1 and has remained so ever since. What we need to resolve the flatness problem is a theory that would automatically set Ω equal or extremely close to 1 in the very early Universe.

The Horizon problem

We have seen already that the CMB is very nearly isotropic with a temperature of $T = 2.728K$. The microwave radiation has been traveling to us for the lifetime of the observable Universe and thus, for an appreciable amount of the history of the Universe. The horizon problem is one of causality and is essentially that opposite parts of the sky could not have interacted with each other during the lifetime of the Universe (if the photons comprising the CMB have been traveling towards us for the majority of the Universe's lifetime, there is no way that a light signal could have been sent from one part of the sky to the opposite part in that same amount of time!). Yet the CMB is extremely isotropic which indicates that the entire Universe was in thermal equilibrium at the time of emission.

If different parts of the Universe have not interacted with each other over the entire history of the Universe, how was this equilibrium established? The problem becomes even worse when we consider that this equilibrium would have to have been established even before decoupling by which time light could have traveled an even smaller distance. It turns out, in fact, that regions on the sky separated by more than 1 or 2 degrees could not have interacted before decoupling (see *e.g.* Kolb & Turner 1990). Also, the anisotropies present in the CMB are thought to be associated with the "seeds" of structure in the Universe. For the same reason that one cannot thermalise causally separated regions, one also cannot create an irregularity. Therefore, these anisotropies or seed perturbations cannot have been created in the big bang — they must have been there already.

Relic Particle Abundances

The Universe remained radiation dominated for at least 1000 years. But we know that radiation falls off as $1/a^4$ — much faster than any other type of matter. So, even if the amount of non-relativistic matter is small, it should still come to dominate very quickly. Modern particle physics theories and grand unified theories (GUTs) predict the existence of magnetic monopoles — extremely massive particles made in high abundance in the early Universe (see *e.g.* Einhorn, Stein & Toussaint 1980). Because they are non-relativistic for almost the entire history of the Universe, these particles should come to dominate very quickly and so, they should be dominating the Universe now. However, magnetic monopoles have never been detected and in order for the hot big bang theory and particle physics to be compatible, the non-existence of magnetic monopoles in the Universe today must be explained. Also, similar problems are caused by particles such as gravitinos and moduli fields which are predicted by more modern particle physics theories.

1.1.11 Basic Inflation Theory

The basic idea behind inflation is to postulate that there was a period in the early Universe when the scale factor was accelerating. Recall from earlier the acceleration equation:

$$\frac{\ddot{a}}{a} = -\frac{4\pi G}{3}\left(\rho + \frac{3p}{c^2}\right).$$

If the scale-factor is accelerating, then $\ddot{a}(t) > 0$ and the condition for inflation becomes:

$$\rho c^2 + 3p < 0.$$

Imposing this condition on the Universe breaks the *Strong Energy Condition* (*e.g.* Kandrup 1992; Chiba, Mukohyama & Nakamura 1997). However, physical processes which break this "law" have been discovered (*e.g.* supercooling of helium) and so, this does not represent a great problem. It does however demonstrate that inflation is an unprecedented theory of the Universe and is indeed "new

physics". Rewriting the above condition, we find an expression for the pressure, p:

$$p < -\frac{\rho c^2}{3}. \tag{1.59}$$

Since the density is always assumed to be positive, a negative pressure is required for inflation to occur. At early times, the Universe is thought to have undergone a series of phase transitions as the Universe cooled (*e.g.* when quarks first condensed to form hadrons). Phase transitions are controlled by an unusual, and as yet, unobserved form of matter known as a *scalar field*. Under certain conditions, these scalar fields behave with a negative pressure and thus can satisfy the requirements for inflation. The classic example of an inflationary Universe is one with a cosmological constant. Once again, the Friedmann equation is:

$$H^2 = \frac{8\pi G}{3}\rho - \frac{kc^2}{a^2} + \frac{\Lambda}{3}.$$

The expansion of the Universe decreases the first two terms while Λ remains constant. So, after a while the first two terms become negligible and we have:

$$\begin{aligned} H^2 &= \frac{\Lambda}{3}, \\ \Rightarrow \dot{a} &= \sqrt{\frac{\Lambda}{3}}\, a, \end{aligned} \tag{1.60}$$

$$\Rightarrow a(t) = \exp\left(\sqrt{\frac{\Lambda}{3}}t\right). \tag{1.61}$$

— a de Sitter model with an exponential expansion. After some time, the inflation stops and the energy in Λ is converted into conventional matter (or the particles acting as Λ decay into normal particles). All this takes place when the Universe is extremely young ($\sim 10^{-34}$ secs. in typical models). It is not clear by what mechanism the cosmological constant "decays" into ordinary matter but inflation is currently a very active research field. Whatever the mechanisms of inflation are, the idea itself is very useful since it solves the problems that are evident when the big bang is considered on its own.

The Flatness problem

With inflation, we have a period in the universe's history when $\ddot{a} > 0$.

$$\begin{aligned} \Rightarrow \frac{d}{dt}(\dot{a}) &> 0, \\ \Rightarrow \frac{d}{dt}(aH) &> 0. \end{aligned} \tag{1.62}$$

we see from the above that the quantity, aH increases during inflation and so, according to equation (1.57), the quantity, $|\Omega(t) - 1|$ tends to 0 during this time. For a perfect exponential expansion,

$$|\Omega(t) - 1| \propto \exp\left(-\sqrt{\frac{4\Lambda}{3}}t\right). \tag{1.63}$$

It turns out that Ω is driven so close to 1 during inflation that the expansion of the Universe since inflation is still not enough to move Ω significantly away from 1.

The Horizon problem

Inflation greatly increases the size of a region of the Universe while keeping its characteristic scale length, the Hubble scale, constant. This means that a small part of the Universe – small enough that thermal equilibrium is established across it prior to inflation – can expand to be much larger than the size of the observable Universe. So, the fact that the CMB is isotropic across the entire sky is just a reflection of the fact that the observable Universe was once small enough that thermal equilibrium was achieved.

If the Universe has undergone an inflationary era, then the entire observable Universe was once small enough that thermal equilibrium could be achieved. Consequently, there was also the opportunity at this time to generate the small irregularities in the matter distribution from which the structure we see today could have formed. This is one of the most powerful (and possibly testable) predictions of inflation since the precise nature of the initial perturbations are dependent on the exact model of inflation employed (see also the discussion on the origin of structure in the next section).

Relic Particle abundances

The extreme expansion of the Universe during inflation reduces the density of any relic particles present faster than the density corresponding to the cosmological constant. Provided enough expansion occurs, the density of these particles will decrease so much that these particles would not be observable today. However, the temperature of the Universe at the end of inflation must be low enough that there is no new production of these particles after inflation.

1.2 Matter in the Universe

1.2.1 Structure Formation

Although we have, until now, been considering a Universe with a smooth (dark) matter distribution, $\rho_{\rm m}$, it is clear that the Universe is not isotropic in general if we go to small enough scales. On the largest scales, the Universe does however seem to be isotropic and so, the cosmological principle can

still be used. Still, the structures that we see need to be explained and galaxy formation is one of the most active and exciting fields of cosmological research today.

Linear Growth of Density Perturbations

The anisotropies in the CMB are thought to be the "seeds" of the structures that we see today. If we ignore, for the moment, the question of how these initial irregularities came to be in the first place, it is fairly straightforward to see how these irregularities could have grown over the history of the Universe to produce the structures that we see today. The driving force behind structure formation is the idea of *gravitational instability*. The only force that can cause structure formation is gravity since a long range force is required and the only other long range force, the electromagnetic force is excluded as a possibility due to the charge neutrality of the Universe. The anisotropies in the CMB are thought to be associated with irregularities in the distribution of matter in the Universe. In this irregular distribution, regions which are over-dense will exert a greater gravitational attraction than their neighbouring regions and so, will draw more material into them. They then become even more dense due to this extra material and the process repeats. This is the basic mechanism used to explain the large-scale structure we see today. The relative matter density contrast, δ at a position, $\mathbf{x}$ is defined as

$$\delta(\mathbf{x}) = \frac{\rho(\mathbf{x}) - \overline{\rho}}{\overline{\rho}} \tag{1.64}$$

where $\overline{\rho}$ is the mean density of the Universe. As long as $\delta(\mathbf{x}) \ll \mathbf{1}$, then fluctuations in the matter distribution can be thought of as perturbations to the underlying homogeneous and isotropic general matter distribution and so, linear perturbation theory can be used to describe the growth of these density inhomogeneities. The linear theory of density perturbations in an expanding universe needs to be relativistic because at sufficiently early times the Universe is radiation dominated and the size of the perturbations is comparable to the curvature radius of space-time. Under these conditions, simple Newtonian arguments break down. In the following Section, we describe the linear perturbation theory in the full general relativistic scenario - the main result of which is that in the Einstein-de Sitter régime, perturbations with $\delta \ll 1$ will grow as

$$\delta(a) \propto a^{n-2} = \begin{cases} a^2 & \text{before } a_{\rm eq} \\ a & \text{after } a_{\rm eq}, \end{cases} \tag{1.65}$$

where $a_{\rm eq}$ is the scale-factor at the time of matter-radiation equality (see Section1.1.9).

Details of the perturbation theory are given in *e.g.* Lifshitz (1946), Bardeen (1980) & chapter 4 of Padmanabhan (1993). Here, we will give an outline of the Lifshitz analysis (see also Kolb & Turner, 1990) which relies on selecting a gauge, finding the solutions in that gauge and then, identifying the gauge modes. An alternative method is to formulate the problem in terms of gauge-invariant quantities - see Bardeen (1980) for such an analysis.

Linear Perturbation Theory in General Relativity

We can express the metric of a universe with small perturbations as

$$g_{\mu\nu} = g^0_{\mu\nu} + h_{\mu\nu} \tag{1.66}$$

where $g^0_{\mu\nu}$ is the underlying RW metric for a flat universe (equation (1.2) with $k = 0$) and $h_{\mu\nu}$ are small metric perturbations. We can also make use of the gauge freedom in the problem to choose a "synchronous gauge" such that $h_{00} = h_{i0} = 0$.[1] This choice of gauge does not, in fact, exhaust all of the gauge freedom available to us - we will see the effect of the residual gauge freedom when we come to finding solutions to the perturbation equations that result.

We can describe perturbations in the stress-energy tensor (equation (1.6)) in terms of perturbations to the energy density, $\rho = \rho_0 + \rho_1$, the pressure, $p = p_0 + p_1$ and the matter velocity, $U^\mu = U^\mu_0 + U^\mu_1$. The equations which need to be solved are the perturbed Einstein equations, which are (setting $c = 1$):

$$\delta R_{\mu\nu} = 8\pi G \delta T_{\mu\nu} - 4\pi G \delta[g_{\mu\nu}\mathcal{T}], \tag{1.67}$$

where $\mathcal{T}$ is the trace of the stress-energy tensor, $\mathcal{T} = \rho - 3p = (\rho_0 - 3p_0) + (\rho_1 - 3p_1)$. We now need to find expressions (to first order in $h_{\mu\nu}$) for each of the δX terms in equation (1.67). To find expressions for $\delta R_{\mu\nu}$, we first need to calculate $\delta\Gamma^\mu_{\nu\alpha}$ to first order in $h_{\mu\nu}$ and then use

$$\delta R_{\mu\nu} = \delta R^\alpha_{\mu\alpha\nu} = \delta\Gamma^\alpha_{\nu\mu,\alpha} - \delta\Gamma^\alpha_{\alpha\mu,\nu} + \delta[\Gamma^\alpha_{\alpha\beta}\Gamma^\beta_{\mu\nu}] - \delta[\Gamma^\alpha_{\nu\beta}\Gamma^\beta_{\mu\alpha}], \tag{1.68}$$

where $R^\alpha_{\sigma\rho\beta}$ is the Riemann curvature tensor. For example, the 00 component can be shown (by the above method) to be

$$\delta R_{00} = \frac{1}{2}\ddot{h} + \frac{\dot{R}}{R}\dot{h}, \tag{1.69}$$

where $h \equiv h^\mu_\mu = h^k_k = -\sum_{k=1}^3 h_{kk}/R^2$ is the trace of the metric perturbation. Using the stress-energy tensor of a perfect fluid, equation (1.6), and $\rho = \rho_0 + \rho_1$ etc., $\delta T_{\mu\nu}$ computes (to first order) to be

$$\delta T_{\mu\nu} = -p_1 g^0_{\mu\nu} + (\rho_1 + p_1)U_{0\mu}U_{0\nu} - p_0 h_{\mu\nu} + (\rho_0 + p_0)(U_{0\mu}U_{1\nu} + U_{1\mu}U_{0\nu}). \tag{1.70}$$

Finally, $\delta[g_{\mu\nu}\mathcal{T}]$ comes out to be

$$\delta[g_{\mu\nu}\mathcal{T}] = g^0_{\mu\nu}(\rho_1 - 3p_1) + h_{\mu\nu}(\rho_0 - 3p_0). \tag{1.71}$$

Substituting the results of equations (1.68) - (1.71) into the perturbed Einstein equations, equation (1.67), results in three equations: the 00, the ij, and the $0i$ components. For example, the 00 compo-

[1] Here, and in what follows, Greek indices run from 0 to 1; Roman indices run from 1 to 3; *i.e.* Roman indices refer only to spatial components.

nent of equation (1.67) gives:

$$\ddot{h} + 2H\dot{h} = 8\pi G(\rho_1 + 3p_1). \tag{1.72}$$

In addition to the Einstein equations, it is also useful to use energy momentum conservation, equation (1.7), in place of one of the field equations. What results from the perturbed version of equation (1.7) is (again to first order):

$$\dot{\rho_1} + 3H(\rho_1 + p_1) + (\rho_0 + p_0)\left[-\dot{h}/2 + \nabla \cdot \mathbf{U_1}\right] = 0. \tag{1.73}$$

The first-order perturbations of the metric are completely governed by equations (1.67) - (1.73). We can consider three different types of perturbations by decomposing the metric into its trace, a transverse traceless tensor and a vectorial part. In this way, we can separate metric perturbations into scalar, tensor and vectorial modes. Here we are interested in discerning the evolution of the scalar density perturbation modes and so we need only consider perturbations in the trace of the metric perturbation, h. We proceed by expressing the perturbed quantities as a Fourier expansion, *i.e.*

$$h,\ \rho_1,\ p_1,\ \mathbf{U_1} \propto \exp(-i\mathbf{k}\cdot\mathbf{x}). \tag{1.74}$$

The perturbed Einstein equations for the density perturbation modes are then

$$\begin{aligned}
\ddot{h} &+ 2H\dot{h} - 3H^2(1+3v_s^2)\delta = 0,\\
\dot{\delta} &+ (1+p_0/\rho_0)(\theta - \dot{h}/2) + 3H(v_s^2 - p_0/\rho_0)\delta = 0,\\
\dot{\theta} &+ (2-3v_s^2)H\theta - \frac{k^2 v_s^2}{R^2(1+p_0/\rho_0)}\delta = 0,
\end{aligned} \tag{1.75}$$

where $k = |\mathbf{k}|$ is the wavenumber of the perturbation, and we have made the substitutions, $\theta = \nabla \cdot \mathbf{U_1} = -i\mathbf{k}\cdot\mathbf{U_1}$ and $\delta = \rho_1/\rho_0$. The sound speed, v_s is given by

$$v_s^2 = \left(\frac{\partial p}{\partial \rho}\right)_{\text{adiabatic}} = p_1/\rho_1. \tag{1.76}$$

If we make the assumption, $p_0/\rho_0 = v_s$, then the above equations simplify to

$$\begin{aligned}
h'' &+ \frac{1}{2}(1-3v_s^2)h' - 3(1+3v_s^2)\delta = 0,\\
\delta' &+ (1+v_s^2)(\phi - h'/2) = 0,\\
\phi' &- \frac{1}{2}(9v_s^2 - 1)\phi = 0,
\end{aligned} \tag{1.77}$$

where we have defined $\phi = \theta/H$ and $y = \ln R$. The prime indicates $d/dy = H^{-1}d/dt$ and we have ignored the last term in the equation for $\dot{\theta}$ since it is negligible for super-horizon sized modes. The above set of equations corresponds to a single fourth-order equation and so, it has four solutions. They

are (*e.g.* Weinberg 1972, Zel'dovich & Novikov, 1983)

$$[\delta,\ \phi,\ h,\ h'] \propto \chi_i t^{\lambda_i}, \tag{1.78}$$

where $\lambda_1 = 0$, $\lambda_2 = -1$, $\lambda_3 = (2 + 6v_s^2)/(3 + 3v_s^2)$ and $\lambda_4 = (9v_s^2 - 1)/(3 + 3v_s^2)$ and the χ_i are given by

$$\begin{aligned}
\chi_1 &= [0,\ 0,\ 1,\ 0], \\
\chi_2 &= [(1 + v_s^2)/2,\ 0,\ 1,\ -3(1 + v_s^2)/2], \\
\chi_3 &= [(1 + v_s^2)/2,\ 0,\ 1,\ (1 + 3v_s^2)], \\
\chi_4 &= [v_s^2(1 + v_s^2)(9v_s^2 - 1),\ (3v_s^2 + 1/2)(1 - v_s^2)(9v_s^2 - 1), \\
&\quad 2(1 + 3v_s^2)(1 + v_s^2),\ (1 + 3v_s^2)(1 + v_s^2)(9v_s^2 - 1)].
\end{aligned} \tag{1.79}$$

In the matter-dominated régime, the sound speed, v_s is zero and we have

$$\begin{aligned}
\lambda_1 &= 0, \quad \chi_1 = [0,\ 0,\ 1,\ 0], \\
\lambda_2 &= -1, \quad \chi_2 = [1/2,\ 0,\ 1,\ -3/2], \\
\lambda_3 &= 2/3, \quad \chi_1 = [1/2,\ 0,\ 1,\ 1], \\
\lambda_4 &= -1/3, \quad \chi_1 = [0,\ -1/2,\ 2,\ -1];
\end{aligned} \tag{1.80}$$

while for the radiation-dominated era ($v_s^2 = 1/3$), the solutions are given by

$$\begin{aligned}
\lambda_1 &= 0, \quad \chi_1 = [0,\ 0,\ 1,\ 0] \\
\lambda_2 &= -1, \quad \chi_2 = [2/3,\ 0,\ 1,\ -2] \\
\lambda_3 &= 1, \quad \chi_1 = [2/3,\ 0,\ 1,\ 2] \\
\lambda_4 &= 1/2, \quad \chi_1 = [8/9,\ 2,\ 16/3,\ 16/3].
\end{aligned} \tag{1.81}$$

Here we see the effect of the residual gauge freedom present in the synchronous gauge - the first two solutions of equation (1.78) represent pure gauge modes and do not describe physical perturbations. In fact, these unphysical perturbations can always be removed by a simple coordinate transformation of the unperturbed metric, $g^0_{\mu\nu}$ (see *e.g.* the discussion on gauge mode solutions in Kolb & Turner, 1990). What we are left with then, is two solutions - a growing mode and a decaying mode which are

$$\begin{aligned}
\delta_+(t) = \delta_+(t_i)(t/t_i)^{2/3}, \quad \delta_-(t) = \delta_-(t_i)(t/t_i)^{-1/3} \qquad &\text{matter-dominated era} \\
\delta_+(t) = \delta_+(t_i)(t/t_i), \quad \delta_-(t) = \delta_-(t_i)(t/t_i)^{1/2} \qquad &\text{radiation-dominated era}
\end{aligned}, \tag{1.82}$$

where t_i is some initial time. With these solutions then, we can describe the evolution of density perturbations in the early Universe. Note that the growing mode solutions become the result stated in equation (1.65) when we note that $a(t) \propto t^{1/2}$ for a radiation dominated universe and $a(t) \propto t^{2/3}$ for the matter dominated era.

The above formalism describes the evolution of density perturbations so long as the perturbations are small ($\delta \ll 1$) and the Universe can be approximated as an Einstein-de Sitter ($\Omega_m = 1, k = 0$) universe. For later times in the Universe's history , $a \gg a_{\rm eq}$ and the Einstein-de Sitter approximation is no longer valid. At these late times, the evolution of density perturbations is given by

$$\delta(a) = \delta_0 \, a \frac{g(a)}{g(a_0)}, \tag{1.83}$$

where δ_0 is the density contrast linearly extrapolated to the present day. The function, $g(a)$ is the density-dependent growth function given by (Carroll et al. 1992):

$$g(a, \Omega_{\rm m}, \Omega_\Lambda) = \frac{5}{2}\Omega_{\rm m}(a) \left[\Omega_{\rm m}^{4/7}(a) - \Omega_\Lambda(a) + \left(1 + \frac{\Omega_{\rm m}(a)}{2}\right)\left(1 + \frac{\Omega_\Lambda(a)}{70}\right)\right]^{-1}, \tag{1.84}$$

where the evolution of the matter and vacuum density parameters is given by equation (1.30).

Suppression of Growth

The **horizon size**, $\lambda'_H(a)$ is the distance, ct by which light can have traveled in the time, t since the big bang. Approximating the age of the Universe as $t = H^{-1}(a)$, the comoving horizon size is then

$$\lambda_H = \frac{c}{aH(a)}. \tag{1.85}$$

It turns out that the horizon size at the time of matter-radiation equality, $\lambda_H(a_{\rm eq})$ is an important length scale for the growth of structure. Its rôle can most easily be appreciated by taking the Fourier transform of the density field,

$$\delta(\mathbf{k}) = \frac{1}{V}\int d^3x \, \delta(\mathbf{x}) e^{i\mathbf{k}.\mathbf{x}}, \tag{1.86}$$

where k is a comoving wave vector and we have normalised by an arbitrary volume, V. In linear perturbation theory, the individual Fourier modes, $\delta(\mathbf{k})$, evolve independently and each perturbation is characterized by a (comoving) wavelength, λ. A perturbation is said to have "entered the horizon" when $\lambda = \lambda_H(a)$. If $\lambda < \lambda_H(a_{\rm eq})$, then the perturbation enters the horizon while the Universe is still radiation dominated. At this time, the Universe is dominated by the radiation density, which evolves as $\rho_{\rm r}(a) = \rho_{\rm r,0}\, a^{-4}$ and the resulting expansion time-scale, $t = H^{-1}(a)$ is smaller than the typical collapse time-scale of the dark matter perturbations, and so, they cannot collapse. That is, the fast radiation-driven expansion prevents these perturbations from collapsing. The growth of such perturbations is therefore suppressed during the period between the time the perturbation entered the horizon and the epoch of matter-radiation equality. Fig. 1.3 demonstrates this suppression of

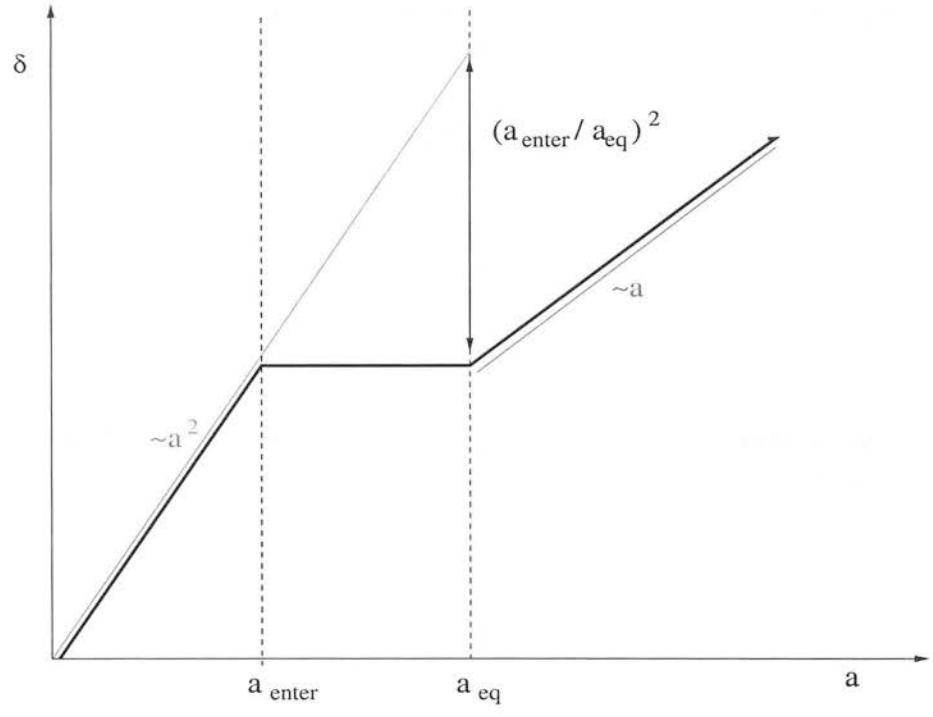

Figure 1.3: The growth of structure for a perturbation with $\lambda < \lambda_H(a_{\rm eq})$. At early times, the perturbation grows as $\delta \propto a^2$. It enters the horizon when the scale-factor is given by $a_{\rm enter} < a_{\rm eq}$. At this point, its growth is suppressed by a factor, $(a_{\rm enter}/a_{\rm eq})^2$ until the epoch of matter-radiation equality – at which point, the perturbation begins to grow linearly with the scale factor.

growth for a perturbation with wavelength, $\lambda < \lambda_H(a_{\rm eq})$ and reading off from this plot gives us the suppression factor:

$$f_{\rm sup} = \left(\frac{a_{\rm enter}}{a_{\rm eq}}\right)^2 = \left(\frac{k_0}{k}\right)^2, \tag{1.87}$$

where k is the wavenumber of the perturbation and k_0 is the wavenumber corresponding to the scale-factor at the time of matter-radiation equality. The second equality in equation (1.87) comes from applying the Einstein-de Sitter approximation (for details, see *e.g.* Bartelmann & Schneider 2001) which is a reasonable approximation for such an early time in the Universe's evolution.

Origin of Structure

There is really only one main contender for the origin of structure, *i.e.* the small irregularities from which structure formation takes place. We have, in fact already met it — inflation. It turns out that as well as solving the flatness and horizon problems, inflation can actually generate these irregularities in the early Universe. According to Heisenberg's uncertainty principle, empty space can be thought of as a sea of particles and antiparticles. If a particle-antiparticle pair is to be created for a very short time, the energy required to create the pair can be "borrowed" from the uncertainty principle and so these

"virtual particles" can exist even in empty space, continually popping in and out of existence. These events are termed "quantum fluctuations". During inflation, the Universe is expanding so rapidly that any fluctuations caught up in the expansion are themselves stretched. This process happens to new fluctuations which are created during inflation, so that by the end of the expansion, small irregularities exist on a wide range of length scales. The details of this process would depend on the particular model of inflation employed and thus would produce slightly different distributions of mass. So it may be possible to decide between competing models of inflation through observations of the large-scale structure we see today.

Other possibilities for the origin of structure – mainly topological defects (*e.g.* cosmic strings, domain walls etc.) — have recently been ruled out from precise observations of the CMB anisotropies, and in particular, from the measurements of the peaks in the CMB power spectrum.

1.2.2 The Power Spectrum of Density Fluctuations, $P(k)$

We have seen in the previous section that the most likely origin of the "seeds" of structure in the Universe is quantum fluctuations which are blown up later in an inflationary stage of the Universe's evolution. If this is the case, then the initial density inhomogeneities are uncorrelated with one another and the distribution of their amplitudes is Gaussian. In other words, the initial irregularities represent a **Gaussian random field** whose statistical properties can be described completely by its **power spectrum**, $P(k)$. To define $P(k)$, we first consider the *two-point correlation function*, $\langle \delta(\mathbf{x}) \delta^*(\mathbf{y}) \rangle$ of the density field, $\delta(\mathbf{x})$, where the asterisk denotes complex conjugation and the angled brackets denote the *ensemble average* taken over many realisations. In reality, of course, we only have access to one realisation - the observable Universe. However, by averaging over a sufficiently large volume of the Universe, we would expect the result to approach the true ensemble average. Fields for which the volume average and ensemble average are equal are called **ergodic** fields and in what follows we assume the cosmological density field, $\delta(\mathbf{x})$ to be ergodic.

Since we are also approximating $\delta(\mathbf{x})$ as a homogeneous and isotropic random field, the correlation function can only depend on the absolute value of the difference vector between the two points, $\mathbf{x}$ and $\mathbf{y}$:

$$\langle \delta(\mathbf{x}) \delta^*(\mathbf{y}) \rangle = C_{\delta\delta}(|\mathbf{x} - \mathbf{y}|). \tag{1.88}$$

Defining the *Fourier transform* pair of δ as

$$\hat{\delta}(\mathbf{k}) = \int d^3x \, \delta(\mathbf{x}) e^{i\mathbf{k}.\mathbf{x}} \;\; ; \;\; \delta(\mathbf{x}) = \int \frac{d^3k}{(2\pi)^3} \hat{\delta}(\mathbf{k}) e^{-i\mathbf{k}.\mathbf{x}}, \tag{1.89}$$

we can calculate the correlation function in Fourier space as

$$\langle \hat{\delta}(\mathbf{k}) \hat{\delta}^*(\mathbf{k}') \rangle = \int d^3x \, e^{i\mathbf{k}.\mathbf{x}} \int d^3x' \, e^{-i\mathbf{k}'.\mathbf{x}'} \langle \delta(\mathbf{x}) \delta^*(\mathbf{x}') \rangle. \tag{1.90}$$

Combining this with equation (1.88) and substituting $\mathbf{x}' = \mathbf{x} + \mathbf{y}$ yields

$$\begin{aligned}\langle\hat{\delta}(\mathbf{k})\hat{\delta}^*(\mathbf{k}')\rangle &= \int d^3x\, e^{i\mathbf{k}.\mathbf{x}} \int d^3y\, e^{-i\mathbf{k}'.(\mathbf{x}+\mathbf{y})} C_{\delta\delta}(|\mathbf{y}|) \\ &= (2\pi)^3\delta_D(\mathbf{k}-\mathbf{k}') \int d^3y\, e^{-i\mathbf{k}.\mathbf{y}} C_{\delta\delta}(|\mathbf{y}|) \\ &= (2\pi)^3\delta_D(\mathbf{k}-\mathbf{k}')P_\delta(|\mathbf{k}|), \end{aligned} \tag{1.91}$$

where $\delta_D(\mathbf{x})$ is the Dirac delta function and we have defined the *power spectrum* of the density field as the Fourier transform of the two-point correlation function:

$$P_\delta(|\mathbf{k}|) = \int d^3y\, e^{-i\mathbf{k}.\mathbf{y}} C_{\delta\delta}(|\mathbf{y}|). \tag{1.92}$$

Equation (1.92) is known as the **Weiner-Kitchiner Theorem**. As mentioned already, a Gaussian random field is fully characterized by its power spectrum, equation (1.92). This is because the Fourier components, $\hat{\delta}(\mathbf{k})$ of the field are mutually statistically independent and the probability densities for the Fourier modes are Gaussian with dispersion, $P_\delta(|\mathbf{k}|)$. Since (due to isotropy) the power spectrum only depends on the modulus of $\mathbf{k}$, it is often referred to as $P_\delta(k)$ or simply $P(k)$ where $k = |\mathbf{k}|$. Note also that the alternative notation, $P(k) \equiv \langle|\delta^2(k)|\rangle$ is often used for the power spectrum. Strictly speaking, the Fourier decomposition is only valid in flat space. However, at early enough times, the Universe is flat for all cosmological models, while for later times, the flat approximation is also an excellent approximation for the scales of interest (*i.e.* for scales much smaller than the curvature radius of the Universe).

Having defined the power spectrum, $P(k)$, we can use the results of Section 1.2.1 to infer its form. Let $P_i(k) = \langle|\delta_i^2(k)|\rangle$ denote the primordial density perturbation spectrum immediately following inflation. Then, since the density contrast grows as $\delta \propto a^{n-2}$, equation (1.65), the power spectrum, therefore, must grow as $P(k) \propto a^{2(n-2)}$. By the time a perturbation with wavenumber, k enters the horizon, we have

$$P_{\rm enter}(k) \propto a_{\rm enter}^{2(n-2)} P_i(k) \propto k^{-4} P_i(k), \tag{1.93}$$

where we have used equation (1.87) with $k \gg k_0$. If we impose the condition of scale-invariance of the total power at a time, $a_{\rm enter}$, then this implies $k^3P(k) = \text{const}$. From equation (1.93) then, we infer the form of the primordial density perturbation spectrum: $P_i(k) \propto k$. This **scale-invariant spectrum** is known as the **Harrison-Zel'dovich spectrum** (Harrison 1970; Peebles & Yu 1970; Zel'dovich 1972). Combining this result with the suppression of growth, equation (1.87) yields:

$$P(k) \propto \begin{cases} k & \text{for } k \ll k_0 \\ k^{-3} & \text{for } k \gg k_0 \end{cases}, \tag{1.94}$$

where $k_0 = \lambda_H^{-1}(a_{\rm eq})$ is the wavenumber corresponding to the horizon size at $a_{\rm eq}$. Finally, the power spectrum is often expressed in dimensionless form as the variance per logarithmic interval in

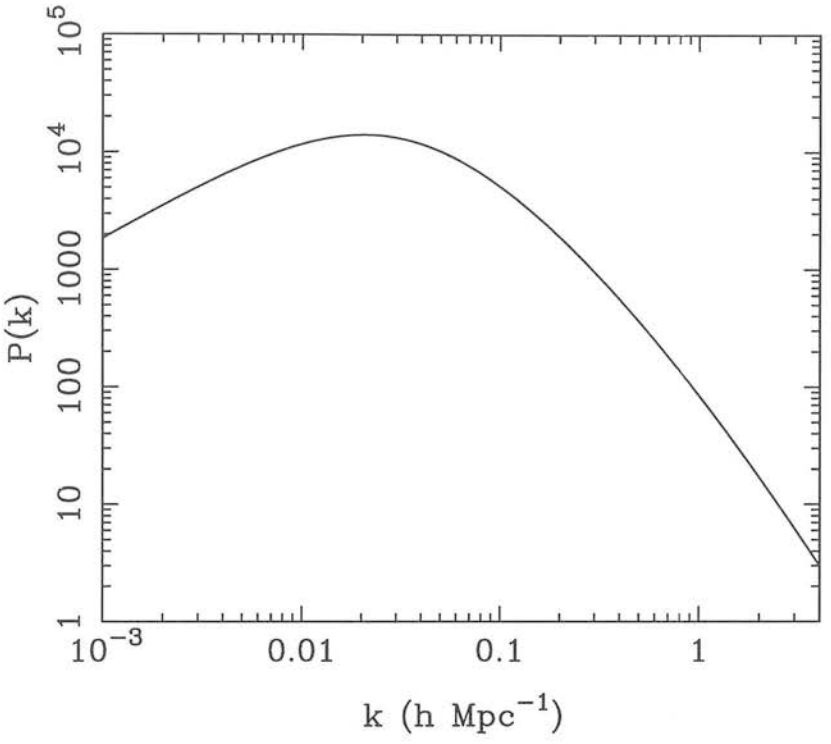

Figure 1.4: The linearly evolved CDM matter power spectrum for the standard ΛCDM cosmological model. On large scales (small k), the power increases linearly with wavenumber while on small scales (large k), the power falls $\propto k^{-3}$ as in equation (1.94).

wavenumber, k, *i.e.* ,

$$\Delta^2(k) = \frac{k^3 P(k)}{2\pi^2}. \tag{1.95}$$

Fig. 1.4 shows a typical linear CDM power spectrum for the standard $\Omega_m = 0.3$, $\Omega_\Lambda = 0.7$ ΛCDM cosmological model which has been normalised to $\sigma_8 = 0.8$ (see next section).

1.2.3 Normalisation of the Power Spectrum

As well as the shape of $P(k)$ discussed above, another important aspect of the matter power spectrum is its normalisation. The most common way of expressing the power spectrum normalisation is by quoting the rms density variation when smoothed with a **top-hat filter** (*i.e.* a sphere of uniform weight) of radius $8h^{-1}$Mpc). This quantity is denoted σ_8 and its value has been the subject of significant debate in the cosmological community over the last couple of years. There are several methods available for calculating the normalisation of $P(k)$ and these are described below.

Normalisation by the CMB and galaxy redshift surveys:

The amplitude of fluctuations in the CMB can be translated into an amplitude for $P(k)$ by virtue of the Sachs-Wolfe effect (Sachs & Wolfe 1967). Until a few of years ago, the only measurements of CMB anisotropies available were those from the COBE satellite which measured the amplitude of

fluctuations on a single angular scale ($\sim 7\,\mathrm{deg}$). Thus an amplitude for $P(k)$ could only be found on these relatively large scales. In recent years, a number of new CMB experiments have measured the CMB power spectrum over a range of scales and to a high degree of accuracy. This data can be combined with other datasets (*e.g.* galaxy redshift surveys; supernovae type Ia measurements) to put strong constraints on the value of σ_8 (*e.g.* Lahav et al. 2002; Percival et al. 2002; Melchiorri & Silk 2002).

In fact, σ_8 can be independently measured from galaxy redshift surveys by measuring the redshift-space distortion parameter, $\beta = \Omega_m^{0.6}/b$ along with the undistorted galaxy power spectrum, $P_{\rm gal}(k) = b^2 P_{\rm m}(k)$, where b is the linear bias of galaxies with respect to the dark matter (*e.g.* Peacock et al. 2001; Taylor et al. 2001a).

Determination of the local variance of galaxy counts:

By measuring the local variance of galaxy counts, and assuming that galaxies are biased tracers of the underlying density field, the amplitude of dark matter fluctuations can be inferred. This method, pioneered by Davis & Peebles (1983), is usually achieved in practice by measuring the variance of galaxy counts within spheres of radius, $8h^{-1}\mathrm{Mpc}$ — hence the use of σ_8 to quantify the normalisation of $P(k)$. The crucial drawback of this method, however, is that a model for the *bias* of galaxies needs to be assumed. Although initial measurements of the bias from galaxy redshift surveys (Verde et al. 2002; Lahav et al. 2002) and weak lensing measurements (Hoekstra et al. 2002a) indicate that galaxies are unbiased tracers of mass on large scales, the bias mechanism on galactic and galaxy cluster scales is still unknown. Consequently the problem of finding the corresponding variance, σ_8 of density fluctuations from a measure of the variance of galaxy counts is still an outstanding issue.

Normalisation by the local abundance of galaxy clusters:

One of the most widely used ways of determining σ_8 is by relating the number density of cosmic structures of a given mass to the linear theory power spectrum through some theoretically predicted (*e.g.* Press & Schechter 1974) mass distribution. This is usually done on the scale of galaxy clusters as it turns out that their abundance is highly sensitive to the amplitude of density perturbations, *i.e.* to σ_8. The mass distribution of galaxy clusters is often determined from X-ray observations. One method uses measurements of the X-ray Luminosity Function (XLF) and a suitable Mass-Luminosity conversion to infer the mass distribution of the clusters (*e.g.* Borgani et al. 2001; Reiprich & Böhringer 2002; Viana, Nichol & Liddle 2002). Another method uses measurements of the X-ray Temperature Function (XTF) and a Mass-Temperature relation to convert the XTF measurements to a mass distribution (*e.g.* Eke et al. 1998; Viana & Liddle 1999; Pierpaoli, Scott & White 2001, Seljak 2002). However, a significant source of uncertainty for both these methods lies in the exact details of the relationships between mass, luminosity and temperature for these massive clusters.

Normalisation by weak gravitational lensing measurements:

A comparatively new method for determining the value of σ_8 is through the use of wide-field weak lensing or *cosmic shear* measurements (see chapter 2). Because gravitational lensing measurements probe the *total* matter distribution in a very direct manner, this represents the most direct method of measuring the amplitude of matter-density perturbations. One of the major sources of error in determining σ_8 from cosmic shear measurements to date (*e.g.* Van Waerbeke et al. 2001; Bacon et al. 2002; Hoekstra et al. 2002b; Refregier, Rhodes & Groth 2002) has been the uncertainty in the median redshift of the lensed source galaxies used in the cosmic shear measurements. One of the key results presented later in this thesis in chapter 3 relates to a measurement of σ_8 using cosmic shear measurements where this uncertainty has effectively been eliminated (see also Brown et al. 2003).

1.2.4 Non-linear Evolution

At late stages of evolution and on small scales, *i.e.* on the scales of galaxies, galaxy clusters etc., the growth of density fluctuations departs from the linear evolution of equation (1.83). In this régime, perturbations begin to grow non-linearly and perturbations of different size interact with one-another. Although, in general, one would think that these effects would complicate the process sufficiently as to put an analytic description of the non-linear growth beyond our grasp, nevertheless analytic formulae describing the non-linear behaviour of $P(k)$ have been derived (Jain, Mo & White 1995; Peacock & Dodds 1996; Smith et al. 2002). The expressions of Jain, Mo & White and Peacock & Dodds rely on the existence of a general scaling law which relates the two-point correlation function in the linear and non-linear régimes (Hamilton et al. 1991) while the Smith et al. method has made use of the analytic "halo model" (*e.g.* Seljak 2000; Peacock & Smith 2000) for nonlinear structure formation which, unlike the two previous works mentioned, does not assume stable clustering. The effect of non-linear evolution is demonstrated in Fig. 1.5 where the dimensionless matter power spectrum, $\Delta^2(k)$ is plotted for both the linear and non-linear cases. The non-linear spectrum has been calculated using the prescription of Peacock & Dodds 1996 and using the recent "halofit" model of Smith et al. 2002.

1.2.5 Evidence for Dark Matter

In the previous two sections we have developed tools for quantifying the amount of matter in the Universe and describing its clustering properties. We now turn to the question of what constitutes the matter in the Universe. Clearly, some of this matter is in the form of "normal" baryonic matter — the stars, galaxies and galaxy clusters which we observe via their emission of light are all examples of baryonic matter. However, there is a large body of evidence to suggest that the vast majority of matter in the Universe is *invisible*. Because it cannot be seen, this type of matter is termed **dark matter**. There is also compelling theoretical evidence that this matter is mostly *non-baryonic* in nature. The evidence and motivation for these assertions are outlined below but let us first examine the implications of what we are claiming.

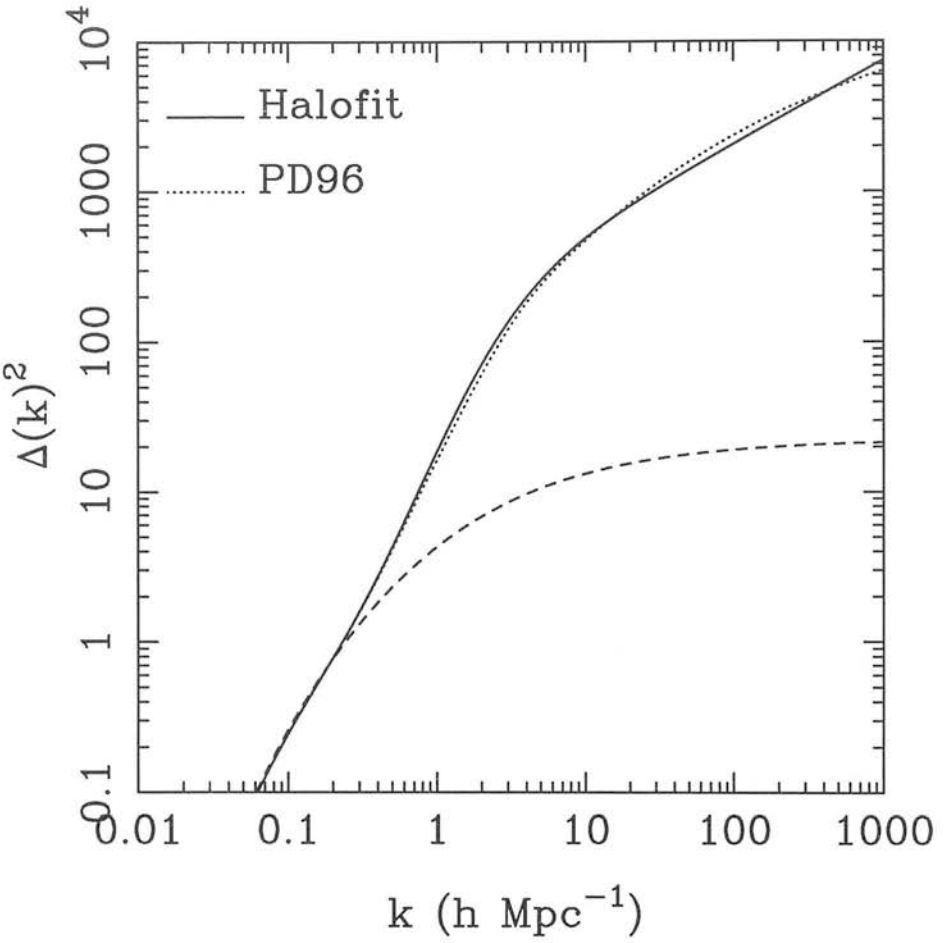

Figure 1.5: The dimensionless matter power spectrum as calculated for the ΛCDM model with $\Omega_m = 0.3$, $\Omega_\Lambda = 0.7$ and normalised to $\sigma_8 = 0.8$. The linear spectrum is shown as the dashed line. The nonlinear spectrum is also shown as calculated using the prescription of Peacock & Dodds 1996 (dotted line) and using the recent "halofit" model of Smith et al. 2002 (full line). Note the much higher power of the non-linear spectra at small scales ($k > 1$).

Our first claim is that the majority ($\sim$ 90%) of the matter in the Universe is dark. This is a rather startling (and worrying!) assertion as it suggests that the stars, galaxies and galaxy clusters that have become the building blocks of observational astronomy and cosmology are, in general **not representative** of the Universe as a whole. How can we, then, be confident that our understanding of the distribution of matter, or the processes involved in structure formation, for example, is correct? Must we simply hope that the matter that we can see is doing roughly the same things as the matter that we can't? Things get even worse when we come to our second claim — that the dark matter is fundamentally different (*i.e.* non-baryonic) in nature. What is this strange stuff that dominates the matter content of our Universe? Surely, we cannot claim to have a sound understanding of the Universe if we don't even know what it contains!

Thankfully, however, this is not the end of the story. We will see that although these two assertions are almost unavoidable given the evidence that we have, there are still ways to use the matter that we can see (*e.g.* galaxy redshift surveys) to infer the distribution of the invisible dark matter. We will also learn in the next chapter that there is one method which can be used to "see" the dark matter directly, *i.e.* **gravitational lensing**, and so, we do not have to simply rely on an assumed relationship between the visible and dark matter. Before we get to this however, let us first review the evidence for the existence of dark matter, after which we will list and briefly discuss the various dark matter candidates.

Galaxies in the Universe

We have already mentioned that anisotropies in the CMB radiation are thought to be associated with the seeds of structure in the Universe. This is due to the Sachs-Wolfe effect (Sachs & Wolfe 1967) by which fluctuations in the temperature of the CMB reflect *baryonic* density fluctuations of the same order of magnitude. The amplitude of the fluctuations seen in the CMB today is about 10^{-5} on large scales and so, by inference, this must be the amplitude of the fluctuations in the baryonic density field at the time of decoupling. We have seen that the scale factor at the time of decoupling was $\sim 10^{-3}$ (Section 1.1.9). Therefore, according to equation (1.65), the density fluctuations should only have reached a level of $\sim 10^{-2}$ by the present day. However, structures with $\delta \gg 1$ (*i.e.* galaxies, clusters etc.) are clearly very common in the Universe and this discrepancy between the amplitude of the CMB fluctuations and the structures we see today must be accounted for. The existence of cosmic structure with $\delta \gg 1$ could arise naturally if there exists an additional matter component which only couples through weak interactions. Such a weakly-interacting matter component would decouple from the cosmic plasma well before photons decoupled from baryons and the CMB was emitted. Therefore, fluctuations in this additional matter component could begin growing much earlier in the Universe's history and so, they could easily have reached the amplitudes we see today. This is one of the strongest arguments in favour of a non-baryonic weakly interacting dark matter component in the Universe.

Nucleosynthesis

Nucleosynthesis, the theory of how the primeval elements formed in the early Universe, has been dealt with earlier in Section 1.1.9. This theory is important when discussing the density of the Universe and dark matter as it restricts the density of *baryonic* matter in the Universe. As we have seen, the theory can only match the observed elemental abundances if Ω_B (the contribution to Ω from baryonic matter) is within the range:

$$0.016 \leq \Omega_B h^2 \leq 0.024 \,. \tag{1.96}$$

This restriction on Ω_B indicates that if the Universe is to have a critical density, the vast majority of matter in the Universe must be non-baryonic in nature.

Galaxy rotation curves

Observations of galaxy rotation curves — rotation speed *vs.* radius are indicative of a large amount of unseen mass in galaxy halos. The expected shape of a typical galaxy rotation curve can be deduced from equating the gravitational force at a distance, r with the centripetal force:

$$\frac{v^2}{r} = \frac{GM(r)}{r^2} , \tag{1.97}$$

where v is the velocity, $M(r)$ is the mass enclosed within radius r and G is Newton's gravitational constant. The expected shape of the curve is made clear when we rewrite this as

$$v = \sqrt{\frac{GM(r)}{r}} . \tag{1.98}$$

This equation implies that as we go to large radii, which enclose most of the visible light of the galaxy, the velocity should drop off as the square root of the radius, r. However, observations of galaxies produce rotation curves that remain more or less constant at these large radii indicating a large amount of unseen dark matter in the galactic halos. Sometimes the inferred amount of dark matter is ten times the amount of visible matter in the galaxy. This halo of dark matter could, in theory be baryonic (*e.g.* brown dwarfs, black holes) but this is thought to be highly unlikely given what we know already.

Bulk motions in the Universe

Motions of galaxies relative to one another are another source of evidence for dark matter, assuming that their motions are due to gravitational attraction between the galaxies. The analyses of these bulk flows tends to be rather complicated but the main result is that the total density of matter in the Universe (visible and dark!) is given by:

$$\Omega_m \geq 0.3 . \tag{1.99}$$

Note that this is much larger than the above nucleosynthesis arguments allow for. This again implies that the majority of matter in the Universe is non-baryonic.

Gravitational lensing

Gravitational lensing (see chapter 2) depends only on the projected 2-dimensional mass distribution of the lens and thus can be used to infer masses for the lensing galaxy or galaxy cluster. Masses derived in this way indicate masses far in excess of the visible matter.

Modern estimates of mass to light ratios, (M/L) range from $M/L \sim 30hM_\odot/L_\odot$ for galaxies to $M/L \sim 200hM_\odot/L_\odot$ for rich clusters of galaxies (see *e.g.* Hoekstra et al. 2002c). It is also possible to actually map out the projected mass distribution of the lensing galaxy, cluster or supercluster (*e.g.* Gray et al. 2002). Mass maps produced in this way generally reveal a smoother distribution for the

total mass of the lens than for the visible matter indicating that the dark matter is more smoothly distributed.

Inflation

Inflation predicts that the geometry of the Universe should be flat. A flat Universe ($\Omega = 1$) together with the result from Nucleosynthesis indicates that the vast majority of matter in the Universe is not only dark but also non-baryonic. $\Omega = 1$ is also much greater than the density derived from galaxy curves indicating that the dark matter may be more smoothly distributed than the visible matter.

Another possibility for a flat Universe is a non-zero cosmological constant. In this case, $\Omega_{\rm m} + \Omega_\Lambda = 1$ would need to be satisfied. This would allow $\Omega_{\rm m}$ to be less than 1 although the restriction, $\Omega_{\rm m} \geq 0.3$ from the analysis of large-scale bulk flows would still apply. Thus, the existence of dark matter is well established whatever cosmology we are dealing with and it is therefore necessary to have some ideas as to what constitutes it.

1.2.6 Dark Matter Candidates

The candidates for dark matter fall into three broad categories; cold dark matter (CDM), hot dark matter (HDM) and compact objects. "Cold" refers to non-relativistically moving particles whereas "hot" refers to relativistically moving particles. These three types are briefly discussed below.

Cold Dark Matter

The existence of at least some cold dark matter in the Universe is highly desirable from the point of view of structure formation. We have seen in Section 1.2.5 that CDM is necessary for the structures we see in the Universe to have formed. The CDM candidates consist mainly of WIMPs — "weakly interacting massive particles" such as the heavy neutrino. It turns out that the cross-section of weakly interacting particles, $\sigma_{\rm weak}$ gives just about the right dark matter density:

$$\Omega_{\rm wimp} \sim \frac{1}{M\sigma_{\rm weak}} \sim 0.3, \tag{1.100}$$

where M is the mass of the WIMP. WIMPs are predicted to exist according to the theory of **Supersymmetry** in which each of the known particles in the Standard Model of particle physics is thought to have associated with it an, as yet undetected, **superpartner**, *i.e.* bosons would have a fermionic superpartner (*e.g.* the photon and the implied photino) while known fermions would have a bosonic superpartner (*e.g.* quarks imply the existence of squarks). Although most supersymmetric particles are predicted to be unstable, it is thought that a lightest supersymmetric particle (**LSP**) should exist. The fact that this has not been detected in particle physics experiments to date implies a lower bound on its mass of $M \geq 10\,\mathrm{GeV}$ and so a supersymmetric LSP would be a good candidate for cold dark matter.

Currently, one of the best prospects for a particle comprising the dark matter is the supersymetrically predicted neutralino. Other WIMP candidates are axions, photinos, and gravitinos (see *e.g.* Jungman, Kamionkowski & Griest (1996) for a comprehensive review of supersymmetric CDM candidates). A crucial test of these supersymmetric theories will come in 2005 when the **large hadronic collider (LHC)** at CERN begins operations — many supersymmetric theories predict the existence of particles with masses of $\sim 1\mathrm{TeV}$ — well within the detection capabilities of the LHC.

Hot Dark Matter

The main hot dark matter candidate is the light neutrino. However, hot dark matter does not have favourable properties for structure formation — if the dark matter was entirely composed of light neutrinos, the structure we see in the Universe today could not have formed — their formation would be damped away by the relativistically moving HDM. For this reason, a CDM Universe is favoured over a HDM one.

Recently, several experiments (Sudbury Neutrino Observatory, SuperKamiokande; see *e.g.* Berezinsky 2002) have been conducted to measure the density of neutrinos in the Universe and initial results from these indicate that $\Omega_\nu \ll \Omega_m$. If this is indeed the case, then it is highly unlikely that HDM comprises the dark matter as the light neutrino was the only serious HDM dark matter candidate.

Compact Objects

Both CDM and HDM are examples of non-baryonic dark matter. Compact objects, on the other hand, may be either baryonic or non-baryonic. One possibility for compact unseen objects is black holes. If these are to be baryonic however, they must have formed before nucleosynthesis because of the restriction from equation (1.96). Black holes that formed before nucleosynthesis in the early Universe are known as *primordial black holes*.

Another possibility for the dark matter is the existence of massive compact halo objects (MACHOs). These are unseen objects in the halos of galaxies and have in fact been detected in the halo of our own galaxy through microlensing of stars in the LMC. The objects detected have been found to have masses $\sim 1M_\odot$ and they may be baryonic (*e.g.* brown dwarfs) or non-baryonic. Compact objects are not thought however to contribute significantly to the density of the Universe — recent results from several ongoing MACHO microlensing projects indicate that compact objects with masses up to a few solar masses contribute $\leq 10\%$ of the halo mass of our own galaxy (*e.g.* Alcock et al. 2000; Lasserre et al. 2000; Zebrun et al. 2001).

1.3 Summary

In this chapter we have reviewed the standard Friedmann-Lemaître cosmological model, beginning with the Robertson-Walker metric which describes the nature of space-time, and the Friedmann and

fluid equations which govern the Universe's evolution. We have considered the effect of the inclusion of a cosmological constant in these equations and also the possibility of the existence of dark energy. We have described the various parameters which we can measure from observations — the Hubble constant, H_0, the density parameters, Ω_m, Ω_B & Ω_Λ and the deceleration parameter, q_0. We have also considered the various distance measures that are available to us and the relationships between them. The nature and origin of the CMB has been examined and its value as a probe of the early Universe has also been highlighted. Other aspects of the early Universe such as the radiation-dominated era, nucleosynthesis, baryogenesis and finally inflation have also been dealt with. The latter part of this introductory chapter has focused on matter in the Universe. We have discussed the origin and growth of structure and we have described how to quantify the clustering of such structure by use of the power spectrum of density fluctuations. We have given particular attention to methods used to measure the amplitude of the matter power spectrum, σ_8. Finally we have listed and discussed the evidence for a dark matter component of the Universe and we have examined the implications of the fact that the majority of matter in the Universe is both unseen and non-baryonic in nature. What results then is a reasonably complete "concordance" model of cosmology:

- The Universe is homogeneous and isotropic on large scales.
- The Universe is expanding and it seems, *accelerating*. It is very close to being spatially flat with a matter content of $\Omega_m = 0.3$ and a non-zero cosmological constant with an energy content of $\Omega_\Lambda = 0.7$. The value of the Hubble constant has been measured to be $H_0 \simeq 72\,\mathrm{kms}^{-1}\mathrm{Mpc}^{-1}$.
- Very early in the Universe's history, some process — possibly inflation — sows the seeds of structure formation.
- Structures evolve linearly at first and then, non-linearly to produce the galaxies and clusters we see today.
- We can quantify the clustering of these structures using the power spectrum of density fluctuations, $P(k)$.
- Most ($\sim 90\%$) of the matter in the Universe is unseen and non-baryonic. This dark matter is most likely to be cold and comprised of WIMPs - weakly interacting massive particles. These are very massive particles predicted from supersymmetry such as the neutralino or the photino. However, they have yet to be detected by particle physics experiments.

CHAPTER 2

Gravitational Lensing

We have seen in Chapter 1 that the existence of dark matter is well established although it is not clear what constitutes it at the present time. The nature of dark matter (whether it is particles or compact objects, hot or cold etc.) and its distribution in the Universe are two of the most interesting and important questions in cosmology today. In answering these questions, no observational method is better placed than gravitational lensing since the lensing effect depends only on how much matter is present — the type of matter has no effect since all matter exerts the same gravitational attraction.

However, before we can attempt to detect and measure a gravitational lensing signal, we need to understand the mechanisms of how it takes place and its effect on the images of lensed sources. The purpose of this chapter is to develop the formalism and tools required for such an understanding. We will review the basics of gravitational lensing theory and describe the deflection of light by mass condensations along the line of sight. We will pay particular attention to the régime of weak lensing where the images of large numbers of background galaxies are coherently distorted by mass condensations. We will consider weak lensing by galaxy clusters and superclusters and will describe the basics of cluster mass reconstruction theory. We will then go on to consider the weak lensing effect of the large scale structure of the Universe — the so-called *cosmic shear* effect. Finally, we will look at another astrophysical phenomenon that can mimic weak lensing and contaminate weak lensing measurements, *i.e.* the *intrinsic alignment* of galaxy shapes.

2.1 Gravitational Light Deflection

Gravitational lensing is the phenomenon whereby the path of a light-ray is perturbed by the presence of mass condensations close to the unperturbed light-ray's path. A full description of gravitational light deflection in the Universe would require a rigorous treatment of the propagation of light in an arbitrary curved space-time. This is, in general, a complicated theoretical problem; however, for almost all cases of interest, this full treatment is not required as there are a number of reliable approximations that we can make to simplify things considerably. Central to the theory of gravitational lensing in this respect is the idea of the *weak field régime* of General Relativity which we now describe.

2.1.1 The Weak Field Régime in General Relativity

As we have seen in Chapter 1, the nature of any space-time can be described by its metric, $g_{\mu\nu}$. We also learned that the evolution of the metric is governed by the Einstein field equations,

$$R^{\mu\nu} - \frac{1}{2}g^{\mu\nu}R = -\frac{8\pi G}{c^4}T^{\mu\nu}, \tag{2.1}$$

where $g^{\mu\nu}$ is the matrix inverse to $g_{\mu\nu}$, $R^{\mu\nu}$ is the Ricci tensor, R is the Ricci scalar and $T^{\mu\nu}$ is the energy-momentum tensor. For the purposes of describing gravitational light deflection, we wish to consider situations where we can approximate the local space-time as differing only slightly from the Minkowski space-time of special relativity. That is, we consider a metric which can be written as

$$g_{\mu\nu} = \left(1 - \frac{1}{2}h\right)\eta_{\mu\nu} + h_{\mu\nu}, \tag{2.2}$$

where $\eta_{\mu\nu} = \mathrm{diag}(1, -1, -1, -1)$ is the Minkowskian metric of special relativity, $h_{\mu\nu}$ is the metric deviation (for which $|h_{\mu\nu}| \ll 1$) and we have defined $h \equiv \eta^{\mu\nu}h_{\mu\nu}$. In the linear approximation, we can choose, without loss of generality, the gauge condition,

$$h^{\mu\nu}_{,\nu} = 0, \tag{2.3}$$

in which case, the Einstein field equations, linearised in $h_{\mu\nu}$, become

$$\left(\Delta - \frac{1}{c^2}\frac{\partial^2}{\partial t^2}\right)h^{\mu\nu} = \frac{16\pi G}{c^4}T^{\mu\nu}. \tag{2.4}$$

The solution, for an isolated source, in the absence of incoming gravitational radiation is (*e.g.* Schneider et al. 1992)

$$h^{\mu\nu}(t, \mathbf{x}) = \frac{-4G}{c^4}\int \frac{T^{\mu\nu}\left(t - \frac{|\mathbf{y}|}{c}, \mathbf{x} + \mathbf{y}\right)}{|\mathbf{y}|}d^3y. \tag{2.5}$$

Specialising to the case of (a) slowly moving ($|\mathbf{v}| \ll c$) and (b) perfect fluid sources, for which $|p| \ll \rho c^2$, then the components of the stress-energy tensor, equation (1.6), simplify to

$$T^{00} \approx \rho c^2 \ ; \ T^{0,i} \approx c\rho v^i \ ; \ T^{ij} \approx \rho v^i v^j + p\delta_{ij}, \tag{2.6}$$

where $v^i \equiv dx^i/dt$ are the components of the 3-velocity, $\mathbf{v}$, ρ is the matter density and p is the pressure. In equation (2.6), we have neglected terms of relative order, v^2/c^2 and $p/(\rho c^2)$. Introducing the retarded potentials,

$$\begin{aligned} \phi(t,\mathbf{x}) &\equiv -G\int \frac{\rho\left(t-\frac{|\mathbf{y}|}{c},\mathbf{x}+\mathbf{y}\right)}{|\mathbf{y}|}d^3y; \\ \mathbf{V}(t,\mathbf{x}) &\equiv -G\int \frac{(\rho v)\left(t-\frac{|\mathbf{y}|}{c},\mathbf{x}+\mathbf{y}\right)}{|\mathbf{y}|}d^3y, \end{aligned} \tag{2.7}$$

we obtain from equations (2.2) and (2.5) – (2.7), the following expression for the metric:

$$ds^2 = g_{\mu\nu}dx^\mu dx^\nu \approx \left(1+\frac{2\phi}{c^2}\right)c^2dt^2 - 8c\,dt\frac{\mathbf{V}\cdot\mathbf{x}}{c^3} - \left(1-\frac{2\phi}{c^2}\right)d\mathbf{x}^2. \tag{2.8}$$

In the near zone of a system of slowly moving bodies, we can ignore the retardation in equation (2.7) and the potentials are

$$\begin{aligned} \phi(t,\mathbf{x}) &\approx -G\int \frac{\rho\,(t,\mathbf{x}+\mathbf{y})}{|\mathbf{y}|}d^3y; \\ \mathbf{V}(t,\mathbf{x}) &\approx -G\int \frac{(\rho v)\,(t,\mathbf{x}+\mathbf{y})}{|\mathbf{y}|}d^3y. \end{aligned} \tag{2.9}$$

The "post-Minkowskian" metric, equation (2.8), satisfies the **weak field condition** if, and only if, as well as satisfying the assumptions (a) and (b) above, the Newtonian potential, $\phi(t,\mathbf{x})$ of the mass distribution, ρ obeys

$$|\phi| \ll c^2. \tag{2.10}$$

Equation (2.10) then, defines the *weak field régime* of General Relativity. In this régime, we have

$$\left|\frac{\mathbf{V}}{c^3}\right| \leq \left|\frac{\mathbf{v}}{c}\right| \cdot \left|\frac{\phi}{c^2}\right| \ll 1, \tag{2.11}$$

and so, to first order in (v/c), the second term on the right-hand side of equation (2.8) can be neglected. Under weak field conditions therefore, the metric at some instant, t is completely determined by the density at that instant - exactly like the gravitational potential in Newton's theory.

The majority of astrophysical situations of interest (including all cases of gravitational lensing!) can be treated using the weak field régime and we implicitly assume weak fields in all of what follows. Note that, for spherical bodies, equation (2.10) implies that $2GM/c^2 = R_s \ll R$ and so, in regions

near the Schwarzchild radius, R_s, the weak field régime doesn't apply. In such cases, we are in the *strong field régime* - examples of such cases are black holes and neutron stars. Note also, that the distinction we have just made between strong and weak gravitational fields is a completely separate issue from the idea of strong and weak gravitational lensing – we address this classification of lensing phenomena later in this chapter in Section 2.1.8.

In addition to the weak field condition, if we further assume that the mass condensations that cause light deflection are local perturbations to the underlying smooth matter distribution, then we can split the path of a particular light-ray into three distinct zones (see also Section 2.1.3 below). In the first zone, light travels unperturbed from the source to a point close to the lens. The second zone is the region near the lens in which the light deflection occurs, and the final zone is the region between the lens and observer through which the light, once again, travels unperturbed. For the purposes of understanding gravitational lensing then, we need only consider the second zone where the light deflection occurs.

2.1.2 Deflection Angle

A gravitational lens is analogous in many ways to an imperfect optical lens and it is possible (*e.g.* Schneider et al. 1992) to define an effective index of refraction, n for the lens:

$$n = 1 - \frac{2}{c^2}\Phi,$$

where Φ is the gravitational potential of the lens and c is the speed of light. Integrating the gradient of n perpendicular to the light path yields the **deflection angle**, $\hat{\alpha}$:

$$\hat{\alpha} = \frac{2}{c^2}\int \vec{\nabla}_\perp \Phi \, dl, \tag{2.12}$$

through which the light has been deflected. In all astrophysical situations of interest $\hat{\alpha}$ is always very small and so the integral above can be carried out along the unperturbed light ray. This approximation is the equivalent of the Born approximation in atomic and nuclear physics. As an example, consider the deflection of a light-ray by a point mass. The potential for a point mass, M can be expressed as:

$$\Phi(b, z) = -\frac{GM}{(b^2 + z^2)^{1/2}},$$

where b is the impact parameter and z is the distance along the unperturbed light ray (see Fig. 2.1). Applying equation (2.12) to this potential yields the deflection angle for a point mass :

$$\hat{\alpha} = \frac{2}{c^2}\int \vec{\nabla}_\perp \Phi \, dz = \frac{4GM}{c^2 b}. \tag{2.13}$$

Comparing this with the **Schwarzchild radius** of the lens, $R_s = 2GM/c^2$, we find,

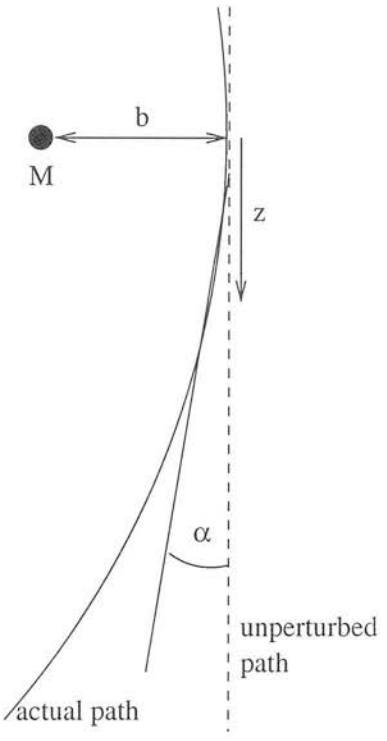

Figure 2.1: Deflection of a light ray due to the gravitational potential of a point mass. The deflection of the light can be quantified by the deflection angle given by $\hat{\alpha} = 2/b$, where b is in units of the Scwarzchild radius of the lens.

$$\hat{\alpha} = \frac{2}{b}, \tag{2.14}$$

where b is in units of the Schwarzchild radius.

2.1.3 Thin screen approximation

This approximation assumes that the lens is thin enough that most of the deflection of the light ray occurs within $\Delta z \sim \pm b$ of the lens centre. Accordingly, we can project the mass of the lens onto the "lens plane" - orthogonal to the line of sight. The lens plane defined in this way is characterized by its surface mass density:

$$\Sigma(\boldsymbol{\xi}) = \int \rho(\boldsymbol{\xi}, z)\, dz\,,$$

where $\boldsymbol{\xi}$ is a 2-dimensional vector in the lens plane and ρ is the mass density at the position $(\boldsymbol{\xi}, z)$. Then, the deflection angle, $\hat{\boldsymbol{\alpha}}$ is just the sum of deflections due to all mass elements in the plane:

$$\hat{\boldsymbol{\alpha}}(\boldsymbol{\xi}) = \frac{4G}{c^2} \int \frac{(\boldsymbol{\xi} - \boldsymbol{\xi}')\Sigma(\boldsymbol{\xi}')}{|\boldsymbol{\xi} - \boldsymbol{\xi}'|^2}\, d^2\xi'. \tag{2.15}$$

For the special case of a circularly symmetric lens, this reduced to

$$\hat{\alpha}(\xi) = \frac{4GM(\xi)}{c^2\xi},$$

where M is the mass enclosed within a radius, ξ:

$$M(\xi) = 2\pi \int_0^{\xi} \Sigma(\xi')\xi' \, d\xi'.$$

2.1.4 The Lens Equation

A typical lensing scenario is shown in Fig. 2.2. We can introduce the **reduced deflection angle**, α, defined by:

$$\boldsymbol{\alpha} = \frac{D_{ds}}{D_s}\hat{\boldsymbol{\alpha}}, \tag{2.16}$$

where D_{ds} is the distance from the lens plane to the source plane and D_s is the distance from the observer to the source plane. All distances are angular diameter distances (see Section 1.1.7). Reading off from the diagram, we find;

$$\begin{aligned} \boldsymbol{\theta} D_s &= \boldsymbol{\beta} D_s + \hat{\boldsymbol{\alpha}} D_{ds} \\ \text{or} \quad \boldsymbol{\beta} &= \boldsymbol{\theta} - \frac{D_{ds}}{D_s}\boldsymbol{\alpha}(\boldsymbol{\theta}), \end{aligned} \tag{2.17}$$

and thus,

$$\boldsymbol{\beta} = \boldsymbol{\theta} - \boldsymbol{\alpha}(\boldsymbol{\theta}). \tag{2.18}$$

Equation (2.18) is the lens equation and is only valid when the distances are angular diameter distances. As an example, consider a lens with a constant surface mass density, Σ. In this case the reduced deflection angle is given by

$$\begin{aligned} \alpha(\theta) &= \frac{D_{ds}}{D_s}\frac{4G}{c^2\xi}(\Sigma\pi\xi^2) \\ &= \frac{4\pi G\Sigma}{c^2}\frac{D_d D_{ds}}{D_s}\theta. \end{aligned} \tag{2.19}$$

Hence, we can define the **critical surface mass density** of the lens, $\Sigma_{\rm cr}$ as

$$\Sigma_{\rm cr} = \frac{c^2}{4\pi G}\frac{D_s}{D_d D_{ds}}. \tag{2.20}$$

For a lens with constant $\Sigma = \Sigma_{\rm cr}$, $\alpha(\theta) = \theta$. Lenses which have $\Sigma > \Sigma_{\rm cr}$ somewhere are said to be "supercritical".

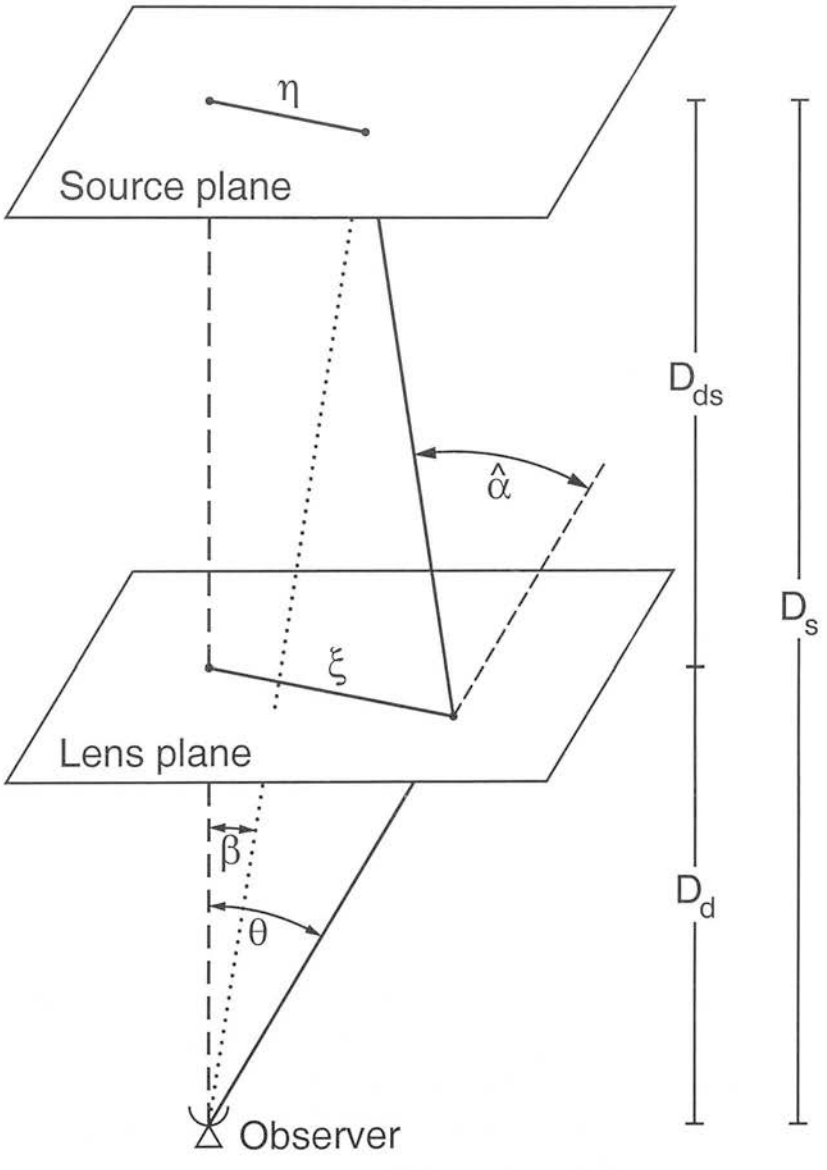

Figure 2.2: A typical lensing scenario showing the source and lens planes. All the distances are angular diameter distances. (From Bartelmann & Schneider 2001.)

2.1.5 Einstein Radius, θ_E

An important discriminatory scale length in gravitational lensing is the Einstein radius, θ_E. To see how this comes about, consider a circularly symmetric lens with an arbitrary mass profile, $M(\theta)$. Then, the lens equation, equation (2.18) becomes

$$\beta(\theta) = \theta - \frac{D_{ds}}{D_d D_s} \frac{4GM(\theta)}{c^2 \theta}.$$

A source lying exactly on the optic axis, $\beta = 0$ is imaged as a ring if the lens is supercritical. Setting $\beta = 0$ in the above expression defines the Einstein radius of the lens:

$$\theta_E = \left(\frac{4GM(\theta_E)}{c^2} \frac{D_{ds}}{D_d D_s} \right)^{1/2}. \tag{2.21}$$

The Einstein radius is useful for a number of reasons. Firstly, the typical separation in multiple images is $\sim 2\theta_E$. θ_E also provides a rough distinction criterion between "strong" and "weak" lensing — sources lying closer than $\sim \theta_E$ to the lens are strongly magnified whereas those further away are weakly magnified. Finally, in many models the Einstein radius represents the boundary between multiple and single imaging. Note also that the mean density inside the Einstein radius is just the critical density, $\Sigma_{\rm cr}$. As an example, consider again the case of a point mass lens for which the lens equation can be rewritten in terms of θ_E as

$$\beta = \theta - \frac{\theta_E^2}{\theta}. \tag{2.22}$$

Equation (2.22) has two possible solutions:

$$\theta_\pm = 1/2(\beta \pm \sqrt{\beta^2 + 4\theta^2{}_E}).$$

Thus, any source is imaged twice by a point mass – one image appears inside θ_E, the other outside. As the source moves away from the lens, one of the images (the one with its parity reversed; see below) moves towards the lens, while the other image moves closer and closer to the true position of the source and tends to a magnification (see below) of unity.

One of the properties of lensing is that the surface brightness of the lensed objects is conserved. This follows from Lioville's theorem (*e.g.* Kristian & Sachs 1966; Sachs 1973). So, the **magnification** is simply given by the relative areas of the image and source:

$$\text{magnification} = \frac{\text{image area}}{\text{source area}}.$$

For a circularly symmetric lens, the magnification, μ is:

$$\mu = \frac{\theta}{\beta} \frac{d\theta}{d\beta}, \tag{2.23}$$

and substituting for β from equation (2.22), we find:

$$\mu_{\pm} = \left[1 - \left(\frac{\theta_E}{\theta_{\pm}}\right)^4\right]^{-1}. \tag{2.24}$$

Note that $\theta_- < \theta_E$ and so, the magnification of the image inside the Einstein ring is negative! This means that its parity is reversed with respect to the source. The net magnification for the lens is given by:

$$\mu = |\mu_+| + |\mu_-|\,. \tag{2.25}$$

2.1.6 Effective lensing potential

We can define the scalar "lensing potential", $\psi(\boldsymbol{\theta})$ of a gravitational lens as the scaled, projected Newtonian potential, Φ of the lens:

$$\psi(\boldsymbol{\theta}) = \frac{D_{ds}}{D_d D_s}\frac{2}{c^2}\int \Phi(D_d\boldsymbol{\theta}, z)\, dz. \tag{2.26}$$

Taking the gradient of ψ, we have:

$$\begin{aligned}\vec{\nabla}_\theta\psi &= D_d\vec{\nabla}_\xi\psi \\ &= \frac{2}{c^2}\frac{D_{ds}}{D_s}\int \vec{\nabla}_\perp\Phi\, dz.\end{aligned} \tag{2.27}$$

Comparing this with equations (2.12) and (2.16), we see that the gradient of the potential is just the reduced deflection angle:

$$\vec{\nabla}_\theta\psi = \boldsymbol{\alpha}. \tag{2.28}$$

The Laplacian of ψ is also useful as it is simply related to the surface mass density of the lens:

$$\begin{aligned}\nabla^2{}_\theta\psi &= \frac{2}{c^2}\frac{D_d D_{ds}}{D_s}\int \nabla^2{}_\xi\Phi\, dz \\ &= \frac{2}{c^2}\frac{D_d D_{ds}}{D_s}4\pi G\Sigma = 2\frac{\Sigma(\boldsymbol{\theta})}{\Sigma_{\rm cr}},\end{aligned} \tag{2.29}$$

where we have used Poisson's equation ($\nabla^2{}_\xi\Phi = 4\pi G\rho(\xi, z)$) to relate the potential to the mass density of the lens. Introducing the dimensionless surface mass density or **convergence**, κ, we have:

$$\nabla^2{}_\theta\psi = 2\kappa(\boldsymbol{\theta})\,, \tag{2.30}$$

where

$$\kappa(\boldsymbol{\theta}) = \frac{\Sigma(\boldsymbol{\theta})}{\Sigma_{cr.}} = \frac{4\pi G\Sigma(\boldsymbol{\theta})}{c^2}\frac{D_{ds}}{D_s}D_d. \tag{2.31}$$

From equation (2.15), the reduced deflection angle is given by

$$\boldsymbol{\alpha}(\boldsymbol{\xi}) = \frac{4GD_{ds}}{c^2 D_s} \int d^2\xi' \frac{(\xi - \xi')\Sigma(\xi')}{|\xi - \xi'|^2}.$$

Substituting $D_d\theta$ for ξ, this may be written as:

$$\boldsymbol{\alpha}(\boldsymbol{\theta}) = \frac{1}{\pi} \int d^2\theta' \kappa(\theta') \frac{\theta - \theta'}{|\theta - \theta'|^2},$$

and using the identity $\nabla \ln x = x/|x|^2$, we have:

$$\boldsymbol{\alpha}(\boldsymbol{\xi}) = \frac{1}{\pi} \int d^2\theta' \kappa(\theta') \nabla_\theta \left[\ln(\theta - \theta')\right].$$

Finally, using equation (2.28), we can relate the scalar potential of the lens to its convergence:

$$\psi(\boldsymbol{\theta}) = \frac{1}{\pi} \int d^2\theta' \kappa(\theta') \ln(\theta - \theta'). \tag{2.32}$$

The local properties of the lens mapping are described by its Jacobian matrix, A:

$$\begin{aligned} A_{ij} &= \frac{\partial \beta_i}{\partial \boldsymbol{\theta}_j} = \frac{\partial}{\partial \boldsymbol{\theta}_j} \left[\boldsymbol{\theta}_i - \boldsymbol{\alpha}_i\right] \\ &= \delta_{ij} - \frac{\partial \alpha_i(\boldsymbol{\theta})}{\partial \theta_j}. \end{aligned} \tag{2.33}$$

i.e. ,

$$A_{ij} = \delta_{ij} - \frac{\partial^2 \psi(\boldsymbol{\theta})}{\partial \theta_i \partial \theta_j} \equiv M_{ij}^{-1}, \tag{2.34}$$

where M is called the *magnification tensor.* If an element of source, $\delta\beta^2$ is mapped onto an element of image, $\delta\theta^2$, then the magnification is given by:

$$\mu = \frac{\delta\theta^2}{\delta\beta^2} = \det M = \frac{1}{\det A}, \tag{2.35}$$

— *cf.* $\mu = \frac{\theta}{\beta}\frac{d\theta}{d\beta}$ for a circularly symmetric lens.
Consider now the Hessian matrix of ψ:

$$\psi_{ij} = \frac{\partial^2 \psi(\boldsymbol{\theta})}{\partial \theta_i \partial \theta_j},$$

which represents the deviation of the lens mapping from the identity mapping. Equation (2.30) can then be written as

$$\kappa = \frac{1}{2}\left(\psi_{11} + \psi_{22}\right). \tag{2.36}$$

There is one other combination of the derivatives of ψ which is important, namely the complex shear, γ which is given by:

$$\gamma = \gamma_1 + i\gamma_2 = \gamma e^{2i\phi} \tag{2.37}$$

where:

$$\begin{aligned} \gamma_1(\boldsymbol{\theta}) = \frac{1}{2}(\psi_{11} - \psi_{22}) &\equiv \gamma(\boldsymbol{\theta})\cos[2\phi(\boldsymbol{\theta})] \\ \text{and} \quad \gamma_2(\boldsymbol{\theta}) = \psi_{21} = \psi_{12} &\equiv \gamma(\boldsymbol{\theta})\sin[2\phi(\boldsymbol{\theta})]. \end{aligned} \tag{2.38}$$

The inverse magnification tensor, A may now be written in terms of the observables, κ and γ as:

$$\begin{aligned} A &= \begin{pmatrix} 1-\kappa-\gamma_1 & -\gamma_2 \\ -\gamma_2 & 1-\kappa+\gamma_1 \end{pmatrix} \\ &= (1-\kappa)\begin{pmatrix} 1 & 0 \\ 0 & 1 \end{pmatrix} - \gamma \begin{pmatrix} \cos 2\phi & \sin 2\phi \\ \sin 2\phi & -\cos 2\phi \end{pmatrix}. \end{aligned}$$

— Convergence causes an isotropic focusing of light rays and an isotropic magnification of the source. If convergence acted alone, the image would have the same shape as the source but would be larger in size.

— Shear introduces an anisotropy into the lens mapping and causes the image to be stretched and distorted out of shape. γ is the magnitude of the shear while ϕ represents its orientation. Note that the shear transforms as $e^{2i\phi}$ under rotations of the coordinate frame, and is therefore not a vector. Quantities which transform under coordinate rotations in this fashion are called spin-2 fields – *cf.* the Q and U components of electromagnetic radiation.

Finally then, we can express the magnification in terms of the convergence, κ and shear magnitude, γ as

$$\mu = \det M = \frac{1}{\det A} = \frac{1}{(1-\kappa)^2 - \gamma^2}. \tag{2.39}$$

Note that what is observable is the magnitude of the magnification, *i.e.* $|\mu|$.

2.1.7 Critical Curves and Caustics

An important concept when discussing the images produced by gravitational lensing is the idea of critical curves and caustics. We have already seen in Section 2.1.5, for the case of a circularly symmetric supercritical lens, that an image lying exactly on the optic axis will be imaged as a ring around the lens with a radius equal to the Einstein radius, θ_E. We have also seen, in the same section, for the case of a point mass lens, that the positions of the images are dependent on the angular distance, β of the source from the lens.

When we move to consider lensing by galaxies, galaxy clusters etc., we need to account for the distributed nature of the mass in the lens. In this case, the nature and positions of the images formed are best described using critical curves and caustics. **Critical curves** are closed curves in the lens

plane where the Jacobian, A is singular, *i.e.* where $\det A = 0$. **Caustics** are their corresponding image curves in the source plane. According to equation (2.39) therefore, images which appear on critical curves should have *infinite magnification*. This, however, does not occur in reality due to the extended nature of real sources. Nevertheless, sources *are strongly magnified* and distorted when they lie close to or on a caustic (or when their images appear near or on a critical curve). This is what's happening in the spectacular images of giant luminous arcs seen in *e.g.* some HST observations (*e.g.* Fig. 2.6). Caustics also represent the boundary between multiple and single imaging of a source. If we imaging moving a source across the source plane, then the number of images changes by ± 2 as the source moves across a caustic. Consequently, two images will appear or disappear at the corresponding critical curve in the lens plane.

In order to gain a physical interpretation of what convergence κ, shear γ and magnification, μ represent, we can make use of a simple lens model for a lensing galaxy. We consider the case of the **singular isothermal sphere** (SIS) with a mass distribution parameterised by (*e.g.* Narayan & Bartelmann 1997)

$$\rho(r) = \frac{\sigma_v^2}{2\pi G}\frac{1}{r^2}, \tag{2.40}$$

where σ_v is the one-dimensional velocity dispersion of the stars in the lens galaxy and r is the distance from the centre of the galaxy. This model is particularly useful for galactic lenses as it naturally reproduces the flat rotation curves observed in galaxies. The SIS model also has the curious property that the shear induced is equal in magnitude to the convergence at the corresponding position, *i.e.* $\gamma(\xi) = \kappa(\xi)$ (see *e.g.* Dye 1999). If we project the density along the line-of-sight, we obtain the surface mass density of the lens;

$$\Sigma(\xi) = \frac{\sigma_v^2}{2G}\frac{1}{\xi}, \tag{2.41}$$

where ξ is the distance from the centre of the two-dimensional profile. Finally, the convergence, κ is simply $\kappa = \Sigma/\Sigma_{\rm cr}$ where $\Sigma_{\rm cr}$ is a constant, given by equation (2.20). We will see in Section 2.2.2 that it is possible to relate the convergence and shear fields in Fourier space. Thus, if we simulate a 2-dimensional mass distribution according to equation (2.41), we can use a Fast Fourier Transform (FFT, *e.g.* Press et al. 1992) to transform κ to Fourier space where we can use equation (2.57) to calculate the shear field. We can then transform γ back to real space and use equation (2.39) to calculate the resulting magnification, μ. We have calculated the shear and magnification in this way for the case of a *softened isothermal sphere* — an SIS with a softened (*i.e.* finite-valued) core. The results of this simulation are summarised in Figs. 2.3 to 2.5. Fig. 2.3 shows the input convergence distribution and the shear magnitude as obtained from the FFT calculation. We see from these plots that the resulting shear distribution is indeed the same as the input convergence distribution except for the very centre of the lens where the effect of the finite core causes a slight discrepancy. In Fig. 2.4, we plot the components of the complex shear, showing the different distortions caused by γ_1 and γ_2. Finally, the resulting magnification is plotted in Fig. 2.5 (left-hand side) where the extreme magnification near or on critical curves is demonstrated. Also shown on the right-hand side of this figure is the binned

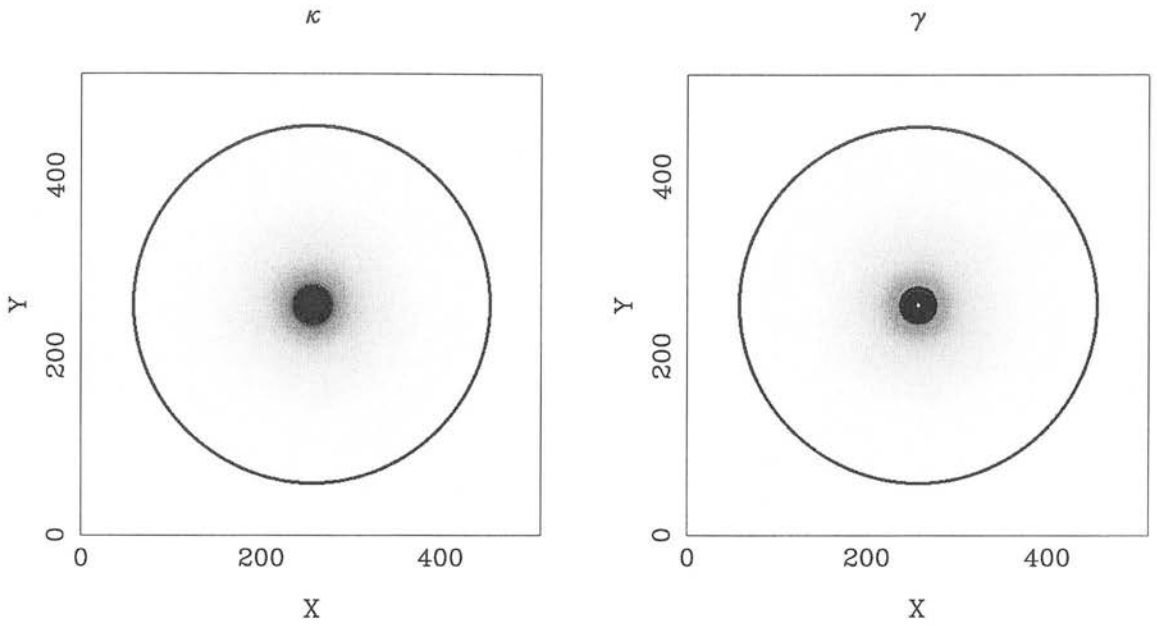

Figure 2.3: Convergence and shear magnitude distributions for the softened isothermal sphere model. The left-hand side shows the input convergence distribution used. The right-hand side shows the shear magnitude distribution as calculated using the FFT method described in the text. A linear greyscale is used in each case. The large dark circles are critical lines of the lens indicating where we expect the magnification to be very large. The calculated shear distribution is very close to the input convergence distribution, as expected for an SIS lens. The slight discrepancy at the very centre is due to the effect of the finite core used in the input model.

ellipticity distribution that would be introduced into a population of perfectly circular background sources.

2.1.8 Strong *vs.* Weak and Macro- *vs.* Microlensing

Having described and quantified the distortion and magnification phenomena that result from gravitational lensing, we can now classify gravitational lensing events into two broad categories — strong and weak lensing. These régimes depend on the severity of the distortions introduced to the lensed objects. We can further separate lensing events into *macro-* and *microlensing*. These two classifications depend on the size of the lens involved — microlensing is lensing by small point-like objects such as stars, planets etc. while macrolensing is lensing by extended mass distributions, *i.e.* galaxies and galaxy clusters.

Strong lensing requires that the surface mass density somewhere in the lens must be greater than the critical surface mass density, *i.e.* $\Sigma \geq \Sigma_{\rm cr}$. It occurs when sources lie within or close to a caustic in the source plane. Thus, multiple images (sources inside a caustic) and giant arcs (sources lying on a caustic) are both cases of strong lensing. Most strong lensing phenomena seen in observations are due to macrolensing by massive galaxy clusters such as the one in Fig. 2.6 which shows an HST image of the Abell 2218 lensing cluster.

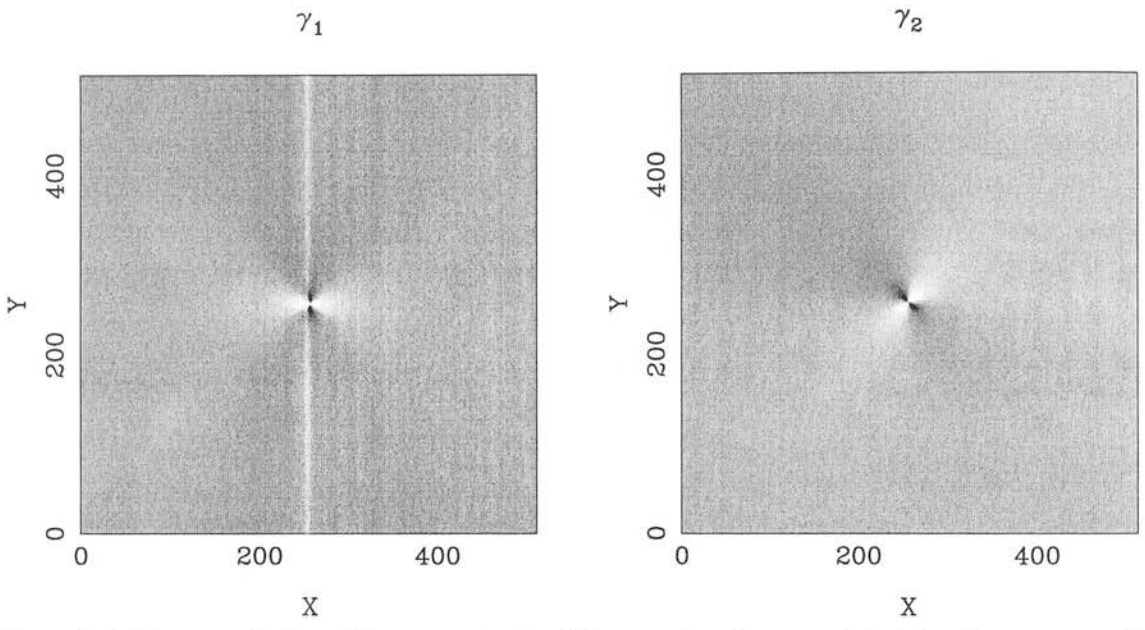

Figure 2.4: The magnitudes of the components of the complex shear, γ plotted in a linear greyscale. The effect of shear is made apparent from these plots — γ_1 (lhs) causes distortions along and perpendicular to the reference (X-) axis, while γ_2 causes distortions at ± 45 degrees to the reference axis.

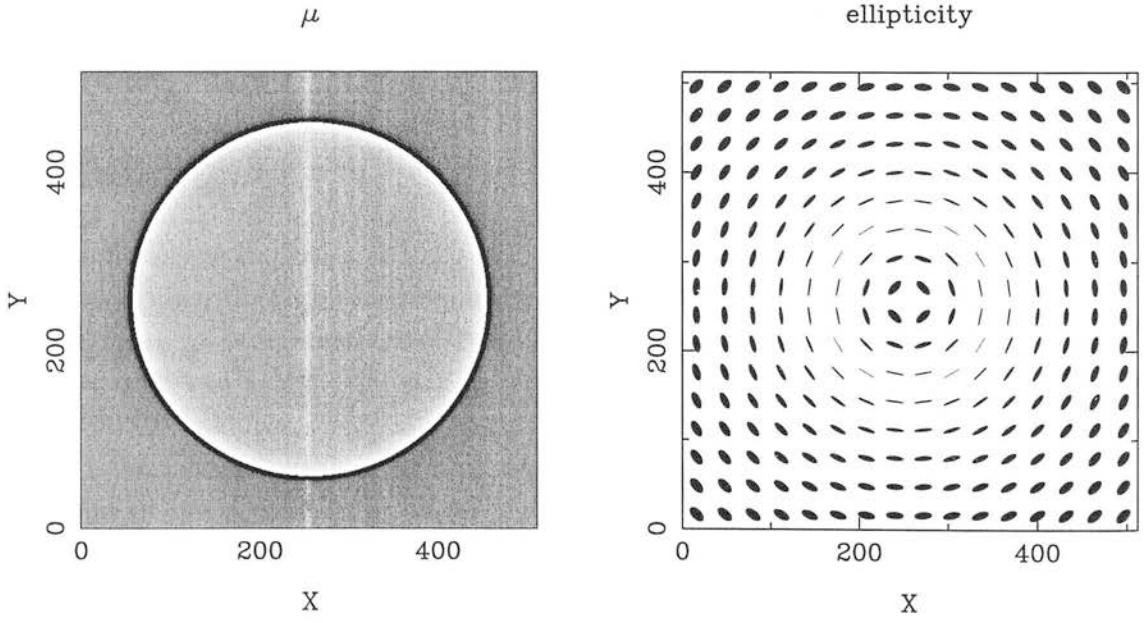

Figure 2.5: The resulting magnification (lhs, plotted in a linear greyscale) and ellipticity distribution from the softened isothermal sphere model described in the text. Note the extreme magnification occurring on and near the critical curves. The ellipticity distribution on the right shows the distortions that would be introduced to a background population of perfectly circular galaxies.

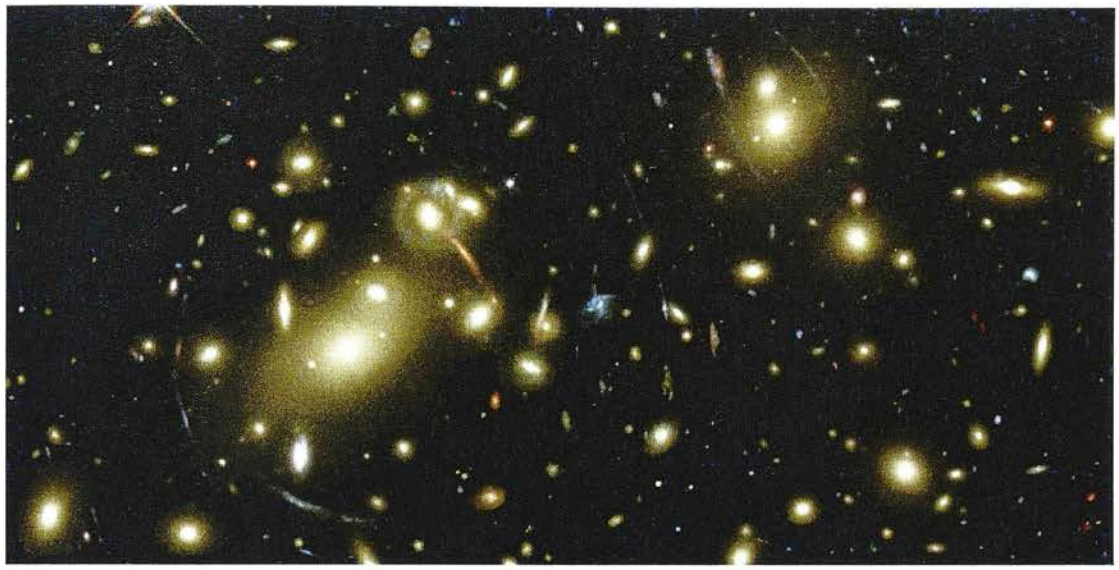

Figure 2.6: Hubble Space Telescope image of the central region of the lensing cluster, Abell 2218 showing a pattern of giant arcs tangentially aligned around the two centres of the cluster. (NASA HST Archive)

In addition to the occasional giant arc and multiple imaging events, a gravitational lens also produces a large number of weakly distorted images of other background sources which are not located inside or near caustics. These images are called arclets and this régime of gravitational lensing is known as **weak lensing**. Observations of weak lensing have become an extremely important astrophysical and cosmological tool over the last decade and weak lensing is discussed in greater detail in Section 2.2.

Most of the microlensing events seen in observations are due to the magnification effect caused by a source and lens moving relative to each other, giving rise to lensing-induced time variability of the source (Chang & Refsdal 1979; Gott 1981). This time-variability of the source flux is due to caustic crossings and so these microlensing events are cases of strong lensing. Microlensing has become a valuable tool in the search for compact objects in our own galaxy. First proposed by Paczyński (1986), this involves monitoring millions of stars in the Small (SMC) and Large (LMC) Magellenic Clouds in search of the time varying signature of microlensing events. Several groups have now detected and measured this effect (*e.g.* Alcock et al. 2000; Lasserre et al. 2000; Zebrun et al. 2001) — one of the results of which was the conclusion, already alluded to in Chapter 1, that compact objects with masses up to a few solar masses comprise $\leq 10\%$ of the dark matter in the halo of our own Galaxy.

2.2 Weak Lensing

In the previous section, we have reviewed the basics of gravitational lensing theory and have illustrated the effects of lensing with a simple lens model. We also separated lensing effects into two broad

categories — strong and weak lensing. In this section, we specialise to the case of *weak lensing* and we shall concentrate on this régime for the remainder of this thesis. First, we will describe how to measure the weak lensing effect, after which we will look, in turn, at weak lensing caused by galaxy clusters and the weak lensing signal due to the large-scale structure in the Universe. Finally we shall discuss another astrophysical phenomenon that can mimic the weak lensing effect — that of *intrinsic galaxy alignments*.

2.2.1 Measuring weak shear

The effects of weak lensing are, in general, twofold — firstly, large numbers of background galaxies are weakly distorted, or *weakly sheared* by the presence of foreground structure. We discuss in detail how to measure this effect below. The second effect is the magnification effect which can be detected by measuring either the change in number density of source galaxies (*e.g.* Broadhurst, Taylor & Peacock, 1995) or the change in image sizes at a fixed surface brightness (*e.g.* Bartelmann & Narayan 1995). Here, we concentrate on the first effect as this is the most commonly used method to measure weak lensing (although see Jain 2002) and indeed, it is this effect that we make use of in the analysis presented in later chapters.

The effect of a weak shear on a galaxy image is to induce an *additional ellipticity* in the image and so, to quantify the strength of the distortions of the background galaxies, a measure of the ellipticity of a galaxy is required. Consider a galaxy image for which the surface brightness, $I(\boldsymbol{\theta})$ is well defined even at large angular separations from the centre, $\overline{\boldsymbol{\theta}}$ of the image,

$$\overline{\boldsymbol{\theta}} \equiv \frac{\int d^2\theta\, w(I)\boldsymbol{\theta} I(\boldsymbol{\theta})}{\int d^2\theta\, w(I) I(\boldsymbol{\theta})}, \tag{2.42}$$

where $w(I)$ is an intensity weight function. The second moments of the surface brightness are then given by:

$$Q_{ij} = \frac{\int d^2\theta\, w(I) I(\boldsymbol{\theta})(\theta_i - \bar{\theta}_i)(\theta_j - \bar{\theta}_j)}{\int d^2\theta\, w(I) I(\boldsymbol{\theta})}, \quad i,j \in \{1,2\}. \tag{2.43}$$

The weight function, $w(I)$ must be chosen carefully to ensure that the above integrals converge. For example, unweighted second moments are impractical shape estimators due to divergent noise far from the centre of the image. Using equation (2.43), the shape of the image can now be quantified in terms of the **complex ellipticity** (*cf.* the complex shear, equation (2.37)) defined by

$$\varepsilon = \varepsilon_i + i\varepsilon_2 = |\varepsilon| e^{2i\phi}, \tag{2.44}$$

where the components, ε_1 and ε_2 are given by

$$\varepsilon_1 = \frac{Q_{11} - Q_{22}}{Q_{11} + Q_{22}} \text{ and } \varepsilon_2 = \frac{2Q_{12}}{Q_{11} + Q_{22}}. \tag{2.45}$$

In terms of the semi-major (a) & semi-minor (b) axes and the position angle (ϕ) of the object then, the

ellipticity of an image is given by:

$$\varepsilon_\alpha = \frac{a^2 - b^2}{a^2 + b^2} \begin{cases} \cos 2\phi & \alpha = 1 \\ \sin 2\phi & \alpha = 2 \end{cases} . \tag{2.46}$$

Using ε^s to represent the ellipticity of the (unlensed) source, defined in an exactly analogous way to the above image ellipticities, it can be shown (e.g. Kochaneck 1990; Miralda-Escudé 1991; Schneider & Seitz 1995) that the ellipticities transform according to

$$\varepsilon^s = \frac{\varepsilon - 2g + g^2\varepsilon^*}{1 + |g|^2 - 2\,\Re(g\varepsilon^*)}, \tag{2.47}$$

where the asterisk denotes complex conjugation, $\Re\,(g\varepsilon^*)$ means the real part of the complex number, $g\varepsilon^*$ and g is the **reduced shear**, defined by

$$g(\boldsymbol{\theta}) \equiv \frac{\gamma(\boldsymbol{\theta})}{1 - \kappa(\boldsymbol{\theta})}. \tag{2.48}$$

In the weak lensing régime ($\kappa \ll 1, |\gamma| \ll 1$), the reduced shear, $|g| \ll 1$ and equation (2.47) reduces to

$$\varepsilon = \varepsilon^s + 2g. \tag{2.49}$$

The above discussion and equation (2.49) apply to individual galaxies but since the intrinsic ellipticity of the source, ε^s is unknown, little information can be gained from individual ellipticity measurements. However, information on the lensing mass distribution can be gained from considering an ensemble of galaxy images. The crucial assumption here is that the *intrinsic ellipticity distribution* of the sources is random. If this assumption holds, then the expectation value of the source ellipticities should vanish:

$$\langle \varepsilon^s \rangle = 0. \tag{2.50}$$

Taking the average of equation (2.49) then gives:

$$\langle \varepsilon \rangle = 0 + 2\langle g \rangle.$$

Assuming the ensemble covers a small enough angular size on the sky such that the light from the ensemble members experience roughly the same shear, an estimator for the shear is then given by

$$\gamma \approx g \approx \langle g \rangle = \frac{\langle \varepsilon \rangle}{2}. \tag{2.51}$$

Note the factor of 2 in equation (2.51) — the expression $\gamma \approx \langle \varepsilon \rangle$ is also often found in the literature. Both of these expressions can be correct depending on how the ellipticity, ε is defined. For ellipticities defined as in equation (2.45), it is correct to include the factor of 2 as we have done in equation (2.51). All of the above assumes that all the sources lie at the same redshift — *i.e.* that the ratio, D_{ls}/D_s in

the expression for κ, equation (2.31) is the same for all sources. However, $\gamma \approx \langle\varepsilon\rangle/2$ is also true to first order when the source distribution in redshift is taken into account (see Bartelmann & Schneider (2001) for a full discussion).

Equation (2.51) suggests that provided we average over a sufficient number of galaxies, a relatively straightforward mechanism exists for measuring the shear distortion field. This would indeed be true were it not for a variety of systematic effects which complicate the relationship between the observed ellipticity field and the underlying shear field tremendously. Atmospheric effects (seeing, atmospheric refraction, atmospheric dispersion), telescope handling (flexure of telescopes, bad guiding) and optical distortions are among the systematic effects that complicate the simple relationship between shear and ellipticity of equation (2.51). There are, however, methods to remove these spurious distortions and to recover the shear field from observed galaxy ellipticities (*e.g.* Kaiser, Squires & Broadhurst 1995; Refregier & Bacon 2003; Bernstein & Jarvis 2002). Here we briefly review the method of Kaiser, Squires & Broadhurst (1995, hereafter KSB) where we have included the refinements of Luppino & Kaiser (1997) and Hoekstra et al. (1998a).

The KSB method separates the corrections to galaxy ellipticities into two groups. Firstly, a correction for *anisotropic smearing* of the galaxies is applied according to

$$\varepsilon^g_{\rm corrected} = \varepsilon^g_{\rm smeared} - P^g_{\rm sm} p, \tag{2.52}$$

where $\varepsilon^g_{\rm smeared}$ is the observed galaxy ellipticity and $\varepsilon^g_{\rm corrected}$ is the galaxy ellipticity corrected for the anisotropic smearing effect of the point spread function (PSF). The tensor, $P^g_{\rm sm}$ is called the *smear polarisability* while p is a measure of the PSF anisotropy which can be measured from the stars in the field: since for stars, $\varepsilon^*_{\rm corrected} = 0$, then $p = (P^*_{\rm sm})^{-1}\varepsilon^*_{\rm smeared}$. Equation (2.52) thus becomes

$$\varepsilon^g_{\rm corrected} = \varepsilon^g_{\rm smeared} - P^g_{\rm sm}(P^*_{\rm sm})^{-1}\varepsilon^*_{\rm smeared}, \tag{2.53}$$

where the superscripts, g and * refer to galaxies and stars respectively. As well as the anisotropic smearing effect of the collective distortions, a far bigger effect is the *circularization* of the galaxy images by the isotropic part of the distortions, *i.e.* by the *seeing*. Luppino & Kaiser (1997) and Hoekstra et al. (1998a) showed that the *pre-smear* shear can be recovered using

$$\gamma = P^{-1}_{\gamma}\varepsilon^g_{\rm corrected}, \tag{2.54}$$

where,

$$P_{\gamma} = P^g_{\rm sh} - \frac{P^*_{\rm sh}}{P^*_{\rm sm}} P^g_{\rm sm}, \tag{2.55}$$

and we have introduced the *shear polarisability*, $P_{\rm sh}$ for both galaxies (g) and stars (*). The shear and smear polarisabilities can be measured (for both galaxies and stars) from higher-order moments of the surface brightness distribution, $I(\boldsymbol{\theta})$ (see *e.g.* KSB, Luppino & Kaiser (1997) and Hoekstra et al. (1998a) for details). Therefore, by measuring the ellipticities of galaxies and stars along with the

four tensors, $P^g_{\rm sm}$, $P^g_{\rm sh}$, $P^*_{\rm sm}$ and $P^*_{\rm sh}$, and by applying equations (2.53),(2.54) & (2.55), we can indeed extract the underlying shear field from real observations.

2.2.2 Weak Lensing by Galaxy Clusters and Mass Reconstruction Theory

Over the last decade, weak lensing has become a valuable tool for investigating the dark matter distribution in galaxy clusters and superclusters. This is mainly due to the algorithm developed by Kaiser & Squires (1993) by which the measured weak shear distribution, $\gamma(\boldsymbol{\theta})$ can be converted into a corresponding convergence field, $\kappa(\boldsymbol{\theta})$. We have seen already in equations (2.36) and (2.38) that both the convergence and the shear can be expressed as linear combinations of second derivatives of the effective lensing potential, $\psi(\boldsymbol{\theta})$. There exists therefore a mathematical relation connecting the two. If we transform κ, $\gamma_{1,2}$ and ψ to Fourier space, then equations (2.36) and (2.38) can be written as

$$\begin{aligned} \hat{\kappa}(\boldsymbol{k}) &= -1/2(k_1^2+k_2^2)\hat{\psi}(\boldsymbol{k}), \\ \hat{\gamma}_1(\boldsymbol{k}) &= -1/2(k_1^2-k_2^2)\hat{\psi}(\boldsymbol{k}), \\ \hat{\gamma}_2(\boldsymbol{k}) &= -k_1k_2\hat{\psi}(\boldsymbol{k}), \end{aligned} \tag{2.56}$$

where we have denoted the Fourier transform of each field with a hat and $\boldsymbol{k}$ is the two-dimensional wave vector conjugate to $\boldsymbol{\theta}$. We can thus relate the shear and the convergence fields in Fourier space by

$$\begin{aligned} \begin{pmatrix} \hat{\gamma}_1 \\ \hat{\gamma}_2 \end{pmatrix} &= k^{-2} \begin{pmatrix} k_1^2-k_2^2 \\ 2k_1k_2 \end{pmatrix} \hat{\kappa}, \\ \hat{\kappa} &= k^{-2} \begin{bmatrix} (k_1^2-k_2^2) & 2k_1k_2 \end{bmatrix} \begin{pmatrix} \hat{\gamma}_1 \\ \hat{\gamma}_2 \end{pmatrix}. \end{aligned} \tag{2.57}$$

The Kaiser-Squires inversion method then, is to measure the shear components, $\gamma_{1,2}$ and to transform to Fourier space where equation (2.57) is used to solve for $\hat{\kappa}$. The convergence can then be transformed back to real space to obtain $\kappa(\boldsymbol{\theta})$ and hence $\Sigma(\boldsymbol{\theta})$. Note that the inversion can also be expressed in real space as (Kaiser & Squires 1993)

$$\kappa(\boldsymbol{\theta}) = \Re\left[\int d^2\boldsymbol{\theta}'\, \mathcal{D}(\boldsymbol{\theta}-\boldsymbol{\theta}')\gamma(\boldsymbol{\theta}')\right], \tag{2.58}$$

where $\mathcal{D}$ is the complex convolution kernel,

$$\mathcal{D} = \frac{(\theta_2^2-\theta_1^2)-2i\theta_1\theta_2}{\theta^4}, \tag{2.59}$$

and γ is the complex shear given by equation (2.37).

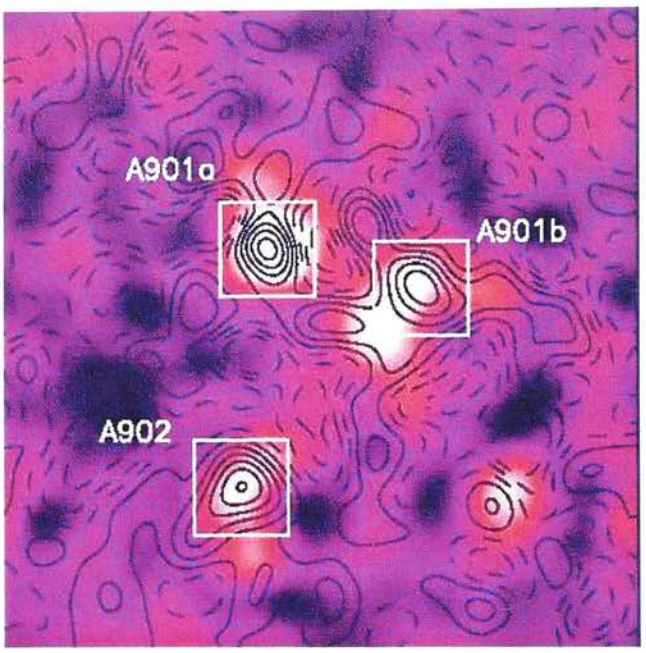

Figure 2.7: The lensing convergence reconstruction of Gray et al. (2002). The convergence distribution is shown as contours while the mass distribution as inferred from the visible light is shown in greyscale. Also shown is the tentative detection of a dark matter "filament" connecting two of the clusters. (From the Edinburgh IfA Gravitational Lensing webpage at `http://www.roe.ac.uk/~meg/darkmatter`.)

Using this prescription, we can convert from shear measurements to surface mass density estimates. However, by design, measurements of the shear distortion alone cannot distinguish whether they were caused by a Jacobian matrix, A or by the matrix multiplied by a scalar, $(1-\lambda)A$, with $\lambda \neq 1$. In both cases, the sizes of the images will be different but their ellipticities will be the same! For $\lambda \ll 1$, this degeneracy transformation reduces to $\kappa' = \kappa + \lambda$ — *i.e.* the convergence can only be determined up to an overall constant. This is commonly referred to as the *sheet mass degeneracy* and is a direct consequence of the fact that homogeneous sheets of mass produce no shear. This also highlights the importance of magnification analysis (see *e.g.* Broadhurst et al. 1995) with which the sheet mass degeneracy may be broken by measuring the lensed distortion of the joint magnitude-redshift distribution of background galaxies.

The methods described above have been applied to a number of clusters in a variety of different environments and "mass maps" for these systems have been obtained (*e.g.* Squires & Kaiser 1996, Squires et al. 1997; Seitz et al. 1996; Fischer 1999). One should bear in mind, however, that these maps are, strictly speaking, *not* mass maps but maps of the lensing convergence and are therefore subject to the mass-sheet degeneracy mentioned above. Nevertheless, some of these maps have very impressive signal-to-noise ratios and have shed light on our understanding of the distribution of dark matter in clusters and superclusters of galaxies (see *e.g.* the supercluster analyses of Kaiser et al. 1998 and Gray et al. 2002). An impressive example of a so-called "mass map" is demonstrated in Fig 2.7

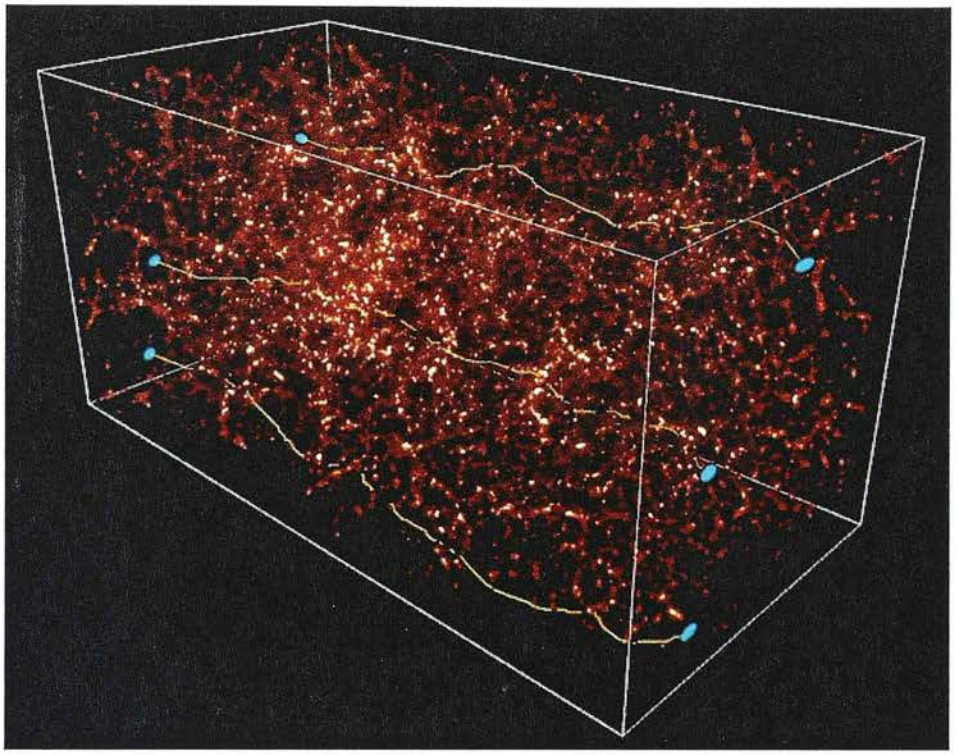

Figure 2.8: Numerical ray-tracing simulation of the cosmic shear effect by Colombi (2000). The images of distant source galaxies (lhs, shown in blue) are distorted by the intervening filamentary structure of the dark matter (shown here in red) resulting in the observed shapes of the galaxies (blue, rhs) being correlated. (From the CFHT Lensing webpage at `http://www.cfht.hawaii.edu/News/Lensing`.)

which shows the lensing convergence reconstruction of Gray et al. (2002) in comparison to the visible light distribution for the Abell 901/902 supercluster of galaxies.

2.2.3 Weak Lensing by Large Scale Structure — Cosmic Shear

As well as the signal from individual clusters and superclusters, we can also measure the weak lensing signal caused by the large-scale structure (LSS) of the Universe. The effect is illustrated in Fig. 2.8 which shows a representation of ray-tracing simulation results where the large-scale distribution of matter imprints its signature by correlating the shapes of distant galaxies. Detecting and measuring this cosmological weak lensing or *cosmic shear* effect has become one of the major goals of the lensing community in recent years. It is, however an extremely difficult task because the distortions in the shapes of the background galaxies are very small ($\sim 1\%$). Therefore, in order to measure cosmic shear, very deep and/or wide surveys are required to give a sufficient number of background galaxies so that the noise due to the galaxies' intrinsic ellipticity dispersion, sampling and cosmic variance doesn't dominate over the expected signal. Since the cosmic shear signal is caused by the LSS, cosmological information can therefore be obtained from the statistical properties of the signal. We can extract this information by comparing the shear signal that we measure with the signals pre-

dicted for various cosmological scenarios. For the purposes of predicting the cosmic shear signal, we restrict ourselves to the case of a spatially flat Universe as this simplifies the expressions somewhat and also because compelling evidence for a flat Universe has already been found from recent CMB observations (*e.g.* de Bernardis et al. 2002; Pryke et al. 2002; Lewis & Bridle 2002).

Particularly useful in terms of statistical measures of the shear field produced by cosmic shear is the **weak lensing effective convergence power spectrum**, $C_\ell^{\kappa\kappa}$, defined in terms of correlations of the Fourier transform of the convergence field:

$$\langle \kappa(\boldsymbol{\ell})\kappa^*(\boldsymbol{\ell}')\rangle = (2\pi)^2 C_\ell^{\kappa\kappa}\delta_D(\boldsymbol{\ell}-\boldsymbol{\ell}'), \tag{2.60}$$

where $\boldsymbol{\ell}$ is the Fourier variable on the sky. In order to derive the form of $C_\ell^{\kappa\kappa}$, we note that in a spatially flat Universe, with comoving distance, r, we can relate the 2-d cosmological lensing potential, $\psi(\boldsymbol{\theta})$ and the 3-d gravitational potential, $\Phi(\boldsymbol{r})$ by (*e.g.* Kaiser 1998; Hu 2000)

$$\psi(\boldsymbol{\theta}) = \frac{2}{c^2}\int_0^r dr' \left(\frac{r-r'}{rr'}\right)\Phi(\boldsymbol{r}'), \tag{2.61}$$

where $\boldsymbol{\theta}$ is the position on the sky and r is the (comoving) distance to the sources. From equation (2.30), we have

$$\begin{aligned}\kappa &= \frac{1}{2}\partial^2\psi \\ &= \frac{1}{c^2}\int_0^r dr' \left(\frac{r-r'}{rr'}\right) r'^2 \frac{\partial^2\Phi(r')}{\partial r'^2}.\end{aligned} \tag{2.62}$$

Applying Poisson's equation to the 3-d potential,

$$\begin{aligned}\nabla^2\Phi(r) &= 4\pi G\rho_m a^2\delta \\ &= \frac{3}{2}H_0^2\Omega_m a^{-1}\delta,\end{aligned} \tag{2.63}$$

yields the expression for the effective convergence at position, $\boldsymbol{\theta}$:

$$\kappa(\boldsymbol{\theta}) = \frac{3}{2}\left(\frac{H_0}{c}\right)^2\Omega_m\int_0^r dr' \left(\frac{r-r'}{r}\right) r'\frac{\delta(r'\boldsymbol{\theta},r')}{a(r')}, \tag{2.64}$$

where ρ_m is the cosmological matter density, Ω_m is the present-day density parameter, a is the scale factor, δ is the relative density contrast and H_0 is the Hubble constant. Equation (2.64) is the convergence observed at a position on the sky, $\boldsymbol{\theta}$ for source galaxies at a distance r. Including a normalised redshift distribution for the source galaxies, $G(r)dr = p(z)dz$ and integrating over this redshift distribution yields the total convergence at position $\boldsymbol{\theta}$ for a distribution of source galaxies:

$$\kappa(\boldsymbol{\theta}) = \frac{3}{2}\left(\frac{H_0}{c}\right)^2\Omega_m\int_0^{r_H} dr' \int_{r'}^{r_H} dr\, G(r)\left(\frac{r-r'}{r}\right) r'\frac{\delta(r'\boldsymbol{\theta},r')}{a(r')}, \tag{2.65}$$

where r_H is the comoving distance to the horizon. Defining the lensing efficiency function, $\overline{W}(r)$ as

$$\overline{W}(r) = \int_r^{r_H} dr'\, G(r') \left(\frac{r' - r}{r'} \right), \tag{2.66}$$

gives

$$\kappa(\boldsymbol{\theta}) = \frac{3}{2} \left(\frac{H_0}{c} \right)^2 \Omega_m \int_0^{r_H} r dr\, \overline{W}(r) \frac{\delta(r\boldsymbol{\theta}, r)}{a(r)}. \tag{2.67}$$

Finally, applying Limber's equation in Fourier space (Kaiser 1992, 1998) to the effective convergence field, equation (2.67), yields the 2-dimensional effective convergence power spectrum, $C_\ell^{\kappa\kappa}$:

$$C_\ell^{\kappa\kappa} = \frac{9}{4} \left(\frac{H_0}{c} \right)^4 \Omega_m^2 \int_0^{r_{\rm H}} dr\, P_\delta \left(\frac{\ell}{r}, r \right) \left(\frac{\overline{W}(r)}{a(r)} \right)^2. \tag{2.68}$$

That is, the convergence power spectrum is simply a weighted projection of the underlying 3-d matter power spectrum and thus represents a direct measure of the projected dark matter distribution. It is this simple relationship between the convergence power spectrum and the matter power spectrum that makes weak lensing such a powerful cosmological probe. Fig. 2.9 shows the effective convergence power spectrum for the concordance ΛCDM model with $\Omega_m = 0.3$, $\Omega_\Lambda = 0.7$, normalised to $\sigma_8 = 0.8$. The figure shows $C_\ell^{\kappa\kappa}$ as calculated using the linear matter power spectrum and using the prescription of Smith et al. (2002) for the non-linear form of $P(k)$. These spectra have been calculated using equation (2.68) with sources being distributed about a median redshift of $z_m = 1.0$.

Equation (2.68) is the fundamental 2-point statistic used for describing the weak lensing signal due to the LSS in the Universe and in Chapter 3 of this thesis, we return to the weak lensing power spectrum where we perform a maximum likelihood reconstruction of $C_\ell^{\kappa\kappa}$ from a weak lensing survey for the first time.

2.3 Intrinsic Galaxy Alignments

We have seen in Section 2.2.1 that we can detect and measure the effects of weak lensing by averaging over the ellipticities of background source galaxies. However, in the process, we have made the critical assumption that the average *intrinsic ellipticity* of the sources will vanish, equation (2.50). This will *not* however, be true in general as there is reason to believe that intrinsic shape correlations are introduced to the galaxy population during the early stages of galaxy formation — theoretically, intrinsic galaxy alignments are expected at some level because nearby galaxies form in similar and related gravitational fields; they should therefore react in similar ways to the influence of these fields and so should have some tendency to align with one another.

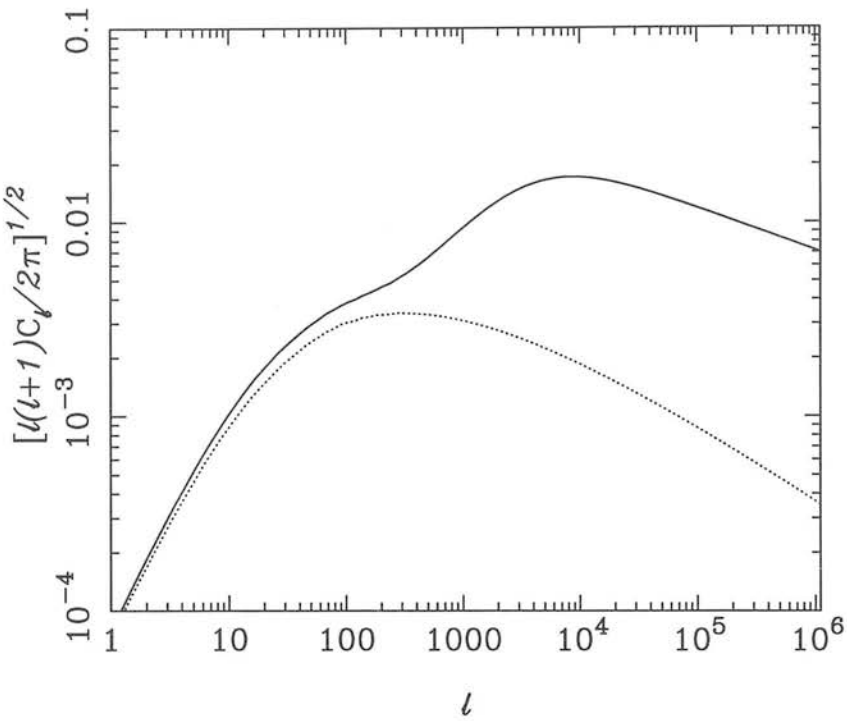

Figure 2.9: The linear (dotted line) and non-linear (solid line) effective convergence power spectrum for the standard ΛCDM cosmological model, normalised to $\sigma_8 = 0.8$ as calculated using equation (2.68). The non-linear matter power spectrum has been calculated using the halo model formulae of Smith et al. (2002). The spectra are plotted in dimensionless units of $[\ell(\ell+1)C_\ell^{\kappa\kappa}/2\pi]^{1/2}$ as a function of the Fourier variable on the sky, ℓ.

2.3.1 Galaxy Alignment Theory

Although it is clear that galaxy shapes will be intrinsically correlated with one another *at some level*, the degree of correlation, and hence its implication for weak lensing measurements is not at all clear although a number of analytical, numerical and observational studies have attempted to address this question in recent years. Most of the analytic models (*e.g.* Lee & Pen 2000, Crittenden et al. 2001 and Mackey et al. 2002) assume the galactic disc to be formed in the plane which is perpendicular to the parent halo's angular momentum vector (Fig. 2.10) and relate this to the surrounding tidal field. The idea that the angular momentum of a galaxy is (at least, partly) determined by the local gravitational field was first suggested by Hoyle (1949) who proposed that galaxy angular momentum arises from the tidal torquing which results whenever the inertia tensor of an object is misaligned with the local gravitational tidal (or shear) tensor. This idea was further developed by Doroshkevich (1970) and White (1984) who calculated the first-order expression for the angular momentum, L_i in terms of the shear tensor, $\boldsymbol{T} = T_{jl} = \partial_j \partial_l \phi$ and the inertia tensor, $\boldsymbol{I} = I_{lk}$ as

$$L_i \propto \epsilon_{ijk} T_{jl} I_{lk}, \tag{2.69}$$

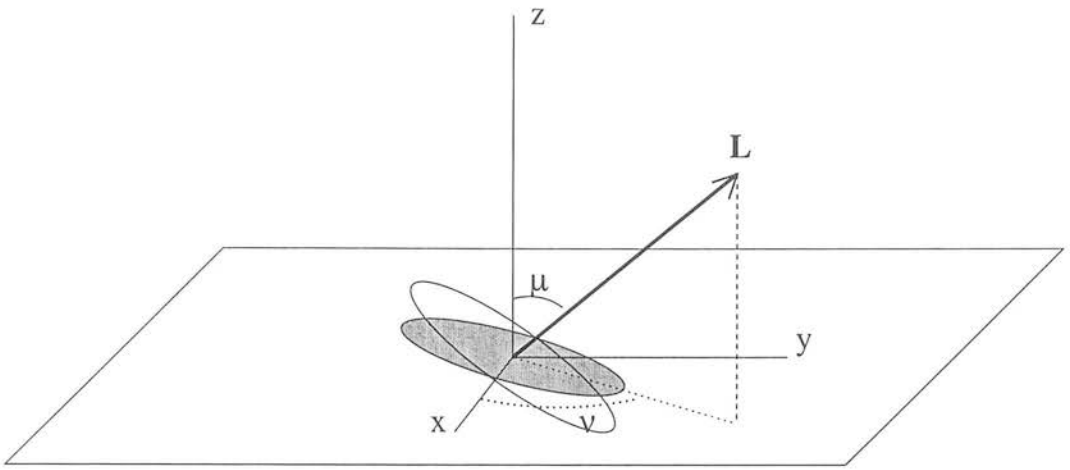

Figure 2.10: A schematic of the spiral model used in the various analyses described in the text. The galaxy is taken to be a thin disc perpendicular to the angular momentum vector, $\boldsymbol{L}$. The sky is in the x-y plane while the line of sight is along the z-axis. The disc of the galaxy is shown as the open ellipse; its projection on the sky as the filled ellipse. The angle, μ is the polar angle of the angular momentum vector, $\boldsymbol{L}$. (From Heavens, Refregier & Heymans 2000.)

where ϕ is the gravitational potential and ϵ_{ijk} is the Levi-Civita symbol. Lee & Pen (2000) have written down the most general quadratic relation between a unit spin (angular momentum) vector and a unit traceless shear tensor:

$$\langle \hat{L}_i \hat{L}_j | \boldsymbol{T} \rangle = \frac{1+a}{3}\delta_{ij} - a\hat{T}_{ik}\hat{T}_{kj}, \tag{2.70}$$

where $a \in [0, \frac{3}{5}]$ is a *correlation parameter* describing the degree of correlation between $\boldsymbol{I}$ and $\boldsymbol{T}$. If $\boldsymbol{I}$ and $\boldsymbol{T}$ are uncorrelated, $a = 3/5$ whereas if they are perfectly aligned, $a = 0$. The parameter a can also be used to parameterise any non-linear effects on the spin-shear correlation. However, it is not clear from theoretical arguments how correlated $\boldsymbol{I}$ and $\boldsymbol{T}$ will be and this leads to a degree of uncertainty in predictions for the initial angular momentum of the dark matter in a halo. There must also be other factors influencing the final galaxy shape such as galaxy merger events and the question of how closely the angular momentum of the gas and stars in the disc follows that of the dark matter in the halo. Various other simplifications are made in the respective analyses including assumptions regarding disc thicknesses in the case of spiral galaxies (*e.g.* Crittenden et al. 2001). Catelan, Kamionkowski & Blandford (2001) have also made analytic predictions for the intrinsic correlation of galaxy shapes. In addition to the tidal torque arguments outlined above, they have also considered the possibility of correlations in galaxy shapes due to halo shape distortions caused by the gravitational tidal field (Fig. 2.11). They claim that this mechanism (which would be more likely to affect elliptical-type galaxies) produces a higher intrinsic alignment signal than that due to the spin-shear correlations. The predictions of the Crittenden et al. (2001) and Catelan et al. (2001) calculations are shown in Fig. 2.12 for galaxies at a median redshift of $z \sim 0.1$ for the ΛCDM model. The statistic plotted is the ellipticity variance as a function of scale, $\sigma_\varepsilon^2(\theta)$ which we shall later see is

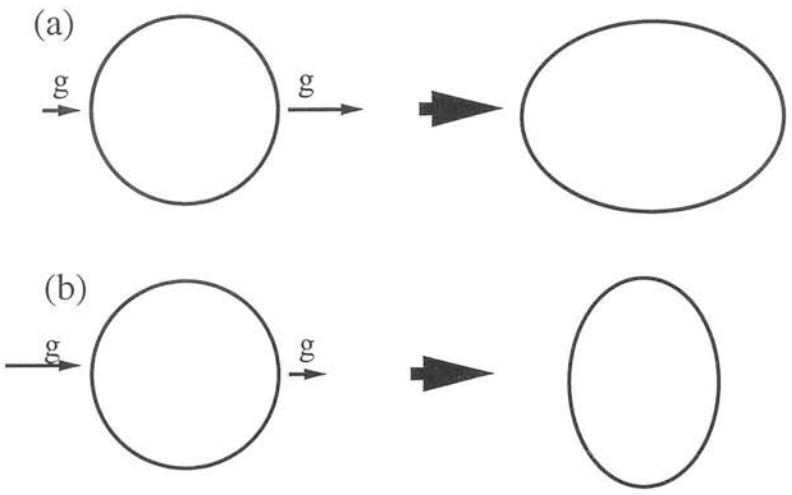

Figure 2.11: A schematic of how a tidal field can cause distortions in a galactic halo. The arrows labeled 'g' indicate the size and direction of the gravitational field. In (a) the tidal field stretches the halo while in (b) the halo is compressed by the tidal field. (From Catelan, Kamionkowski & Blandford 2001.)

a commonly used statistic when discussing cosmic shear measurements.

2.3.2 Numerical Simulations

The degree of intrinsic galaxy shape correlations has also been measured from numerical simulations. Both Heavens, Refregier & Heymans (2000, hereafter HRH) and Croft & Metzler (2001, hereafter CM) have used publicly available N-body simulations run by the Virgo Consortium (Jenkins et al. 1998). The HRH study considers two models for the galaxies — an "elliptical model" where the shape of the galaxy is assumed to coincide with the shape of its parent halo and a "spiral model" where the ellipticity of the galaxy is determined by its angular momentum vector (Fig. 2.10). CM consider only the "elliptical" model. The results of the CM elliptical model are 2 or more times greater than the spiral model results of HRH. The results from both these groups (again for a ΛCDM model with galaxies situated at $z \sim 0.1$ are also plotted in Fig. 2.12. Very recently, Jing (2002) has claimed a much higher measurement of the intrinsic signal from numerical simulations. He has used higher resolution simulations and claims the discrepancy between the HRH and CM measurements and his own to be due to a lack of convergence in the ellipticity correlations measured by HRH and CM. He suggests that the HRH and CM results are underestimated by a factor of ~ 2. He also finds that the ellipticity correlations measured are a strong function of the range of halo masses used in the simulations.

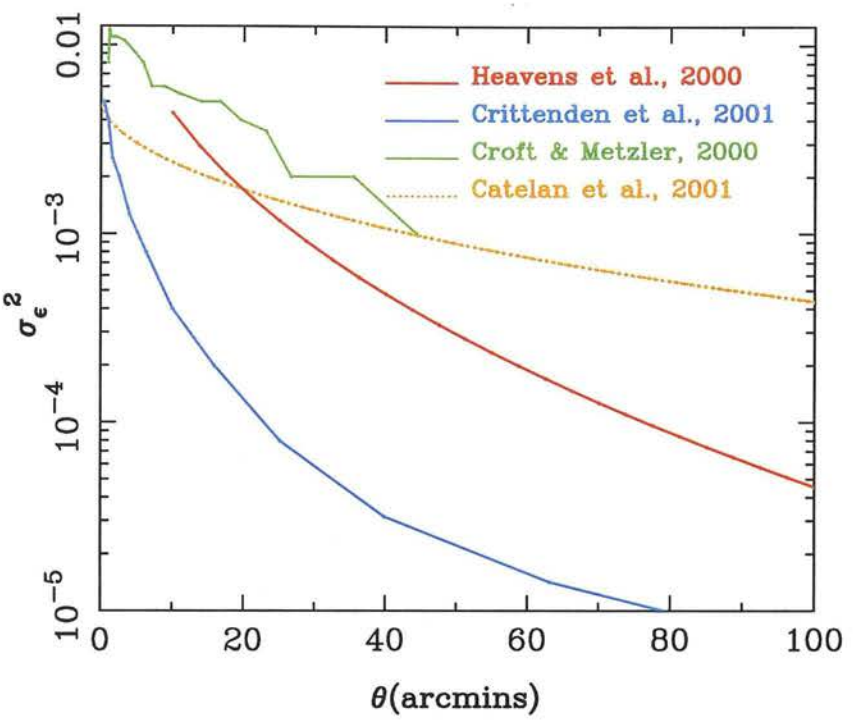

Figure 2.12: Predictions for the intrinsic galaxy ellipticity variance, $\sigma_\epsilon^2(\theta)$ as a function of scale, as calculated from the analytic models of Crittenden et al. (2001) and Catelan et al. (2001) and from the numerical simulations analyses of Heavens et al. (2000) and Croft & Metzler (2001).

2.3.3 Observational Status

It is clear from Fig. 2.12 that there is a great deal of uncertainty as to what the true level of intrinsic shape correlations is. In order to gain a more complete understanding of how these alignments form, we need to discriminate between the different models. In addition, the intrinsic alignment signal can mimic the cosmic shear signal from large scale structure, and so a precise knowledge of the intrinsic alignment amplitude would help a great deal in putting the interpretation of cosmic shear results on a much firmer footing — if a precise measure of the alignment effect were available, it could simply be subtracted off the measured cosmic shear signal to yield the uncontaminated lensing signal. Finally, intrinsic galaxy alignments are interesting *in their own right* since they can, in principle, be used to measure the underlying tidal field and hence, the underlying matter distribution (Lee & Pen 2001). In light of these concerns then, an observational detection and measurement of intrinsic galaxy alignments would be highly desirable. Pen, Lee & Seljak (2000) have made a tentative detection of spin-spin correlations in the Tully catalogue although it is uncertain how these spin-spin correlations translate into correlations in the galaxy ellipticities. Lee & Pen (2002) have detected a correlation between the galaxy spin field and the local tidal shear field in the Point Source Catalogue Redshift (PSCz) survey although, again, the implication for ellipticity correlations from this measurement is not obvious.

In Chapter 4 of this thesis, we present a measurement of the intrinsic correlation of galaxy elliptic-

ities in the SuperCOSMOS Sky Survey (Hambly et al. 2001a). It is this intrinsic *ellipticity correlation* that has the greatest implications for weak lensing studies since it can be directly subtracted off the lensing measurements.

2.4 Summary

In this chapter, we have reviewed the basics of gravitational lensing theory, where we have described the magnification and distortion effects of a gravitational lens. We have developed useful analytic expressions for quantities such as the effective lensing potential, magnification, convergence and the shear, which we can use to categorise various types of lens. We have seen that lensing can be split up into distinct régimes — strong *vs.* weak and macro- *vs.* microlensing and we have paid particular attention to the case of weak macrolensing.

We have discussed, in detail, how to measure the weak lensing effect through measurements of the ellipticities of background galaxies. We have gone on to consider weak lensing by galaxy clusters where we have seen how to reconstruct the convergence field of a cluster or supercluster. We have also considered the weak lensing effect of the large scale structure of the Universe. Termed "cosmic shear", we have seen that this effect can be used as a strong probe of cosmology through statistical measures of the shear field it produces. We have defined and derived the fundamental two-point statistic of weak lensing — the effective convergence weak lensing power spectrum, $C_\ell^{\kappa\kappa}$.

Finally, we have discussed the intrinsic alignment of galaxy shapes. We have reviewed the recent theoretical and numerical attempts at predicting the intrinsic alignment signal. Although these studies show very rough agreement, a definitive work in this field has yet to emerge. In particular, we have seen that observational constraints on the amplitude of the intrinsic alignment effect are rare and until now, have all been indirect.

CHAPTER 3

Maximum Likelihood Cosmic Shear Analysis of the COMBO-17 survey

Having reviewed the standard cosmological model in Chapter 1, and gravitational lensing/intrinsic alignment theory in chapter 2, we are now in a position to measure and interpret the galaxy alignment signal from real observations.

In this chapter, we perform a statistical weak lensing or "cosmic shear" analysis of the COMBO-17 survey. We undertake a full maximum likelihood analysis to measure directly from the data the weak lensing power spectra, $C_\ell^{\kappa\kappa}$, $C_\ell^{\beta\beta}$ and $C_\ell^{\kappa\beta}$ in 5 band powers from $\ell = 400$ to $\ell = 10^4$, where κ is the usual lens convergence and β is an odd-parity 'curl' component of the shear signal. We find a strong measurement of the convergence power over five fields. The non-gravitational β-field has a much lower significance, indicating our data is free of major systematics, while the cross-correlation of κ and β is consistent with zero.

We have used our results to measure cosmological parameters, constraining the normalisation of the matter power spectrum to be $\sigma_8 = (0.72 \pm 0.09)(\Omega_m/0.3)^{-0.49}$. We have significantly reduced the usual additional uncertainty in the median redshift (z_m) of the source galaxies by estimating z_m directly from our data using accurate photometric redshift information from the COMBO-17 multi-band wide-field survey. To demonstrate the power of accurate redshift information, we have also measured parameters from a shear analysis of only those galaxies for which accurate redshift estimates are available. In this case, we have eliminated the uncertainty in the redshift distribution of sources and we show that the uncertainty in the resulting parameter constraints are reduced by more than a factor of 2 compared to the typical uncertainties found in cosmic shear surveys to date. Finally, we combine our parameter measurements with constraints from the 2dF Galaxy Redshift Survey and with those from the CMB. With these additional constraints, we measure the normalisation of the matter power spectrum to be $\sigma_8 = 0.73^{+0.06}_{-0.03}$ and the matter density of the Universe to be $\Omega_m = 0.27^{+0.02}_{-0.01}$.

3.1 Introduction

There continues to be great interest and significant progress in measuring the weak lensing signal arising from large-scale structure. As we have seen in chapter 2, this phenomenon, observed as the weak coherent distortion of background galaxies due to light ray deflection by intervening matter, offers us a direct probe of the mass distribution in the Universe. We can consequently measure cosmologically important quantities (see *e.g.* Bernardeau et al. 1997; Jain & Seljak 1997; Kamionkowski et al. 1998; Kaiser 1998; Hu & Tegmark 1999) such as the bias (see *e.g.* Hoekstra et al. 2001) and the normalisation of the matter power spectrum (*e.g.* Bacon et al. 2002; Hoekstra et al. 2002b; Refregier, Rhodes & Groth 2002; Van Waerbeke et al. 2002).

Of particular interest is the prospect of reconstructing the power spectrum of mass fluctuations from the weak lensing signal. Pen et al. (2002) have used an estimator for the weak lensing shear power spectrum, obtainable from correlation function measurements, to measure the shear power spectrum from the DESCART survey, while Schneider et al. (2002) have further developed estimators for this purpose. Meanwhile, Hu & White (2001) have demonstrated the utility of a maximum likelihood approach to reconstructing the shear power spectrum. Here we will apply a full maximum likelihood analysis to a cosmic shear survey for the first time.

In this chapter, we describe the results of a weak shear analysis of the COMBO-17 dataset, acquired with the La Silla 2.2m telescope in Chile (Wolf et al. 2001). This survey includes 1.25 square degrees of deep R-band observations from which we draw our sample of background galaxies for shear measurements. In addition, the survey has yielded photometric redshifts for approximately 40% of the objects in our selected sample of galaxies, which we use to improve our understanding of the shear signal. We apply a maximum likelihood reconstruction to our dataset to obtain the shear power spectrum, and we fit cosmological models to measurements of both the shear power spectrum and the correlation functions to measure joint constraints on the matter density Ω_m and normalisation of the matter power spectrum σ_8. We obtain further constraints on these parameters by combining our measurements with constraints from both the 2dF Galaxy Redshift Survey (2dFGRS, Percival et al. 2002) and from CMB data (*e.g.* Lewis & Bridle, 2002).

Cosmic shear studies require careful data reduction followed by assessment and removal of systematic effects, such as shear induced by a telescope, anisotropic PSF, and circularization of galaxy shapes. We demonstrate in this chapter that our shear catalogues have almost negligible systematic errors after applying appropriate corrections, and we carefully audit the remaining sources of error (from *e.g.* sample size, redshift uncertainty and shot noise) in order to interpret our results.

3.2 Weak lensing quantities

In the last few years weak gravitational lensing has emerged as the most direct method for measuring the distribution of matter, regardless of its nature, in the Local Universe (Mellier 1999, Bartelmann

& Schneider 2001). This is largely due to its basis in well understood physics: weak lensing is essentially a scattering experiment of photons off the gravitational field generated by cosmological structure. Here, we briefly review the various weak lensing fields that we have introduced in Chapter 2 and we describe their statistical properties.

3.2.1 Weak lensing fields

We have already seen that one of the effects of weak gravitational lensing is to induce distortions into the images of distant source galaxies. This distortion can be parameterised by measuring the ellipticities,

$$\varepsilon_{ij} = \begin{pmatrix} \varepsilon_1 & \varepsilon_2 \\ \varepsilon_2 & -\varepsilon_1 \end{pmatrix} \tag{3.1}$$

of each galaxy from its quadrupole moments at a given isophotal threshold (Kaiser, Squires and Broadhurst, 1995) or by examining the distortion to a set of orthogonal modes describing the galaxy shape (Refregier & Bacon 2003; Bernstein & Jarvis, 2002). In the first instance – which is the approach we adopt in the following analysis – the effect of lensing is to induce an additional ellipticity on the galaxy image;

$$\varepsilon'_{ij} = \varepsilon_{ij} + 2\gamma_{ij}, \tag{3.2}$$

where

$$\gamma_{ij} = \begin{pmatrix} \gamma_1 & \gamma_2 \\ \gamma_2 & -\gamma_1 \end{pmatrix} \tag{3.3}$$

is the trace-free lensing shear matrix. The components γ_1 and γ_2 of the shear matrix represent the two orthogonal modes of the distortion (see *e.g.* Fig. 2.4). The shear matrix is recoverable since in the absence of intrinsic alignments of galaxies, the galaxy ellipticities average to zero, $\langle e \rangle = 0$.

Since gravity is a potential theory in the weak-field regime, the shear field can be related to a lensing potential

$$\gamma_{ij} = \left(\partial_i \partial_j - \frac{1}{2} \delta^K_{ij} \partial^2 \right) \psi, \tag{3.4}$$

where $\partial_i \equiv r(\delta_{ij} - \hat{r}_i \hat{r}_j) \nabla_i$ is a dimensionless, transverse differential operator, and $\partial^2 \equiv \partial_i \partial^i$ is the transverse Laplacian. The indices (i, j) each take the values $(1, 2)$, and we have assumed a flat sky. On the scales currently of interest (*i.e.* from $\sim 100\,h^{-1}$kpc to $100\,h^{-1}$Mpc), this is an excellent approximation.

The lensing potential is also observable via the lens convergence field

$$\kappa = \frac{1}{2} \partial^2 \psi, \tag{3.5}$$

which can be estimated from the weak magnification of sources,

$$\mu = |(1 - \kappa)^2 - \gamma^2|^{-1} \approx 1 + 2\kappa. \tag{3.6}$$

This can be measured from either the change in galaxy number density (Broadhurst, Taylor & Peacock 1995; Taylor et al. 1998) or from the change in size of sources (Bartelmann & Narayan, 1995; Jain 2002). Although this has a lower signal-to-noise than the shear distribution, it is an independent estimator of the lensing potential.

The convergence field is related to the shear field by the differential relation, first used by Kaiser & Squires (1993);

$$\kappa = \partial^{-2}\partial_i\partial_j\gamma_{ij}, \tag{3.7}$$

where ∂^{-2} is the inverse 2-D Laplacian operator defined by

$$\partial^{-2} \equiv \int d^2\hat{\boldsymbol{r}}' \ln|\hat{\boldsymbol{r}} - \hat{\boldsymbol{r}}'|. \tag{3.8}$$

A useful quantity for tracing noise and systematics in gravitational lensing is the divergence-free field, β, defined by

$$\beta = \partial^{-2}\varepsilon_i^n\partial_j\partial_n\gamma_{ij}. \tag{3.9}$$

where ε_i^n is the Levi-Civita symbol in two dimensions,

$$\varepsilon_i^n = \begin{pmatrix} 0 & -1 \\ 1 & 0 \end{pmatrix}. \tag{3.10}$$

If γ_{ij} is generated purely by the lensing potential, this quantity vanishes. But if there are non-gravitational sources, due to noise, systematics or intrinsic alignments, β will be non-zero. In addition β terms can arise from finite fields, due to mode-mixing of the κ and β fields (Bunn, 2002).

We have already seen in chapter 2 that in a spatially flat Universe, with comoving distance r we can relate the lensing potential and the gravitational potential by

$$\psi(\boldsymbol{r}) = 2\int_0^r dr' \left(\frac{r - r'}{rr'}\right)\Phi(\boldsymbol{r}'). \tag{3.11}$$

Although the lensing potential depends on the distance to the source galaxy, this dependence is usually lost by averaging all lensing quantities over the source distribution. However with redshift information the full 3-D character of lensing can be usefully recovered (Taylor 2001, Bacon & Taylor 2002, Hu & Keaton 2002).

3.2.2 Statistical properties

Shear covariance matrix

We may define a shear covariance matrix by

$$C_{ab}(\hat{\boldsymbol{r}}) = \langle\gamma_a(0)\gamma_b(\hat{\boldsymbol{r}})\rangle, \tag{3.12}$$

where the indices (a, b) each take the values (1,2). Fourier transforming the shear field,

$$\gamma_{ij}(\boldsymbol{\ell}) = \int d^2\hat{\boldsymbol{r}}\, \gamma_{ij}(\hat{\boldsymbol{r}}) e^{-i\boldsymbol{\ell}.\hat{\boldsymbol{r}}}, \tag{3.13}$$

and decomposing it using equations (3.7) and (3.9), we may generate the shear power spectra from correlations of κ and β:

$$\begin{aligned} \langle \kappa(\boldsymbol{\ell})\kappa^*(\boldsymbol{\ell}')\rangle &= (2\pi)^2 C_\ell^{\kappa\kappa}\delta_D(\boldsymbol{\ell}-\boldsymbol{\ell}'), \\ \langle \beta(\boldsymbol{\ell})\beta^*(\boldsymbol{\ell}')\rangle &= (2\pi)^2 C_\ell^{\beta\beta}\delta_D(\boldsymbol{\ell}-\boldsymbol{\ell}'), \\ \langle \kappa(\boldsymbol{\ell})\beta^*(\boldsymbol{\ell}')\rangle &= (2\pi)^2 C_\ell^{\kappa\beta}\delta_D(\boldsymbol{\ell}-\boldsymbol{\ell}'). \end{aligned} \tag{3.14}$$

The fact that gravitational lensing is produced by a scalar potential and the parity invariance of weak lensing suggest that $C_\ell^{\beta\beta} = C_\ell^{\kappa\beta} = 0$. However other effects, such as noise and systematics, as well as intrinsic galaxy alignments may give rise to a non-zero $C_\ell^{\beta\beta}$. Hence in our analysis we shall leave its amplitude to be determined by the data. The cross-correlation of $\kappa(\ell)$ and $\beta(\ell)$ is expected to be zero but it will also allow a second check on noise and systematics in the shear field, and we shall treat is as another free function. In particular finite field and boundary effects can lead to leakage of power between these three spectra, which we shall attempt to monitor.

The shear power spectrum and the convergence power are related by

$$C_\ell^{\gamma\gamma} = C_\ell^{\kappa\kappa} \tag{3.15}$$

in the flat-sky approximation. For a spatially flat Universe, these are in turn related to the matter power spectrum, $P_\delta(k, r)$ by the integral relation (see Chapter 2 for details):

$$C_\ell^{\kappa\kappa} = \frac{9}{4}\left(\frac{H_0}{c}\right)^4 \Omega_m^2 \int_0^{r_{\rm H}} dr\, P_\delta\left(\frac{\ell}{r}, r\right)\left(\frac{\overline{W}(r)}{a(r)}\right)^2, \tag{3.16}$$

where a is the expansion factor and r is comoving distance. $r_{\rm H}$ is the comoving distance to the horizon:

$$r_{\rm H} = c\int \frac{dz}{H(z)}, \tag{3.17}$$

where the Hubble parameter is given in terms of the matter density, Ω_m, the vacuum energy density, Ω_V and the spatial curvature, Ω_K as

$$H(z) = H_0[(1+z)^3\Omega_m + (1+z)^2\Omega_K + \Omega_V]^{1/2}. \tag{3.18}$$

The weighting, $\overline{W}$, is given in terms of the normalised source distribution, $G(r)dr = p(z)dz$:

$$\overline{W}(r) \equiv \int_r^{r_{\rm H}} dr'\, G(r')\,\frac{r'-r}{r'}. \tag{3.19}$$

The covariance of the components of the shear field are related to the power spectra by (Hu & White 2001)

$$\begin{aligned} C_{11}(\hat{\boldsymbol{r}}) &= \int \frac{d^2\ell}{(2\pi)^2} (C_\ell^{\kappa\kappa} \cos^2 2\varphi_\ell + C_\ell^{\beta\beta} \sin^2 2\varphi_\ell \\ &\quad - C_\ell^{\kappa\beta} \sin 4\varphi_\ell) |W(\ell)|^2 e^{i\boldsymbol{\ell}.\hat{\boldsymbol{r}}}, \\ C_{22}(\hat{\boldsymbol{r}}) &= \int \frac{d^2\ell}{(2\pi)^2} (C_\ell^{\kappa\kappa} \sin^2 2\varphi_\ell + C_\ell^{\beta\beta} \cos^2 2\varphi_\ell \\ &\quad + C_\ell^{\kappa\beta} \sin 4\varphi_\ell) |W(\ell)|^2 e^{i\boldsymbol{\ell}.\hat{\boldsymbol{r}}}, \\ C_{12}(\hat{\boldsymbol{r}}) &= \int \frac{d^2\ell}{(2\pi)^2} (\frac{1}{2}(C_\ell^{\kappa\kappa} - C_\ell^{\beta\beta}) \sin 4\varphi_\ell \\ &\quad + C_\ell^{\kappa\beta} \cos 4\varphi_\ell) |W(\ell)|^2 e^{i\boldsymbol{\ell}.\hat{\boldsymbol{r}}}, \end{aligned} \tag{3.20}$$

where $\cos\varphi_\ell = \hat{\boldsymbol{\ell}}.\hat{\boldsymbol{\ell}}_x$ and $\hat{\boldsymbol{\ell}}_x$ is a fiducial wavenumber projected along the x-axis. We have included here a smoothing or pixelisation window function;

$$W(\boldsymbol{\ell}) = j_0(\ell_x \theta_{\rm pix}/2) j_0(\ell_y \theta_{\rm pix}/2), \tag{3.21}$$

where $j_0 = \sin(x)/x$ is the zeroth order spherical Bessel function and $\theta_{\rm pix}$ is the smoothing/pixel scale.

The rotated shear correlation function

Another important two-point statistical measure of the weak lensing signal are the correlation functions, defined by

$$\begin{aligned} C_1(\theta) &= \langle \gamma_1^r(\hat{\boldsymbol{r}}) \gamma_1^r(\hat{\boldsymbol{r}} + \theta) \rangle, \\ C_2(\theta) &= \langle \gamma_2^r(\hat{\boldsymbol{r}}) \gamma_2^r(\hat{\boldsymbol{r}} + \theta) \rangle, \\ C_3(\theta) &= \langle \gamma_1^r(\hat{\boldsymbol{r}}) \gamma_2^r(\hat{\boldsymbol{r}} + \theta) \rangle, \end{aligned} \tag{3.22}$$

where the angled brackets denote the average over all galaxy pairs separated by an angle θ. The superscript, r denotes rotated shear components which are equivalent to γ_1 and γ_2 in a rotated coordinate frame, defined by the line joining the centroids of the two galaxies in question. In terms of the elements of the shear matrix, equation (3.3), these rotated shear components are

$$\begin{aligned} \gamma_1^r &= \gamma_1 \cos(2\phi) + \gamma_2 \sin(2\phi) \\ \gamma_2^r &= -\gamma_1 \sin(2\phi) + \gamma_2 \cos(2\phi), \end{aligned} \tag{3.23}$$

where ϕ is the angle between the original and rotated coordinate frames. Once again, the parity invariance of weak lensing predicts that the cross-correlation function $G_3(\theta)$ should be zero. A non-

zero $C_3(\theta)$ is, therefore, an indication of residual systematic effects present in the data. The correlation functions, $C_1(\theta)$ & $C_2(\theta)$ are related to the underlying convergence power spectrum via

$$C_i(\theta) = \int_0^\infty \frac{d\ell\,\ell}{4\pi} C_\ell^{\kappa\kappa} \left[J_0(\ell\theta) + (-1)^{i+1} J_4(\ell\theta)\right], \tag{3.24}$$

where $J_n(x)$ are Bessel functions.

Shear variance in cells

Finally, we can define the variance, $\sigma_\gamma^2(\theta)$ of the shear field, measured in circular cells of radius θ. In terms of the convergence power spectrum, this variance is

$$\sigma_\gamma^2(\theta) = \frac{1}{2\pi} \int_0^\infty d\ell\,\ell C_\ell^{\kappa\kappa} \left(\frac{2J_1(\ell\theta)}{\ell\theta}\right)^2. \tag{3.25}$$

In the following analysis, we have chosen to measure the shear variance in square cells of side length, θ. However, the corresponding variance in circular apertures can be recovered, to a good approximation, by scaling our measurements by $1/\sqrt{\pi}$ (*e.g.* Bacon, Refregier & Ellis 2000).

Having considered the shear field and its statistical properties we now turn to our dataset. In Sections 3.3 & 3.4 we describe the COMBO-17 dataset and our method used in producing the high quality deep R-band images from which we measure the shear field. In Sections 3.5 & 3.6 we shall use this data to determine the statistical properties of the observed shear field.

3.3 Observations and Data Reduction

3.3.1 The COMBO-17 survey

The observations analysed in this study have been undertaken as part of the COMBO-17 survey (Wolf et al. 2001). This survey is being carried out with the Wide-Field Imager (WFI) at the MPG/ESO 2.2m telescope on La Silla, Chile. The survey currently consists of five $0.5° \times 0.5°$ fields totaling 1.25 square degrees with observations taken in five broad-band filters ($UBVRI$) and 12 narrow-band filters ranging from 420 to 914 nm. The quantum efficiency and wavelength range of this filter set is shown in Fig. 3.1. The chosen filter set facilitates accurate photometric redshift estimation ($\sigma_z \approx 0.05$) reliable down to an R-band magnitude of 24. During the observing runs, to facilitate accurate weak lensing studies, the best seeing conditions were reserved for obtaining deep R-band images of the five fields. It is these R-band images, along with the photometric redshift tables, that we make use of in this analysis.

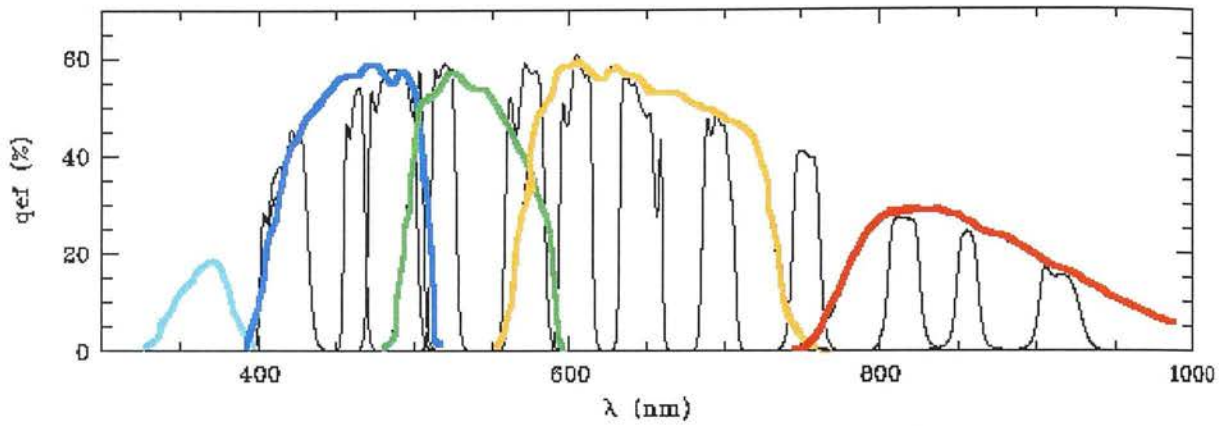

Figure 3.1: The COMBO-17 filter set showing the five broad-band filters ($UBVRI$, shown here in colour) and the 12 narrow-band filters (shown in black) covering a wavelength range from 420 to 914 nm.

3.3.2 Initial data processing

The initial reduction of the data proceeded along the lines of that described in Gray et al. (2002, hereafter GTM+). The WFI instrument consists of a 4×2 array of 2048×4096 pixel CCDs. With a pixel scale of $0.238''$, the resulting total field of view (FOV) of the WFI is $0.56° \times 0.55°$. The standard COMBO-17 pre-processing pipeline (Wolf et al. in prep.) produces mosaics of eight 2K $\times$ 4K chip images which have been debiased, corrected for non-linearity, normalized, flat-fielded and cleaned of cosmic rays. The resulting mosaics have been simply skewed as an approximate correction for rotational mis-alignments between the chips. We have removed this skewing of the mosaiced images in order to restore the original chip configurations on the detector. The individual chip images were then extracted from the mosaics so that astrometric calibrations could be applied to each of the chip images individually.

3.3.3 Artificial shear introduced due to instrument and image co-addition

We have investigated the level of distortions introduced by the telescope optics and the WFI instrument by comparing the location of the same objects on dithered chip exposures. As documented in Bacon Refregier & Ellis (2000, hereafter BRE), the respective positions of the same object on two dithered frames, f and f' can be expressed as

$$x^{f'} - x^{f} \simeq \Psi(\bar{x}^{f} - \bar{x}^{f'}), \tag{3.26}$$

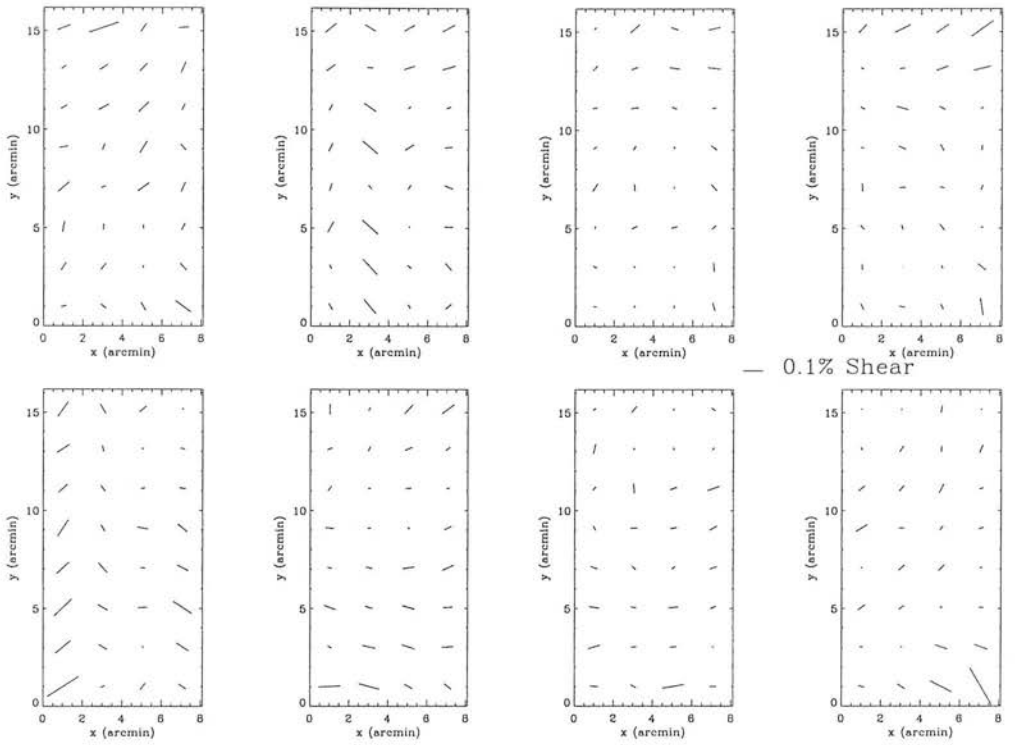

Figure 3.2: Instrumental shear pattern for the 8 chips of the WFI instrument as measured from the observed positions of the same objects on three dithered frames. The length of each vector represents the magnitude of the instrumental shear at the indicated position on the chip and the direction indicates the orientation of the distortion. For comparison, a 0.1% shear is also shown on the same scale. These distortions are the distortions that exist prior to application of the precise astrometric solution.

where x^f ($x^{f'}$) is the position of the object on frame f (f'), $\bar{x}^f$ ($\bar{x}^{f'}$) is the position of the centre of frame f (f') and $\mathbf{\Psi}$ is the distortion matrix, which may be expressed in terms of observables as

$$\mathbf{\Psi} \equiv \begin{pmatrix} \kappa + \gamma_1 & \gamma_2 \\ \gamma_2 & \kappa - \gamma_1 \end{pmatrix}. \tag{3.27}$$

Here, κ and γ_i are the spurious convergence and shear introduced by the geometrical distortions. By measuring the positions of the same objects on three dithered frames, the resulting two equations of form (3.26) can be solved for κ and γ_i. We have used this method to map the instrumental distortion across the 8 component chips of the WFI and the resulting shear pattern is shown in Fig. 3.2 along with an indication of a 0.1% shear signal. We find that the induced shear due to telescope and instrument distortions is small ($\gamma < 0.2\%$) over the entire field compared to the typical weak lensing signal one would wish to measure. Even these distortions, however, should be removed by performing precise astrometric fits of the data - we now describe our procedure for doing this.

3.3.4 The precise astrometric solution

After extraction from the mosaics, catalogues of objects were created for each chip exposure using SExtractor (Bertin & Arnouts 1996). Using pointing information from the image headers, an approximate transformation was calculated to convert the SExtractor (x, y) pixel coordinates of the objects to celestial coordinates (α, δ) for each exposure. These objects were then matched with objects from the digitized SuperCOSMOS Sky Survey (SSS)[1] (Hambly et al. 2001a) to within a tolerance of $5''$. The resulting coordinate pairs were then used to iteratively calculate a linear astrometric solution for each chip image with the optical axis being used as the tangent point for projection. Typically around 300 objects per chip image were used for the final astrometric fits which had rms residuals of $\sim 0.2''$ (*cf.* the pixel scale of $0.238''$/pixel). Including higher order terms and/or a radial distortion term in the astrometric solution has been investigated by GTM+. Although, in some cases, the fit was improved when a radial distortion term was included, they found no improvement for the instrument as a whole. Details concerning the artificial shear introduced by such a radial distortion are discussed in GTM+ who deduced a radial distortion of $\delta r/r \sim 0.025\%$ and a resulting instrumental shear pattern with amplitude $\gamma < 0.0001$. This level of distortion is clearly negligible in comparison to a typical ΛCDM cosmic shear signal of $\gamma \sim 0.01$ and so we have used the simple linear solution to perform astrometry on all the chip images. Having produced linear astrometric fits for all the chip images in each of the five fields, these fits were then used to register the images to the same coordinate system. The images were thus aligned and combined, using 3σ bad pixel rejection with weighting by exposure time and scaling by the median pixel value. All bad columns and pixels were removed during the co-addition procedure due to the large number of images combined. The five resulting 8K $\times$ 8K images were trimmed to remove the under-sampled edges of the fields resulting in five 8192 $\times$ 8192 pixel ($32.5' \times 32.5'$) images.

We have estimated the uncertainty introduced in the ellipticity measurements of objects on the combined images as a result of the co-adding procedure. Having registered the original exposures to the same coordinate frame, we then calculated the dispersion in the positions of many objects from the measured positions of those objects on all frames. We found a mean rms of ≈ 0.5 pixels in the positions of objects. Using this mean uncertainty in the position of objects, we can simulate the effect of image co-addition on a circular source of size ~ 0.7 arcsec, similar to the mean seeing disc size on the individual frames. We simulate the stacking of 78 frames (*cf.* no. of frames for CDFS field - see Table 3.1) where we apply to each image an offset, $dx = dx^{\rm true} + \delta x$ where $dx^{\rm true}$ is the true offset position of the object and δx is a vector whose magnitude is taken from a Gaussian distribution centred on 0.5 pixels and whose orientation is taken from a uniform distribution between 0 and 2π. The size and ellipticity of the resulting stacked object was then computed using the formalism described in section 5.3 of BRE. Fig. 3.3 shows a histogram of the resulting ellipticity measurements for 1000 such simulations demonstrating that the shear arising from co-addition is again well below the sought-after cosmic shear signal. The median ellipticity induced in a circular source as measured from these

[1] Full access to the SSS is available via the World Wide Web at URL `http://www-wfau.roe.ac.uk`

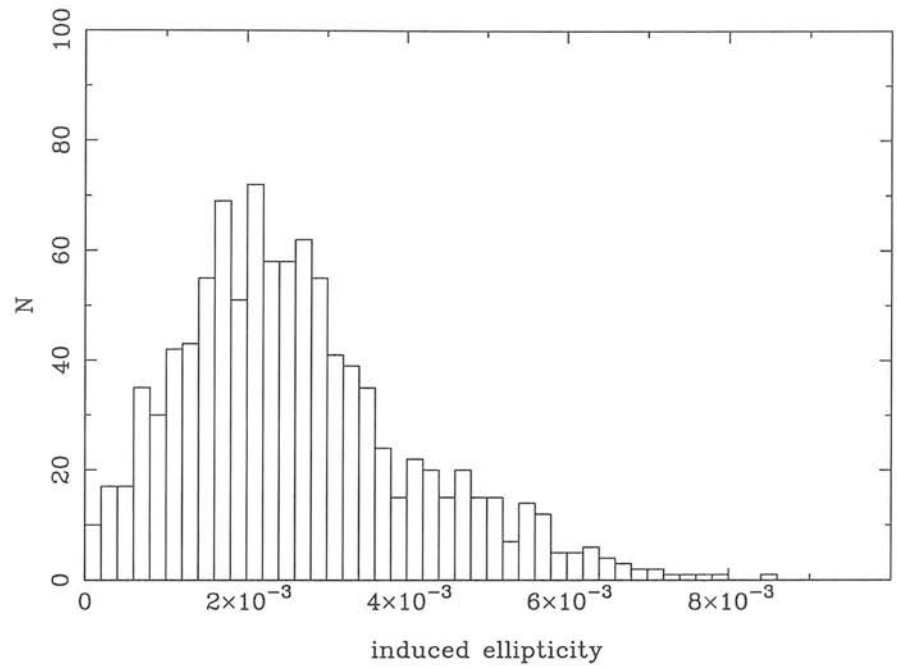

Figure 3.3: Ellipticity introduced in a circular source due to co-addition of individual frames as measured from 1000 simulations of the stacking of 78 frames.

simulations was $\varepsilon_m = 0.0037$ and the inter-quartile range was $\delta\varepsilon_m = 0.002$. These numbers are well within our error budget for a precise measurement of cosmic shear.

3.3.5 Point spread function corrections and generation of object catalogues

We have used the `imcat` software (Kaiser, Squires and Broadhurst, 1995; hereafter KSB) to generate object catalogues for the five fields, measure shape parameters for all objects and to correct for such effects as the isotropic smearing of the point spread function (PSF) of objects by the atmosphere and telescope as well as any anisotropic smearing introduced by tracking errors, imperfect dither alignments and co-addition of the individual frames. We have used the `hfindpeaks` routine to locate objects, followed by the `getsky, apphot and getshapes` routines to estimate the local sky background, measure aperture magnitudes and half-light radii, r_h and to calculate shape parameters for all detected objects (see Chapter 2 and *e.g.* KSB; BRE; GTM+, for details of how the KSB procedure and the `imcat` software work).

This procedure produced an image catalogue for each field, containing positions, magnitudes, sizes and shapes for all the objects detected. We then applied reasonably conservative cuts on image size, signal-to-noise (S/N) and object ellipticity ($r_g > 1.0, \nu > 5, \varepsilon < 0.5$) to remove spurious and/or untrustworthy detections. Note that the S/N cut we have used ($\nu > 5$) is much less stringent than that adopted in BRE who used a S/N cut of $\nu > 15$. The motivation in BRE for using such a conservative

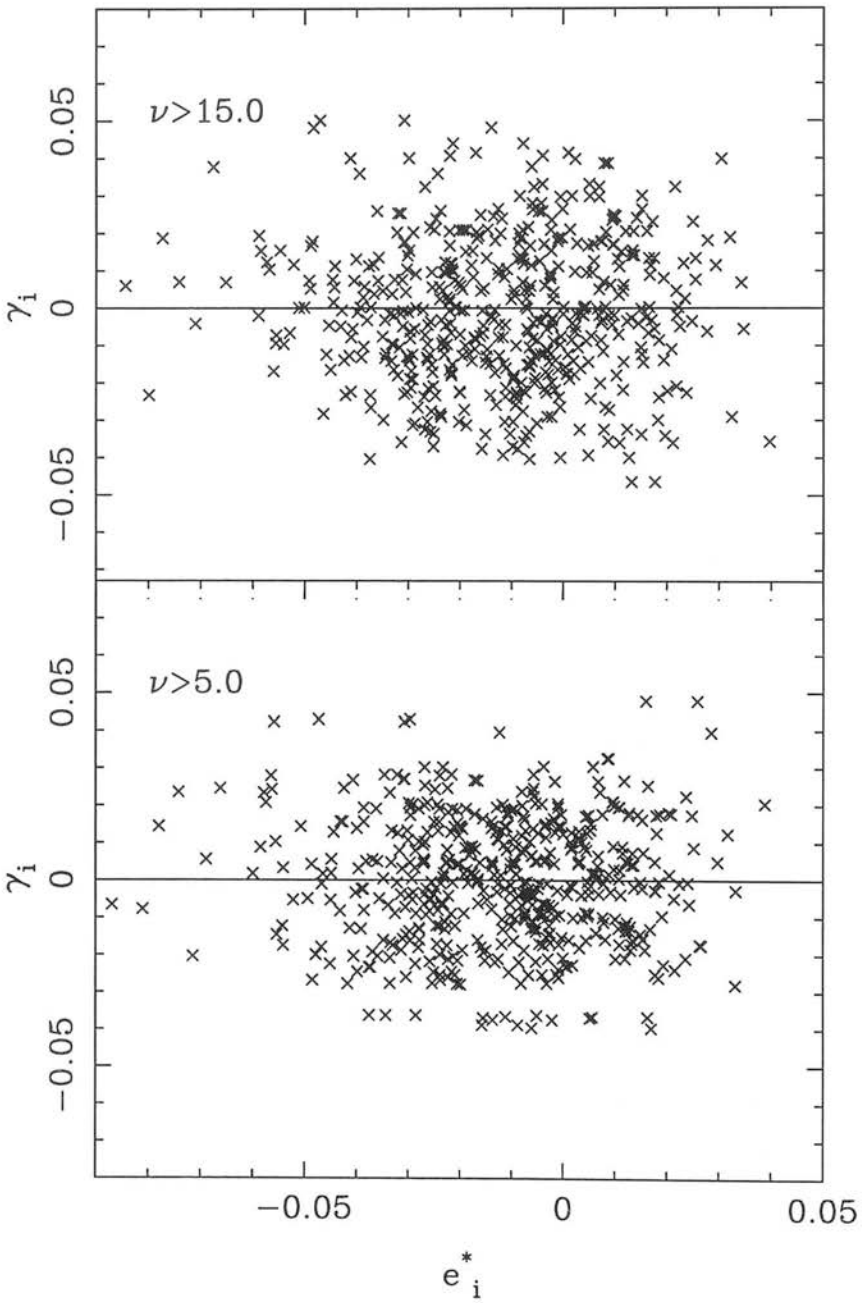

Figure 3.4: Mean shear components in cells plotted against the mean stellar ellipticity components for a cell size of 8×8 arcmin. The upper panel is for a S/N threshold of $\nu > 15$ and the lower panel is for a threshold of $\nu > 5$. The anti-correlation of γ_i with $\overline{\varepsilon_i^*}$ found in the analysis of BRE is not present in the COMBO-17 data for either of the S/N cuts.

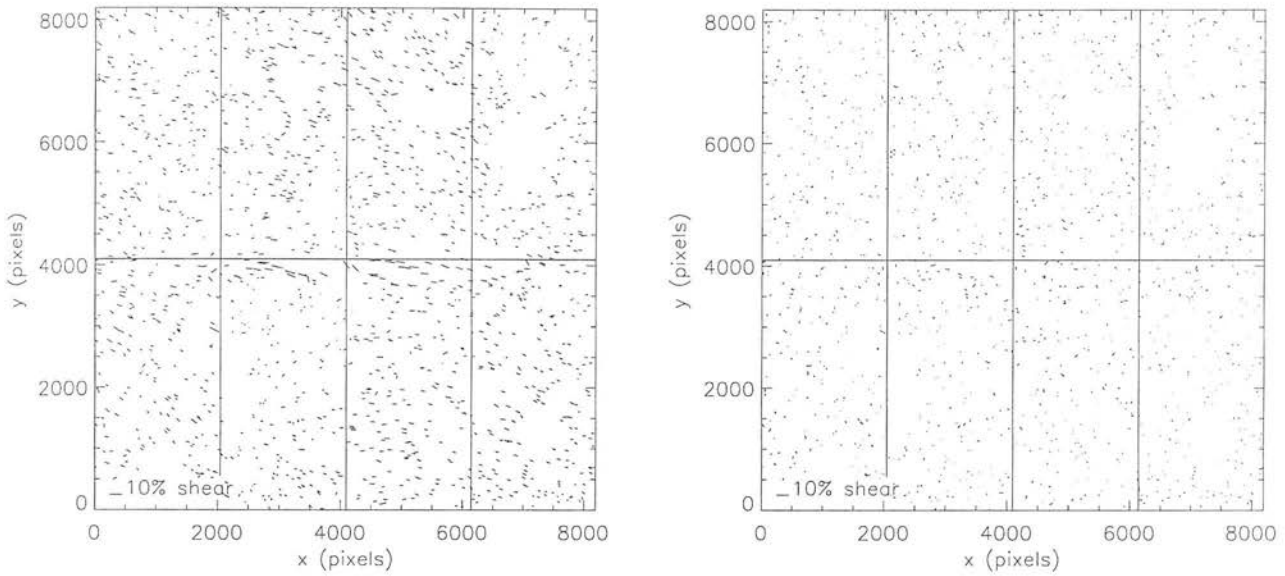

Figure 3.5: Stellar ellipticity pattern across the S11 field before (*left*) and after (*right*) correction for PSF anisotropy. A 10% shear signal is also shown for comparison. The horizontal and vertical lines show the sections used for the stellar ellipticity polynomial model fitting. Rms stellar ellipticity values before correction were $\varepsilon_{1,\mathrm{rms}} = 0.029$ and $\varepsilon_{2,\mathrm{rms}} = 0.013$. After correction, these had dropped to $\varepsilon_{1,\mathrm{rms}} = 0.009$ and $\varepsilon_{2,\mathrm{rms}} = 0.009$.

cut was the existence in their data of a highly significant anti-correlation between their measured mean shear values and the corresponding mean stellar ellipticities for a S/N cut of $\nu > 5$. We have searched for this effect in our data on several different smoothing scales and have found no evidence of correlations between our shear and stellar ellipticity values.

For example, Fig. 3.4 shows the mean shear components in cells plotted against the mean uncorrected stellar ellipticity components for a cell size of 8×8 arcmin. This is the same cell size as that shown in BRE's figure 7 where a clear anti-correlation is present. It is clear from Fig. 3.4 however, that this effect is absent from our data. We have looked for such an effect on scales ranging from 1 to 30 arcmin and have found none. We have therefore used a $\nu > 5$ cut in our analysis. We also note that this is the same S/N cut as used in GTM+ for their supercluster analysis of the A901 field.

Having applied these cuts to the data, the `imcat` software was then used to correct the measured shapes of the galaxies for the effects mentioned above. In particular, we correct the galaxy shapes for (a) anisotropy and (b) circularization. Details of the correction scheme used by `imcat` have been described elsewhere (*e.g.* Chapter 2 of this work; KSB; Luppino & Kaiser 1997; Hoekstra et al. 1998a; Kaiser et al. 1999) and will not be repeated here. The KSB method has also been tested extensively on simulations by several groups. In particular Bacon et al. (2001) have tested the implementation of KSB used in this analysis on numerical simulations and have found that the KSB shear measurements slightly underestimate the true shear values. Since we are using the same implementation of KSB

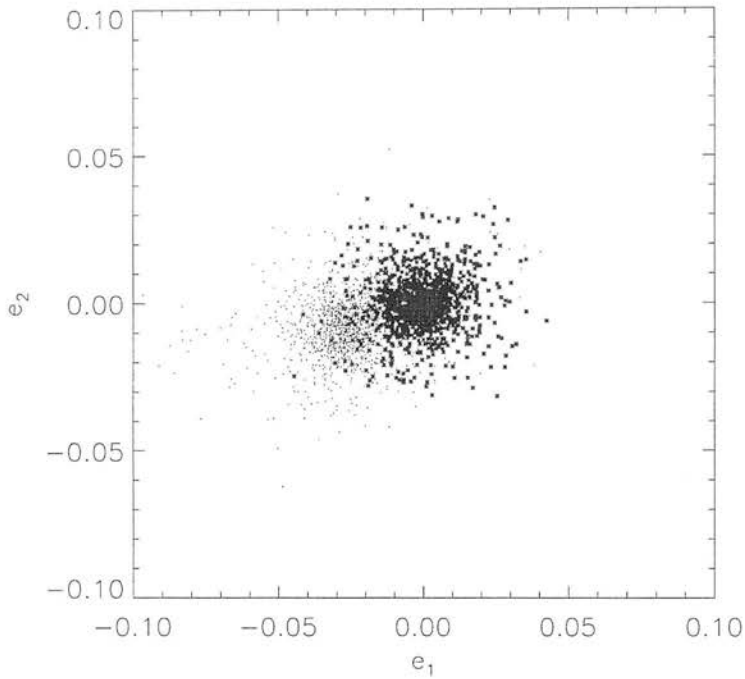

Figure 3.6: Ellipticity distribution of stars in the S11 field before (grey dots) and after (black crosses) correction for PSF anisotropy. Mean stellar ellipticity components of $\overline{\varepsilon_1} = -0.025 \pm 0.013$ and $\overline{\varepsilon_2} = -0.007 \pm 0.011$ are removed to leave an essentially randomly orientated stellar ellipticity distribution with mean residual components of $\overline{\delta\varepsilon_1} = -0.0005 \pm 0.010$ and $\overline{\delta\varepsilon_2} = -0.0002 \pm 0.009$.

in this analysis, we have therefore applied to the data the 0.8 calibration factor that Bacon et al. suggest. Note that these corrections were done on sections (size $8' \times 16'$) of the fields rather than the full $32.5' \times 32.5'$ fields themselves. This was done to ensure that an accurate model of the PSF distortions was obtained. Performing the corrections on the full fields would possibly lead to residual PSF distortions in the dataset due to inaccurate modeling of the stellar ellipticities over such a large field.

A demonstration of the anisotropic PSF correction at work for the S11 field is given in Figs. 3.5 and 3.6. The smoothly varying stellar ellipticity pattern apparent in the stars before correction (Fig. 3.5, left-hand side) is successfully removed to produce residual stellar ellipticities with essentially random orientations (Fig. 3.5, right-hand side) and mean residuals of $|\delta\varepsilon_1| \approx 5 \times 10^{-4}$ and $|\delta\varepsilon_2| \approx 2 \times 10^{-4}$. Fig. 3.6 shows the stellar ellipticities after correction randomly distributed about $\varepsilon_1 = \varepsilon_2 = 0$. Note however that these plots are for illustrative purposes only. Rigorous tests of the systematics introduced by residual spurious ellipticities are performed later in Section 3.5, where we measure the star-galaxy cross-correlation functions for the dataset.

3.4 The COMBO-17 fields

3.4.1 Content of the fields

The five fields observed are quite different from one another in terms of their content. Three are blank fields; one (CDFS) was chosen so it would overlap with the Chandra Deep Field South; another (SGP) is centred on the South Galactic Pole, and the third blank field is the shallower FORS deep field (FDF). A fourth, randomly selected field (S11) contains a fairly large cluster (Abell 1364) at a redshift of $z = 0.11$. The fifth field (A901) was chosen so as to include a supercluster system (Abell 901/902) at redshift $z = 0.16$ and the COMBO-17 observations of this field have already been the subject of an extensive weak lensing analysis (see GTM+). Images of the five fields are shown in Figs. 3.7 to 3.11 and details of the R-band observations for the fields are given in Table 3.1. Note that at the time of writing, the full 17-band photometric information was not available for the SGP or FDF fields.

The significant mass concentrations present in the two fields containing clusters (S11 & A901) raise the question as to whether these fields should be included in a cosmic shear analysis at all. The significant difference between these fields is the pre-selection of A901 to include a supercluster system. Strictly speaking, therefore, the A901 field is not a randomly selected piece of sky and is unlikely to be a fair representation of the Universe. We have therefore chosen not to include this field in our final parameter estimation and shear power spectrum calculations. We have also experimented with including/excluding both the S11 and A901 fields from the analysis. For both the shear power spectrum reconstruction and the parameter estimation, we find that the A901 field biases our results significantly, whereas the S11 field is consistent with the dataset as a whole (see Section 3.6). The cell-averaged shear distributions for the five fields are shown in Fig. 3.12, showing regions in the fields which have been masked out due to contamination by bright stars, diffractions spikes and ghosting.

3.4.2 Including redshift information

As mentioned earlier, the COMBO-17 survey has the unique advantage, in terms of weak lensing surveys, of having accurate photometric redshift measurements for $\sim 90\%$ of objects detected down to a magnitude of $m_R \leq 24$ (for a detailed description of the photometric methods used to assign redshifts to the galaxies, see Wolf et al. 2003). For these galaxies, the estimated typical uncertainty in redshift is $\sigma_z \sim 0.05$. At the time of writing, photometric data is available for three of our five fields (CDFS, A901 & S11). We have used this information to estimate, directly from the data, the redshift distribution and in particular, the median redshift, z_m of the lensed source galaxies in the survey. For the z_m calculation, we have only included those galaxies used in the final weak lensing analysis. This subset of galaxies does, in fact, include galaxies with magnitudes $m_R > 24$ for which the redshift estimations are unreliable. To account for this, we must extrapolate the redshift distribution beyond $m_R = 24$. For the three fields for which photometric data is available, accurate redshifts have been found for 31649 out of the 83514 galaxies used in the final shear analysis ($\sim 38\%$).

Table 3.1: Properties of the five COMBO-17 shear catalogues. In the sixth column we quote the median R-band magnitude of each catalogue. In the case of the SGP and FDF fields, the median $m_{\rm R}$ listed is an approximate value as magnitudes for these fields have been roughly calibrated using the APM galaxy survey. The mean galaxy density values ($n_{\rm gal}$) are calculated as $n_{\rm gal} = N_{\rm f}/A_{\rm f}$ where $N_{\rm f}$ and $A_{\rm f}$ are the total number of galaxies in the final shear catalogues and the total useable area of the fields respectively, after excluding regions contaminated by bright stars, diffraction spikes and ghosting (see Fig. 3.12). The FWHM values listed are the average FWHM of stars on each field as measured from the final co-added images. The final column indicates whether photometric redshift information is currently available for the field.

Field	RA(2000)	Dec.(2000)	R-band Exposures	Total Exp. Time	Median $m_{\rm R}$	$n_{\rm gal}$ (arcmin^{-2})	FWHM	Redshift info.?
CDFS	$03^{\rm h}\,32^{\rm m}\,25^{\rm s}$	$-27°\,48'\,50''$	$42 \times 500s + 36 \times 420s$	$36120s$	24.4	37.5	$0.81''$	Yes
SGP	$00^{\rm h}\,45^{\rm m}\,56^{\rm s}$	$-29°\,35'\,15''$	$42 \times 500s$	$21000s$	23.6	36.2	$0.81''$	Pending
FDF	$01^{\rm h}\,05^{\rm m}\,49^{\rm s}$	$-25°\,51'\,42''$	$20 \times 500s + 5 \times 400s$	$12000s$	23.7	28.4	$0.82''$	No
S11	$11^{\rm h}\,42^{\rm m}\,58^{\rm s}$	$-01°\,42'\,50''$	$39 \times 400s + 5 \times 500s$	$18100s$	23.7	27.7	$0.78''$	Yes
A901	$09^{\rm h}\,56^{\rm m}\,17^{\rm s}$	$-10°\,01'\,25''$	$36 \times 500s + 8 \times 600s$	$22800s$	24.0	36.1	$0.76''$	Yes

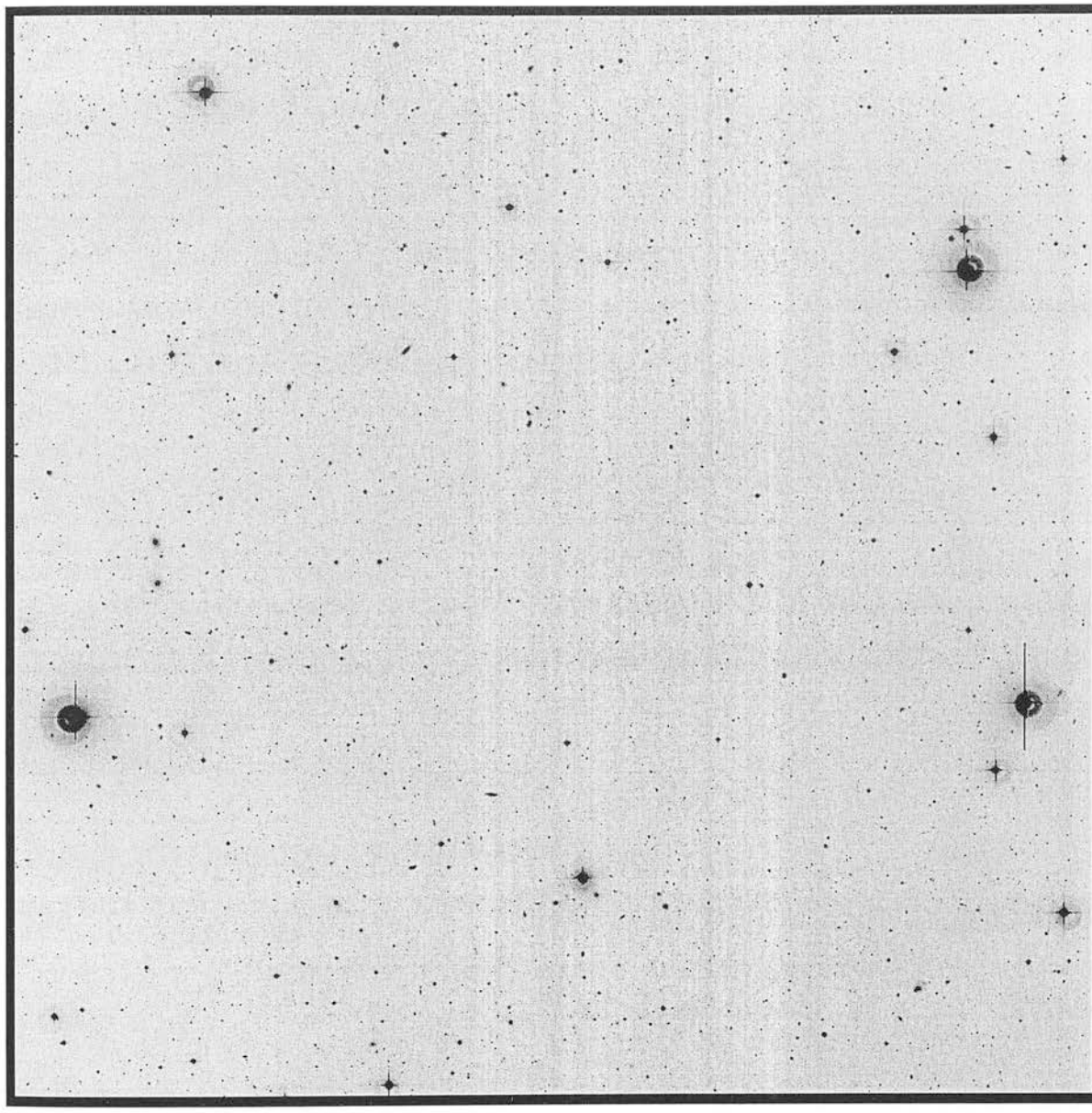

Figure 3.7: The Chandra Deep Field South (CDFS) R-band image.

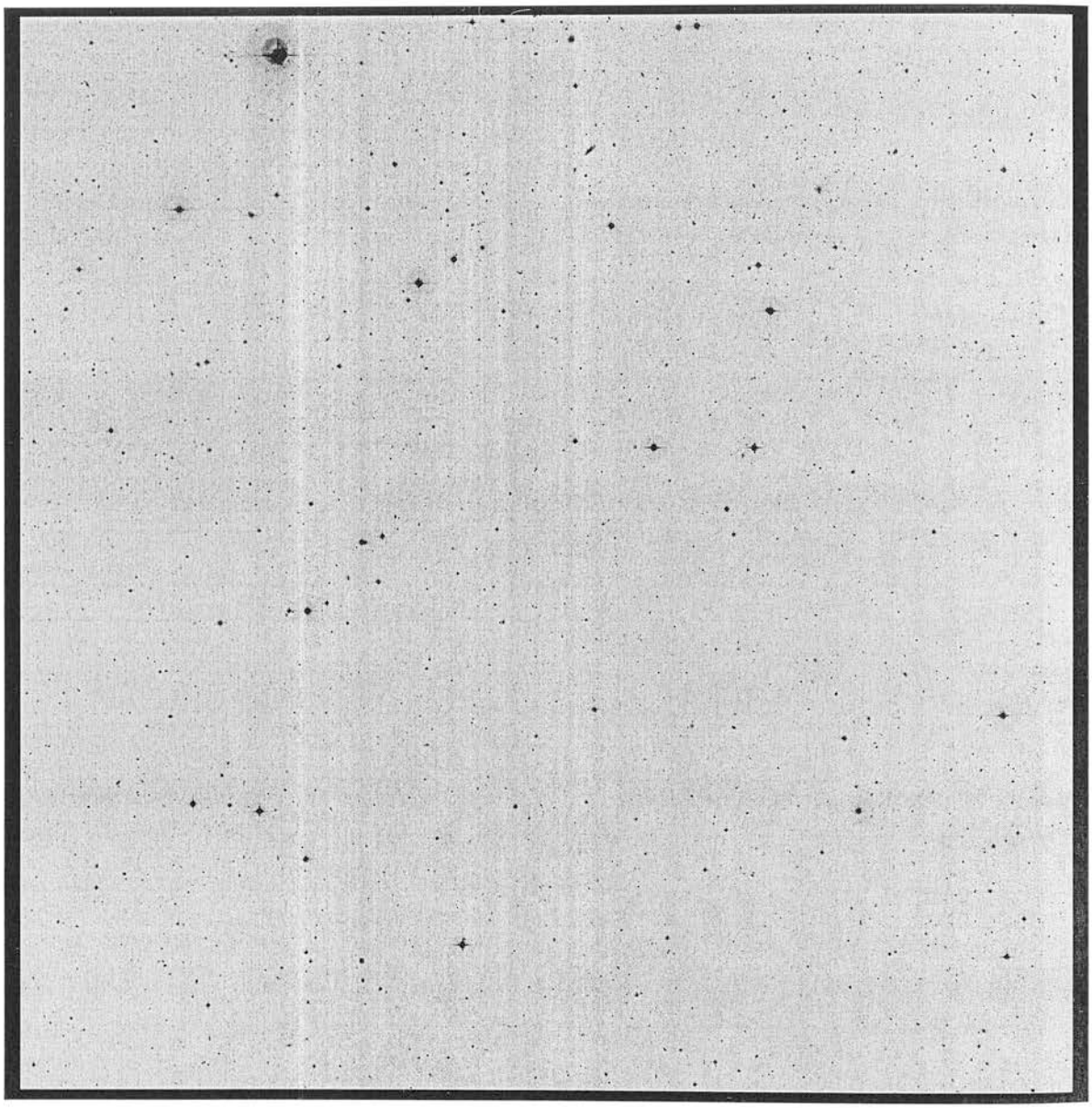

Figure 3.8: The South Galactic Pole (SGP) R-band image.

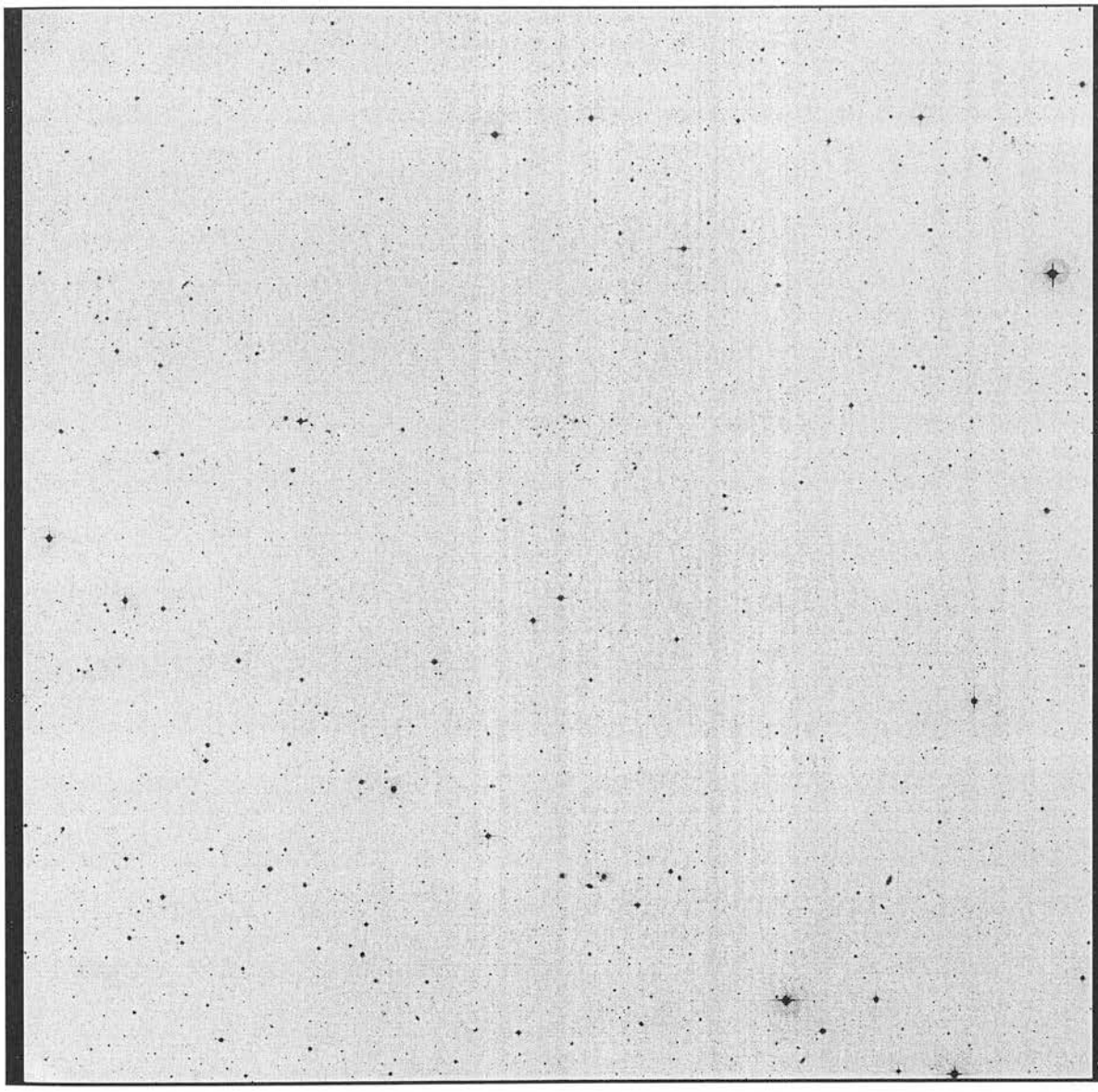

Figure 3.9: The FORS Deep Field (FDF) R-band image.

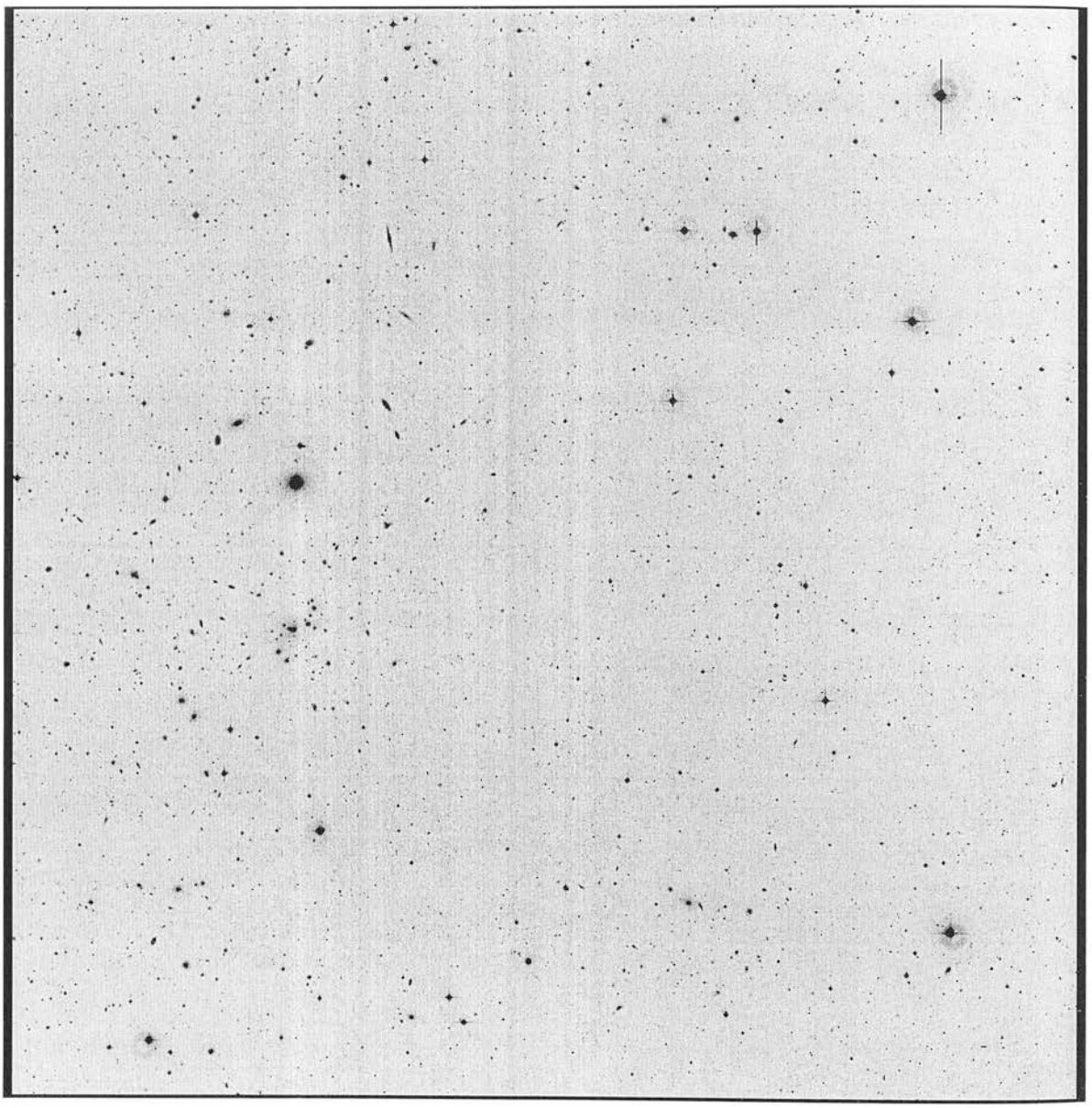

Figure 3.10: The Survey 11 hours (S11) R-band image.

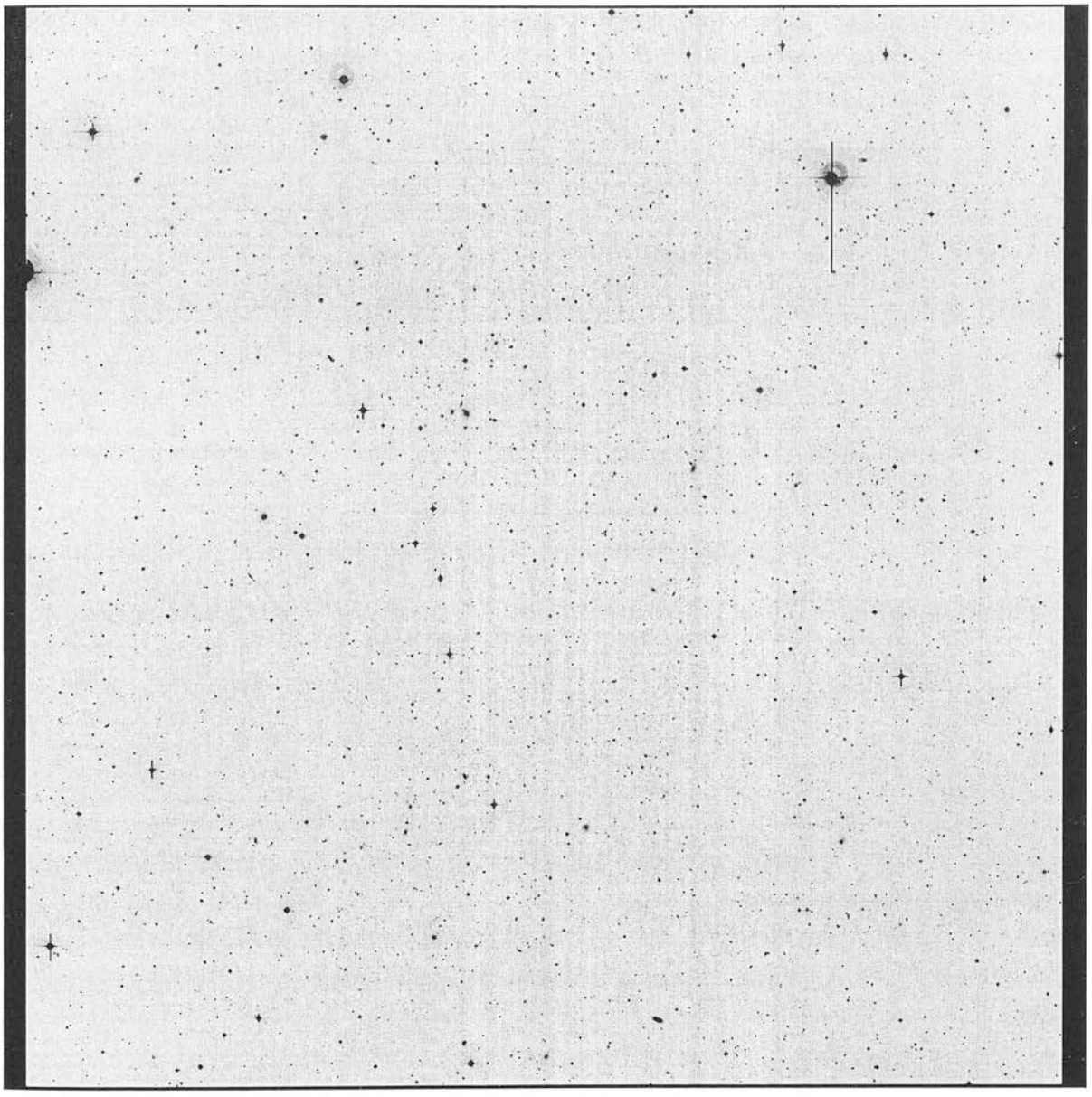

Figure 3.11: The Abell 901/902 supercluster field (A901) R-band image.

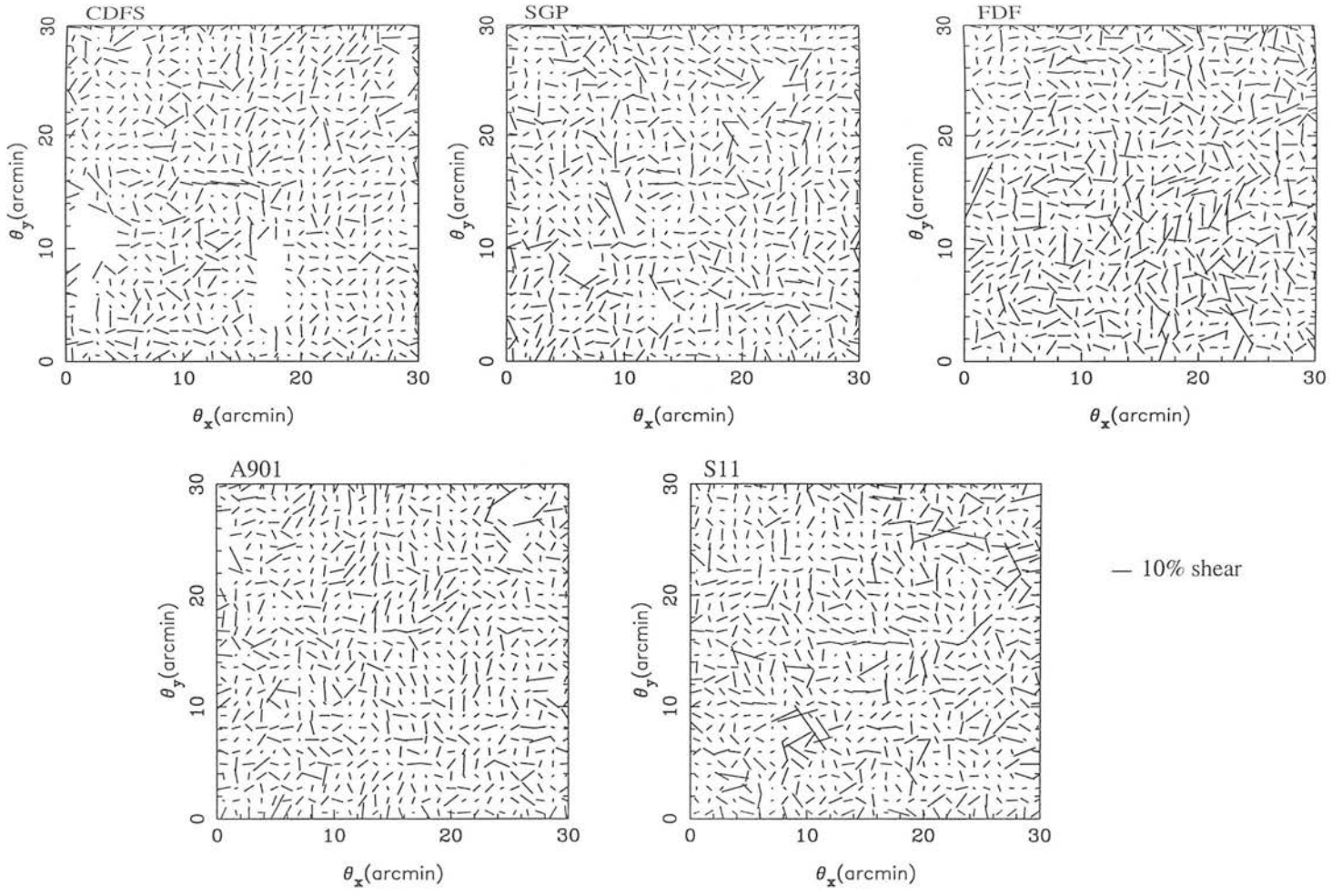

Figure 3.12: The shear distribution on the five COMBO-17 fields. The fields are (clockwise from top left) CDFS, SGP, FDF, S11 and A901. The shear measurements for each field have been binned into 30×30 pixels, giving a pixel scale of ~ 1 arcmin. For each pixel, the length of the vector drawn is proportional to the magnitude of the mean shear in that pixel and its direction indicates the orientation of the shear. A 10% shear signal is also shown for comparison. The apparent holes in the distributions are regions which have been masked out due to bright stars, diffraction spikes etc.

Table 3.2: Measured median magnitudes and redshifts (z_m) for the three fields, CDFS, A901 & S11 for different limiting magnitude cut-offs. Also listed are the number of galaxies ($N_{\rm gal}$) used in the median calculations and the completeness of each magnitude-limited sample (*i.e.* the fraction of galaxies in the sample for which accurate redshifts have been obtained). Extrapolating the median $m_{\rm R} - z_m$ relation (see Fig. 3.13) to the median magnitude of the combined shear catalogues for all fields ($= 24.0$), we infer a median redshift for the COMBO-17 weak lensing survey of $z_m = 0.85 \pm 0.05$.

Limiting $m_{\rm R}$	$N_{\rm gal}$	Median $m_{\rm R}$	z_m	Completeness
< 20.0	1485	19.15	0.184 ± 0.004	87%
< 21.0	3267	20.13	0.285 ± 0.030	87%
< 22.0	7316	21.14	0.404 ± 0.026	88%
< 23.0	16387	22.14	0.520 ± 0.023	87%
< 24.0	31649	22.96	0.673 ± 0.092	76%

For a number of different limiting magnitudes, we have measured the median magnitude of the galaxies and the corresponding median redshift (z_m) of those same galaxies. Details of these measurements are given in Table 3.2. We take our median redshift measurements as lower limits for the true median redshift as the magnitude-limited samples are not complete in redshift (see Table 3.2) and those galaxies without an assigned redshift are most likely to be at a higher redshift than our measured median value. To calculate an upper limit for our z_m estimates, for each magnitude limited sample, we have placed those galaxies without redshift measurements at $z = \infty$ and have re-calculated z_m. We take our final median redshift estimate to be simply the midpoint between our upper and lower limits. We have then extrapolated the median $m_{\rm R} - z_m$ relation to find an estimate of the median redshift of our galaxy sample as a whole, which has a measured median magnitude of 24.0. The median $m_{\rm R} - z_m$ relation is shown in Fig. 3.13. Here we plot both the COMBO-17 data points and data from the HDF redshift survey of Cohen et al. 2000, with which we are fully compatible. The curve plotted is the best-fit quadratic model to the COMBO-17 data and is given by

$$z_m = 2.53 - 0.33\, m_{\rm R,m} + 0.01\, m^2_{\rm R,m}, \tag{3.28}$$

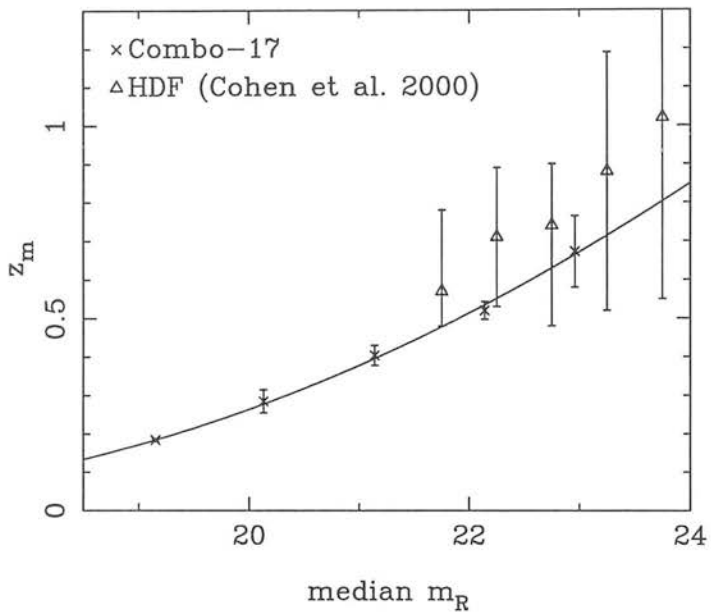

Figure 3.13: The dependence of the median redshift (z_m) of the COMBO-17 galaxies on the median magnitude of the galaxies as measured from the 3 fields for which we have photometric data. A simple quadratic model (solid curve) for the $m_{\rm R} - z_m$ relation is also plotted for comparison. For our final weak lensing dataset, which has a median R-band magnitude of $m_{\rm R} = 24.0$, we infer from this trend a median redshift of $z_m = 0.85 \pm 0.05$.

where $m_{\rm R,m}$ is the median R-band magnitude of the galaxy sample. From this, we estimate a median redshift of $z_m = 0.85 \pm 0.05$ for the COMBO-17 weak lensing survey.

There is, of course, more information in the measured redshift distribution than just the median value. The advantage of including photometric information in a weak lensing analysis lies in reducing or eliminating uncertainties in the redshift distribution of the source galaxies when it comes to comparing weak lensing measurements with those predicted from theory (see Sections 3.6 & 3.7). To this end, we have included the measured redshift distribution for our comparison with theoretical models. There are, of course, many more galaxies for which we have no redshift estimate than there are galaxies with reliable measurements. This situation will improve as the COMBO-17 survey nears completion, but for the purposes of this analysis and predicting the expected weak lensing signal for different cosmological scenarios, we need to assign redshifts to the galaxies with unknown redshifts. We do this by distributing these galaxies in z according to (Baugh & Efstathiou 1991)

$$\frac{dN}{dz} = \frac{\beta z^2}{z_\star^3} \exp\left[-\left(\frac{z}{z_\star}\right)^\beta\right], \tag{3.29}$$

with $\beta = 1.5$ and $z_\star = z_m/1.412$. A distribution of the form, equation (3.29) has a median redshift of z_m. We have tuned the value of z_m in equation (3.29) to ensure that the final *total* redshift distribution has a measured median value of $z_m = 0.85$. After assigning values to the galaxies with unknown redshifts according to equation (3.29), we now have the final $n(z)$ distribution which we can use for

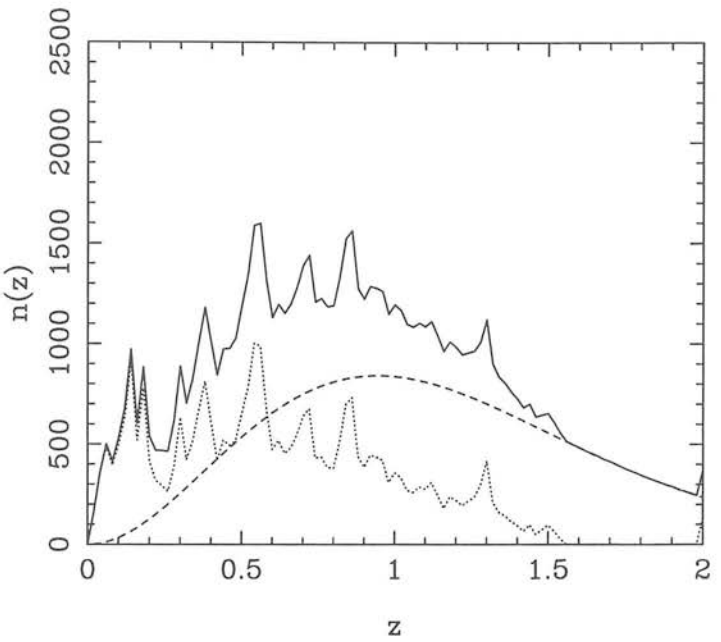

Figure 3.14: The final redshift distribution (solid line) used for making model predictions to compare with the observed weak lensing signal from the COMBO-17 dataset. This composite distribution has a median redshift of $z_m = 0.85$ and is composed of a measured $n(z)$ distribution (from the three fields, CDFS, S11 and A901; shown here as the dotted line) and a parameterised model (equation (3.29); dashed line) for the galaxies with unknown redshifts.

making predictions for the weak lensing signal expected in the COMBO-17 survey. This final $n(z)$ distribution is shown in Fig. 3.14.

3.5 Correlation functions and shear variance estimators

It is useful to estimate the correlation functions of the shear field both as a first approach at measuring the strength of the cosmic shear signal, but also as a test for unwanted systematics in the data. These tests have now become a standard part of shear analysis (*e.g.* Van Waerbeke et al. 2001; Pen, Van Waerbeke & Mellier 2002; Bacon et al. 2002). Measuring correlation functions also allows a direct comparison of our measurements with previous cosmic shear studies. Here we present both an unweighted correlation function analysis and a minimum variance weighted shear variance analysis. Note that, for the remainder of the analysis, we have excluded the A901/2 supercluster field from our measurements except where specifically indicated.

3.5.1 Correlation analysis

To estimate the unweighted correlation functions, we follow Bacon et al. (2002). For the purposes of the correlation analysis, we have divided each of the COMBO-17 fields into eight, chip-sized

sections. In the following analysis, we make the approximation that these sections are uncorrelated. Although the sections are not, in fact, independent, the approximation is a reasonable one on scales small compared to the size of the sections ($= 8 \times 16$ arcmin).

This division of the fields allows for a better estimate of the field-to-field covariance between our measurements than would be possible using the original $0.5^\circ \times 0.5^\circ$ fields. The correlation functions for the individual sections can be measured by averaging over galaxy pairs:

$$\begin{aligned} C_{1,s}(\theta) &= \frac{1}{n_s}\sum_{i=1}^{n_s}\gamma_1^r(\hat{\boldsymbol{r}}_i)\gamma_1^r(\hat{\boldsymbol{r}}_i+\theta), \\ C_{2,s}(\theta) &= \frac{1}{n_s}\sum_{i=1}^{n_s}\gamma_2^r(\hat{\boldsymbol{r}}_i)\gamma_2^r(\hat{\boldsymbol{r}}_i+\theta), \\ C_{3,s}(\theta) &= \frac{1}{n_s}\sum_{i=1}^{n_s}\gamma_1^r(\hat{\boldsymbol{r}}_i)\gamma_2^r(\hat{\boldsymbol{r}}_i+\theta), \end{aligned} \tag{3.30}$$

where n_s is the number of pairs of galaxies in each section and where we average over all galaxy pairs separated by an angle, θ — *cf.* equation (3.22). The signal averaged over all sections is simply

$$\overline{C}_i(\theta) = \frac{1}{N_s}\sum_{s=1}^{N_s} C_{i,s}(\theta), \tag{3.31}$$

where N_s is the total number of sections. The covariance of the correlation function measurements is given by

$$\begin{aligned} &\mathrm{cov}[\overline{C}_i(\theta)\overline{C}_j(\theta')] \simeq \\ &\quad \frac{1}{N_s^2}\sum_{s=1}^{N_s}[C_{i,s}(\theta)-\overline{C}_i(\theta)][C_{j,s}(\theta')-\overline{C}_j(\theta')]. \end{aligned} \tag{3.32}$$

Fig. 3.15 shows the correlation functions, $C_1(\theta)$ and $C_2(\theta)$ after averaging over all sections of the four fields, CDFS, S11, SGP and FDF. As can be seen, our data agrees well with the expected correlations, for both C_1 and C_2, for a $\Omega_m = 0.3$ ΛCDM model with a power spectrum normalisation of $\sigma_8 = 0.8$ (see Section 3.7 for our measurements of Ω_m & σ_8 from COMBO-17). These theoretical curves have been calculated using equation (3.24) where we have used the halofit model of Smith et al. (2002)[2] to calculate the non-linear matter power spectrum. We have also input our combined redshift distribution (Fig. 3.14) into the calculation. We should point out that on smaller scales than those shown on Fig. 3.15, *i.e.* $\theta \lesssim 0.3$ arcmin, we have measured an inconsistently large signal ($\gtrsim 5 \times 10^{-4}$) for the C_1 correlation function. We suspect that this greatly enhanced signal is probably due to either systematic effects on very small scales due to imperfections in the correction for PSF anisotropy, or alternatively, the result of overlapping isophotes of nearby galaxies. Either

[2]the halofit code is publicly available at URL `http://www.as1.chem.nottingham.ac.uk/~res/software.html`

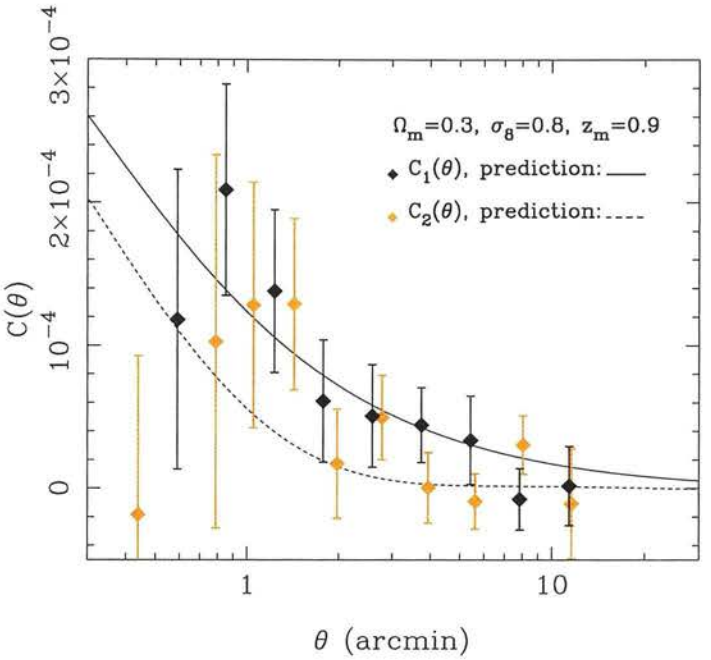

Figure 3.15: The unweighted shear correlation functions $C_1(\theta)$ and $C_2(\theta)$ from the COMBO-17 data. The solid dark line is the expected C_1 correlation for a $\Omega_m = 0.3$ ΛCDM model, normalised to $\sigma_8 = 0.8$, while the lighter dashed line is the expected C_2 signal. The C_2 points have been slightly displaced horizontally for clarity. Note that we measure an inconsistently large C_1 signal ($> 5 \times 10^{-4}$) on the very smallest scales ($\theta < 0.3$ arcmin, not shown) which, we suspect is due to residual systematic effects.

way, we exclude this single data point for our parameter estimations in Section 3.7. We also note that the error bars on $C_1(\theta)$ and $C_2(\theta)$ may be slightly underestimated on the very largest scales due to correlations between neighbouring sections of the same field. Fig. 3.16 shows the cross-correlation between shear components, $C_3(\theta)$ which is consistent with zero, as expected.

In Fig. 3.17, we show the star-galaxy cross-correlations for our data. The systematically-induced cross-correlation between the galaxies (corrected for PSF anisotropy) and the uncorrected stars is defined by (Bacon et al. 2002):

$$C_i^{\rm sys} = \frac{\langle \gamma_i e_i^* \rangle^2}{\langle e_i^* e_i^* \rangle}, \tag{3.33}$$

where $i = 1, 2$. A correlation here would indicate a problem in the correction of systematic image distortions. Again we find that no correlations are detected at scales $\theta \gtrsim 0.3$ arcmin, indicating that our PSF correction procedure has worked well. Note, however that the star-galaxy cross-correlations are significant at scales $\theta < 0.3$ arcmin, indicating a possible systematic problem at these very small scales – this motivates our exclusion of the smallest-scale $C_1(\theta)$ data point for our parameter estimations in Section 3.7.

We can use our correlation function measurements to compare our results with those of previous cosmic shear studies. We perform such a comparison by looking at the total correlation function, $C(\theta) = C_1(\theta) + C_2(\theta)$ for each dataset. In Fig. 3.18, we plot $C(\theta)$ as measured from COMBO-17,

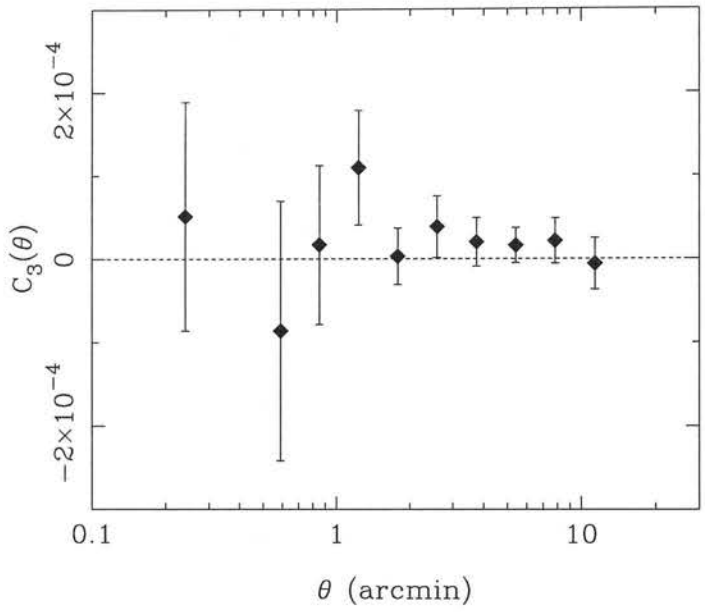

Figure 3.16: The cross-correlation of the shear components $C_3(\theta)$, as measured from the COMBO-17 dataset. The signal is consistent with zero on all scales in agreement with theoretical predictions.

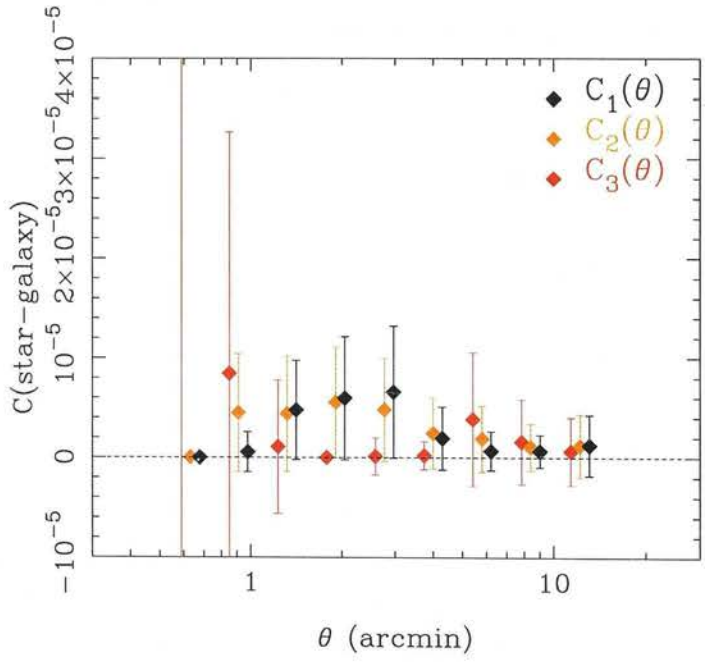

Figure 3.17: The star-galaxy cross-correlation functions, equation (3.33) for the COMBO-17 data. The C_1 and C_2 points have been slightly offset horizontally for clarity. These measurements are a strong test of how successfully the galaxies have been corrected for distortions introduced by PSF anisotropy. The residual correlations between galaxies and stars are consistent with zero on all scales. In the worst-case scenario, represented by the upper end of the error bars shown, our correlation function measurements would include $< 10\%$ contamination from residual distortions left over from the PSF corrections applied.

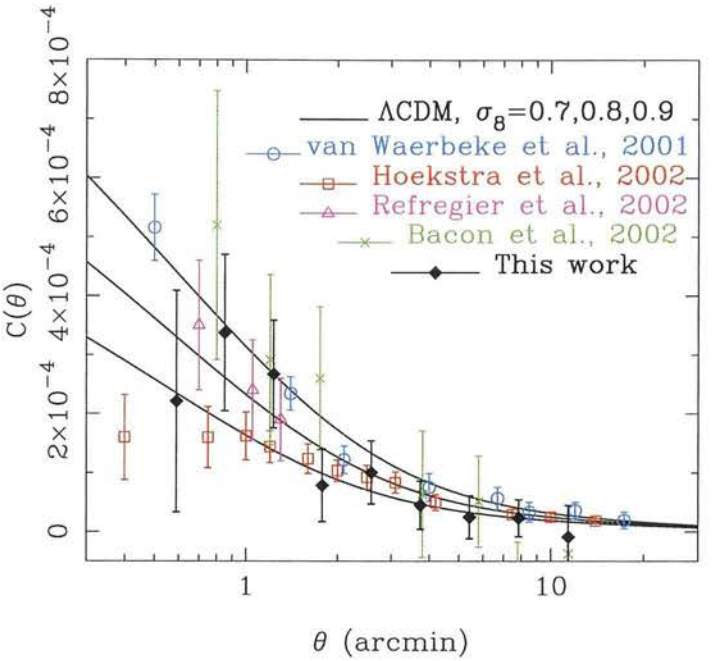

Figure 3.18: The total correlation function, $C(\theta)$, as measured from COMBO-17, along with the most recent cosmic shear measurements from the four other groups indicated. Beyond a scale of 1 arcmin, the measurements are in broad agreement. The correlation function predictions for a flat ΛCDM cosmology, for three values of the power spectrum normalisation (from top to bottom: $\sigma_8 = 0.9, 0.8, 0.7$) are also plotted.

along with the most recent results from four other groups (Van Waerbeke et al. 2001; Bacon et al. 2002; Refregier et al. 2002; Hoekstra et al. 2002b). Note that we have scaled each groups' results to a median redshift of $z_s = 0.85$ using the scaling suggested by the numerical simulations of Barber (2002), *i.e.* $C(\theta) \propto z_m^2$. We have also, in the case of Refregier et al. and Hoekstra et al. , assumed that $\sigma_\gamma^2(\theta) \approx C(\theta)$, where $\sigma_\gamma^2(\theta)$ is the shear variance statistic measured by these two groups. That this is a reasonable assumption can be seen by comparing the $\sigma_8 = 0.9$ models in Figs. 3.18 and 3.19. Fig. 3.18 shows that, beyond a scale of $\theta \sim 1$ arcmin, all groups are in broad agreement with each other, although the COMBO-17 signal does seem to be slightly lower in amplitude. At scales smaller than 1 arcmin, comparisons are more difficult to make because of the larger error bars involved. Indeed, it is the measurements at the larger scales ($\theta \gtrsim 1$ arcmin) that provide our best constraints on cosmological models.

3.5.2 Shear variance

We have also applied the minimum variance estimator of Brown et al. 2002 (see also Chapter 4) to measure the shear variance in square cells in excess of the noise:

$$\sigma^2_{\rm lens}(\theta) = \frac{\sum_{\rm cell} w_{\rm cell}(\gamma^2_{\rm cell} - N_{\rm cell})}{\sum_{\rm cell} w_{\rm cell}}, \tag{3.34}$$

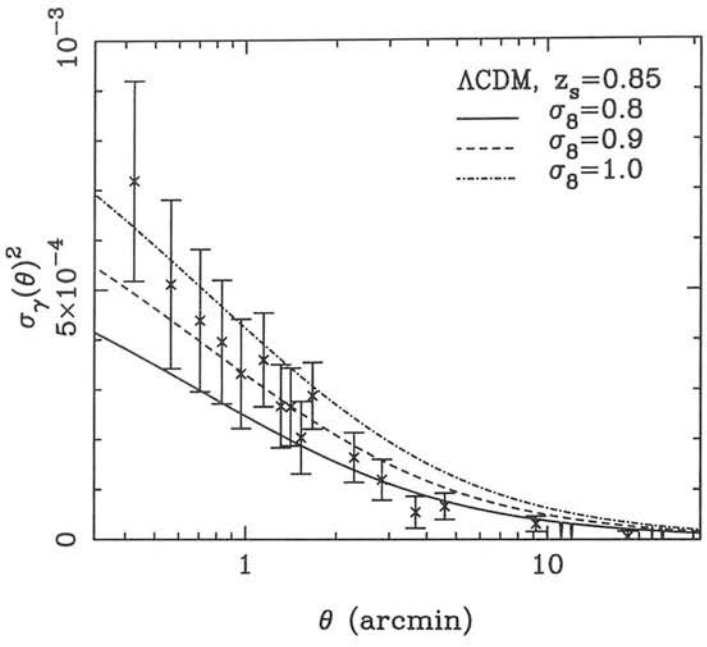

Figure 3.19: The minimum variance shear variance as measured from the COMBO-17 dataset. Also plotted are predictions for the shear variance for a $\Omega_m = 0.3$ ΛCDM cosmology for three different normalisations of the matter power spectrum.

where $\gamma_{\rm cell}$ is the cell averaged shear and $w_{\rm cell}$ is a minimum variance weight;

$$w_{\rm cell} = \frac{1}{2[\sigma_\gamma^4(\theta) + N_{\rm cell}^2(\theta)]}. \tag{3.35}$$

Here $N_{\rm cell}$ is the noise in the cell measured from the data due to the intrinsic dispersion in galaxy ellipticities,

$$N_{\rm cell}(\theta) = \frac{1}{n^2}\sum_{i=1}^{n}\left(\gamma_1^2(\hat{\boldsymbol{r}}_i) + \gamma_2^2(\hat{\boldsymbol{r}}_i)\right), \tag{3.36}$$

where n is the number of galaxies in a cell and σ_γ^2 is the predicted shear variance for square cells which we calculate for a ΛCDM model using $\sqrt{\pi}\times$ equation (3.25). Varying the cell side length yields the cell variance as a function of scale, $\sigma_{\rm lens}^2(\theta)$. The error in equation (3.34) is given by

$$\mathrm{Var}[\sigma_{\rm lens}^2] = \frac{1}{\sum_{\rm cell} w_{\rm cell}}. \tag{3.37}$$

In Fig. 3.19, we plot our shear variance measurements along with the predicted shear variance signal for a ΛCDM model, and for three values of the power spectrum normalisation, $\sigma_8 = 0.8, 0.9$ & 1.0. By comparing the data points in Figs. 3.18 and 3.19 with the $\sigma_8 = 0.9$ model plotted in each case, one sees that the shear variance statistic is measuring a somewhat higher signal than the correlation function on scales $\lesssim 2$ arcmin. We suspect that this is the same effect as that seen in the correlation functions at very small scales, *i.e.* that at these scales residual systematics and/or overlapping

isophotes become important.

One other effect that may contaminate the lensing signal on all scales is intrinsic galaxy alignments. Very recently, methods have been developed for separating the intrinsic and lensing signals (Heymans & Heavens 2003; King & Schneider 2002) by effectively down-weighting physically close pairs of galaxies when calculating the correlation functions. Such methods are dependent on accurate photometric information being available for the individual galaxies. In this respect, the COMBO-17 survey is ideal for the separation of the intrinsic and lensing signals, and we are currently applying such an analysis to the survey.

We note, for the purposes of the current lensing analysis, however, that intrinsic alignments are unlikely to contribute significantly to our signal beyond scales of a few arcmin in the shear variance or beyond $\sim$ 1 arcmin in the correlation functions. Indeed, the few observational studies of intrinsic alignments carried out to date (Chapter 4 of this work; Pen, Lee & Seljak 2000; Brown et al. 2002; Lee & Pen 2002) support arguments from both theoretical considerations (Crittenden et al. 2001; Catelan et al. 2001; Mackey et al. 2002) and numerical simulations (Heavens, Refregier & Heymans 2000; Croft & Metzler 2001) that predict the intrinsic contribution to be no more than $\sim$ 10% for deep surveys such as COMBO-17. We do, however, urge caution when interpreting these statistics on scales $\lesssim$1 arcmin.

3.6 Cosmic Shear Likelihood Analysis

Having tested our data for sources of systematic errors and measuring the cosmic shear signal using the correlation function and shear variance statistics, we now apply a new maximum likelihood analysis to estimate the cosmic shear power spectrum from the COMBO-17 dataset. This section contains the key results of the analysis.

3.6.1 Maximum Likelihood Estimators

The problem of estimating model parameters from a given dataset is a well studied one (*e.g.* Fisher 1935) and it turns out that the *maximum likelihood estimator* (ML-estimator) is a key quantity in this context. In general, a dataset will consist of n real numbers, $x_1, x_2, \cdots, x_n$ which can be formatted as an n-dimensional vector, $\boldsymbol{x}$. Before collecting the data, $\boldsymbol{x}$ can be thought of as a random variable which, in general, will have a probabilitiy distribution, $L(\boldsymbol{x}, \boldsymbol{\Theta})$. This probability distribution or *likelihood function* will, in turn depend in some known way on a vector of model parameters, $\boldsymbol{\Theta} = (\theta_1, \theta_2, \cdots, \theta_m)$. If $\boldsymbol{\Theta}$ represents our model parameter estimates and the true model parameters are denoted $\boldsymbol{\Theta}_0$, the challenge then is to find an unbiased and optimal estimator for the model parameters, *i.e.* one for which $\langle \boldsymbol{\Theta} \rangle = \boldsymbol{\Theta}_0$ and which minimizes the errors on the parameter estimates given by,

$$\Delta\theta_i \equiv \left(\langle \theta_i^2 \rangle - \langle \theta_i \rangle^2 \right)^{1/2} . \tag{3.38}$$

What we need then is the "Best Unbiased Estimator" or BUE for the θ_i's. In this respect, the following three theorems have been proven (*e.g.* Kenney & Keeping 1951; Kendall & Stuart 1969):

- For any unbiased estimator, $\Delta\theta_i \geq 1/\sqrt{F_{ii}}$.
- If there is a BUE $\boldsymbol{\Theta}$, then it is the ML-estimator or a function thereof.
- The ML-estimator is asymptotically a BUE.

The first theorem above, which is known as the Craemér-Rao inequality, expresses the minimum attainable errors on the parameter estimates in terms of the *Fisher information matrix*, which is given by

$$F_{ij} \equiv \left\langle \frac{\partial^2 \mathcal{L}}{\partial\theta_i \partial\theta_j} \right\rangle, \tag{3.39}$$

where $\mathcal{L} \equiv -\ln L$. Note that this is the minimum error attainable on θ_i in the case where all the other parameters are known. If the other parameters are also estimated from the data, then the minimum attainable error rises to $\Delta\theta_i \geq (\boldsymbol{F}^{-1})_{ii}^{1/2}$. The second theorem demonstrates the motivation for using ML-estimators: if there exists a best method for estimating the parameters from the data then the ML-estimator is it. Finally the third theorem tells us that in the limit of very large datasets, the ML-estimator becomes the BUE for the model parameters, $\boldsymbol{\Theta}$. Given these considerations then, a maximum likelihood analysis of the data seems a highly desirable and judicial thing to do and it is in light of these arguments that we have adopted the ML approach to reconstructing the cosmic shear power spectra.

3.6.2 Likelihood procedure

Our approach is based on the prescription of Hu & White (2001, hereafter HW), who use a maximum likelihood method to reconstruct the three power spectra, $C_\ell^{\kappa\kappa}$, $C_\ell^{\kappa\beta}$ and $C_\ell^{\beta\beta}$, directly from pixelised shear data. More precisely HW proposed reconstructing $C_\ell^{\kappa\kappa}$ as a series of step-wise "band powers", extracted from the data via an iterated quadratic estimator of the ML solution. This approach, which is similar to methods used in analyses of CMB polarisation fields (*e.g.* Tegmark & de-Oliviera Costa 2001), has the advantage that it automatically accounts for irregular survey geometries and produces error estimates which include sampling variance and shot noise. In addition this approach can account for the effects of pixelisation.

HW have tested the ML-estimator on both Gaussian realisations of a ΛCDM power spectrum and on N-body simulations. In both cases, the estimator performs well, recovering the input power accurately with error estimates from the Fisher matrix showing excellent agreement with run-to-run errors. We also investigate the method with our own simulations in the next section.

Another advantage of this approach for reconstructing the shear power spectrum is that it provides a simple method for performing a decomposition of the signal into curl (β) and curl-free (κ) modes. The weak lensing shear power spectrum is predicted to be completely curl-free in the absence of

significant lensing from gravitational waves (Stebbins 1997; Kamionkowski et al. 1998) although the predictions for intrinsic galaxy alignments are less certain (*e.g.* Crittenden et al. 2001, Mackey et al. 2002). The κ/β decomposition, therefore, represents a useful method for the detection of non-lensing artefacts (*e.g.* intrinsic alignments, systematic effects) in the data.

If we write our data as a vector,

$$\boldsymbol{d} = (\gamma_1(\hat{\boldsymbol{r}}_1), \gamma_2(\hat{\boldsymbol{r}}_1), \cdots, \gamma_1(\hat{\boldsymbol{r}}_n), \gamma_2(\hat{\boldsymbol{r}}_n)),$$

then, in the case where the shear distribution is Gaussian, the likelihood function is simply

$$-2\ln L(\boldsymbol{C}|\boldsymbol{d}) = \boldsymbol{d}^t \boldsymbol{C}^{-1} \boldsymbol{d} + \mathrm{Tr}\,[\ln \boldsymbol{C}], \tag{3.40}$$

where

$$\boldsymbol{C} = \langle \boldsymbol{d}\boldsymbol{d}^t \rangle \tag{3.41}$$

is the data covariance matrix, and we assume uniform priors. We can interpret the data covariance matrix as the sum of the shear covariance matrix, equation (3.20) and a noise term

$$\boldsymbol{N} = \frac{\gamma_{\mathrm{rms}}^2}{N_{\mathrm{pix}}} \boldsymbol{I}, \tag{3.42}$$

which we measure directly from the data. Here, $\boldsymbol{I}$ is the identity matrix, γ_{rms} is the intrinsic dispersion of galaxy ellipticities within a pixel and N_{pix} is the pixel occupation number.

Following HW, we maximise the likelihood as a function of the model parameters. Here, our model parameters are just the band powers of the three power spectra, $C_\ell^{\kappa\kappa}, C_\ell^{\beta\beta}$ and $C_\ell^{\kappa\beta}$ and we perform the maximization iteratively with a Newton-Raphson scheme. That is, from an initial guess of the band powers, θ_i, a new estimate,

$$\theta_i{}' = \theta_i + \Delta\theta_i \tag{3.43}$$

is made for the band powers where we have adjusted our previous estimate by

$$\Delta\theta_j = 2 \left(\frac{\partial \ln L}{\partial \theta_i} \right) \left(\frac{\partial^2 \ln L}{\partial \theta_i \partial \theta_j} \right)^{-1}. \tag{3.44}$$

Here, we can replace the second derivative of the likelihood by its expectation value,

$$\left\langle \left(\frac{\partial^2 \ln L}{\partial \theta_i \partial \theta_j} \right)^{-1} \right\rangle \approx F_{ij}^{-1}, \tag{3.45}$$

and at the same time, in the limit where the likelihood is sufficiently Gaussian in the parameters, we

can use the Fisher Information matrix (*e.g.* Tegmark, Taylor & Heavens 1997),

$$F_{ij} = \frac{1}{2}\mathrm{Tr}\left[\boldsymbol{C}^{-1}\partial_{\theta_i}\boldsymbol{C}\right].\left[\boldsymbol{C}^{-1}\partial_{\theta_j}\boldsymbol{C}\right] \tag{3.46}$$

to estimate the uncertainties on the band power measurements. That is, we approximate the covariance matrix of our band power estimates as

$$\mathrm{cov}[\theta_i\,\theta_j] \approx F_{ij}^{-1}. \tag{3.47}$$

We should re-iterate at this point that the ML technique depends crucially on the assumption that the shear field which we are probing is Gaussian. On the largest scales, this is not a problem since the Gaussian approximation for the shear field is an excellent one. However, in the following analysis, we apply the ML technique to relatively small fields. On small scales the shear field is expected to be significantly non-Gaussian and so this needs to be borne in mind when interpreting our results.

3.6.3 Testing the likelihood on simulations

Although HW test the likelihood reconstruction of the various power spectra on both Gaussian and N-body simulations, we have also conducted our own simulations of the likelihood reconstruction. We do this because of the small size of our data fields (30×30 arcmin) relative to HW's simulated fields, which are about 50 times larger in area.

We have applied the ML-estimator to one hundred 30×30 arcmin fields where the pixelised shear distribution in each field is a Gaussian realisation of a shear power spectrum calculated for a ΛCDM cosmology and for all source galaxies lying at $z = 1$. Following HW's approach, we have added Gaussian distributed noise to each of the 20×20 pixels (pixel size, 1.5×1.5 arcmin) of our shear distribution according to equation (3.42) where we have taken $\gamma_{\rm rms} = 0.4$ for the intrinsic dispersion in galaxy ellipticity components. For the number of galaxies in each cell, we employ a mean galaxy density of $\overline{n}_g = 32.0$ arcmin^{-2}, similar to the measured galaxy density of our dataset (see Table 1), and we calculate the pixel occupation number with $N_{\rm pix} = \overline{n}_g\theta_{\rm pix}^2$ where $\theta_{\rm pix}$ is the pixel side length in arcmin. The results from all the simulations are summarised in Fig. 3.20 where we plot the recovered band powers of the three power spectra, $C_\ell^{\kappa\kappa}$, $C_\ell^{\beta\beta}$ and $C_\ell^{\kappa\beta}$, averaged over all simulation runs. Here, we plot both the run-to-run errors and the errors as estimated from the Fisher matrix which agree well with one another, supporting the use of the Fisher matrix to estimate errors on the band power measurements. We see from these simulation results that the ML reconstruction recovers the input power very accurately for Fourier modes in the range $1000 \lesssim \ell \lesssim 5000$. There is some indication from the simulations, however, that the method may slightly over-estimate the power for $\ell-$modes outside this range. However, this discrepancy is much smaller that the precision to which we measure the signal. Finally, we note that the likelihood reconstruction estimates of the β-mode power spectrum, $C_\ell^{\beta\beta}$ and the cross-correlation, $C_\ell^{\kappa\beta}$ are both consistent with zero on all scales, as expected for the input Gaussian shear model used to create the shear distributions.

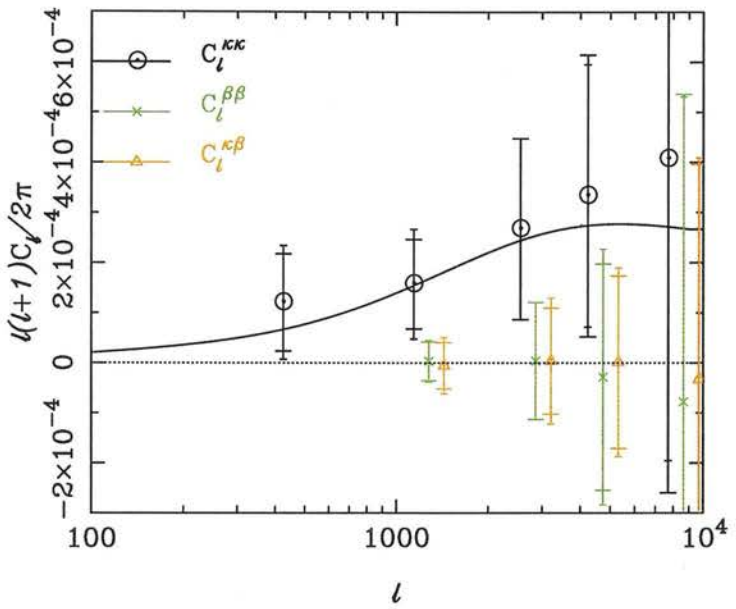

Figure 3.20: The recovered band powers of the three spectra, $C_\ell^{\kappa\kappa}$, $C_\ell^{\beta\beta}$ and $C_\ell^{\kappa\beta}$ as averaged over 100 Gaussian realisations. Note that the κ/β decomposition cannot be done for the $\ell = 400$ bin because on scales comparable to the size of the field, the κ and β modes are essentially indistinguishable (a full wavelength is needed to perform the decomposition). Error bars are shown as calculated from the run-to-run variations (smaller terminal ends) and also as estimated from the Fisher matrix (larger terminal ends). The solid curve is the input ΛCDM power spectrum used to create the simulated shear distributions. The $C_\ell^{\beta\beta}$ and $C_\ell^{\kappa\beta}$ points have been slightly offset horizontally for clarity.

3.6.4 Maximum likelihood results

Shear power spectra

Having tested the method on simulations, we now apply the ML reconstruction to our five data fields, CDFS, SGP, FDF, S11 and A901/2. As these fields are widely separated on the sky we can treat them as independent and optimally combine them afterwards.

Fig. 3.21 shows the results of estimating $C_\ell^{\kappa\kappa}$, $C_\ell^{\kappa\beta}$ and $C_\ell^{\beta\beta}$ for the five fields, in 5 band powers. Also plotted is a model curve for the ΛCDM model with $\Omega_\Lambda = 0.7, \Omega_m = 0.3, h = 0.68$, normalised to $\sigma_8 = 0.8$ (see Section 3.7). The linear power spectrum has been transformed to a nonlinear one using the halofit formulae of Smith et al. (2002) and, again, we have included the composite redshift distribution shown in Fig. 3.14 in this calculation.

In general we find that the fields containing clusters, S11 and A901/2, both yield higher results than the other fields. However, as mentioned already, the results for the S11 field seem consistent with the dataset as a whole while those for the A901/2 field clearly are not. That the shape is broadly the same for the A901 field is to be expected since this part of the nonlinear power spectrum is dominated by massive clusters (Cooray & Hu 2001). At the median redshift of the sample, the peak of the nonlinear convergence power spectrum corresponds to around $3h^{-1}$Mpc, the scale on which

Table 3.3: Details of the maximum likelihood reconstructed band powers as obtained from the optimal combination of the four fields, CDFS, S11, SGP and FDF. The first two columns list the ℓ-range of the five band powers. Also listed are the detections and uncertainties in each band where we quote the band powers, $P_{ii} = \ell(\ell+1)C_\ell^{ii}/2\pi$ for $i = \kappa, \beta$. The first band only has $P_{\kappa\kappa}$ measurements as the κ and β powers are essentially indistinguishable at these large scales.

$\ell_{\rm min}$	$\ell_{\rm max}$	$P_{\kappa\kappa}(\times 10^5)$	$P_{\beta\beta}(\times 10^5)$	$P_{\kappa\beta}(\times 10^5)$
247	594	2.92 ± 2.05	–	–
595	1790	4.95 ± 2.43	-1.45 ± 1.26	2.21 ± 1.45
1791	2986	2.20 ± 4.75	-4.38 ± 3.76	-1.99 ± 3.27
2987	6324	26.62 ± 8.12	13.85 ± 7.34	0.49 ± 5.54
6325	13906	11.57 ± 22.39	7.87 ± 22.03	14.83 ± 14.64

we expect collapsed clusters to have virialised.

The other fields, CDFS, the SGP and FDF, are fields without large structures and have correspondingly lower amplitude spectra. Interestingly on the smallest scales, $\ell \approx 4000$, the power is roughly the same in all five fields.

Fig. 3.22 shows the power from an optimal inverse weighting combination of the fields excluding A901/2. Details of the optimally combined power spectra measurements are also given in Table 3.3. Three of our five band power measurements agree within their error bars with the $\sigma_8 = 0.8$ normalised ΛCDM model plotted. The high level of power measured at $\ell \sim 4000$ seems to be present in each of the fields we have analysed. The largest discrepancy between the model and the measurements occurs at $\ell = 2000$ where less than half the power is found.

In order to interpret the scales that we are probing with our power spectrum measurements, we note that, in a flat cosmology, the angular size will scale roughly as

$$R \simeq \frac{2\pi D_A}{\ell}, \tag{3.48}$$

where, for a flat ΛCDM Universe, the angular diameter distance, D_A is well approximated by (Broad-

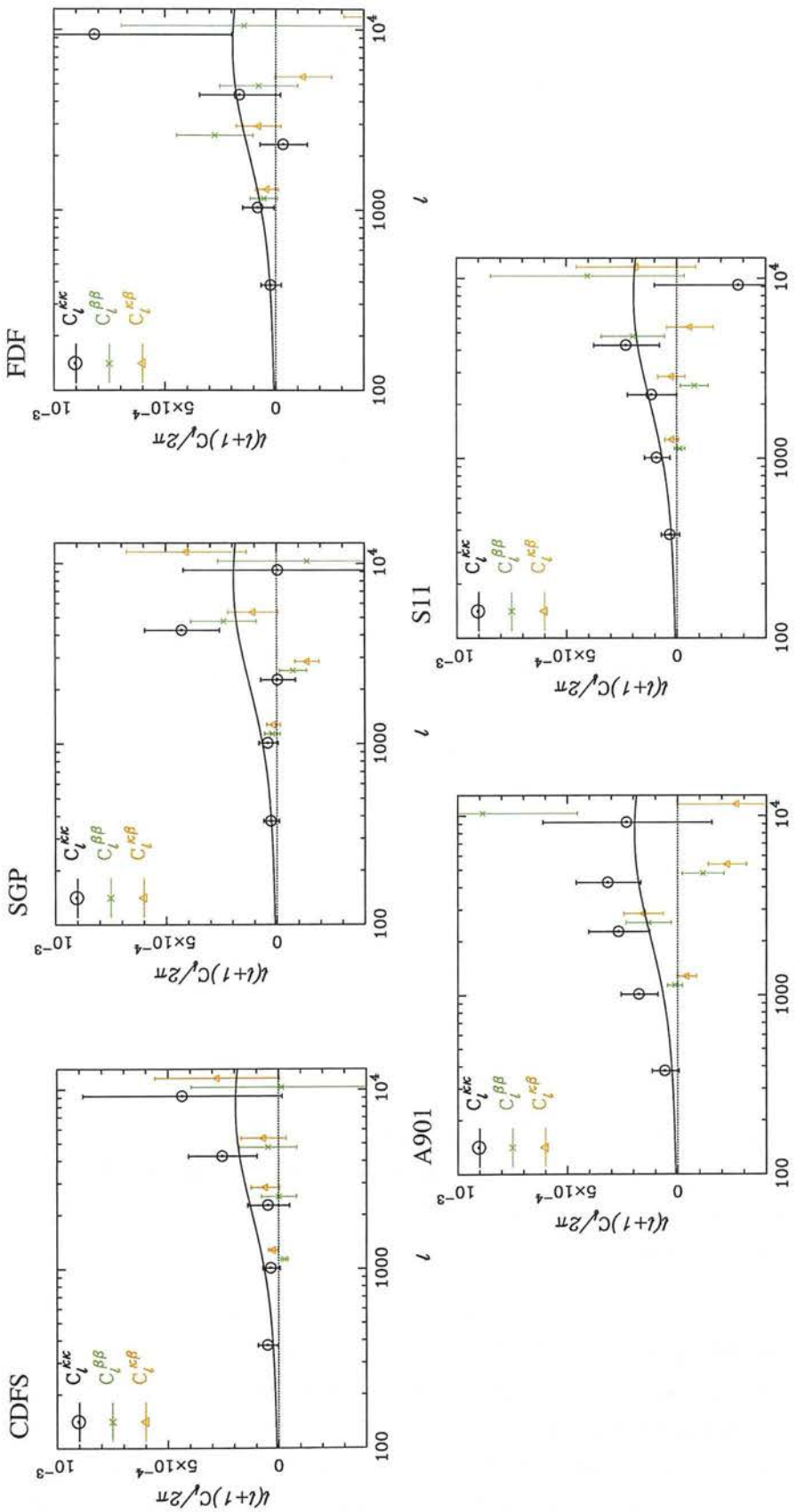

Figure 3.21: The cosmic shear power spectra estimated from each of the five individual fields in the COMBO-17 dataset. The spectra are for (clockwise, from top left) CDFS, SGP, FDF, S11 and A901. Note the much higher power recovered from the A901 supercluster field. The $C_\ell^{\beta\beta}$ and $C_\ell^{\kappa\beta}$ points have been slightly offset horizontally for clarity. Note again that the κ/β decomposition cannot be done for the $\ell = 400$ bin because on scales comparable to the size of the field, the κ and β modes are essentially indistinguishable (a full wavelength is needed to perform the decomposition).

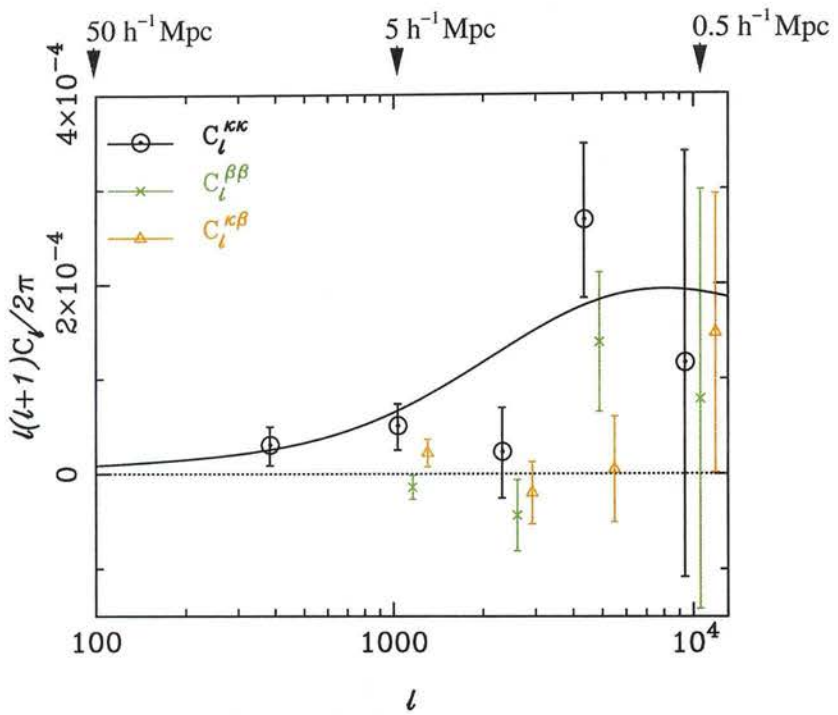

Figure 3.22: The cosmic shear power spectra from COMBO-17, after excluding the A901 supercluster field. Plotted on a linear-log scale are $C_\ell^{\kappa\kappa}$ (circles), $C_\ell^{\beta\beta}$ (crosses) and $C_\ell^{\kappa\beta}$ (triangles) in 5 band-averaged band powers, as a function of multipole, ℓ, estimated from the optimal combination of a maximum likelihood analysis of the four COMBO-17 fields, CDFS, SGP, FDF, and S11. The error bars are estimated from the Fisher matrix. Note that the κ/β decomposition cannot be done for the $\ell = 400$ bin because on scales comparable to the size of the field, the κ and β modes are essentially indistinguishable (a full wavelength is needed to perform the decomposition). The solid curve is the shear power spectrum expected fora $\sigma_8 = 0.8$ normalised ΛCDM model. Once again, the $C_\ell^{\beta\beta}$ and $C_\ell^{\kappa\beta}$ points have been slightly horizontally displaced for clarity.

hurst, Taylor & Peacock 1995)

$$D_A(z) \simeq \frac{c}{H_0} \frac{z}{(1+z)(1+3/4\Omega_m z)}. \tag{3.49}$$

An estimate for the redshift of typical deflectors in the survey is $z_d \approx 0.5 z_m$ and we have estimated $z_m \sim 0.85$ (see Section 3.4.2) for the median redshift of our survey. Combining these relations (with $\Omega_m = 0.3$) gives the following approximate conversion between the physical scale being probed and the Fourier variable on the sky:

$$R \simeq \frac{5130}{\ell}\ h^{-1}\mathrm{Mpc}. \tag{3.50}$$

This relation gives the approximate physical scale indicated at the top of Fig. 3.22.

We can check our results for systematic effects by estimating the power in the β-β modes, as well as the κ-β cross correlation. In all of our band powers the β-β correlation is below the detected signal in κ and is consistent with zero in all but one band power at $\ell \sim 4000$. Similarly the κ-β cross correlation is well below our measurement of shear power, and is consistent with zero except at

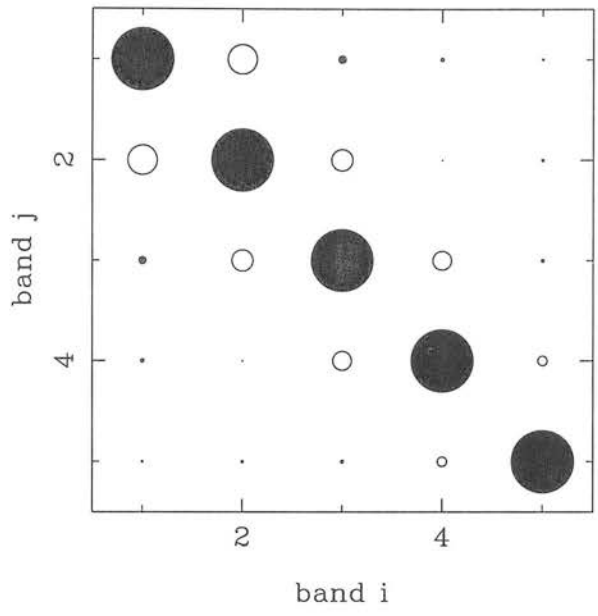

Figure 3.23: The correlation matrix (see text for details) of the optimally combined band power measurements recovered from the maximum likelihood reconstruction of $C_\ell^{\kappa\kappa}$. The area of each circle is proportional to the degree of correlation between bands i and j. Filled circles denote that the bands are correlated whereas unfilled circles denote an anti-correlation between the bands. The bands are the same as those plotted in Fig. 3.22, numbered 1 to 5, in order from left to right. Note the small values of the off-diagonal elements, indicating small (anti-)correlations between different band power measurements.

$\ell \sim 1000$ where a significant detection appears. We conclude from the minimal power found in these spectra that our results are not strongly contaminated by systematic effects.

Covariance matrix of band powers

In addition to measuring the amplitude of the shear power spectrum, it is also important to consider the correlations between band powers. We can quantify how much the bands are correlated with one another with the correlation matrix, defined by

$$\mathrm{Cor}_{ij} = \frac{\mathrm{Cov}_{ij}}{\sqrt{\mathrm{Cov}_{ii}\mathrm{Cov}_{jj}}}, \tag{3.51}$$

where Cov_{ij} is the covariance matrix of the band powers, which we estimate from the Fisher matrix during the likelihood procedure. In Fig. 3.23, we plot the correlation matrix of the optimally combined band power measurements shown in Fig. 3.22. It is clear from this figure that our band power measurements show very little correlation with one another, the biggest effect being the slight anti-correlation of neighbouring bands. Thus, our ML band powers are almost independent measures of power.

3.6.5 Integral power spectra approximations

As well as a maximum likelihood approach, more direct methods have been proposed for recovering the shear power spectra. We have applied one of these direct methods, proposed by Schneider et al. (2002, hereafter SvWKM), to our data. SvWKM proposed reconstructing $C_\ell^{\kappa\kappa}$ directly from a correlation function analysis of the data, via an inversion of equation (3.24). Pen et al. (2002) have also suggested a similar approach, but with a somewhat different implementation, which they apply to the DESCART dataset.

The correlation function estimator, which can also be formulated in terms of band powers, is not dependent on the spatial distribution of the shear and, as pointed out by SvWKM should not suffer from bleeding of power between bands due to pixelisation of the data. SvWKM test their estimator by reconstructing the power spectrum from a fiducial weak lensing survey of area, A=25 deg^2 from which they assume they have measured the correlation functions for $0.'1 \leq \theta \leq 2^\circ$. For such a survey, the estimator recovers the input power very accurately for ℓ-modes in the range $200 \lesssim \theta \lesssim 2 \times 10^5$ and SvWKM also measure minimal covariance between their band powers over this range. Over the range, $2\pi/\theta_{\rm max} \lesssim \ell \lesssim 2\pi/\theta_{\rm min}$, the correlation function estimator is practically unbiased where $\theta_{\rm min}(\theta_{\rm max})$ is the smallest (largest) scale at which the correlation functions have been measured. Here we apply a modified version of the SvWKM statistic to our dataset. If we define two new correlation functions, $\xi_+(\theta) = C_1(\theta) + C_2(\theta)$ and $\xi_-(\theta) = C_1(\theta) - C_2(\theta)$, the correlation function estimator of SvWKM can be written as

$$C_\ell = 2\pi \int_{\theta_{\rm min}}^{\theta_{\rm max}} d\theta\, \theta \left[K_1 \xi_+(\theta) J_0(\ell\theta) + K_2 \xi_-(\theta) J_4(\ell\theta)\right], \tag{3.52}$$

where $J_{0,4}(\ell\theta)$ are the usual Bessel functions and K_1 & K_2 describe the relative contribution from the $\xi_{+,-}(\theta)$ correlators to the integral. In order to achieve an optimal combination of ξ_+ and ξ_- contributions to the integral, SvWKM have constructed a function, $K_1(\ell)$ and imposed the constraint, $K_2 = 1 - K_1(\ell)$. However, in order to decompose our signal into κ and β modes, we have chosen K_1 and K_2 to be constants, independent of ℓ. Setting $K_1 = K_2 = 1/2$ yields a purely κ-mode estimator, whereas if we set $K_1 = 1/2$ and $K_2 = -1/2$, the estimator should recover only the β-mode power. Following SvWKM, we have formulated the correlation function estimator in terms of band powers.

Fig. 3.24 shows the result of applying the correlation function estimator to COMBO-17. Again, we have excluded the A901 supercluster field from this calculation. We note that only the third band power on this plot is within the stated range of validity of the SvWKM estimator. Indeed, this data point is in good agreement with the $\Omega_m = 0.3$ ΛCDM model plotted and the power in β for this band power is consistent with zero. On both larger and smaller scales however, as predicted by SvWKM, the estimates becomes unreliable, measuring equal κ and β modes on large scales. Ideally, of course, one would measure the correlation functions out to as large a scale as possible to extend the range of applicability of the estimator. However, for our dataset, we only have correlation function measurements in the range $20'' \lesssim \theta \lesssim 12'$ giving us a valid ℓ-range of $1800 \lesssim \ell \lesssim 5000$.

We have also found that the SvWKM estimator introduces significant correlations between our band power measurements. The correlation matrix, equation (3.51) of the band powers, plotted in

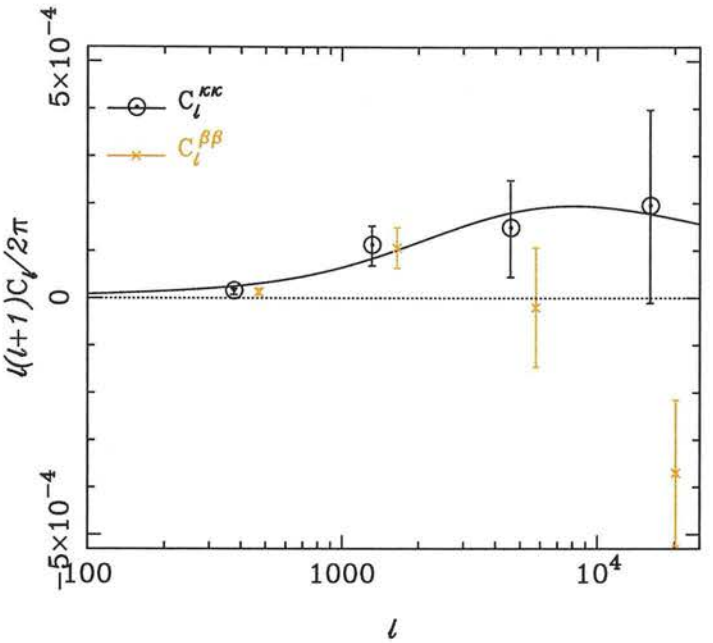

Figure 3.24: The shear power spectrum, $C_\ell^{\kappa\kappa}$ and the β-mode spectrum, $C_\ell^{\beta\beta}$ as estimated via a modified version (see text for details) of SvWKM's correlation function estimator. The $C_\ell^{\beta\beta}$ points have been laterally displaced for clarity. Again, we have excluded the A901 supercluster field for these measurements. Also shown is the shear power spectrum expected for a $\sigma_8 = 0.8$ normalised ΛCDM model.

Fig. 3.25, as estimated by the SvWKM method shows a very strong correlation between the large-scale bands (bands 1 and 2) while the bands on smaller scales (bands 3 and 4) are highly anti-correlated. We have already seen in Section 3.6.4 that the maximum likelihood approach avoids this type of contamination across scales.

We conclude, therefore, that although reconstructing the shear power spectrum from a correlation function analysis can be useful for datasets with larger fields, for our purposes, the full maximum likelihood analysis is clearly the most suitable approach.

3.7 Cosmological parameter estimation

3.7.1 Ω_m and σ_8 from COMBO-17

Having measured various statistics from the data, we are now in a position to use both our measured shear correlation functions and our reconstructed shear power spectrum estimates to obtain a joint measurement of the normalisation of the mass power spectrum σ_8, and the matter density Ω_m. We can achieve this by fitting theoretical shear correlation functions and power spectra, calculated for particular values of these parameters, to our measurements.

Again, we use the fitting functions of Smith et al. (2002) to produce dark matter power spectra $P_\delta(k, r)$ for values of σ_8 ranging from 0.1 to 1.5 and Ω_m from 0.1 to 1.0, exploring all values on a

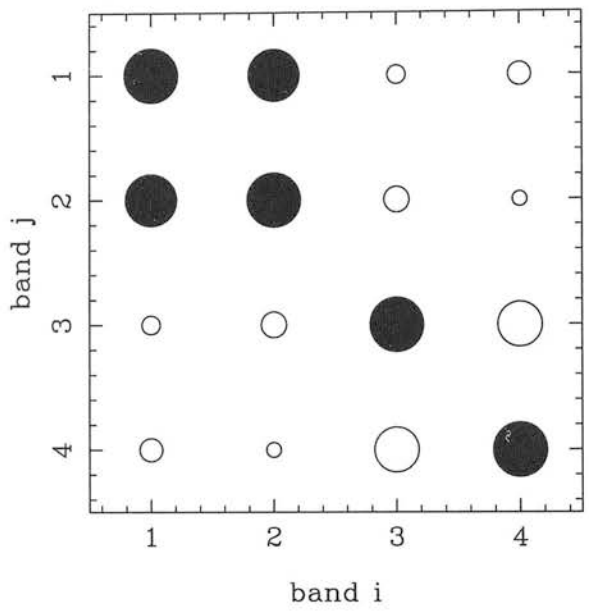

Figure 3.25: The correlation matrix of the SvWKM $C_\ell^{\kappa\kappa}$ band powers. The bands are the same as those plotted in Fig. 3.24, numbered 1 to 4, in order from left to right. Filled circles indicate positive correlations, whereas unfilled circles indicate an anti-correlation between bands. The area of the circle plotted is proportional to the degree of correlation found between the bands. Note the strong (anti-) correlations between neighbouring bands.

grid with 0.01 spacing in these parameters. We choose to fix $\Omega_m + \Omega_\Lambda = 1$. For all our theoretical power spectra and correlation functions, we use $H_0 = 100h = 68\,\mathrm{km\,s^{-1}Mpc^{-1}}$ for the value of the Hubble constant and $n = 1$ for the initial slope of the power spectrum of density fluctuations. For the linear matter power spectrum we use the fitting formulae of Eisenstein & Hu (1998) with a shape parameter $\Gamma = 0.21$. For each set of parameters, we calculate the corresponding shear power spectrum using equation (3.16). Note that we input our composite redshift distribution (Fig. 3.14) into the calculation for the shear power spectra. Having calculated the shear power spectra we obtain the correlation functions $C_{1,2}$ using equation (3.24).

We fit the above models to our correlation function and shear power spectrum data (where the A901 supercluster field has been excluded in both cases) using a χ^2 fitting procedure (*cf.* Bacon et al. 2002). We order our correlation function measurements as a vector $\mathbf{d} \equiv \{C_1(\theta_n), C_2(\theta_n)\}$, where $C_{1,2}(\theta_n)$ is the mean correlation function (averaged over all sections) for a given angular separation (see Section 3.5). Similarly, we order our theoretical correlation functions as vectors $\mathbf{x}(a)$ with the same format, where $a = (\sigma_8, \Omega_m)$.

We use the log-likelihood estimator

$$\chi^2 = [\mathbf{d} - \mathbf{x}(a)]^T \mathbf{V}^{-1} [\mathbf{d} - \mathbf{x}(a)], \tag{3.53}$$

where

$$\mathbf{V} = \langle \boldsymbol{d}\boldsymbol{d}^t \rangle \tag{3.54}$$

is the covariance matrix of our correlation function measurements, which we measure directly from our data using equation (3.32). This estimator is valid in the case of Gaussian errors, which we achieve since we have averaged over many sections. We calculate χ^2 for our fine grid of (σ_8, Ω_m) theoretical correlation functions, and find the minimum and confidence intervals.

The χ^2 fitting for the shear power spectrum measurements is done in exactly the same way as for the correlation function analysis.

Correlation function results

For the correlation function analysis, we find a best fit $\sigma_8(\Omega_m/0.3)^{0.52} = 0.75$, with reduced χ^2 of 1.21. The 1σ error bar on this value, for a 1 parameter fit, is given by the boundary $\Delta\chi^2 = 1.0$, which occurs here at $\sigma_8 = 0.81$ and 0.69. To date, one of the biggest sources of error in cosmic shear measurements of cosmological parameters has been the uncertainty in the median redshift of the source galaxies. The cosmic shear signal scales as $\sigma_\gamma^2 \propto \sigma_8^{2.5} z^{1.6}$ (see *e.g.* BRE). So the uncertainty in the median redshift contributes to the error in σ_8 as

$$\left(\frac{\delta\sigma_8'}{\sigma_8'}\right)^2 = \left(\frac{\delta\sigma_8}{\sigma_8}\right)^2 + 0.64^2 \left(\frac{\delta z}{z}\right)^2 . \tag{3.55}$$

Using our estimate of the median redshift of the COMBO-17 galaxies, $z_m = 0.85 \pm 0.05$ (see Section 3.4.2), we have investigated the extra uncertainty introduced into our measurement of σ_8 by equation (3.55). We find the additional error introduced due to the median redshift uncertainty to be 0.01. Thus we obtain a measurement signal-to-noise of ~ 9 for the amplitude of the power spectrum, with a measurement of the amplitude

$$\sigma_8(\Omega_m/0.3)^{0.52} = 0.75^{+0.08}_{-0.08}. \tag{3.56}$$

Shear power spectrum results

The results for the shear power spectrum analysis yield a slightly lower amplitude for the power spectrum normalisation. A good fit to the parameter constraints as calculated using our shear power spectrum measurements is $\sigma_8(\Omega_m/0.3)^{0.49} = 0.72$, with a reduced χ^2 of 2.21. The additional error due to the uncertainty in z_s is again 0.01. Our final measurement for the normalisation of the mass power spectrum, as calculated from our shear power spectrum measurements is

$$\sigma_8(\Omega_m/0.3)^{0.49} = 0.72^{+0.08}_{-0.09}. \tag{3.57}$$

These constraints, as calculated using both of our methods are shown as contours in the $\sigma_8 - \Omega_m$

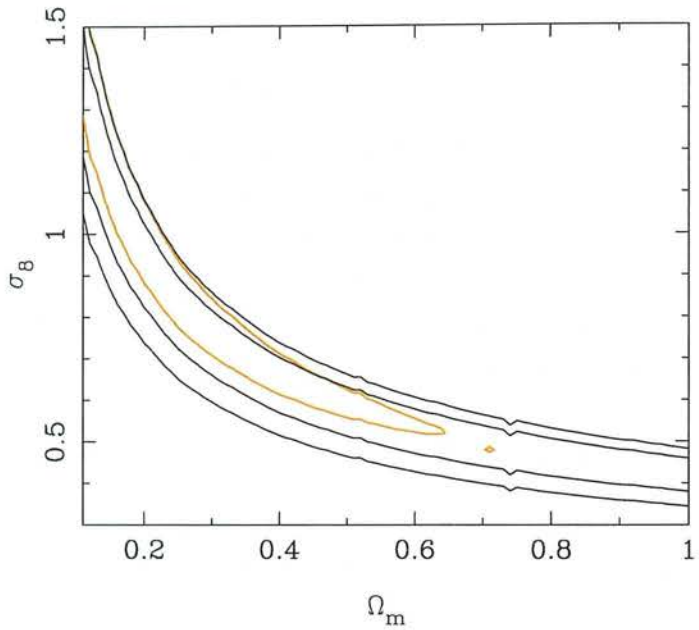

Figure 3.26: The likelihood surface of σ_8 and Ω_m from COMBO-17 as calculated using our correlation function measurements (lighter contour) and as calculated using our shear power spectrum measurements (dark contours). For the power spectra measurements we plot the 1 and 2σ contours. For the correlation functions, we plot only the 1σ contour for clarity.

plane in Fig. 3.26. Note that in the case of the correlation function constraints, values of $\Omega_m \gtrsim 0.63$ are excluded at the 1σ level.

3.7.2 Including the actual redshift distribution

In order to demonstrate the power of accurate redshift information we have also measured parameters from correlation functions which have been calculated using only galaxies with reliable redshift estimates. In this case, for our theoretical curves, we input the *actual* redshift distribution of the lensed source galaxies (*i.e.* the dotted curve in Fig. 3.14). For the purposes of this demonstrative calculation, we have included the A901/2 supercluster field. We do this simply to increase the number of galaxies – at present, photometric redshifts are only available for the CDFS, S11 and A901 fields and there were too few galaxies with reliable redshifts in CDFS and S11 alone (19143 galaxies) to constrain parameters significantly. Adding the 12506 galaxies with accurate redshifts in the A901 field to this sample enabled us to obtain reasonable constraints on Ω_m and σ_8. The result, therefore, will clearly be biased by the A901/2 field and cannot be taken as a measure of the power spectrum amplitude. However, it does dramatically demonstrate the increase in accuracy attainable with accurate photometric information.

The results are shown in Fig. 3.27. For comparison, we also plot the constraints obtained from the same set of correlation function measurements where we have assumed a median redshift and uncertainty of $z_m = 0.6 \pm 0.2$. Here, $z_m = 0.6$ is the measured median redshift of galaxies with reliable assigned redshifts in the COMBO-17 survey and $\Delta z = 0.2$ is typical of the estimated uncertainty

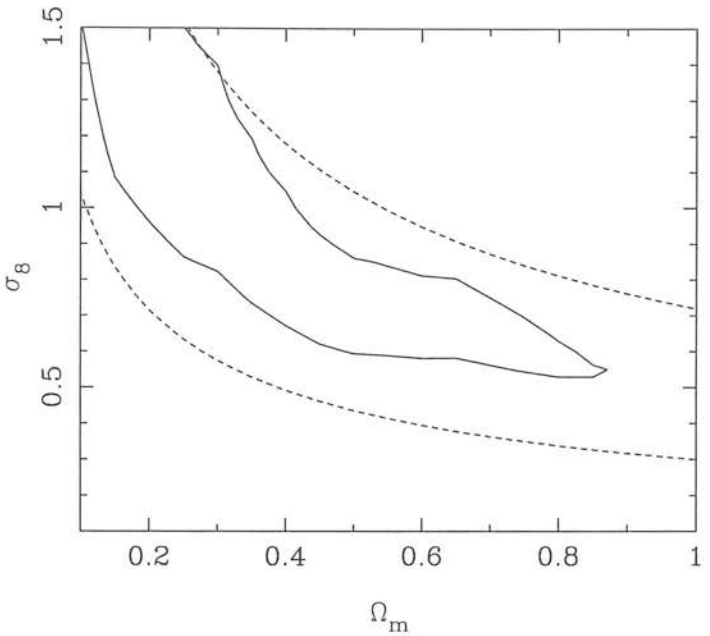

Figure 3.27: The likelihood surface of σ_8 and Ω_m from COMBO-17 using correlation functions measured only from galaxies with accurate redshift estimates. This subset of galaxies only includes galaxies in the CDFS, S11 and A901 fields with R-band magnitudes ≤ 24.0. The 1σ contour is plotted as a full line. For comparison, we also plot the 1σ confidence region (dashed contour) obtained from the same correlation functions excluding the redshift information. For this calculation the only redshift information we assume is an estimate of the median redshift of the survey ($z_m = 0.6 \pm 0.2$).

in the median redshift of cosmic shear surveys to date. In agreement with the shear power spectrum analysis (Section 3.6), we see the effect of the A901 supercluster pushing the best-fit σ_8 value up to ~ 1 for a matter density of $\Omega_m = 0.3$. Once again, we emphasize that we are not presenting this as a measurement of σ_8 – we simply wish to demonstrate the dramatic improvement in parameter constraints obtainable with the inclusion of accurate photometric information. Clearly for accurate parameter estimates, a greater understanding of the source redshift distribution must be a priority for cosmic shear surveys in the future.

3.7.3 Combination with the 2dFGRS and CMB experiments

We can combine the confidence region given by equation (3.57) or by Fig. 3.26, with parameter estimations from other sources such as the 2dF Galaxy Redshift Survey (2dFGRS, Percival et al. 2002) and the various CMB experiments (Lewis & Bridle 2002 & references therein).

In order to combine our measurements with those from the 2dFGRS and the CMB data, we first impose some priors on the various datasets. Firstly, we consider only flat Universe models ($\Omega_\Lambda + \Omega_m = 1$) as compelling evidence for a flat Universe has already been found from the CMB data (*e.g.* de Bernardis et al. 2002; Pryke et al. 2002; Lewis & Bridle 2002). For the slope of the power spectrum of the primordial density perturbations, we take $n_s = 1$ and for the baryon fraction $f_b = \Omega_b/\Omega_m$, we take $f_b = 0.16$. These values are consistent with those measured from joint analyses of CMB and

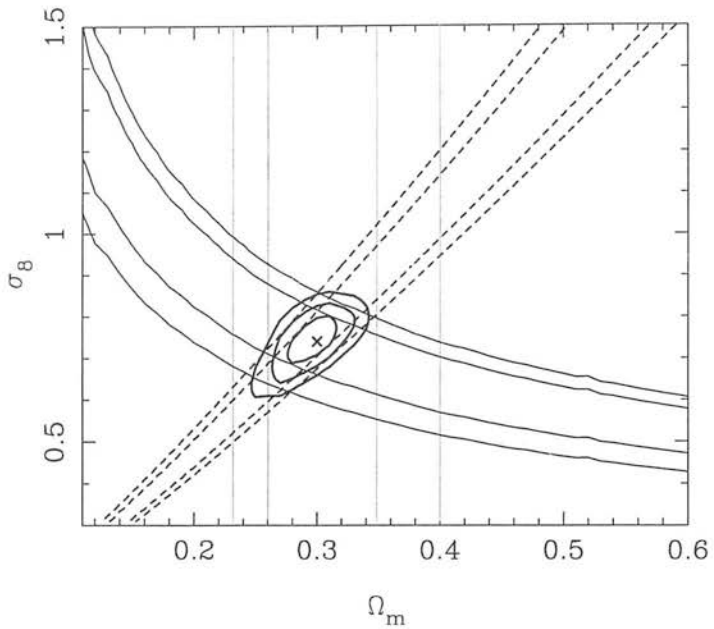

Figure 3.28: The likelihood surface of σ_8 and Ω_m from combining the COMBO-17 dataset with the 2dFGRS and the latest CMB constraints. The dark thin solid contours are the constraints obtained from our shear power spectrum analysis described in the previous section. The lighter vertical contours are the constraints on Ω_m obtained from the 2dFGRS where we have applied the priors described in the text to the 2dF data. The dashed set of contours are the constraints from a compilation of six CMB experiments (see text for details) where we have assumed an optical depth to reionization of $\tau = 0.10$. The dark heavy contours are the 1,2 and 3σ combined constraints from the three methods. The best fit values of Ω_m and σ_8 are also indicated.

Large Scale Structure (LSS) data (*e.g.* Efstathiou et al. 2002; Wang, Tegmark & Zaldarriaga 2002; Percival et al. 2002; Knox, Christensen & Skordis 2002). To display the additional constraints in the $\sigma_8 - \Omega_m$ plane, we also need to choose a value for the Hubble parameter, h. We have taken the value $h = 0.68$, found from a joint analysis of the CMB and 2dF data for a flat Universe and for a scalar-only spectral index, n_s (Percival et al. 2002; Efstathiou et al. 2002). Note that this is the same value of h which we adopted when making our model predictions in the previous section. Finally, we note that this value is consistent with the HST Key Project within the quoted errors (Freedman et al. 2001).

Having set these various parameters, in the case of the 2dFGRS, for each of our grid points in the (Ω_m, σ_8) plane, we simply add the corresponding likelihood values from Percival et al. (2002) to the likelihoods already obtained in the previous section from our shear power spectrum data. For the CMB constraints, we have adopted the results of Lewis & Bridle (2002) who provide the following joint constraint on Ω_m and σ_8 as found from a compilation of six CMB experiments:

$$\nu = \Omega_m h^{2.35} (\sigma_8 e^{-\tau}/0.7)^{-0.84} = 0.115 \pm 0.0047. \tag{3.58}$$

Here, τ is the optical depth to reionization. For each point on our (Ω_m, σ_8) grid, we calculate likeli-

hoods for the CMB data as

$$\chi^2_{\rm CMB} = \frac{\left(\nu - \Omega_m h^{2.35}(\sigma_8 e^{-\tau}/0.7)^{-0.84}\right)^2}{(\delta\nu)^2} \tag{3.59}$$

with $\nu = 0.115, \delta\nu = 0.0047$ and $h = 0.68$. Finally, we add the likelihoods from the various data to get our final measurements of Ω_m and σ_8. The results of this combination are shown in Fig. 3.28 for an optical depth of $\tau = 0.10$. Note that the 2dFGRS data we have used for this estimation constrains Ω_m only and so the constraints shown on σ_8 come wholly from the cosmic shear and CMB measurements. We measure best-fit values of $\Omega_m = 0.27^{+0.02}_{-0.01}$ and $\sigma_8 = 0.73^{+0.06}_{-0.03}$ from the combined data.

We have also investigated the effect a non-zero τ has on these measurements. We find that increasing/decreasing τ has the effect of increasing/decreasing the slope of the CMB constraints somewhat, but the resulting combined constraints are not altered drastically. For example, for an optical depth of $\tau = 0.00$, the best-fit Ω_m and σ_8 values change to 0.29 and 0.72 respectively, while increasing τ to 0.25 changes the best-fit values to $\Omega_m = 0.25$ and $\sigma_8 = 0.77$.

3.8 Summary

We have presented an analysis of the cosmic shear signal in the COMBO-17 survey, a 1.25 square degree survey with excellent data quality, including photometric redshifts for $\sim 38\%$ of our galaxy sample for three of the five $0.5^\circ \times 0.5^\circ$ fields. Our measurements follow a process of careful data reduction, assessment of the level of telescope-induced shear, and correction for PSF anisotropy and circularization of galaxies. In this fashion we reduce the residual systematic effects to a level $< 5\%$ of the cosmic shear signal.

We have measured shear correlation functions and variance-weighted shear cell-variance for our galaxy sample, detecting the cosmic shear signal at the 5σ level. On scales $\gtrsim$1 arcmin, where we are confident of the cosmological origin of the signal, we find a somewhat lower amplitude than other cosmic shear surveys have measured to date.

In contrast to previous cosmic shear surveys, we have substantially reduced the usual uncertainty introduced into the interpretation of cosmic shear measurements due to a lack of knowledge of the redshift distribution. We have done this by estimating from the data the median redshift of the lensed source galaxies to be $z_m = 0.85 \pm 0.05$.

We have used our catalogues of galaxy positions and shear estimates to apply a maximum likelihood analysis, obtaining the shear power spectrum for each COMBO-17 field and for the entire survey. We have measured the κ-field power spectrum expected to arise from gravitational shear, from $\ell = 400$ to 10^4, and have shown that the systematically-induced β-field power spectrum is substantially below our shear signal throughout this ℓ range. We find that the power spectrum for a supercluster field has a significantly higher amplitude than that for random fields, as expected, and we have therefore excluded this field from our final optimally combined result. Simulations of the

maximum likelihood procedure demonstrate that our method is unbiased to within $\sim 10\%$. We have measured the covariance matrix of our shear power spectrum band powers directly from the data and find our band powers to be essentially independent measures of power.

We have also investigated the use of correlation function estimators (*e.g.* SvWKM) for the shear power spectrum and find, in agreement with SvWKM, that their success is dependent on the correlation functions being measured over a large range of scales. Such estimators are therefore difficult to apply to datasets composed of small fields.

We have used our shear correlation function and power spectrum measurements to estimate constraints on the cosmological parameters Ω_m and σ_8. We have made χ^2 fits of our measurements to predicted functions for various values of these cosmological parameters, and we measure the amplitude of the mass power spectrum, from our shear power spectrum results to be $\sigma_8 \left(\frac{\Omega_m}{0.3}\right)^{0.49} = 0.72 \pm 0.09$ with $0.10 < \Omega_m < 0.63$, including uncertainties due to statistical noise, sample variance, and redshift distribution.

We have demonstrated the potential of including photometric redshift information by constraining these cosmological parameters with only those galaxies with assigned redshifts. For this calculation, we have input the actual measured redshift distribution into the theoretical predictions and have compared the resulting constraints with those that would be obtained with only an estimate of the median redshift of the survey. We thus demonstrate the dramatic increase in precision obtained by including accurate redshift information for the source galaxy distribution.

We have combined our constraints with those from the 2dF Galaxy Redshift Survey, and the latest CMB experiments, finding a power spectrum normalisation of $\sigma_8 = 0.73^{+0.06}_{-0.03}$ and a matter density of $\Omega_m = 0.27^{+0.02}_{-0.01}$.

These results (for both the lensing alone, and for the combined constraints) are lower than previous constraints found from cosmic shear surveys (*e.g.* Bacon et al. 2002, Refregier et al. 2002, Van Waerbeke et al. 2002, Hoekstra et al. 2002b) which have, until now found power spectrum normalisations of $\sigma_8 \sim 0.85 - 1.0$. However, our measurements are much more in agreement with recent cluster abundance estimates of the power spectrum normalisation (Borgani et al. 2001; Seljak 2002; Reiprich & Böhringer 2002; Viana, Nichol & Liddle 2002, Allen et al. 2002; Schuecker et al. 2003, Pierpaoli et al. 2002) and those found from combining constraints from the 2dFGRS and CMB results (*e.g.* Lahav et al. 2002, Melchiorri & Silk 2002).

During the preparation of this thesis, two other groups have presented cosmic shear results yielding somewhat lower values of σ_8 – Jarvis et al. 2003 measure the shear signal from the 75 sq. degree CTIO survey and find a power spectrum normalisation of $\sigma_8 = 0.71$ while Hamana et al. 2002 have used the Suprime-Cam instrument on the Subaru telescope to measure the cosmic shear signal from 2.1 sq. degs. of deep R band data, with which they constrain the power spectrum normalisation to be $\sigma_8 = 0.69$. The results from both these studies are in excellent agreement with the results presented here.

We have tested our dataset extensively for systematic effects by measuring galaxy cross-correlations, star-galaxy correlations and by decomposing the cosmic shear signal into its constituent curl and curl-

free modes. However, we have found our dataset to be largely free of any systematic effect that could account for the discrepancy found between our parameter constraints and those obtained from previous weak lensing studies. One factor, which must be important, is the increased understanding of the source redshift distribution which we have gained from the 17-band photometric information contained in the COMBO-17 survey. With the increase in area of cosmic shear surveys in the future, this type of redshift information is likely to become vital as the uncertainties due to the redshift distribution become dominant over other sources of error such as shot noise and sampling variance.

CHAPTER 4

Intrinsic Shape Alignments in the SuperCOSMOS Sky Survey

In Chapter 3 we have conducted a maximum likelihood reconstruction of the weak lensing shear power spectrum for the first time. The raw input to this method is, of course, the observed shapes of large numbers of background galaxies and we have, until now, assumed the *intrinsic* shapes of the galaxies to be uncorrelated with one another. However, we have seen in Chapter 2 that the intrinsic shapes of galaxies will be correlated with one another at some level. If this effect is large enough, it could mimic the cosmic shear signal due to large scale structure and could potentially contaminate all cosmic shear studies conducted to date — including the analysis presented in Chapter 3.

In this chapter, we present a measure of the alignment effect in the local Universe, over a range of scales, using digitized photographic data from the SuperCOSMOS Sky Survey. We find for a magnitude cut of $b_J < 20.5$, corresponding to a median galaxy redshift of $z \approx 0.1$, and 2×10^6 galaxies, that the galaxy ellipticities exhibit a non-zero correlation over a range of scales between 1 and 100 arcmin. We detect this correlation in two colours, b_J and R and, most significantly, in the cross-correlation between the two bands, which is less likely to be contaminated by systematics. Considering the low median redshift of the galaxies in the sample and hence the relatively low effective cross-section for lensing of these galaxies by the large-scale structure of the Universe, we propose that we have detected an intrinsic alignment of galaxy ellipticities. We compare our results to recent analytical and numerical predictions made for the intrinsic galaxy alignment and find reasonable agreement. We discuss the importance of these results for measuring cosmic shear from upcoming shallow surveys (*e.g.* Sloan Digital Sky Survey) and we outline how these measurements could possibly be used to constrain models of galaxy formation and/or measure the mass distribution in the local universe.

4.1 Introduction

We have seen in Chapter 2 that considerable interest has been directed towards the measurement and analysis of galaxy ellipticities as a means to estimate shear induced by weak gravitational lensing. On the scale of galaxy clusters, this is now a well-established method, with tools to invert the shear pattern and measure the distribution of Dark Matter. Recently attention has moved to larger scales to measure the cosmological weak shear signal of lensing by large-scale structure and a number of groups made the first consistent detections of the effect in early 2000 (Bacon, Refregier & Ellis 2000; Kaiser, Wilson & Luppino 2000; van Waerbeke et al. 2000; Wittman et al. 2000). Since then, the field has expanded rapidly with extended surveys and more accurate measurements yielding strong constraints on cosmologically important quantities such as the bias of galaxies with respect to the Dark Matter (Hoekstra et al. 2002a) and the normalisation of the matter power spectrum (*e.g.* Chapter 3 of this work; Brown et al. 2003; Bacon et al. 2002; Hoekstra et al. 2002b; Refregier, Rhodes & Groth 2002; Van Waerbeke et al. 2002; Hamana et al. 2002; Jarvis et al. 2003).

Despite the remarkable success of the shear analysis, up until recently very little attention had been paid to the prospect of intrinsic alignments mimicking the gravitational shear signal. As we have seen in Section 2.3, the most likely ways for this to occur is during the tidally induced spin-up of galaxies (Hoyle 1949), where the angular momentum axes, and hence ellipticities, are aligned, or through the alignment of galaxy and halo shapes.

This problem has recently been addressed by a number of groups using a combination of numerical (Heavens, Refregier & Heymans 2000; Croft & Metzler 2001; Jing 2002) and analytic methods (Catelan, Kamionkowski & Blandford 2001, Crittenden et al. 2001; Lee & Pen 2001; Mackey et al. 2002) and we have briefly reviewed these works in Section 2.3. Although these results are in rough agreement, a complete understanding of alignments is less secure, with the main problems lying in understanding the coupling of the tidal and inertial tensors of dark matter halos, and the alignment of galaxies and halos. It is these uncertainties that lead to the spread in amplitude of the models plotted in Fig. 2.12. On the observational side Pen, Lee & Seljak (2000) have recently claimed a weak detection of spin-spin correlations in the Tully catalogue while Lee & Pen (2002) have reported the detection of a correlation between galaxy spin axes and the local tidal shear field in the Point Source Catalog Redshift (PSCz) survey. In this analysis (see also Brown et al. 2002), we have measured the variance of ellipticities of galaxies at low-redshift, where the effect of intrinsic alignments is predicted to be orders of magnitude higher than a lensing effect. These observations may help to distinguish between models for alignments.

4.2 Observational material

The observations used for the analysis are taken from the SuperCOSMOS Sky Survey program (Hambly et al. 2001a). This digitised photographic sky survey consists of Schmidt photographic plates

($6^\circ \times 6^\circ$; plate scale, 1 cm = 11.2′) and covers the entire southern sky (894 individual Schmidt fields) in two colours, b_J and R. The material used in this analysis consisted of 436 Schmidt plates corresponding to $\sim 10,000$ square degrees.[1].

We have constructed an object catalogue (including both stars and galaxies) for the 436 fields by pairing the scanned b_J and R plates. Apart from a small number of large overlap regions near the 0^h boundary in the survey which were used for internal consistency checks (see Section 4.3.4), we created a 'seamless' catalogue from the overlapping plates using the scheme described in Hambly et al. (2001a). This scheme attempts to include the image with the best parameters (and exclude the others) when there is a choice to be made for the same image appearing on more than one plate. Pairing the b_J and R plates has the advantage over single–colour catalogues in that spurious objects on one plate are eliminated. This is particularly important for galaxy studies from Schmidt photographs since these defects are broken up into many co-aligned 'galaxies' by the image analyser. Such a large source of contaminants could potentially ruin any shear analysis.

Regions around bright stars and blended (ie. multiple) images have been excluded from the object catalogue to further eliminate spurious and/or poorly parameterised images. A demonstration of the removal of spurious objects is given in Fig. 4.1. Panel (a) shows the b_J band pixel data in the region of a bright star which is contaminated by diffraction spikes and ghosting. Panel (b) shows all the objects detected using the b_J band image. Panel (c) shows the objects remaining after a (somewhat arbitrary) ellipticity cut of $\varepsilon \leq 0.25$. Panel (d) shows the objects having an R-band pair. Panel (e) shows the objects detected when deblending (separation of multiple images) is not used. Finally, panel (f) shows the objects remaining when regions around bright stars and multiple images are removed. The observations used in this analysis have been 'cleaned' with the same methods used to produce panels (d) and (f). With these procedures applied, we are confident that the vast majority of spurious objects have been removed from the dataset. Further details concerning image parameterisation, classification and photometry are given in Hambly et al. (2001b).

Image parameters included in the final object catalogue generated for this study consisted of (for both the b_J and R bands) celestial co-ordinates, local plate co-ordinates, second–order moments (semi–major/minor axes and celestial position angle, see Section 4.3.1), b_J and R magnitudes, (b_J–R) colour, image classification flag and stellarness index. Hambly et al. (2001b) have investigated the detection efficiency and external reliability of the image classification by comparing with the observations of Carter (1980). Their findings are summarised in Table 4.1, showing that for the magnitude cut of $b_J < 20.5$ which we have used in this analysis, the SSS data has $> 97\%$ completeness and $> 92\%$ image reliability. Photometric accuracy for galaxies is around 0.25 mag (Hambly et al. 2001b). The internal consistency and accuracy in image ellipticity parameters is demonstrated later in Section 4.3.4.

[1]Full details and online access to the data are available via the World Wide Web at URL `http://www-wfau.roe.ac.uk/sss`

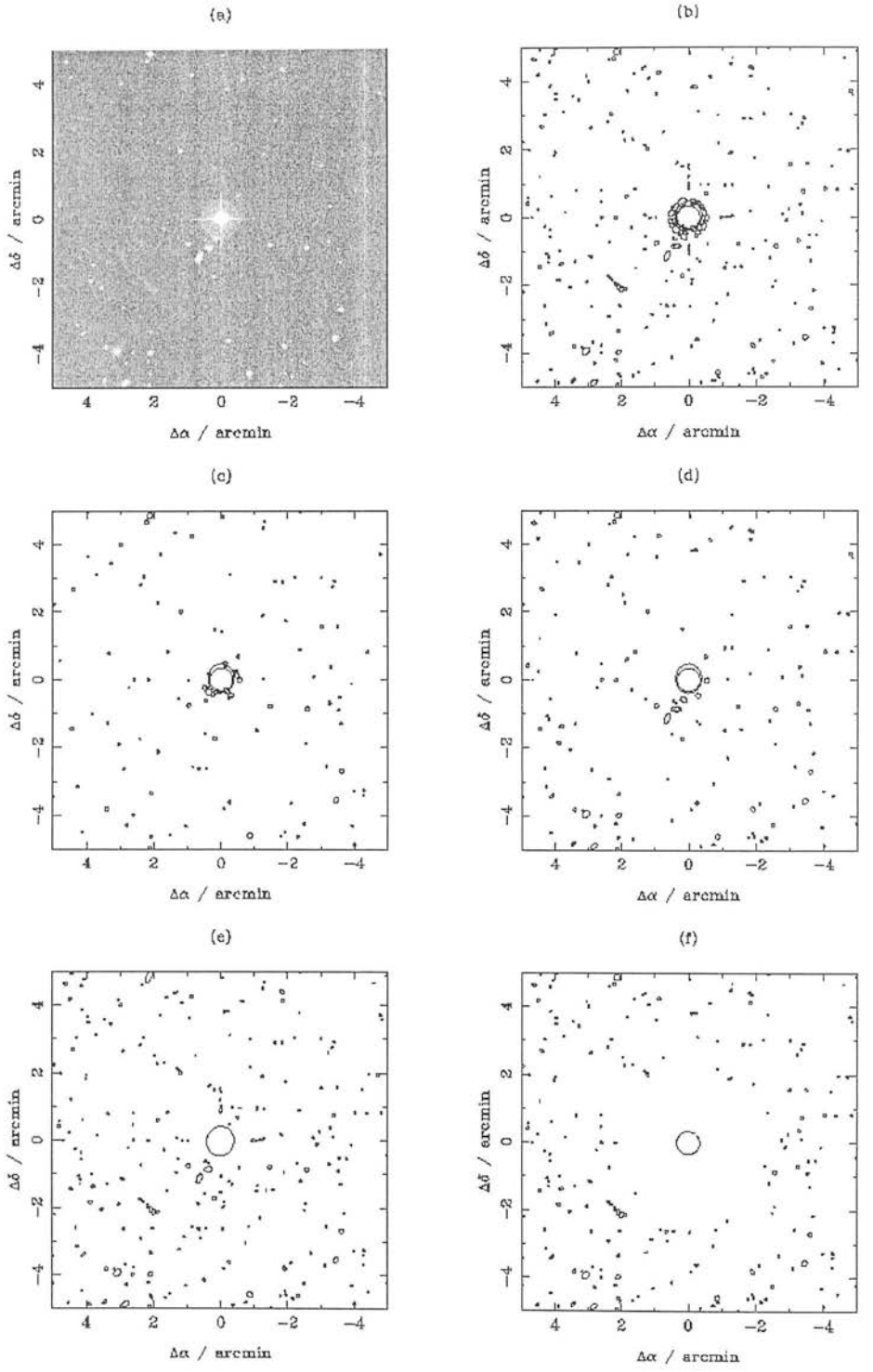

Figure 4.1: Removal of spurious objects near a bright star: (a) the b_J-band pixel data; (b) all objects detected; (c) objects remaining after an ellipticity cut $\varepsilon \leq 0.25$; (d) objects having an R-band pair; (e) objects remaining when deblending is not used, and (f) objects remaining after a quality flag is used to exclude all detections in the vicinity of the bright star. (From Hambly et al. 2001a.)

Table 4.1: Comparison of the galaxy sample of Carter (1980) against the corresponding SSS b_J data as compiled by Hambly et al. 2001b. For the magnitude cut of $b_J \leq 20.5$ which we have used in this analysis, this indicates a completeness $\gtrsim 97\%$ and a reliability of $\gtrsim 92\%$.

Magnitude range	No. of gals in Carter (1980)	No. of objects found in SSS	No. classed as galaxies	No. classed as stellar	Completeness %	Reliability %
$16.5 < b_J < 17.5$	3	3	3	0	100.0	100.0
$17.5 < b_J < 18.5$	28	28	28	0	100.0	100.0
$18.5 < b_J < 19.5$	92	91	91	0	98.9	100.0
$19.5 < b_J < 20.5$	180	174	160	14	96.7	92.0
$20.5 < b_J < 21.5$	307	302	227	75	98.4	75.2
$21.5 < b_J < 22.5$	584	515	253	262	88.2	49.1
$22.5 < b_J < 23.5$	350	149	57	92	42.6	38.3

4.3 Analysis methods

4.3.1 Measuring the ellipticities

In order to measure the intrinsic alignment of galaxies, we first divide the survey into square cells of angular side length, θ. We define the mean ellipticity of galaxies within each cell, $\bar{\varepsilon}_i$, as

$$\begin{aligned} \bar{\varepsilon}_{1,i} &= \frac{1}{N}\sum_{j=1}^{N}\varepsilon_{1,j}, \qquad \bar{\varepsilon}_{2,i} = \frac{1}{N}\sum_{j=1}^{N}\varepsilon_{2,j}, \\ \bar{\varepsilon}_i^2 &= \bar{\varepsilon}_{1,i}^2 + \bar{\varepsilon}_{2,i}^2, \end{aligned} \tag{4.1}$$

where N is the number of galaxies in the i^{th} cell and $\varepsilon_{1,j}$ and $\varepsilon_{2,j}$ are the ellipticity components of the j^{th} galaxy which are defined with respect to the cell axes as

$$\varepsilon_{\alpha,j} = \frac{a_j^2 - b_j^2}{a_j^2 + b_j^2}\begin{cases} \cos 2\varphi_j & \alpha = 1 \\ \sin 2\varphi_j & \alpha = 2 \end{cases}. \tag{4.2}$$

Here, a and b are the semi-major and semi-minor axes of the galaxy and φ is the orientation of the semi-major axis with respect to the cell axes. The weighting scheme used is $w(\theta) = H(I(\theta) - I_{\rm th})$ where $I(\theta)$ is the measured intensity at position θ, $I_{\rm th}$ is a threshold intensity corresponding to the sky background and H is the Heaviside step function. That is, the SuperCOSMOS analyser measures second moments for each object detected as (Stobie 1986)

$$\begin{aligned} Q_{xx} &= \int d^2\theta\, w(\theta)I(\theta)(\theta_x - \bar{\theta}_x)^2 / \int d^2\theta\, w(\theta)I(\theta), \\ Q_{xy} &= \int d^2\theta\, w(\theta)I(\theta)(\theta_x - \bar{\theta}_x)(\theta_y - \bar{\theta}_y) / \int d^2\theta\, w(\theta)I(\theta), \\ Q_{yy} &= \int d^2\theta\, w(\theta)I(\theta)(\theta_y - \bar{\theta}_y)^2 / \int d^2\theta\, w(\theta)I(\theta), \end{aligned} \tag{4.3}$$

where $\bar{\theta}_x$ and $\bar{\theta}_y$ are the centroids of the object and are given by

$$\begin{aligned} \bar{\theta}_x &= \int d^2\theta\, \theta_x w(\theta)I(\theta) \Big/ \int d^2\theta\, w(\theta)I(\theta), \\ \bar{\theta}_y &= \int d^2\theta\, \theta_y w(\theta)I(\theta) \Big/ \int d^2\theta\, w(\theta)I(\theta)\ . \end{aligned} \tag{4.4}$$

In terms of second moments, the ellipticity components of equation (4.2) are

$$\begin{aligned} \varepsilon_1 &= \frac{Q_{xx} - Q_{yy}}{Q_{xx} + Q_{yy}}, \\ \varepsilon_2 &= \frac{2Q_{xy}}{Q_{xx} + Q_{yy}}. \end{aligned} \tag{4.5}$$

The weighting scheme used corresponds to measuring unweighted second moments within an isophotal threshold for all the objects detected. We have varied this threshold limit and have found the resulting measurements to be largely insensitive to the isophotal threshold used (see Section 4.4.2). To quantify the degree of alignment of the cell ellipticities, we calculate the variance of ξ on a given scale across the entire survey. Since this statistic has been used to measure cosmic shear (*e.g.* Bacon et al. 2000, Kaiser et al. 2000), we can directly compare the contributions of intrinsic and extrinsic galaxy alignments. In order to obtain an accurate estimate of ξ_i for a cell, a number of corrections to the raw image catalogue are required. We now describe the sources of error on the ellipticity measurements of galaxies and the corrections we have applied to the dataset.

4.3.2 Correction for PSF anisotropy

There are several possible sources of error which could potentially compromise any shear analysis. These distortions result in spurious ellipticities for all the objects detected and must be removed before a shear analysis can be performed. Firstly, there may be slight astrometric distortions present in the dataset due to emulsion shifts in the photographic plates. However, these should be negligible — the dataset we have used has very precise astrometry and has been used as a standard for making astrometric corrections in other shear analyses (*e.g.* Gray et al. 2002). We have therefore not corrected for astrometric distortions in this analysis. For a detailed discussion of the astrometric accuracy of the catalogue, see Hambly et al. (2001c).

The first correction we have made to the dataset is a correction for anisotropy in the point spread function (PSF). The are several sources of error contributing to the PSF anisotropy. Atmospheric dispersion along with emulsion shifts and mechanical plate distortions, are minor contributors to the PSF anisotropy. By far the most important factors, however, are tracking errors and field rotation (for an analysis of the alignment, pointing accuracy and field rotation of the UK Schmidt Telescope, see Wallace & Tritton (1979); further details of the telescope optics are given in Wynne (1981)). These effects combine to produce a systematic PSF anisotropy pattern across each plate which needs to be corrected for before the galaxy ellipticity measurements can be trusted. We have done this by comparing with the ellipticity field for the stars. Stars should have no intrinsic ellipticity and so the measured stellar ellipticities are due to the PSF anisotropy. As shown in Kaiser, Squires & Broadhurst (1995, hereafter KSB) and discussed in Chapter 2, the perturbation to the galaxies' ellipticity components is given by

$$\delta\varepsilon = P^g_{\rm sm}\, p, \tag{4.6}$$

where $P^g_{\rm sm}$ is the "smear polarisability tensor" which describes the response of the individual galaxy images to the PSF anisotropy, p which in turn can be measured from the stars. The analysis described in KSB, which is for a general weighting of quadrupole moments, is to measure the quantities, $P^g_{\rm sm}$ for each individual galaxy and p from the foreground stars and to apply the correction in equation (4.6) to the individual galaxies.

The weighting scheme used in this analysis is the Heaviside step function, $w(\theta) = H(I(\theta) - I_{\rm th})$.

In the limit where the threshold intensity, $I_{\rm th} \rightarrow 0$, this weighting scheme reduces to measuring unweighted second moments. Later in this chapter, in Section 4.4.2, we investigate the effect of varying the value of $I_{\rm th}$ on the resulting galaxy ellipticity measurements. The general conclusion from these tests is that the galaxy ellipticity measurements are relatively insensitive to changes in the value of $I_{\rm th}$ used and so for the purposes of the PSF correction, we have approximated our quadrupole moment measurements as unweighted quadrupole moments.

This approximation simplifies the PSF correction considerably since, in the case of unweighted moments, $P^g_{\rm sm}$ is diagonal with $P^g_{11} = P^g_{22}$ being a measure of the inverse galaxy size and the KSB correction reduces to

$$\delta\varepsilon = \frac{Q^*_{xx} + Q^*_{yy}}{Q_{xx} + Q_{yy}}\,\varepsilon^*, \tag{4.7}$$

where the Q^*'s and the Q's are stellar and galaxy second moments respectively and ε^* are the measured stellar ellipticity components. In terms of semi-major and semi-minor axes, this becomes

$$\delta\varepsilon = \frac{a^{*2} + b^{*2}}{a^2 + b^2}\,\varepsilon^*, \tag{4.8}$$

where again, the superscript refers to the stars.

We have applied the correction in equation (4.8) to individual galaxy ellipticities using cell-averaged measurements for the "stellar size" ($a^{*2} + b^{*2}$), and where the ε^*'s are the stellar ellipticity components in the cell. The size of the cells used for this correction was 10×10 arcmin^2.

To perform the correction, the plates are gridded up and an average stellar ellipticity is calculated for each cell in the grid. This ellipticity field is then Gaussian smoothed across the plate. Different smoothing scales were investigated in order to find an optimum value. The resulting measurements however did not change significantly for smoothing scales between 10 and 30 arcmin. The individual galaxy ellipticities are then corrected according to equation (4.8). If the grid used for smoothing is too small, a coherent distortion pattern cannot be made and an essentially random pattern is generated. Fig. 4.2 illustrates the b_J band stellar ellipticities on three plates before and after this correction. A strong, coherent distortion of $\bar{\varepsilon} \approx 10^{-2}$ is corrected to produce a random ellipticity pattern with mean $\bar{\varepsilon} \approx 10^{-4}$. Fig. 4.3 shows a scatter plot of the ellipticities (ε_1 vs. ε_2) for both stars (left-hand side) and galaxies (right-hand side) before (dots) and after (crosses) correction. Each point corresponds to a cell, with an ellipticity value given by equation (4.2), and an uncertainty given by equation (4.15).

To test the success of the PSF correction further we calculated the linear correlation coefficients of the cell-averaged stellar and galaxy ellipticity components (*cf.* Bacon et al. 2000),

$$C_\alpha = \frac{\langle \varepsilon^*_\alpha \varepsilon_\alpha \rangle - \langle \varepsilon^*_\alpha \rangle \langle \varepsilon_\alpha \rangle}{\sigma(\varepsilon^*_\alpha)\sigma(\varepsilon_\alpha)}, \tag{4.9}$$

where ε^*_α and ε_α are the cell-averaged stellar and galaxy ellipticity components respectively and $\sigma(\xi^*_\alpha)$ and $\sigma(\varepsilon_\alpha)$ are the errors on those two quantities as measured from the data. In Fig. 4.4, we plot C_1 and C_2 as measured from the total dataset after correction for PSF anisotropy along with the 3σ

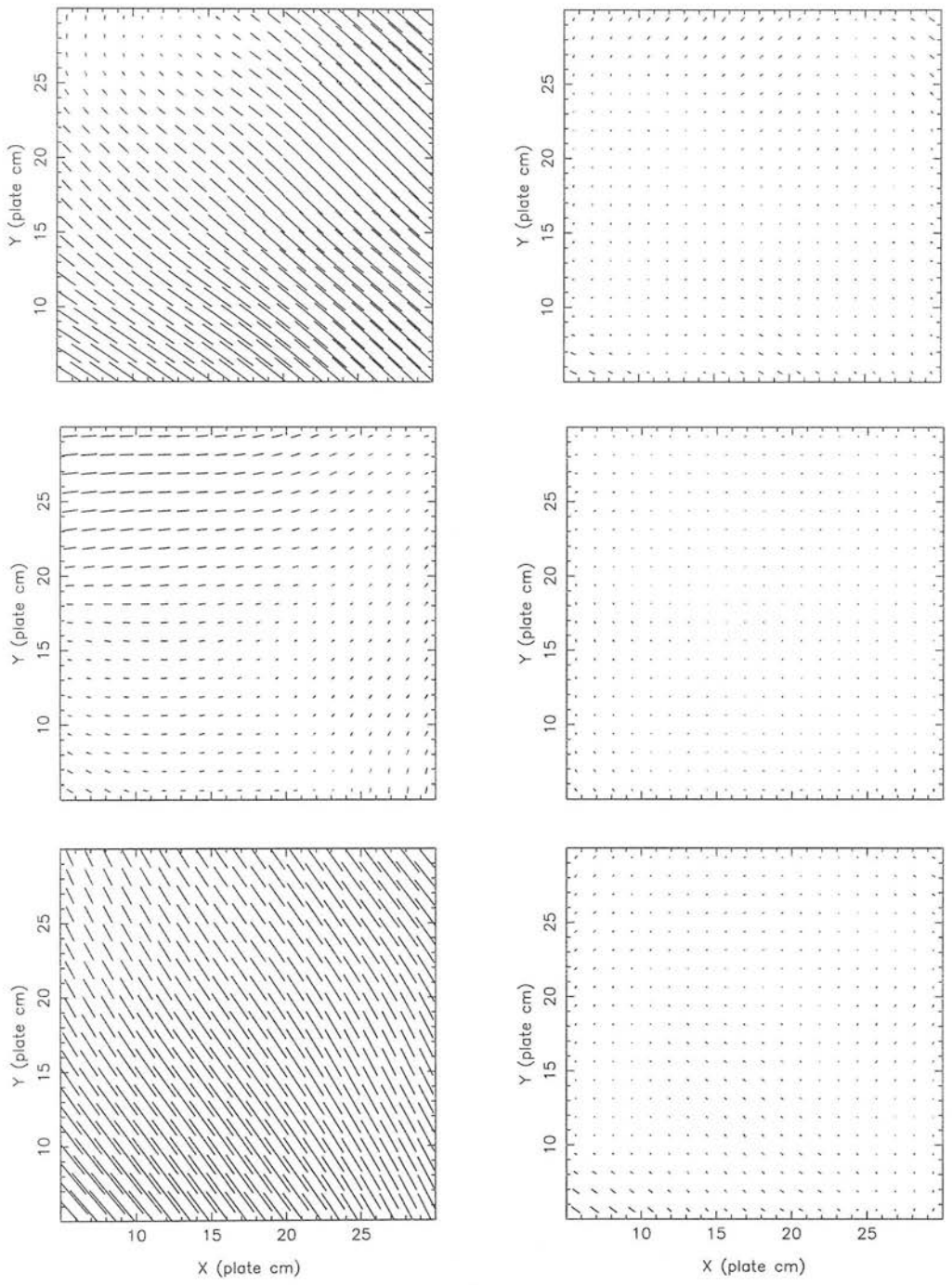

Figure 4.2: Ellipticity fields for raw (left-hand side) and corrected (right-hand side) stars for three of the b_J-band SuperCOSMOS fields. Each field is approximately 32 square degrees in area with a plate scale of 1 cm $= 11.2$ arcmin. Stars are binned into cells of a side 10 arcmin and smoothed with a Gaussian with a smoothing scale 15 arcmin. For each plot, the length of each vector drawn is 25 cm times the measured cell ellipticity. The average ellipticity in a cell in the raw fields is $\bar{\varepsilon} \approx 10^{-2}$, while the average ellipticity in a corrected cell is $\bar{\varepsilon} \approx 10^{-4}$. These plots are typical for the PSF anisotropy distributions on a plate and the corresponding R-band plots are generally very similar.

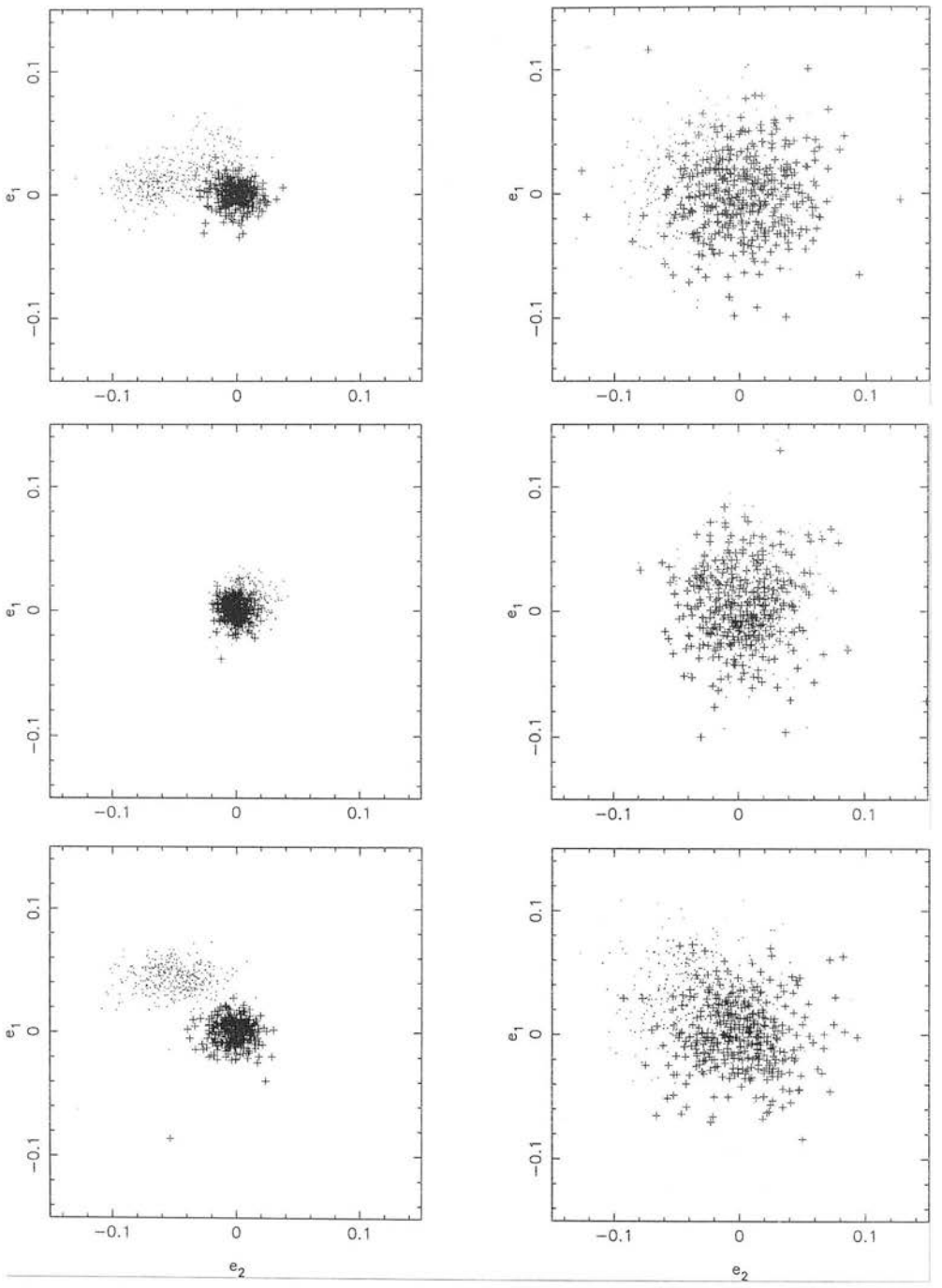

Figure 4.3: Ellipticity distribution per cell (stars on the left, galaxies on the right) for the same three b_J-band fields shown in Fig. 4.2. The dots are the raw stars/galaxies, the crosses the corrected values. Each cell has an ellipticity estimated from equation (4.2) and has an uncertainty given by equation (4.15). Average stellar distortions in the raw fields of $\bar{\varepsilon}_1 \sim \bar{\varepsilon}_2 \approx 10^{-2}$ are corrected to produce flattened stellar ellipticity distributions with residual ellipticities, $\bar{\varepsilon}_1 \sim \bar{\varepsilon}_2 \approx 10^{-4}$. Similar "before" and "after" distributions are found for the R plates.

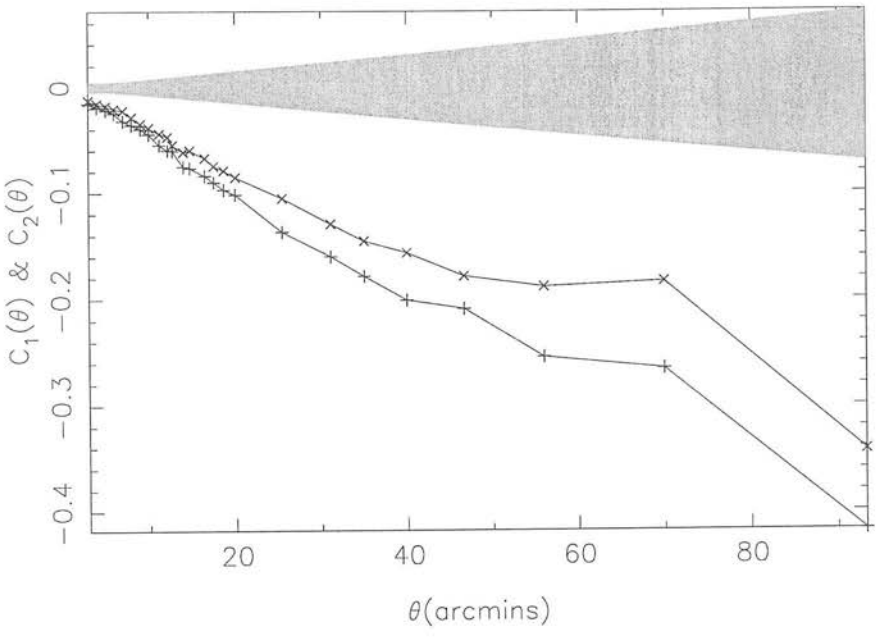

Figure 4.4: The linear correlation coefficients, C_1 and C_2 of the cell-averaged stellar and galaxy ellipticity components as described in the text, after correction for PSF anisotropy. The shaded region is the 3σ significance level.

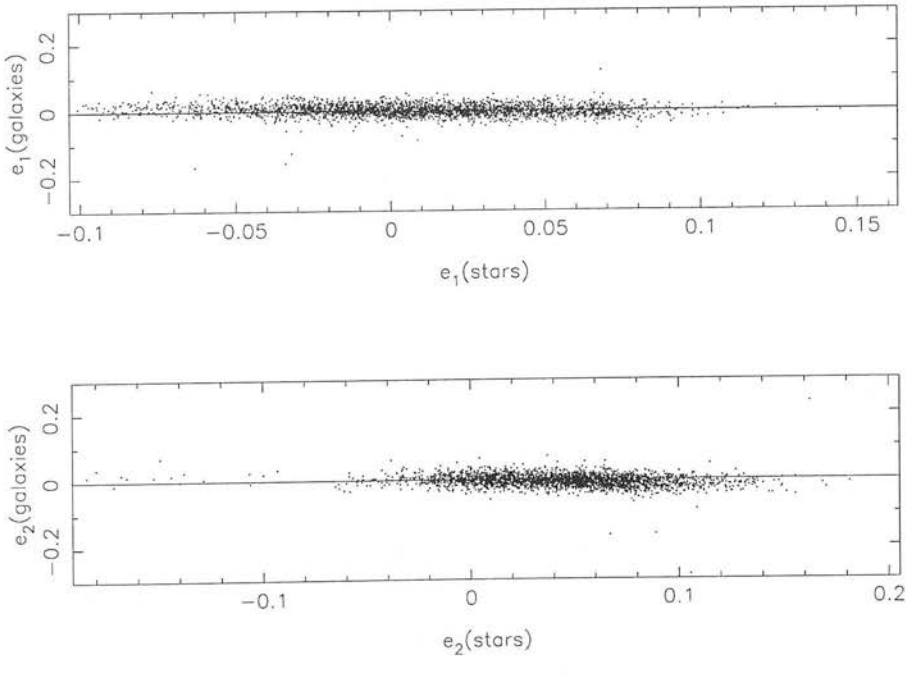

Figure 4.5: The observed anti-correlation of corrected galaxy cell ellipticity components (ε_1 on top, ε_2 on bottom) with the corresponding observed stellar ellipticities.

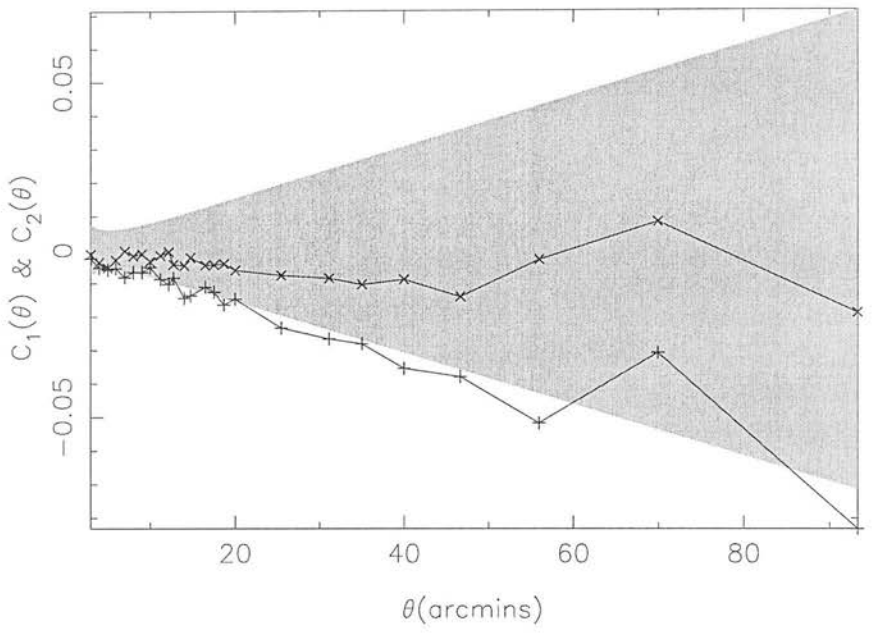

Figure 4.6: C_1, C_2 and the 3σ significance level after excluding all galaxies with sizes, $\theta_g < 0.8\,\langle\theta_g\rangle$ from the catalogue.

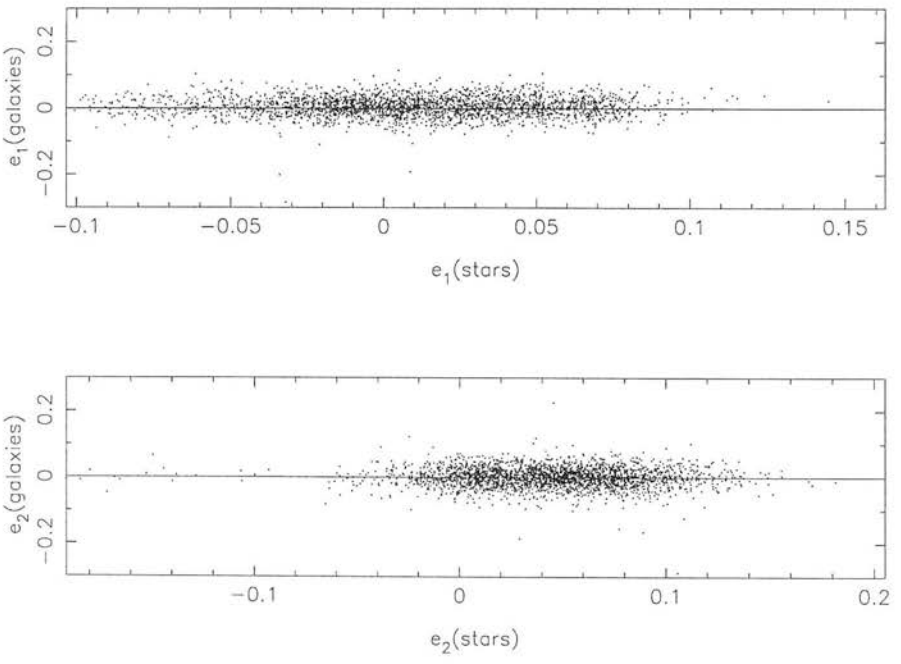

Figure 4.7: Cell-averaged galaxy ellipticity components (ε_1 top, ε_2 bottom) plotted as a function of the corresponding stellar ellipticities after applying the galaxy size cut described in the text.

significance level. It can be seen from this figure that there is a clear anti-correlation between the corrected galaxies and the raw stars and furthermore, it is a $\gg 3\sigma$ effect, especially at large bin sizes. This anti-correlation is clearly seen in Fig. 4.5 where we plot the corrected galaxy and raw stellar ellipticity components for a bin size of $\theta = 70$ arcmin. This anti-correlation is the same effect seen in the cosmic shear analysis of Bacon et al. (2000) and is due to an over-correction of the PSF anisotropy for small galaxies. To remove this effect, we have imposed a cut on galaxy size, only taking galaxies with $\theta_g > 0.8\,\langle\theta_g\rangle$, where $\theta_g = a^2 + b^2$ is the individual galaxy size, and $\langle\theta_g\rangle$ is the mean galaxy size over the whole survey. Only galaxies satisfying this condition have been used in the final analysis. The correlation coefficients, equation (4.9), calculated after applying this cut, are shown in Fig. 4.6. It is clear from this plot that the star-galaxy anti-correlation is much less significant with the cut on galaxy size applied. This can be seen by eye in Fig. 4.7 where the corrected galaxy and raw stellar ellipticity components are plotted after applying the cut on galaxy size, again for a bin size of 70 arcmin.

4.3.3 Seeing correction

After correcting for PSF anisotropy, we model all other sources of error (atmospheric turbulence, wind shake etc.) as random effects. Collectively called seeing, we assume also it is isotropic and we apply a correction to remove its effects. The effect of seeing on the galaxy ellipticities is to circularize the images, causing a decrease in ellipticities. The seeing across all of the plates is typically $2''$. This is comparable to the size of a galaxy near the magnitude limit of our survey ($b_J < 20.5$) and thus, needs to be corrected for before the galaxy ellipticities can be trusted.

For the seeing correction, we again approximate our galaxy ellipticity measurements (which are unweighted within an isophotal threshold) as unweighted ellipticities (see Section 4.4.2 for tests of the validity of this approximation). With this approximation, the semi-major and semi-minor axes of each galaxy will transform under the effect of seeing as

$$a_j'^{\,2} = a_j^2 + r_i^2, \qquad b_j'^{\,2} = b_j^2 + r_i^2, \tag{4.10}$$

where (a_j, b_j) and (a'_j, b'_j) are the axes of the j^{th} galaxy before and after the effect of seeing respectively and r_i is the average seeing in the i^{th} plate. The effect of seeing on the measured ellipticities is

$$\varepsilon'_{\alpha,j} = f_{ij}\varepsilon_{\alpha,j}, \tag{4.11}$$

where $\varepsilon'_{\alpha,j}$ is the post-seeing ellipticity and we have defined a "seeing factor" which is, in terms of the observed semi-major and semi-minor axes,

$$f_{ij} = 1 - \frac{2r_i^2}{a_j'^{\,2} + b_j'^{\,2}}. \tag{4.12}$$

Here, a and b are the axes of the galaxies after correction for PSF anisotropy and the uncertainty on

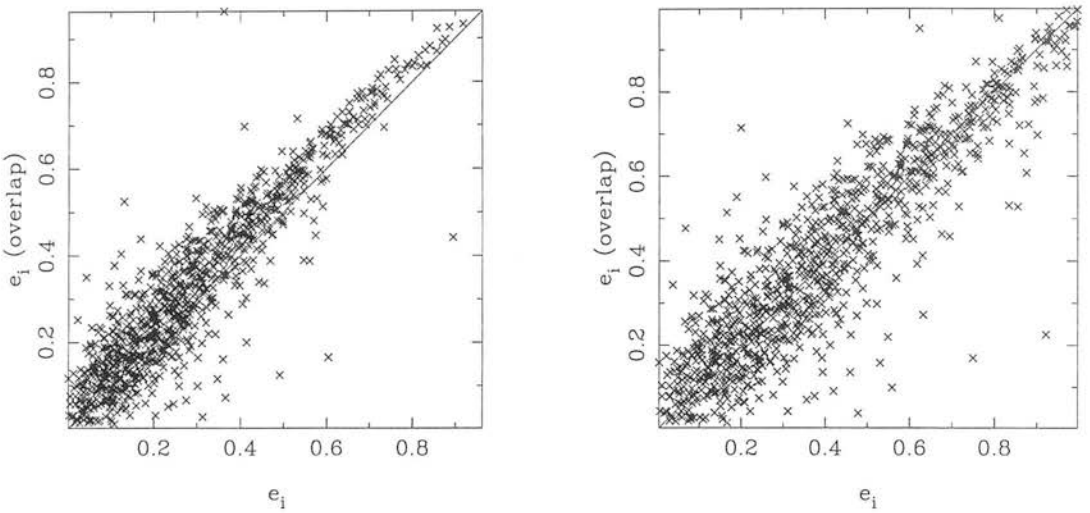

Figure 4.8: Individual galaxy ellipticities measured from overlapping SuperCOSMOS fields. The left-hand panel shows the ellipticity measurements before the seeing correction is applied. The plate plotted on the horizontal scale has greater seeing than the plate plotted on the vertical axis. The right hand panel shows the ellipticities after the correction.

individual galaxy sizes was too large after this correction to use equation (4.11) directly. Instead we estimated an effective galaxy size for all plates for a given flux cut. We have done this by looking at plate overlap regions. We have applied the correction in equation (4.11) to galaxies in these regions and have "fine tuned" the effective galaxy size so that consistency is achieved in the measurement of both individual and binned galaxy ellipticities between the overlapping plates (see Section 4.3.4). In the case of $b_J \leq 20.5$, the optimum effective galaxy size was $2.5''$, which closely matched the directly measured mean galaxy size. This was then used to correct all the plates, using the measured seeing from each plate.

4.3.4 Internal consistency tests

We have tested the seeing correction of the previous section by comparing ellipticity measurements in the plate overlap regions. The ellipticity measurements for a galaxy in an overlap region as measured on the two overlapping plates should agree to within the limits of the measuring process (the measurement errors are dominated by noise on the original photographs) assuming that we have corrected for the effect of seeing accurately enough.

Figs. 4.8 and 4.9 show the correlation between different plates in the overlap region, after correction for PSF anisotropy, for individual galaxies (Fig. 4.8) and binned cells (Fig. 4.9). The left-hand-side of Figs. 4.8 and 4.9 show the correlation before correcting for seeing. There is an apparent decrease in the ellipticities of the galaxies plotted on the horizontal axis, where the seeing on the plate is larger. The right-hand-side of Figs. 4.8 and 4.9 show the correlation after correction for seeing. As we are only scaling ellipticities the scatter is slightly increased, but the correlation is significantly greater. These plots are typical for the overlap regions.

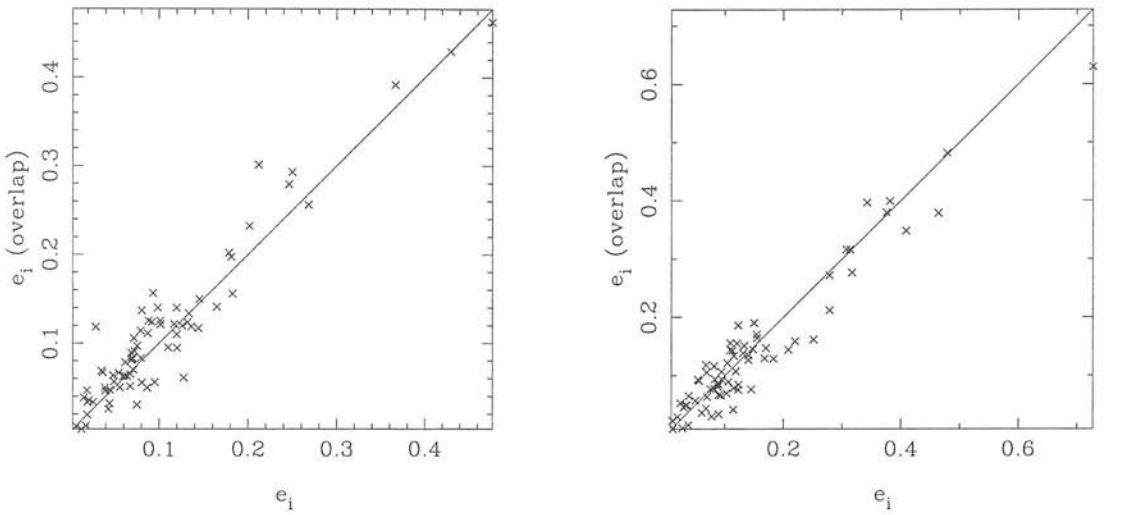

Figure 4.9: Binned cell ellipticities, ε_i measured from the same plates as shown in Fig. 4.8. The left- and right-hand panels are the measurements before and after the seeing correction is applied respectively.

4.3.5 Comparison with APM Sky Catalogue data

To check our results further, we have performed a comparison test for similar alignments in APM data[2] in order to test for any systematic effects introduced by the SuperCOSMOS scanning procedure. We took a J-R paired star/galaxy catalogue from the APM survey for one field and paired it up with the SuperCOSMOS data. Since the APM data is derived from a copy of the plate that SuperCOSMOS has scanned, any discrepancies in the scanning procedure should be highlighted by this test. Although the weighting for galaxy shapes is different, being density rather than intensity weighted, the magnitude cut is low enough that the difference should not matter. Fig. 4.10 shows a scatter plot for individual galaxy ellipticities for a plate on both SuperCOSMOS and APM surveys, and for the binned data, indicating a strong agreement between the surveys. Having checked for internal and external consistency in the ellipticity catalogue, we now turn to estimating the variance of the ellipticities in cells of varying scale, across all of the plates.

4.3.6 Estimator for the ellipticity variance

The variance of the cell ellipticities can be expressed as the sum of the contributions from all possible sources of alignment (*e.g.* Bacon et al. 2000)

$$\sigma^2_{\rm tot} = \sigma^2_{\rm lens} + \sigma^2_{\rm int} + \sigma^2_{\rm noise} + \sigma^2_{\rm sys} \tag{4.13}$$

where we have included the contributions from lensing, intrinsic alignments, shot noise and systematics. We assume in what follows that the lensing signal is negligible compared to that from intrinsic

[2]available on `http://www.ast.cam.ac.uk/~mike/apmcat/`

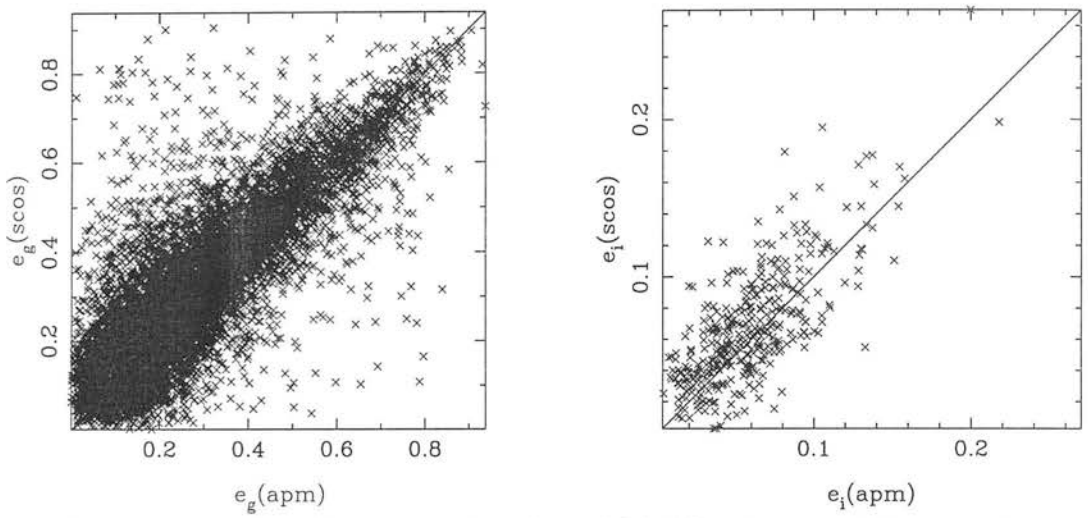

Figure 4.10: Left-hand side: Scatter plot of the SuperCOSMOS galaxy ellipticities on a plate against those from the APM galaxy survey. Right-hand side: The same as the left-hand side but for binned cells.

alignments for the median redshift of the galaxies in our sample ($z \approx 0.1$). The noise term, $\sigma^2_{\rm noise}$ is due to intrinsic scatter in galaxy ellipticities and the random error in the measurement of the galaxy ellipticities. Since we are averaging over a very large area of sky (436 plates covering $\approx 10,000$ sq. degrees with $\approx 2 \times 10^6$ galaxies), we can expect to beat this term down statistically. The final term in equation (4.13) is due to systematic sources of error. In Section 4.3.4, we demonstrated the internal consistency of the catalogue, indicating that contributions to this term from variations in the catalogue are small. Further tests are presented in Section 4.4.2.

We have used a minimum variance estimator for the intrinsic ellipticity variance, $\sigma^2_{\rm int}$ due to intrinsic alignments in excess of the noise,

$$\sigma^2_{\rm int} = \frac{\sum_i w_i(\varepsilon_i^2 - \mathcal{N}_i)}{\sum_i w_i}, \tag{4.14}$$

where $\mathcal{N}_i$ is the random noise on the estimated cell ellipticity, ε_i, in the i^{th} cell, and w_i is an arbitrary weighting factor. We use this minimum variance weighting scheme in order to reduce the errorbars on our measurements as a flat weighting results in upper limits for the ellipticity variance only. We assume that the mean cell ellipticity components are zero (see Section 4.4.2). For the moment we will ignore systematic terms. Following the analysis of Van Waerbeke et al. 2000, we estimate the noise term in the i^{th} cell as

$$\mathcal{N}_i = \frac{1}{N^2}\left(\sum_{j=1}^{N}\varepsilon^2_{1,j} + \sum_{j=1}^{N}\varepsilon^2_{2,j}\right), \tag{4.15}$$

where N is the number of galaxies in the cell. For a minimum variance estimator, we wish to choose the weights, w_i such that equation (4.14) is minimised with respect to w_i. Denoting the true intrinsic

ellipticity variance as $\sigma^2_{\rm true}$, this optimal weighting scheme is given by

$$w_i = [\sigma^2(\sigma^2_{\rm true}) + \sigma^2(\mathcal{N}_i)]^{-1} = (2\sigma^4_{\rm true} + 2\mathcal{N}_i^2)^{-1}, \tag{4.16}$$

where $\sigma^2(\sigma^2_{\rm true})$ is the uncertainty on the true ellipticity variance, and $\sigma^2(\mathcal{N}_i)$ is the uncertainty on the estimated noise term. The uncertainty on the true ellipticity variance will be $\sigma^2(\sigma^2_{\rm true}) = \langle\sigma^4_{\rm true}\rangle - \langle\sigma^2_{\rm true}\rangle^2$, and, assuming $\sigma^2_{\rm true}$ to be Gaussian distributed, we have,

$$\begin{aligned}\sigma^2(\sigma^2_{\rm true}) &= \langle\sigma^4_{\rm true}\rangle - \langle\sigma^2_{\rm true}\rangle^2 \\ &\approx 3\langle\sigma^2_{\rm true}\rangle^2 - \langle\sigma^2_{\rm true}\rangle^2 \\ &= 2\langle\sigma^2_{\rm true}\rangle^2. \end{aligned} \tag{4.17}$$

The uncertainty in the noise term can be estimated by noting that the noise contribution from randomly orientated galaxies will be $\mathcal{N}_i = \varepsilon^2_{\rm rms}/N$ where $\varepsilon_{\rm rms}$ is the root mean squared random ellipticity of the galaxies. The variance of the noise is then given by

$$\sigma^2(\mathcal{N}_i) = \langle\varepsilon_g^4\rangle/N^2 - \varepsilon^4_{\rm rms}/N^2,$$

where ε_g is the ellipticity of the individual galaxies in cell i. Assuming a Gaussian distribution for the galaxy ellipticities, we can make the approximation, $\langle\varepsilon_g^4\rangle \approx 3\langle\varepsilon^2\rangle^2 = 3\varepsilon^4_{\rm rms}$ and we have

$$\sigma^2(\mathcal{N}_i) = 2\varepsilon^4_{\rm rms}/N^2 = 2\mathcal{N}_i^2.$$

Combining these variances yields the weighting in equation (4.16). Substituting this into the expression for $\sigma^2_{\rm int}$ yields the minimum variance estimator:

$$\sigma^2_{\rm int} = \frac{\sum_i(\varepsilon_i^2 - \mathcal{N}_i)/(2\sigma^4_{\rm true} + 2\mathcal{N}_i^2)}{\sum_i(2\sigma^4_{\rm true} + 2\mathcal{N}_i^2)^{-1}}. \tag{4.18}$$

The error in this expression is given by

$$\sigma^2(\sigma^2_{\rm int}) = \frac{1}{\sum_i w_i} = \left(\sum_i(2\sigma^4_{\rm true} + 2\mathcal{N}_i^2)^{-1}\right)^{-1}. \tag{4.19}$$

Equations (4.18) and (4.19) form the basis of our analysis.

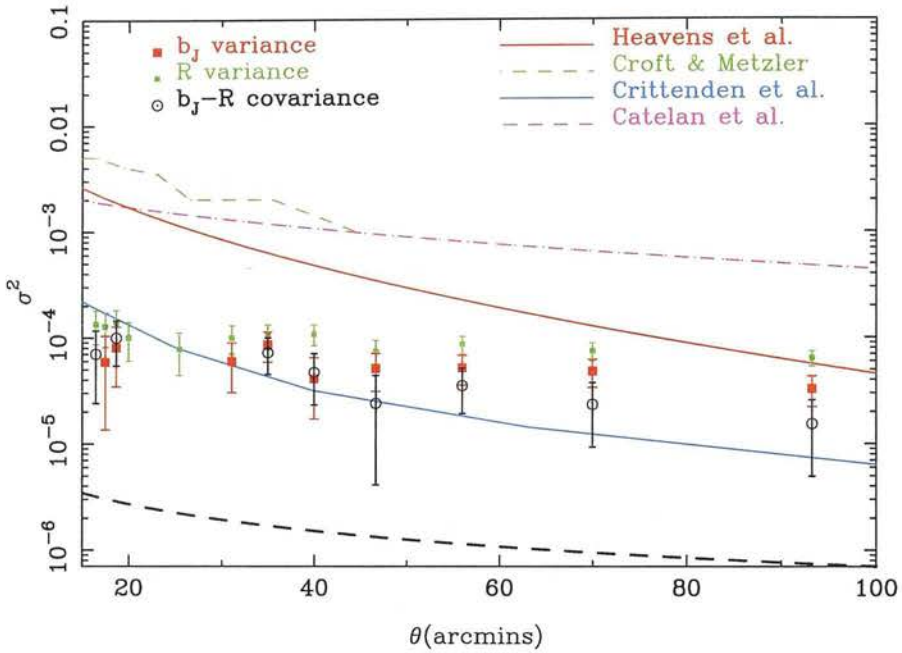

Figure 4.11: Measured ellipticity variance, $\sigma^2_{\rm int}$ over 436 SuperCOSMOS fields as a function of angular scale, θ along with the weak lensing prediction (heavy dashed line) for a ΛCDM model and a median redshift equal to that of our galaxy sample. Also shown are various predictions for the intrinsic signal — see text for details.

4.4 Results

4.4.1 Measurement of the ellipticity variance

We have used equation (4.18) with $\sigma_{\rm true} = 0.01$ to calculate the variance of the intrinsic cell ellipticities, $\sigma^2_{\rm int}$ over a wide range of angular scales. Even so, the results are fairly insensitive to the value of $\sigma_{\rm true}$ used. We have measured both the $\rm b_J$ band variance, $\langle\varepsilon_i(\rm b_J)\varepsilon_i(\rm b_J)\rangle$, and the R band variance, $\langle\varepsilon_i(R)\varepsilon_i(R)\rangle$ as well as the cross-correlation between the two bands, $\langle\varepsilon_i(\rm b_J)\varepsilon_i(R)\rangle$. Here, the angled brackets denote the weighted average as in equation (4.18). Measuring the cross-correlation has the advantage that systematic effects that are uncorrelated between the two bands are canceled out. The results of all these measurements are shown in Fig. 4.11. In the final analysis, we have made use of 1.86×10^6 galaxies for the $\rm b_J$ band variance, 1.97×10^6 for the R band variance and 1.68×10^6 for the covariance measurement. Note that the scale at which the stellar ellipticities are smoothed for the PSF anisotropy correction is 15 arcmin and so, at scales smaller than this, our results may be compromised by residual PSF anisotropy distortions. We have therefore not plotted results below this scale in Fig. 4.11. Beyond this scale, we are confident that our measurements are not dominated by systematics. This assertion is supported by the agreement between the two single band variance measurements and the cross-correlation signal. Further tests for systematics are presented in Section 4.4.2.

In addition to using equation (4.19), we have also estimated the errors on our measurements from

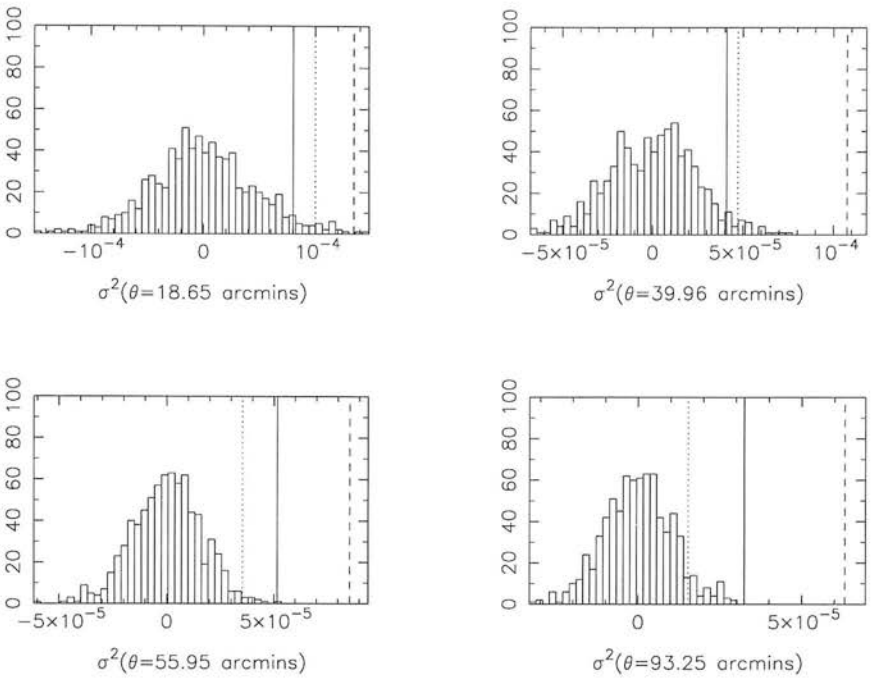

Figure 4.12: The variance measurements from the 1000 randomised catalogues (histograms) along with the measured signal for four different values of the cell side length, θ. In each case, the full line is the b_J band variance, the dashed line is the R band variance and the dotted line is the covariance measured between the two bands.

1000 randomisations of the dataset. In these randomisations, only galaxies used in the final analysis were included. The galaxies were assigned a position angle taken from a random distribution between 0 and 180 degrees while their semi-major and semi-minor axes were left unchanged. Equation (4.18) was then used to measure the ellipticity variance from the 1000 randomised datasets. The resulting distributions of 1000 variance measurements are centered on zero at all scales, indicating that our estimator is unbiased. These distributions are shown in Fig. 4.12, along with the measured signal, for four scales: 19, 40 and 56 and 93 arcmin. The errors on the signal measured from the real dataset were then calculated as the standard deviation of the measurements from the randomised catalogues. These errors agree quite well with the errors calculated using equation (4.19) although those taken from the randomisations are, in general, slightly larger. We have therefore plotted the 1σ errors from the randomisations in Fig. 4.11.

Our measurements are two orders of magnitude larger than the signal expected from weak lensing (see *e.g.* Jain & Seljak, 1997) for a median source redshift of $z \approx 0.1$ corresponding to the magnitude cut of $b_J \leq 20.5$ which we have used in our analysis. In Figure 4.11 we plot our results along with the predicted weak lensing signal for a cluster normalised ΛCDM model, with $\Omega_m = 0.3$ and $\Omega_\Lambda = 0.7$. The discrepancy is exhibited over the entire range of angular scale, θ suggesting that we have not measured extrinsic gravitational lensing.

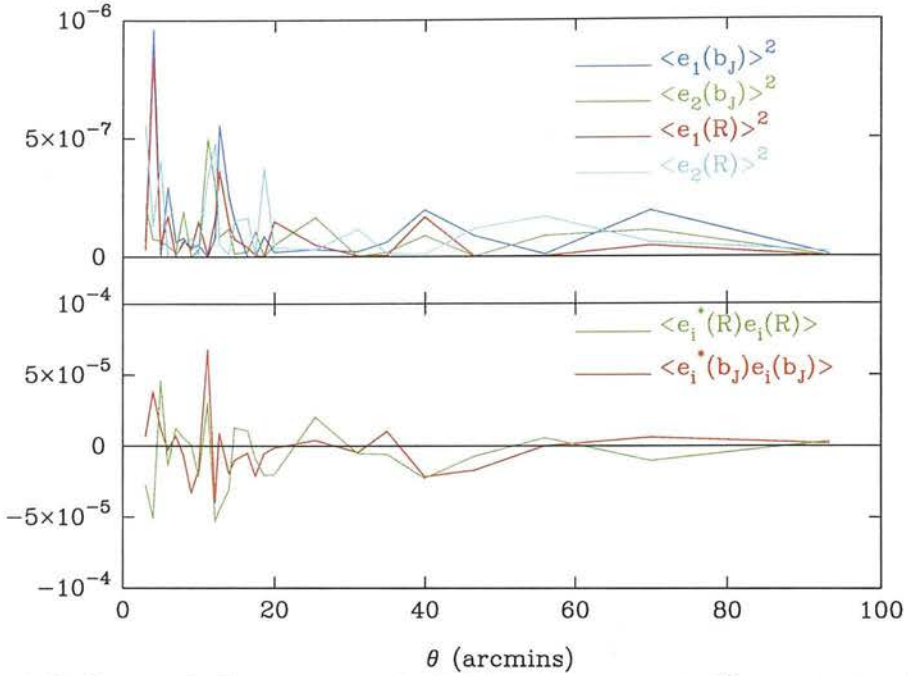

Figure 4.13: Top panel: The average cell ellipticity components, $\langle\varepsilon_\alpha\rangle^2$ over the 436 SuperCOSMOS plates for the $\mathrm{b_J}$ and R bands. Here, ε_α are the average cell ellipticity components *within* a cell and the further averaging is performed over the total number of cells. We plot the result as a function of cell size. Bottom panel: The star-galaxy covariance, $\langle\varepsilon_i^*\varepsilon_i\rangle$ measured over the whole survey for the two bands.

4.4.2 Tests for systematics

To test our results for internal systematics we have estimated the means of the cell ellipticity components averaged over all plates. In Fig. 4.13 we show that the mean fields are negligible ($\langle\varepsilon_\alpha\rangle^2 < 10^{-7}$) on all scales. We have also estimated the star-galaxy covariance,

$$\langle\varepsilon\varepsilon^*\rangle = \langle\varepsilon_1\varepsilon_1^*\rangle + \langle\varepsilon_2\varepsilon_2^*\rangle, \tag{4.20}$$

where ε^* is the stellar ellipticity. This is also shown in Fig. 4.13, and is well below our results ($|\langle\varepsilon\varepsilon^*\rangle| < 10^{-5}$) on all scales, indicating that, after applying the cut on galaxy size (Section 4.3.2), galaxy ellipticities are no longer correlated with stellar values. We have estimated the cross-correlation of ε_1 and ε_2 for the galaxies, $\langle\varepsilon_1\varepsilon_2\rangle$. This is plotted in Fig. 4.14 along with the measured signal for the two single band variance measurements as well as for the shear covariance signal. In all cases, the galaxy cross correlation, $\langle\varepsilon_1\varepsilon_2\rangle$ is consistently below the measured signal. In particular, for the covariance measurement, we have estimated the galaxy cross correlation as

$$\langle\varepsilon_1\varepsilon_2\rangle = \langle(\varepsilon_1(\mathrm{b_J})\varepsilon_2(R) + \varepsilon_1(R)\varepsilon_2(\mathrm{b_J}))/2\rangle \tag{4.21}$$

and this is consistent with zero at the 10^{-9} level on all scales, indicating that $\langle\varepsilon_i(\mathrm{b_J})\varepsilon_i(R)\rangle$ is free of significant residual systematics and is a robust estimate of the galaxy alignment signal.

As a test for systematics introduced by the measuring process we have pushed the APM data

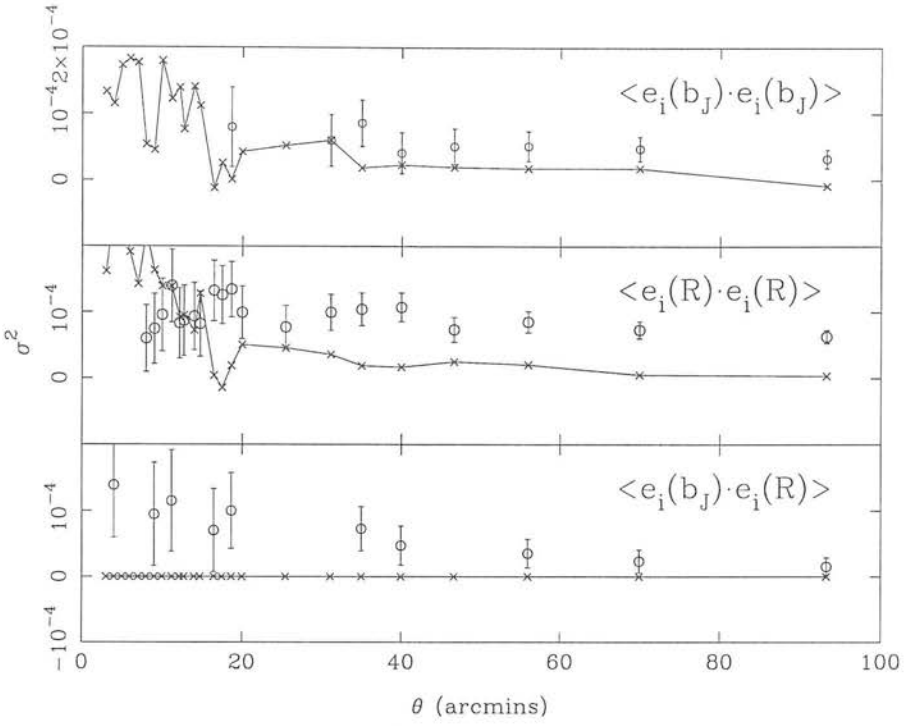

Figure 4.14: The signal measured (points with error bars) in b_J (top), R (middle) and the cross-correlation between the two bands (bottom) along with the cross correlation of ε_1 with ε_2 for the galaxies, $\langle \varepsilon_1 \varepsilon_2 \rangle$ (joined crosses). Note the much higher significance of the shear covariance measurement, $\langle \varepsilon_i(b_J) \varepsilon_i(R) \rangle$ compared with the shear variance measurements from the individual bands alone.

(Section 4.3.5) through our analysis for one plate. In Fig. 4.15 we plot the variance as measured by the two machines for this field. Again we find a very good agreement between both catalogues, suggesting that any systematic effects in our analysis are small, $\sigma^2_{\rm sys} < 10^{-5}$, and below our measurement. This agreement between the catalogues is demonstrated in Fig. 4.16 where the difference in variance measurements from the two surveys is plotted. This difference is consistent with zero on all scales.

As noted in Section 4.3.1, the SuperCOSMOS machine measures unweighted second moments of all objects detected within an isophotal threshold, $I_{\rm th}$. The nominal value of this threshold in the SuperCOSMOS Sky Survey is 2.3σ above the sky background, $I_{\rm sky}$. To further establish the reliability of our ellipticity measurements, we have varied $I_{\rm th}$ about its nominal value for one field and compared the resulting galaxy ellipticity measurements with those from the main analysis for this field. The results of this test are shown in Fig. 4.17 showing that the determination of the galaxy ellipticities is largely insensitive to the isophotal threshold used to measure the object parameters.

4.4.3 Intrinsic alignments

Recent numerical and analytic studies (Heavens et al. 2000; Croft & Metzler 2001; Catelan et al. 2001; Crittenden et al. 2001) have put constraints on the shear signal expected from intrinsic galaxy alignments. As we have seen in Section 2.3, in these studies, the galaxy shape is estimated either from

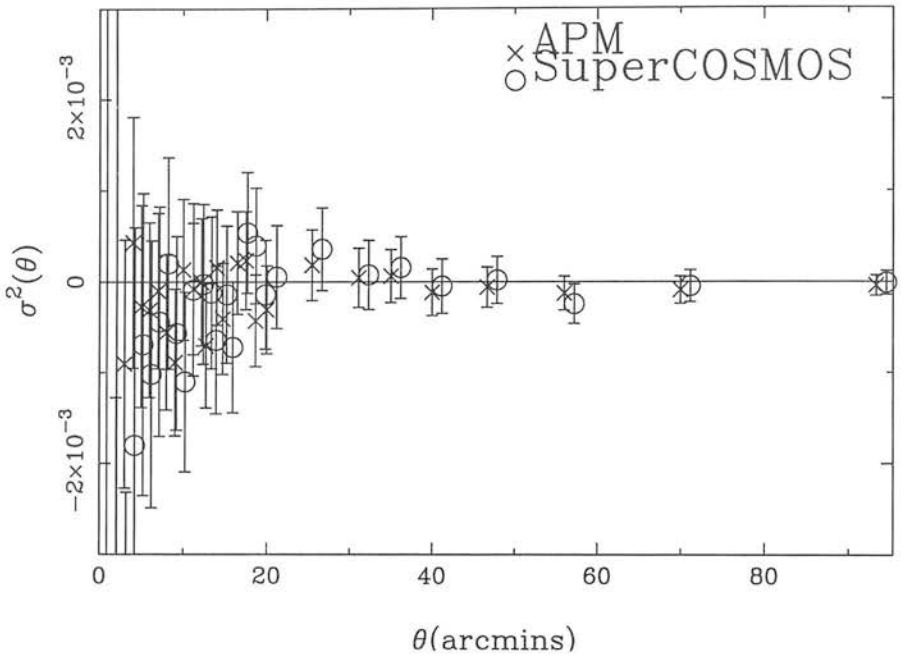

Figure 4.15: Comparison of the SuperCOSMOS variance of ellipticities and the APM variance for one plate (UKST field 78). Note the errors are much larger than in the final analysis due to the much smaller number of galaxies measured. The SuperCOSMOS points have been slightly laterally displaced for clarity.

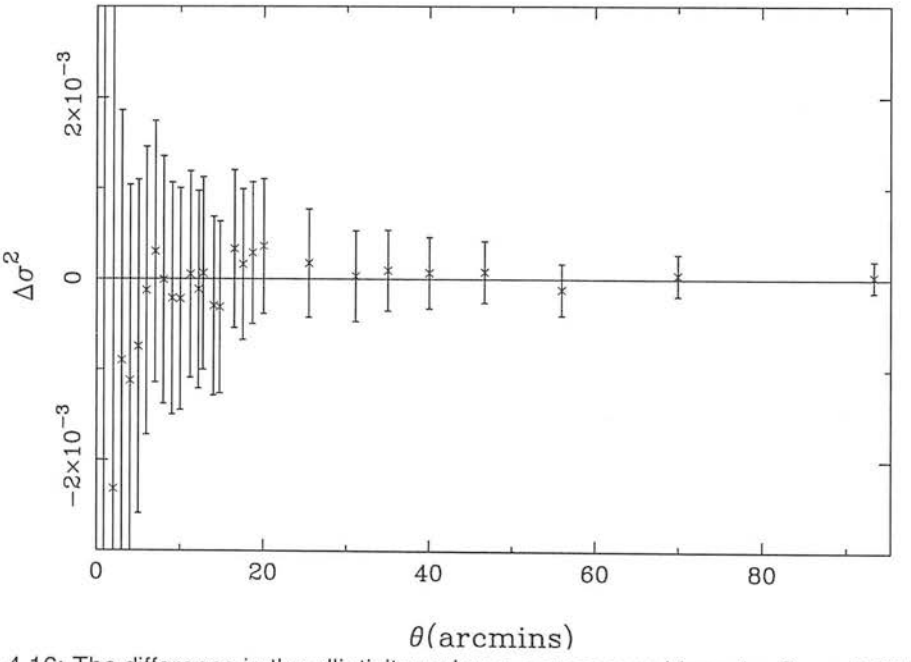

Figure 4.16: The difference in the ellipticity variance as measured from the SuperCOSMOS and APM machines ($\Delta\sigma^2 = \sigma^2_{\rm apm} - \sigma^2_{\rm scos}$) for the same field as shown in Fig. 4.15. The value of $\Delta\sigma^2$ is consistent with zero on all scales indicating that systematic errors introduced by the plate scanning procedure are small.

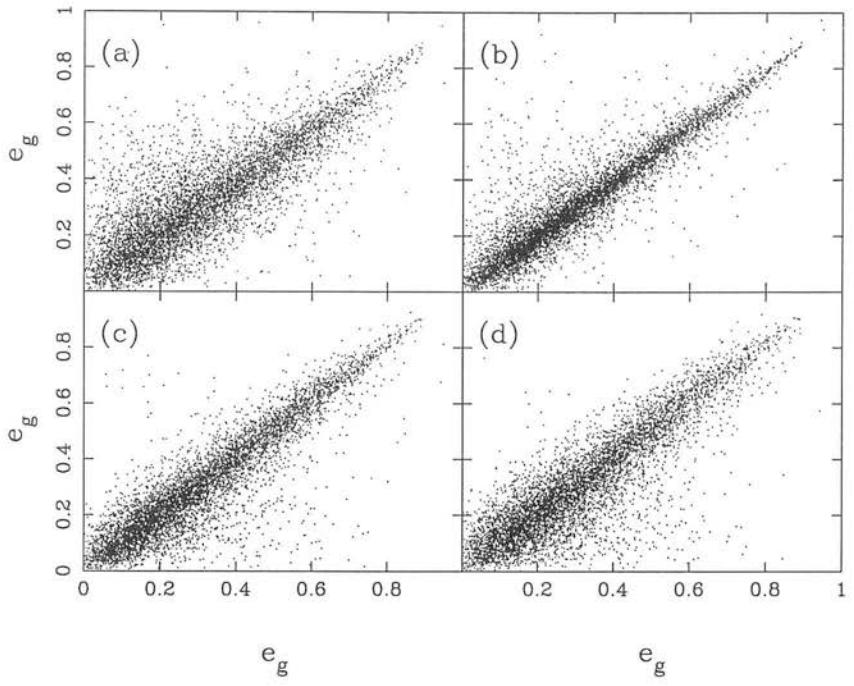

Figure 4.17: Individual galaxy ellipticities as measured from UKST field 78 with different isophotal thresholds applied. In each of the four panels, the horizontal axis measurements are from the Sky Survey data with an isophotal threshold value of 2.3σ above the sky background. The vertical axes measurements have been made using isophotal threshold values of (a) 1.5σ, (b) 2.0σ, (c) 3.5σ and (d) 4.5σ above the sky background.

the perpendicular to the halo angular momentum vector for spirals, or from the shape of the halo for ellipticals.

In Fig. 4.11 we have plotted our results along with the alignment effect estimated from each group. Also shown are results from an extension to the numerical simulations work of Heavens et al. 2000 for the spiral galaxy model at $z = 0.1$ (A. Heavens, private communication). The spread in models can be accounted for by the choice of mechanism and galaxy type, assumptions about alignments between halos and galaxies, correlations between tidal and inertial fields and disc thicknesses. We have used the redshift scaling z^{-2n}, suggested by Crittenden et al. (2001) where n is the slope of the matter correlation function, to scale the results from different redshifts. We have also assumed $\sigma^2(\theta) = 2/(2-n)C(\theta)$, where $C(\theta)$ is the ellipticity correlation function.

Generalising the arguments by Crittenden et al. (2001), at large scales the ellipticity variance should scale as

$$\sigma^2(\theta) \approx Az^{-2n}|1 + (\theta/\theta_0)^2|^{-n}. \tag{4.22}$$

Since our results show that the variance is roughly independent of scale, this suggests that the matter correlation function may be roughly constant on scales $> 4\,h^{-1}\mathrm{Mpc}$. This is in contrast to the galaxy correlation function, which scales as $n = -1.8$. This may indicate that on these scales the clustering pattern of galaxies is different to that of dark matter - although it is more likely that equation (4.22) is an incorrect description of the ellipticity variance scaling due to our poor understanding of the

physical mechanisms which cause intrinsic galaxy alignments.

4.5 Summary

In this chapter we have presented a measurement of the intrinsic alignment effect of galaxies on scales from a few arcmin to 100 arcmin. Using 2 million galaxy ellipticities measured from the digitized SuperCOSMOS Sky Survey, to a depth of $b_J = 20.5$ and median redshift $z = 0.1$ and covering 436 plates or 10,000 sq. deg. in two passbands, we have corrected the data for distortions due to PSF anisotropy and seeing, and applied a new minimum variance estimator to the data.

After applying these corrections to the dataset and excluding the over-corrected small galaxies, we find our measurements are internally consistent, with good agreement in regions where the plates overlap, with effectively zero star-galaxy ellipticity correlations and zero ε_1-ε_2 cross-correlations. The ellipticity variance measurements from the b_J and R passbands agree well with each other and with the cross-correlation between the two bands — further confirmation that systematic effects are small. We have also demonstrated external consistency with the APM sky catalogue data over a restricted region of sky, indicating that we are not contaminated by measurement systematics.

Our resulting estimates of the ellipticity variance over a wide range of scales are two orders of magnitude higher than that expected from gravitational lensing by large-scale structure, but roughly in line with those predicted from intrinsic alignments in the gravitational instability scenario, although the predictions for intrinsic alignments are still uncertain. For instance, it is not clear if the effect is dominated by tidal spin or shape alignments. This agreement suggests that we are not contaminated by internal systematics.

Our results imply that other shallow surveys, such as the Sloan Digital Sky Survey, should measure roughly the same contribution to the total variance from intrinsic alignments and gravitational lensing shear. Since the intrinsic alignment signal is expected to scale as z^{-2} (Crittenden et al. 2001) and the lensing signal as $z^{1.5}$ (Jain & Seljak 1997), on scales between 10 and 100 arcmin, we expect the ratio of intrinsic alignment to gravitational shear to scale as

$$\frac{\sigma^2_{\rm int}}{\sigma^2_{\rm lens}} \approx 10^2 \left(\frac{z}{0.1}\right)^{-3.5}. \tag{4.23}$$

This ratio is unity at around $z \approx 0.37$. Higher redshift surveys, such as the VST Lensing Survey (Taylor et al. 2001b) with $z \approx 1$, will measure gravitational lensing shear.

While one would hope that the correlations between ellipticity, spin and the shear field would allow one to measure the amplitude of the dark matter density field, the spin is also determined by the inertial tensor of the dark matter halo. At present, the relation between shape and the local shear field of halos, and the relationship between galaxy ellipticity and halo shape, introduces a large uncertainty in our understanding of intrinsic shape alignments. However, the flatness of the measured variance of alignments suggests that the matter correlation function is very flat, in contrast to the observed galaxy correlation function. With present and future observations and theory we can hope to resolve these issues.

CHAPTER 5

Conclusions

In this final chapter, the main conclusions of the thesis are summarized. Possible future research work following on from the analyses presented here is also identified and discussed.

5.1 Weak lensing by large scale structure

The central theme of this thesis was the use of weak gravitational lensing measurements to constrain cosmology and, in particular, to investigate the dark matter distribution on cosmological scales. In Chapters 1 and 2, we learned that dark matter was a fundamental and dominant constituent of the Universe and yet, its nature and distribution were still open questions. We also learned that the technique of gravitational lensing is in a unique position in the sense that it directly probes the dark matter distribution. In Chapter 3 we have used this quality of weak lensing to directly probe the dark matter distribution on a range of physical scales between 0.5 and $30\,h^{-1}\mathrm{Mpc}$ using the COMBO-17 multi-band wide-field survey. We have shown the dataset to be unique in terms of weak lensing surveys — the minimal distortions introduced by the WFI instrument and the deep high quality R-band images make the COMBO-17 data particularly suitable for weak lensing measurements. In addition, we have included depth information in a cosmic shear study for the first time by using accurate photometric redshift estimates from the 17 band wide-field survey.

On scales from 0.5 to $30\,h^{-1}\mathrm{Mpc}$, we have made the most direct measurement of the clustering properties of dark matter ever obtained by conducting a full maximum likelihood (ML) reconstruction of the three shear power spectra, $C_\ell^{\kappa\kappa}, C_\ell^{\beta\beta}$ and $C_\ell^{\kappa\beta}$ in 5 band powers from $\ell = 400$ to $\ell = 10^4$ where ℓ is the Fourier variable on the sky. We have conducted these reconstructions individually for the 5 fields of the COMBO-17 survey and we have optimally combined our measurements to yield our final power spectrum estimates. This is the first time an ML approach has been used to measure cosmic shear. In addition to this analysis, we have also conducted a standard cosmic shear analysis by measuring both the shear correlation functions and the shear variance over the entire survey.

Our measurements of $C_\ell^{\kappa\kappa}$ are a *direct measure* of the projected dark matter distribution and so, they can be compared with predictions for various cosmological scenarios. In doing so, we find that our estimates are entirely consistent with the ΛCDM cosmological model whereas our measurements of minimal power in $C_\ell^{\beta\beta}$ and $C_\ell^{\kappa\beta}$ are confirmation of the gravitational origin of the signal. We have also shown that our band power estimates are essentially *independent* measures of power by measuring the covariance matrix of the band power estimates directly from the data.

For the first time in a cosmic shear survey, we have estimated the median redshift of the source galaxies directly from the data using the photometric information in the COMBO-17 survey. We have found that our source galaxies are distributed about a median redshift of $z_m = 0.85$ and we have input this information into the model predictions when comparing with theory. By doing so, we have reduced (to a negligible level) one of the major sources of uncertainty in cosmic shear surveys to date.

We have also used our band power measurements to constrain cosmological parameters. Using our measurements of $C_\ell^{\kappa\kappa}$, we have constrained the normalisation of the matter power spectrum to be $\sigma_8 = (0.72 \pm 0.09)(\Omega_m/0.3)^{-0.50}$ where the errors quoted are 1-σ due to the intrinsic dispersion in galaxy ellipticities, cosmic and sampling variance. We have combined these parameter constraints with those from the 2dF Galaxy Redshift Survey and with those from the CMB. These three different methods are complimentary to one another and we have shown all three to be compatible. Using the

combination of the three experiments, we have constrained the power spectrum normalisation to be $\sigma_8 = 0.73^{+0.06}_{-0.03}$ and the matter density of the Universe to be $\Omega_m = 0.27^{+0.02}_{-0.01}$.

In addition to the simulation work and systematic tests presented in this thesis, we are continuing to investigate potential sources of error in the ML analysis. In particular, a number of assumptions go into the ML band power reconstructions regarding Gaussianity of both the shear field and the noise distribution. We have also assumed the noise to be uncorrelated between pixels. We are currently looking into the implications of these assumptions although they are unlikely to have a dramatic effect on our shear power spectra results.

We are also looking into the possibility of including the A901 supercluster field in the optimally combined spectra. Although this field was pre-selected to include a supercluster and was therefore excluded from our final measurements, it may be possible to weight the A901 power spectra measurements according to the likelihood of finding such a supercluster structure in a randomly selected 0.25 sq. deg. field.

We are also in the process of adapting the ML analysis so that it takes as its raw input the individual galaxy shear distribution rather than the pixelised distribution we have used in the work presented here. This should allow for the removal of physically close pairs of galaxies, thereby suppressing the intrinsic alignment signal expected from these close pairs. It would also allow a κ/β decomposition of the intrinsic alignment signal itself which would be extremely beneficial in discriminating between analytical and numerical models for the intrinsic alignment effect.

The ML approach to cosmic shear measurements which we have pioneered in this thesis opens up new possibilities for weak lensing measurements, particularly in the context of large scale wide-field surveys that are currently being planned for and/or proposed. The ML approach can be developed and extended in order to apply it to much larger areas of sky and we have shown in Chapter 3 that it is the most suitable method for reconstructing the weak lensing power spectrum. Applying the ML analysis to one of these large scale surveys would enable the shear power spectrum to be measured to much greater accuracy (*e.g.* better than 5% with the proposed VST lensing survey; Taylor et al. 2001b). This is demonstrated in Fig. 5.1 which shows the constraints obtainable on the shear power spectrum from a 250 sq. degree VST survey in comparison to the $C'^{\kappa\kappa}_\ell$ measurements obtained in Chapter 3.

The nature of the COMBO-17 dataset with its unique redshift information also opens up the possibility of performing 3D lensing (Taylor, 2001) on real data. Such an analysis is, in fact, underway on the COMBO-17 dataset, results of which should be appearing in the near future.

The method can also be extended in order to measure other quantities such as the bias of galaxies with respect to the dark matter or even the fundamental 3-d matter power spectrum, $P(k)$. A full ML analysis — like the one presented in this thesis — coupled with the large amounts of quality data expected from several upcoming experiments will truly bring the technique of weak gravitational lensing into the field of precision cosmology. Such a project would be competitive with and complementary to other cosmological probes such as galaxy redshift surveys and measurements of the CMB. For example, weak lensing measurements can be used to probe the dark energy, $\Omega_{\rm de}$ in a way complementary to and completely independent from CMB + Supernovae (SN) measurements (*e.g.* Tyson et al. (2002)

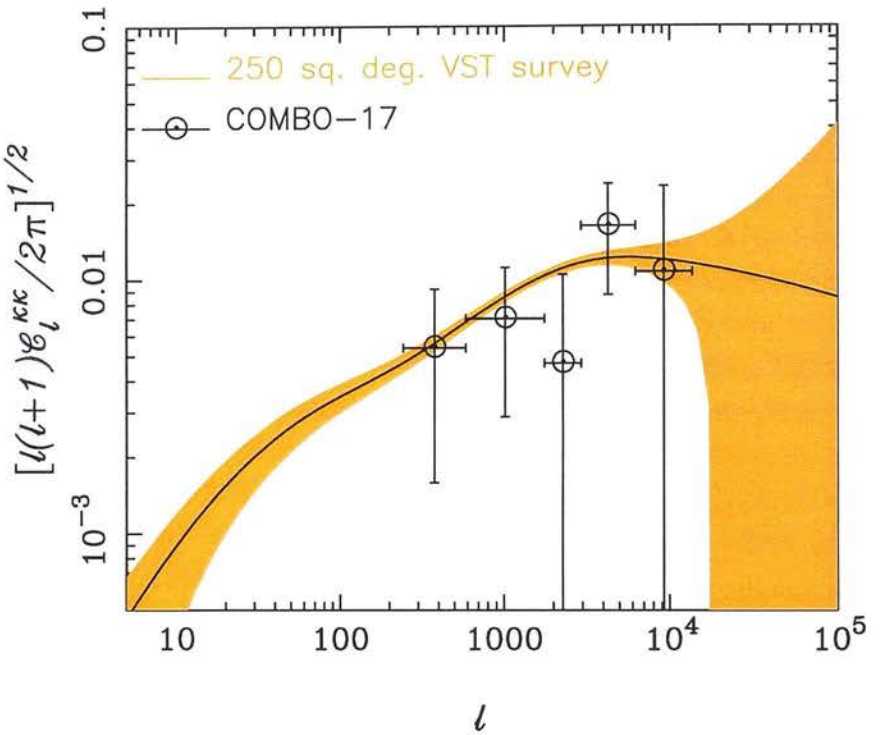

Figure 5.1: Constraints obtainable (shaded area) on the weak lensing shear power spectrum with the proposed 250 sq. degree VST survey assuming median seeing conditions of $\theta_s = 0.7$ arcsec and a galaxy number density of 30 arcmin^{-2}. The measurements obtained in Chapter 3 are shown for comparison. The full solid line is the non-linearly evolved shear power spectrum for source galaxies located at $z_m = 1$ for the $\Omega_m = 0.3$ ΛCDM model normalised to $\sigma_8 = 1.0$.

and references therein), and to sharply constrain the dark energy equation of state, w through the time evolution of the number of mass over-densities (Hu 2002). The work presented in Chapter 3 of this thesis represents a significant step along the road in achieving some of these very ambitious aims.

5.2 Intrinsic Galaxy Alignments

In Chapter 4 of this thesis we presented a measurement of the *intrinsic alignment* of galaxy shapes in the SuperCOSMOS Sky Survey. In this analysis we measured the shapes of $\sim 2 \times 10^6$ galaxies and found them to be correlated with one another over a range of scales between 1 and 100 arcmin. We found that the intrinsic alignment effect would be important in other shallow surveys (*e.g.* the Sloan Digital Sky Survey) and thus could dominate the weak lensing signal of large scale structure in such surveys. It is interesting to ask to what degree intrinsic galaxy alignments might contaminate the cosmic shear analysis presented in Chapter 3. We have already seen in Chapter 4 that we expect the

ratio of intrinsic alignment to gravitational shear to scale as

$$\frac{\sigma^2_{\rm int}}{\sigma^2_{\rm lens}} \approx 10^2 \left(\frac{z}{0.1}\right)^{-3.5}. \tag{5.1}$$

For the median redshift of the source galaxies in COMBO-17 of $z_m = 0.85$, this ratio is $\sim 5\%$ which is well within the error bars on *e.g.* the shear power spectrum measurements of Fig. 3.22. Our conclusions of Chapter 3 are therefore not altered by the measurement of intrinsic shape correlations presented in Chapter 4.

We have already touched on the fact that intrinsic shape alignments are interesting in their own right. It should, in principle, be possible to probe the underlying matter distribution with measurements such as those presented in Chapter 4 (*e.g.* Lee & Pen 2001). However, at present the relationships between the inertial and tidal tensors and between galactic discs and the angular momentum of the parent halos are not sufficiently well understood to make such an investigation possible. It may be that the answer to this puzzle lies in further simulation work. If the relation between the underlying shear field and the induced intrinsic alignment signal could be calibrated from simulations, then this calibration could be used to interpret observations of intrinsic shape alignments and hence, to infer the underlying matter distribution from these observations. Such a method would represent a powerful new probe of dark matter on local scales and would act as a natural complement to weak lensing measurements which probe the dark matter distribution at higher redshift and on larger scales.

Bibliography

Alcock C., et al. , 2000, ApJ, 545, 281

Allen S. W., Schmidt R. W., Fabian A. C., Ebeling H., 2002, MNRAS, submitted (astro-ph 0208394)

Bacon D. J., Massey R. J., Refregier A., Ellis R., 2002, MNRAS, submitted (astro-ph 0203134)

Bacon D. J., Refregier A., Ellis R., 2000, MNRAS, 318, 625 (BRE)

Bacon D. J., Refregier A., Clowe D., Ellis R., 2001, MNRAS, 325, 1065

Bacon D. J., Taylor A. N., 2002, MNRAS, submitted (astro-ph 0212266)

Barber A., 2002, MNRAS, 335, 909

Bardeen J.M., 1980, Phys. Rev. D., 22, 1882

Bartelmann M., Narayan, R., 1995, ApJ, 451, 60

Bartelmann M., Schneider, P., 2001, Physics Reports, 340, 291

Baugh C. M., Efstathiou G., 1991, MNRAS, 265, 145

Berezinsky V., 2002, Astroparticle Physics, 17, 509

Bernardeau F., Van Waerbeke L., Mellier Y., 1997, A&A, 322, 1

Bernstein G., Jarvis M., 2002, AJ, 123, 583

Bertin E., Arnouts S., 1996, A&AS, 117, 393

Borgani S. et al., 2001, ApJ, 561, 13

Broadhurst T. J., Taylor A. N., Peacock J. A., 1995, MNRAS, 299, 895

Brown M. L., Taylor A. N., Hambly N. C., Dye S., 2002a, MNRAS, 333, 501

Brown M. L., Taylor A. N., Bacon D. J., Gray M. E., Meisenheimer K., Dye S., Wolf C., 2003, MN-

RAS, 341, 100 (astro-ph 0210213)

Bunn E., 2002, Phys. Rev. D., 65, 4

Carroll S. M., Press W. H., Turner E. L., 1992, ARA&A, 30, 499

Carter D., 1980, MNRAS, 190, 307

Catelan P., Kamionkowski M., Blandford R. D., 2001, MNRAS, 323, 713

Chang K., Refsdal S., 1979, Nature, 282, 561

Chiba T., Mukohyama S., Nakamura T., 1997, Phys. Lett. B, 408, 47

Cohen J. G., Hogg D. W., Blandford R., Cowie L. L., Hu. E., Songaila A., Shopbell P., Richberg K., 2000, ApJ, 538, 29

Cooray A., Hu W., 2001, ApJ, 554, 56

Crittenden R., Natarajan P., Pen U., Theuns, T., 2001, ApJ, 545, 561

Croft. R. A. C., Metzler C. A., 2001, ApJ, 545, 561 (CM)

Davis M., Peebles P. J. E., 1983, ApJ, 267, 465

de Bernardis P. et al., 2002, ApJ, 564, 559

Doroshkevich A. G., 1970, Afz, 6, 581

Dye S., 1999, Ph. D. Thesis, University of Edinburgh

Efsthathiou G. et al., 2002, MNRAS, 330, L29

Einhorn M. B., Stein D. L., Toussaint D., 1980, Phys. Rev. D, 21, 3295

Eisenstein D., Hu W., 1998, ApJ, 496, 605

Eke V. R., Cole S., Frenck C. S., Henry J. P., 1998, MNRAS, 298, 1145

Fischer P., 1999, AJ, 117, 2024

Fisher, R. A., 1935, J. Roy. Stat. Soc., 98, 39

Freedman W. L. et al., 2001, ApJ, 553, 47

Garnavich P. M., et al. , 1998, ApJ, 493, L53

Gott J. R., 1981, ApJ, 243, 140

Gray M. E., Taylor A. N., Meisenheimer K., Dye S., Wolf C., Thommes E., 2002, ApJ, 568, 141 (GTM+)

Hamana T. et al., 2002, ApJ, submitted (astro-ph 0210450)

Hambly N.C., et al., 2001a, MNRAS, 326, 1279

Hambly N.C., Irwin M.J., MacGillivray H.T., 2001b, MNRAS, 326, 1295

Hambly N.C., Irwin M.J., Davenhall, A.C., MacGillivray H.T., 2001c, MNRAS, 326, 1315

Hamilton A. J. S., Kumar P., Lu E., Matthews A., 1991, ApJ, 374, L1

Harrison E. R., 1970, Phys. Rev. D, 1, 2726

Heavens A. F., Refregier A., Heymans C., 2000, MNRAS, 319, 649 (HRH)

Heymans C., Heavens A. F., 2003, MNRAS, 339, 711 (astro-ph 0208220)

Hoekstra H., Franx M., Kuijken K., Squires G., 1998a, New Astronomy Review, 42, 137

Hoekstra H., Franx M., Kuijken K., Squires G., 1998b, ApJ, 504, 636

Hoekstra H., Yee H. K. C., Gladders M. D., 2001, ApJ, 558, L11

Hoekstra H., Van Waerbeke L., Gladders M. D., Mellier Y., Yee H. K. C., 2002a, ApJ, 577, 604

Hoekstra H., Yee H. K. C., Gladders M. D., Barrientos L. F., Hall P. B., Leopoldo I., 2002b, ApJ, 572, 55

Hoekstra H., Franx M., Kuijken K., van Dokkum P. G., 2002c, MNRAS, 333, 911

Hoyle, F., 1949, in Burgers J.M., van de Hulst H.C., eds., in Problems of Cosmic Aerodynamics, Central Air Documents, Dayton, Ohio, p195

Hu W., 2000, Phys. Rev. D., 62, 3007

Hu W., 2002, Phys. Rev. D., 66, 083515 (astro-ph 0208093)

Hu W., Keaton C. R., 2002, Phys. Rev. D., 66, 063506 (astro-ph 0205412)

Hu W., Tegmark M., 1999, ApJ, 514, L65

Hu W., White M., 2001, ApJ, 554, 67 (HW)

Jain B., 2002, ApJ, 580, L3

Jain B. Mo H. J., White S. D. M., 1995, MNRAS, 276, L25

Jain B., Seljak U., 1997, ApJ, 484, 560

Jarvis M., Bernstein G. M., Fischer P., Smith D., Jain B., Tyson J. A., Wittmann D., 2003, AJ, 125, 1014 (astro-ph 0210604)

Jenkins A. et al. , 1998, ApJ, 499, 20

Jing Y. P., 2002, 335, L89

Jungman G., Kamionkowski M., Griest K., 1996, Physics Reports, 267, 198

Kaiser N., 1992, ApJ, 388, 272

Kaiser N., 1998, ApJ, 498, 26

Kaiser N., Squires G., 1993, ApJ, 404, 441

Kaiser N., Squires G., Broadhurst T. J., 1995, ApJ, 449, 460 (KSB)

Kaiser N., Wilson G., Luppino G., et al. , 1998 ApJ, submitted (astro-ph/9809268)

Kaiser N., Wilson G., Luppino G., 2000, ApJ, submitted (astro-ph 0003338)

Kaiser N., Wilson G. Luppino G., Dahle H., 1999, PASP submitted (astro-ph 9907229)

Kamionkowski M., Babul A., Cress C. M., Refregier A., 1998, MNRAS, 301, 1064

Kandrup H. E., 1992, Phys. Rev. D, 46, 5360

Kendall M. G., Stuart A., 1969, "The Advanced Theory of Statistics", Volume II, Griffin, London

Kenney J. F., Keeping E. S., 1951, "Mathematics of Statistics, Part II", 2nd. ed., Van Nostrand, New York

King L., Schneider P., 2002, A&A, 396, 411 (astro-ph 0208256)

Kirkmann D., Tytler D., O'Meara J. M. et al. , 2001, ApJ, 2001, 559, 23

Knox L., Christensen N., Skordis C., 2002, ApJ, 563, L95

Kochaneck C. S., 1990, MNRAS, 247, 135

Kolb E. W., Turner M. S., "The Early Universe", 1990, Addison-Wesley

Kristian J., Sachs R. K., 1966, ApJ, 143, 379

Lahav O. et al., 2002, MNRAS, 333, 961

Lasserre T., et al. , 2000, A&A, 355, L39

Lee J., Pen U., 2000, ApJ, 532, L5

Lee J., Pen U., 2001, ApJ, 555, 106

Lee J., Pen U., 2002, ApJ, 567, L111

Lewis A., Bridle S., 2002, Phys. Rev. D., 66, 103511 (astro-ph 0205436)

Lifshitz E. M., 1946, J. Phys. USSR, 10, 116

Luppino G. A., Kaiser N., 1997, ApJ, 475, 20

Mackey J., White M., Kamionkowski M., 2002, MNRAS, 332, 788

Melchiorri A., Silk, J., 2002, Phys. Rev. D., 66, 041301 (astro-ph 0203200)

Mellier Y., 1999, ARA&A, 37, 127

Miralda-Escudé J., 1991, ApJ, 370, 1

Narayan R., Bartelmann M., 1997, in Proc. of the 1995 Jerusalem Winter School, eds. Dekel A., Ostriker J. P.

O'Meara J. M., Tytler D., Kirkmann D., Suzuki N., Prochaska J. X., Lubin D., Wolfe A. M., 2001, ApJ, 552, 718

Paczyński B., 1986, ApJ, 304, 1

Padmanabhan T., 1993, "Structure Formation in the Universe", C.U.P.

Peacock J. A., 1999, "Cosmological Physics", C.U.P.

Peacock J. A., Dodds S. J., 1996, MNRAS, 280, L19

Peacock J. A., Smith R. E., 2000, MNRAS, 318, 1144

Peacock J. A., et al. , 2001, Nature, 410, 169

Peebles P. J. E., Yu J. T., 1970, ApJ, 162, 815

Pen U., Lee J., Seljak U., 2000, ApJ, 543, L107

Pen U., Van Waerbeke L., Mellier Y., 2002, ApJ, 567, 31

Percival W. J. et al., 2002, MNRAS, 337, 1068

Perlmutter S. et al. , 1999, ApJ, 517, 565

Pierpaoli E., Borgani S., Scott D., White M., 2002, MNRAS, submitted (astro-ph 0210567)

Pierpaoli E., Scott D., White M., 2001, MNRAS, 325, 77

Press W., Schechter P., 1974, ApJ, 187, 425

Press W. H., et al. , 1992, "Numerical Recipies", Second Ed., C.U.P.

Pryke C., Halverson W., Leitch E. M., Kovac J., Carlstrom J. E., Holzapfel W. L., Dragovan M., 2002, ApJ, 568, 46

Riess A. G., et al. , 1998, AJ, 116, 1009

Reiprich, T. H., Böhringer H., 2002, ApJ, 567, 716

Refregier A., Bacon D. J., 2003, MNRAS, 338, 48

Refregier A., Rhodes J., Groth E. J., 2002, ApJ, 572, L131

Sachs R. K., 1973, in Relativity, Astrophysics and Cosmology, ed. Israel W., Reidel

Sachs R. K., Wolfe A. M., 1967, ApJ, 147, 73

Schneider P., Ehlers J., Falco E., 1992, "Gravitational Lenses", Springer

Schneider P., Seitz C., 1995, A&A, 294, 411

Schneider P. Van Waerbeke L., Kilbinger M., Mellier Y., 2002, A&A, 396, 1 (SvWKM)

Schuecker P., Böhringer H., Collins C. A., Guzzo L., 2003, A&A, 398, 867 (astro-ph 0208251)

Seitz S., Kneib J. P., Schneider P., Seitz C., 1996, A&A, 314, 707

Seljak U., 2000, MNRAS, 318, 203

Seljak U., 2002, MNRAS, 337, 769

Smith R. E., Peacock J. A., Jenkins A., White S. D. M., Frenk C. S., Pearce F. R., Thomas P. A.,

Efstathiou G., Couchman H. M. P., 2002, MNRAS, submitted (astro-ph 0207664)

Squires G., Kaiser N., 1996, ApJ, 473, 65

Squires G., Neumann D. M., Kaiser N., Arnaud M., et al. , 1997, ApJ, 482, 648

Stebbins A., 1997, preprint (astro-ph 9609149)

Stobie R.S., 1986, Pattern Recognition Letters, 4, 317

Taylor A. N., 2001, Phys. Rev. Lett, submitted (astro-ph 0111605)

Taylor A. N., Ballinger W. E., Heavens A. F., Tadros H., 2001a, MNRAS, 327, 689

Taylor A. N., et al. , 2001b, VST Observing Proposal

Taylor A. N., Dye S., Broadhurst T. J., Benitez N., van Kampen E., 1998, ApJ, 501, 539

Tegmark M., de-Oliviera Costa A., 2002, Phys. Rev. D, 64, 63001

Tegmark M., Taylor A. N., Heavens A. F., 1997, ApJ, 480, 22

Tyson J., Wittmann D. W., Hennawi J. F., Spergel D. N., 2002, in Proc. 5th International UCLA Symposium on Sources and Detection of Dark Matter, Marina del Rey, ed. Cline D. (astro-ph 0209632)

Van Waerbeke L., et al, 2000, A&A, 358, 30

Van Waerbeke L., et al., 2001, A&A, 374, 757

Van Waerbeke L., Mellier Y., Pelló R., Pen U., McCracken H. J., Jain B., 2002, A&A, 393, 369

Verde L., Heavens A. F., Percival W. J. et al. , 2002, MNRAS, 335, 432

Viana P. T., Liddle A. R., 1999, MNRAS, 303, 535

Viana P. T., Nichol R. C., Liddle A. R., 2002, ApJ, 569, L75

Wallace, P.T., Tritton, K.P., 1979, MNRAS, 189, 115

Wang L., Caldwell R. R., Ostriker J. P., Steinhardt P. J., 2000, ApJ, 530, 17

Wang X., Tegmark M., Zaldarriaga M., 2002, Phys. Rev. D., 65, 123001, in press (astro-ph 0105091)

Webb J. K., Carswell R. F., Irwin M. J., Penston M. V., 1991, MNRAS, 250, 657

Weinberg S., 1972, "Gravitation and Cosmology", New York: Wiley

White S. D. M., 1984, ApJ, 286, 38

Wittman D.M., Tyson J.A, Kirkman D., Dell'Antonio I., Bernstein G., 2000, Nature, 405, 143

Wolf C., Dye S., Kleinheinrich M., Rix H.-W., Meisenheimer K., Wisotzki L., 2001, A&A, 377, 442

Wolf C., Meisenheimer K., Rix H.-W., Borch A., Dye S., Kleinheinrich M., 2003, A&A, 401, 73 (astro-ph 0208345)

Wynne, C.G., 1981, Q. Jl. RAS, 22, 146

Zebrun K., et al. , 2001, Acta Astronomica, 51, 317

Zel'dovich Y. B., 1972, MNRAS, 160, 1

Zel'dovich Y. B., Novikov I. D., 1983, "Relativistic Astrophysics, Volume 2: The Structure and Evolution of the Universe", The University of Chicago Press